Analytical and numerical studies of thalamo-cortical neural population models during general anesthesia

Meysam Hashemi

To cite this version:

Meysam Hashemi. Analytical and numerical studies of thalamo-cortical neural population models during general anesthesia. Other [cs.OH]. Université de Lorraine, 2016. English. NNT : 2016LORR0014 . tel-01754610v1

HAL Id: tel-01754610
https://hal.univ-lorraine.fr/tel-01754610v1

Submitted on 30 Mar 2018 (v1), last revised 1 Feb 2016 (v2)

UNIVERSITÉ
DE LORRAINE

École doctorale IAEM Lorraine

Modélisation mathématique et simulation numérique de populations neuronales thalamo-corticales dans le contexte de l'anesthésie générale

Analytical and numerical studies of thalamo-cortical neural population models during general anesthesia

THÈSE

présentée et soutenue publiquement le 14 Janvier 2016

pour l'obtention du

Doctorat de l'Université de Lorraine

(mention informatique)

par

Meysam HASHEMI

Composition du jury

Directeur :	HUTT Axel, Directeur de Recherche à l'INRIA Nancy Grand-Est.
Rapporteurs :	BOJAK Ingo, Professeur à l'University of Reading, UK. GUTKIN Boris, Directeur de Recherche à l'École Normale Supérieure. COLLET Pierre, Professeur à l'Université de Strasbourg.
Examinateurs :	HENAFF Patrick, Professeur à l'École des Mines de Nancy. BUHRY Laure, Maître de conférences à l'Université de Lorraine.

Laboratoire Lorrain de Recherche en Informatique et ses Applications — UMR 7503

Mis en page avec la classe thesul.

Abstract

Although general anesthesia is an indispensable tool in today's medical surgery, its precise underlying mechanisms are still unknown. During the propofol-induced sedation, the anesthetic actions on the microscopic single neuron scale lead to specific changes in macroscopic-scale observables such as electroencephalogram (EEG) signals. For low concentration of propofol these characteristic changes comprised increased activity in the $\delta-$ (0.5-4 Hz) and $\alpha-$ (8-13 Hz) frequency bands over the frontal head region, but increased $\delta-$ and decreased $\alpha-$power activity over the occipital region. In this thesis, we employ thalamo-cortical neural population models, and based on the experimental data, the propofol effects on the synaptic and extra-synaptic GABAergic receptors located in the cortex and thalamus are modelized to understand the mechanisms underlying the observed certain changes in EEG-spectral power. It is shown that the models reproduce well the characteristic spectral features observed experimentally. A key finding of this work is that the origin of $\delta-$rhythm is fundamentally different from the $\alpha-$rhythm. Our results indicate that dependent on the mean potential values of the system resting states, an increase or decrease in the thalamo-cortical gain functions results in an increase or decrease in the $\alpha-$power, respectively. In contrast, the evolution of the $\delta-$power is rather independent of the system resting states; the enhancement of spectral power in the $\delta-$band results from the increased synaptic or extra-synaptic GABAergic inhibition for both increasing and decreasing nonlinear gain functions. Furthermore, we aim to identify the parameters of a thalamo-cortical model by fitting the model power spectrum to the EEG recordings. To this end, we address the task of parameter estimation in the models that are described by a set of stochastic ordinary or delay differential equations. Two case studies dealing with noisy pseudo-experimental data are first carried out to compare the performance of different optimization methods. The results of this elaboration show that the method used in this study is able to accurately estimate the independent model parameters while it allows us to avoid the computational costs of the numerical integration. Taken together, the findings of this thesis provide new insights into the the mechanisms responsible for the specific changes in EEG patterns that are observed during propofol-induced sedation.

Keywords: general anesthesia, thalamo-cortical neural population models, propofol, EEG-spectral power, optimization algorithms.

Résumé

Bien que l'anesthésie générale est un outil indispensable dans la chirurgie médicale d'aujourd'hui, ses mécanismes sous-jacents précis sont encore inconnus. Au cours de la sédaction induite par le propofol les actions anesthésiques à l'échelle microscopique du neurone isolé conduisent à des changements spécifiques à l'échelle macroscopique qui sont observables comme les signaux électroencép-halogrammes (EEG). Pour une concentration faible en propofol, ces changements caractéristiques comprennent une augmentation de l'activité dans les bandes de fréquence δ (0.5-4 Hz) et α (8-13 Hz) dans la région frontal, une l'activité augmentée de δ et une l'activité diminuée de α dans la région occipital. Dans cette thèse, nous utilisons des modèles de populations neuronales thalamo-corticales basés sur des données expérimentales. Les effets de propofol sur les synapses et sur les récepteurs extra-synaptiques GABAergiques situés dans le cortex et le thalamus sont modélisés afin de comprendre les mécanismes sous-jacents aux changements observés dans certains puissance de l'EEG-spectrale. Il est démontré que les modèles reproduisent bien les spectrales caractéristiques observées expérimentalement. Une des conclusions principales de ce travail est que l'origine des $\delta-$rythmes est fondamentalement différente de celle des $\alpha-$rythmes. Nos résultats indiquent qu'en fonction des valeurs moyennes des potentiels de l'état du système au repos, une augmentation ou une diminution des fonctions de gain thalamo-corticale résulte respectivement en une augmentation ou une diminution de $\alpha-$puissance. En revanche, l'évolution de la $\delta-$puissance est plutôt indépendant de l'état du système au repos; la amélioration de la puissance spectrale de $\delta-$bande résulte de l'inhibition GABAergique synaptique ou extra-synaptique pour les fonctions de gain non linéaire à la fois croissante et décroissante. De plus, nous cherchons à identifier les paramètres d'un modèle de thalamo-corticale en ajustant le spectre de puissance de modèle pour les enregistrements EEG. Pour ce faire, nous considérons la tâche de l'estimation des paramètres dans les modèles qui sont décrits par un ensemble d'équations différentielles ordinaires ou bien stochastiques avec retard. Deux études de cas portant sur des données pseudo-expérimentale bruyants sont d'abord effectuées pour comparer les performances des différentes méthodes d'optimisation. Les résultats de cette élaboration montrent que la méthode utilisée dans cette étude est capable d'estimer avec précision les paramètres indépendants du modèle et cela nous permet d'éviter les coûts de calcul des intégrations numériques. En considérant l'ensemble, les conclusions de cette thèse apportent de nouveaux éclairages sur les mécanismes responsables des changements spécifiques qui sont observées pendant la sédation propofol-induite dans les modèles de EEG.

Mots-clés: L'anesthésie générale, modèles de populations neuronales thalamo-corticales, propofol, spectre de puissance de I'EEG, algorithmes d'optimisation.

To reaserchers, teachers, students, and everybody
who sacrificed his/her life to achieve
what we know today.

Acknowledgments

I take this opportunity to thank all the people who have helped and supported me to pursue my studies towards obtaining my Ph.D. degree. First and foremost, I am incredibly grateful to my thesis advisor, Prof. Axel Hutt, for all his invaluable help and advice during my dissertation. I deeply appreciate his extremely constructive guidance to progress my thesis. Without his continuous support it would not be possible to conduct this research. Besides my advisor, I wish to thank Prof. Jamie Sleigh for supplying the experimental records and his excellent advice that greatly improved my research. I am also very grateful to Laurence Benini for all of her generous help in dealing with administrative issues.

I would like to express sincere gratitude to my thesis committee: Prof. Ingo Bojak, Prof. Boris Gutkin, Prof. Pierre Collet, Prof. Patrick Henaff and Dr. Laure Buhry, for their insightful comments. I am also thankful to all Neurosys members for their constructive comments on my dissertation research and for sharing their expertises with me. I am deeply indebted to my master advisor, Dr. Alireza Valizadeh, who supported me to start my Ph.D. in France.

A huge thanks goes to my officemates Benoit Chappet de Vangel, Mariia Fedotenkova, Francesco Giovannini, Cecilia Lindig-Leon and Georgios Detorakis who provided a very friendly environment to work. I am immensely grateful to Pedro Garcia Rodriguez and Laure Buhry for fruitful discussions throughout my dissertation. I would also like to thank my friends Nicoles Voges, Yones Rahmani and Yaser Hafeznia for all the enjoyable moments we have had during my settling in Nancy. Furthermore, I would like to thank my dear friend, Ramin Shariat Moharreri, for supporting me from Iran.

Last but certainly not least, I would like to express the deepest appreciation to my beloved mother for all her encouragement and support and the sacrifices she has made for me through my entire life. I would also like to extend my heartfelt gratitude to my lovely brothers Amir, Mehdi and Ehsan for the unceasin encouragement and priceless support. A special thanks goes to my elder brother, Amir, who has always been a tremendous mentor for me.

I wish my father was still alive to have him by my side. He always encouraged and supported me spiritually to continue my studies. I am eternally grateful to him, forever.

The research resulting to the presented work has received funding from the European Research Council under the European Unions Seventh Framework Programme (FP7/2007-2013)/ERCgrant agreement no.257253.

Contents

Chapter 3
Modeling the anesthetic action on synaptic and extra-synaptic receptors 37

Chapter 4
Modeling of EEG power spectrum over frontal and occipital regions during propofol sedation 54

Chapter 5
Spectral power fitting using stochastic optimization algorithms 78

References

List of Figures

List of Tables

General Introduction

General anesthesia is a reversible drug-induced medical procedure, which aims to achieve amnesia (lack of memory), **sedation** (reduced arousability), unconsciousness (lack of awareness also called hypnosis), and immobility (lack of movement) in patients. Muscle relaxation and analgesia (lack of pain) are sometimes included in definitions of the anesthetized state. The word **"Anesthesia"** comes from Greek word anesthesia meaning *"lack of sensation"*; **"an"**- means *"without"*, and **"aisthesis"** means *"feeling"*. General anesthesia is an indispensable tool in today's medical surgery. For instance, it has been reported that in the United States more than 21 million patients [1] and in North America around 40 million patients [2] each year receive general anesthesia for surgery . However, despite the widespread use of general anesthesia in today's medical practice, its precise underlying mechanism is still unknown.

General anesthetics include a large number of drugs, which without them, the modern clinical surgery would not have been possible. Joseph Priestley discovered nitrous oxide, also known as laughing gas, in 1772. Some years later, Humphry Davy started experimenting with nitrous oxide [3]. In 1844, dentist Horace Wells first used nitrous oxide as an anesthetic during tooth surgery treatment of a patient. However, the anesthetic was incomplete and his attempt was unsuccessful. After Horace Wells unsuccessfully promoted nitrous oxide as an anesthetic, William Morton concentrated on the possibility of ether [3]. In 1842, physician Crawford Williamson Long was the first to use ether as a general anesthetic during a surgery to remove a tumor. His experiments, however, was unrecorded, and on 16 October 1846, the first successful public demonstration of ether anesthesia was performed by William Thomas Green Morton at theatre of the Massachusetts General Hospital [3]. Whereas, neither ether nor chloroform is used in today's surgery, nitrous oxide is one of the most widely used anesthetics in dentistry and emergency centers. Since then, many anesthetic drugs such as barbiturates, thiopental, etomidate, halothane, isoflurane, sevoflurane, ketamine, and propofol were introduced as anesthetic drugs [3]. **Propofol**, an emulsion formulation of 2,6-di-isopropylphenol, is a short-acting, intravenously administered hypnotic agent, which is popular among patients because of its relatively fast onset and offset, and anti-emetic effects [4]. The present work is primary focussed on the mechanism actions of this agent, since it is widely used in clinical medicine and theoretical studies, and its molecular effects is relatively well-understood.

During most of the 20th century, anesthetics were widely thought to work by dissolving in the cell membrane and the lipid cell membrane of neurons are the action target of anesthetic agents [5, 6]. In other words, anesthetic agents act through a common and nonspecific mechanism. However, in recent years, significant progress has been made toward our understanding of how anesthetic agents act on the single neurons (microscopic scale) [7, 8, 9]. An enormous body of evidence indicates that anesthetics directly bind to specific proteins, known as receptors, and there is not a single mechanism of action for all anesthetic agents [10, 11, 12]. Among different candidates, the ligand-gated ion channels are the most likely molecular targets for the anesthetics [10, 13]. Now, there is a general agreement that **GABA** receptors as the major inhibitory neurotransmitter in the CNS play a central part in the actions of anesthetic drugs [2, 14]. It is widely accepted that GABA subtype A, or $\mathrm{GABA_A}$ receptor is a primary target for anesthetics [15, 16]. Anesthetics prolong the duration of chloride channel opening at the $\mathrm{GABA_A}$ receptors and thereby the function of this target is enhanced by the anesthetics action [10]. Due to the molecular effects of anesthetics, during transition to anesthesia, specific changes in brain imaging data such as **EEG** patterns can be observed experimentally [17]. For clinically relevant concentration of propofol these characteristic changes comprised increased activity in the **delta** (0.5-4 Hz) and **alpha** (8-13 Hz) frequency bands over the frontal head region, but increased delta and decreased alpha activity over the occipital region [18, 19]. An important question raised here is how the anesthetic actions on the microscopic single neuron scale could lead to changes in EEG and behavior that can be observed at macroscopic scales. It is one major aim of this thesis to address this important question by establishing a link between the two scales.

Today general anesthesia works well in most cases, however, it is certainly not without risk. Approximately, one out of 13,000 patients die from anesthesia-related incidents, and about one or two patient in every 1,000 cases may gain awareness while receiving general anesthesia. Broadly speaking, the procedure of anesthesia is mainly based on the experience of the anesthesiologists and it depends strongly on the general health of the patients. In other word, it is performed according to the clinical responses of individual patients. During the operation, anesthesiologists monitor the physiological systems as well as the electrical brain activities of the patient to adapt the anesthetic concentration constantly to control the depth of anesthesia. Clinical and physiological signs such as blood pressure, heart rate or involuntary movements can be affected by the administration of other drugs and thus can be difficult to interpret in practice. In contrast, recording the anesthetic effects in the EEG signals provides more reliable assessment of a patient's level of consciousness during the administration of anesthetic agents. Consequently, several EEG-based monitoring parameters have been widely used for estimating the anesthetic depth. According to EEG information, indicators such as BIS index, spectral edge frequency (SEF50 or SEF95) and median frequency have been designed to quantitatively determine the depth of anesthesia. However, estimating the depth of anesthesia is still a challenging area in anesthesia research. A thorough understanding of the mechanisms underlying anesthesia is crucial to improve the monitoring methods. **Mathematical modeling** of electrical brain activities offer a promising avenue for exploring the validity of hypotheses about the mechanisms of anesthesia, and in general, the mechanisms underlying the brain activities during different functional states.

The modeling of brain activities can be performed in different scales from single neurons to neural populations. To reveal the molecular actions of anesthetics at microscopic level, we can rely on the models that describe the dynamics of the single neurons. However, simulation of the activity of even a small brain region by the detailed biophysical modeling of synapses and spiking neurons is very computationally expensive. For instance, a realistic neuronal network such as a cortical column has a huge number of neurons (on the order of 10^4-10^8 neurons), while each neuron can be synaptically connected with 10^4-10^5 others [20]. In addition, the physiological topology of real neuronal networks is rather unknown. Relating the behavioral phenomena that are observed at the macroscopic scales to the individual elements of such large ensembles is also extremely challenging. In contrast, most of the coarse-scale observables such as EEG data reflect the overall activity of a large population of neurons [21, 22]. This aspect allows us to successfully simulate the empirical EEG signals by **mean-field** approximation [23, 24, 25]. The details of individual neurons such as action potentials and the dynamic of ion channels do not explicitly appear in mean field models, but are considered indirectly in the description. The general aim of mean field models is to describe average properties of population of neurons in small spatial patches and short time windows, through a set of differential equations or integral-differential equations [26, 27]. This approach typically considers ensembles of excitatory and inhibitory neurons, which incorporates the connection elements between neurons as excitatory and inhibitory synapses [23, 28]. A factor common to all versions of mean field models is that the mean membrane potentials and mean firing rates of neurons are related to each other by a sigmoidal function.

In recent decades, mean field models have been extensively employed to reproduce the EEG signals [29, 30, 31, 24]. The simulation results of such coarse-grained models display remarkably close agreement with the empirical observations [32, 33]. This description has proven successful in reproducing key features of electrical brain waves observed in humans during different brain functional states such as sleep states [29, 34], and anesthesia condition [35, 36, 37]. It is important to note that the mean field models consider neural populations on a mesoscopic spatial level (hundreds of micrometers). Such a mesoscopic model allows us to bridge the various spatial scales in the brain, from the microscopic scale of single neurons to the macroscopic scale i.e., the level of EEG/MEG recordings [20, 25]. Today, there exists a reasonable understanding on the molecular mechanisms of anesthetic actions [10]. However, how the microscopic effects at receptor sites can be related to the specific changes in macroscopic observables such as EEG data is poorly understood. The present work employs mean field models to provide a link between the effects of anesthetics on single neurons and their impact on the global activity of the neural populations as recorded by neuroimaging techniques.

In the last decades many works have been focussed onto the study of molecular effects of anesthetic agents [10, 9]. The study of neural population models under the effect of anesthetics has been triggered by the work of Steyn-Ross et al. (1999), who proposed a model for a cortical macro column which received external stochastic stimuli from subcortical areas [38, 39, 40]. Since then, many mathematical models at population level and single neuron level have been proposed to understand the mechanisms underlying general anesthesia [24, 41, 28, 35]. Most of previous theoretical studies focussed on the dynamic of cortical neurons [24, 41, 28]. However, several lines of evidence indicate that the thalamus and the thalamo-cortical circuits are important target sites for the general anesthetics [9, 42, 43]. While the **cortex** is known as the source of the brain's spontaneous electrical activity, the **thalamus** acts as both the gate for sensory input to the cortex and the site for feedback from cortical cells [44, 45]. It has been demonstrated that the thalamus is central to the processing and transmission of nearly all sensory information that ultimately reaches the cortex. Furthermore, there is accumulating evidence showing that the **thalamo-cortical** circuits crucially involve in the formation of sleep, normal physiologic activities, consciousness processing and anesthetic-induced unconsciousness [10, 44, 45, 46]. According to these findings, we use a model consisting of cortex and thalamus to reach more precise elucidation of physiological mechanisms. The present work considers a mean-field model of thalamo-cortical system to understand the mechanisms responsible for the specific changes in EEG patterns that are observed during propofol sedation. It includes excitatory and inhibitory cortical populations which are synaptically connected to thalamic reticular and relay neuron populations by delayed thalamo-cortical axonal fibres. The model takes into account anesthetic action at inhibitory GABAergic **synaptic** and **extra-synaptic** receptors located in cortical and thalamic neural populations.

Although it is known that the cortex, the thalamus, and the thalamo-cortical feedback loops contribute to the EEG oscillations [35], the precise role of each structure to the dynamics of EEG is unknown. By manipulation of system topology, we can obtain deeper insights into the mechanisms responsible for generation of EEG rhythms. In particular, we focus on delta and alpha frequency ranges, since during altered states of arousal, characteristic changes can be observed in these frequency bands [18, 19]. Moreover, we aim to investigate the role of synaptic and extra-synaptic inhibition mediated in cortex and thalamus in generating the key EEG signatures recorded during propofol induced sedation. For instance, we can neglect the propofol effect in cortical cells and concentrate just on the effect of propofol in thalamic neurons. This simplification emphasizes the importance of the thalamus and weakens the impact of the cortex for major neural effects under anesthesia. Since $\mathrm{GABA_A}$ receptors mediate most of the inhibitory synaptic transmission (apart from $\mathrm{GABA_B}$ receptors which are not included into model), we assume all inhibitory synaptic transmissions are mediated by $\mathrm{GABA_A}$ receptors. It has been observed experimentally that propofol increases the decay time constant of $\mathrm{GABA_A}$ synapses, and hence increases the total charge transfer in these synapses but not that of excitatory synapses [10, 9]. Interestingly propofol has been shown to have a negligible effect on the amplitude synaptic receptors in cortical neurons [47], it markedly increases amplitude, decay time, and charge transfer of $\mathrm{GABA_A}$ inhibitory postsynaptic currents evoked in relay neurons in the ventrobasal complex [48]. We modelize the mentioned propofol effects in a very close agreement with the empirical observations. Then, we seek to address the important question how these propofol effects on $\mathrm{GABA_A}$ receptors lead to the observed specific changes in **EEG-power spectrum**. In addition, we aim to investigate how the effect of the anesthetic drug propofol on GABAergic extra-synaptic receptors can change the neural population activity and the EEG signals.

Mathematical modeling is a key task in studying systems biology. The goal of modeling is to build mathematical formulations which quantitatively describe the dynamical behavior of the system under study [49, 50, 51, 52]. To achieve this goal, we first need a successful model formulation which should be able to reproduce the specific features observed in experimental data, at least qualitatively [53, 54, 55]. This task is referred to as *structure identification* [56, 57]. The subsequent task is **parameter estimation** [58, 59]. After the model identification, we need to determine the unknown model parameters. Since the model output depends on the values of model's parameters, reproducing the certain features of the experimental measurements requires selecting a suitable set of the unknown parameters. Although some of the model parameters may be measured directly in experiments, the majority of parameters has to be estimated from experimental measurements. Therefore, parameter estimation i.e. identification of the the unknown model parameters from experimental observations is one of the major steps in developing mathematical models. Nevertheless, finding a set of model parameters which accurately fits the recorded data is an extremely difficult task, especially for the nonlinear dynamic models with many parameters and constraints [54, 60].

In the recent years, considerable attention has been paid to the **optimization algorithms**. Consequently, several optimization algorithms have been proposed and successfully applied in various scientific fields. One of the successful approaches for estimating model parameters is using optimization techniques. In this approach, the parameter inference problem is converted into a functional optimization problem, i.e., minimizing a fitness function which is defined by the discrepancy between the simulated data and the measured data [61, 62, 54]. In fact the dynamic of majority of biological systems are described by differential equations rather than explicit algebraic functions [63]. Moreover, biological systems are often subject to external noise from signal stimuli and environmental perturbations. Thereby, we focus on the parameter estimation of systems whose dynamics are governed by stochastic ordinary or delay differential equations. At the final elaboration of this thesis, we aim to address the task of parameter estimation in models that are described by a set of stochastic (**ODEs** or **DDEs**) from measured data. In

this study three case studies are investigated by employing different optimization algorithms including gradient descent local search and stochastic global search methods. The performance of optimization methods is then compared to determine which search algorithm is more suitable for each of the considered parameter estimation problem. To evaluate the performance of these algorithms two case studies dealing with a set of pseudo-experimental data referred to as *in silico* parameter estimation problem are investigated: a stochastic damped harmonic oscillator, and a stochastic linear delay differential equation, which pose an unimodal and a multimodal optimization problem, respectively. In the third case study, a thalamo-cortical model is fitted to the power spectra of EEG recordings (an *in vivo* parameter estimation problem). Since the power spectrum analysis is valid only if the resting state of the system is stable, we seek the conditions which guarantee the **system stability**. The derived inequality conditions reduce the parameter searching space and thereby greatly facilitate the nonlinear estimation task. We show that the proposed model fits very well to the EEG power spectra, particularly to the power spectral peaks observed in delta and alpha frequency ranges.
Another challenge in parameter estimation problems is the identifiability of the estimates, i.e., whether the model parameters can be uniquely determined by the given experimental data [59, 64]. This task referred to as *practical identifiability* [55]. We employ different methods to address this issue. The confidence regions of the estimates are plotted and the correlation and sensitivity matrices are analyzed to examine the reliability of the estimates in each case study.

Summarizing, in this thesis we aim to touch on an important question: What is the mechanism underlying propofol sedation? To answer this question using modeling approach, based on the issues mentioned above we have to address these questions: how we can link the anesthetic actions on the molecular targets to their impact on the macroscopic observables such as EEG signals? What is the role of cortex, thalamus and thalamo-cortical circuits in generating the EEG rhythms in delta and alpha frequency ranges? Given a set of coupled differential equations and a set of experimental data, how we can identify the unknown model parameters? These questions raise a general question: What are challenging in the modeling approach to reveal the mechanisms underlying the system under study.

This thesis comprises of five chapters. Chapters 1 and 2 present the fundamental physiological and mathematical elements that we need to carry out the analytical and numerical studies. Subsequently, the results of the work are given in chapters 3-5. These latter sections are organized into two major parts. The first part is devoted to the mathematical and computational modeling of the problem, which are presented in chapters 3 and 4. In the second part, shown in chapter 5, we utilize a data-driven approach to gain new insights into the mechanisms of the system under study. In following we outline each chapter in more details.

Chapter 1 summarizes current knowledge of the neural mechanisms by which anesthetics induce general anesthesia, from single neuron level to macroscopic observations. The chapter begins with the clinical definition and the components of general anesthesia. We then briefly introduce the anesthetic agents that are most commonly used in today's medical practice and the ongoing clinical studies. Subsequently, the available information on the mechanisms of action of anesthetics at single neuron level and their molecular targets is reviewed. It is very important to study the molecular action of anesthetics since it allows us to identify which structures of the brain are essential targets for anesthetics and in turn play a major role in the induction of altered states of arousal. Following this part, we summarize the propofol effects on the EEG signals, which can be monitored experimentally to track the brain states under anesthesia. Major part of the work in this elaboration aims to link the anesthetic action at single neuron level to their effects on the macroscopic observables such as EEG data. Finally, in the last section we outline briefly the current hypotheses on the mechanisms underlying the observed changes associated with induction and maintenance of anesthesia.

Chapter 2 is devoted to the essential mathematical tools, which are basis for the research presented in the subsequent chapters. In this chapter we first describe the DDEs, and we concentrate on their stability analysis in numerical and analytical frameworks. The study of DDEs is important since the dynamics of many physical and biological systems are characterized by DDEs. In particular, we are interested in DDEs since the mean field models used in this work are governed by a set of coupled DDEs. The latter section focuses on the neural population models. We briefly describe the neural field models, which enable us to successfully simulate the electrical brain waves in a physiologically accurate approach. Finally, two well-tried neural field models in reproducing the key EEG features during different brain activities are presented: a mean field model developed by Peter Robinson and colleagues (referred to as Robinson model) and an extended neural field model based on the works of Axel Hutt (referred to as Hutt model), which will be employed in chapters 3 and 4, respectively.

Chapter 3 focuses on the role of extra-synaptic receptors in the context of anesthesia. In this chapter, we first review briefly the literature on extra-synaptic receptors and their affinity to anesthetic drugs. Then the effects of anesthetic propofol on synaptic and extra-synaptic receptors located in cortical and thalamic neural populations are modelized. Subsequently, we show how the specific features observed in frontal EEG power spectrum during propofol sedation can be reproduced by incorporating a neural population model with the anesthetic effects on GABAergic extra-synaptic receptors. Finally, the origin of spectral power peaks in delta and alpha frequency bands is discussed briefly. In the following chapter, the origin of observed delta and alpha activities in EEG spectral power is investigated in more details.

In Chapter 4, we aim to understand the mechanisms underlying the observed specific changes in frontal and occipital EEG rhythms during the propofol induced sedation. The neural population model employed in this chapter is analyzed in details to reveal the origin of spectral power peaks in delta and alpha frequency ranges. In this chapter we propose a reduced thalamo-cortical model, which is still adequate to reproduce the observed changes in EEG rhythms. In addition, the low dimensionality of this model allows us to investigate the role of system resting states, model sub-circuits and the neural populations in an analytic scheme. In final chapter, the proposed model is fitted to the EEG power spectra to quantify how close its predictions are to the experimental observations.

Chapter 5 is devoted to parameter estimation (inverse problem) i.e., the inference of model parameter values from experimental observations. In this chapter we solve the considered inverse problems by minimizing the discrepancy between the simulated output and the measured data. To this end, we apply different optimization algorithms namely Levenberg-Marquardt (LM), Particle Swarm Optimization (PSO), Differential Evolution (DE), Monte Carlo Markov Chain (MCMC) and Simulated Annealing (SA). The performance of these search algorithms is compared in the case of unimodal and multimodal optimization problems. In addition, in each of the considered case study, the precision of estimates is evaluated by plotting the confidence regions and by analyzing the sensitivity and correlation matrices.

The results obtained in this thesis are based on the experimental data that was made available by Prof. Jamie Sleigh (University of Auckland, New Zealand).

Introduction générale

L'anesthésie générale est un acte médical médicamenteux réversible dont l'objectif principal est de réaliser l'amnésie (manque de mémoire), **la sédation** (arousability réduit), l'inconscience (manque de conscience également appelé l'état d'hypnose), et l'immobilité (manque de mouvement) aux patients. La relaxation musculaire et l'analgésie (manque de douleur) sont parfois incluses dans les définitions de l'état anesthésié. Le mot **"anesthésie"** provient du mot grec *"anaisthesia"* signifie la manque de sensation ou bien l'insensibilité aux douleurs. En fait, le mot **"an"** veut dire *"la manque"* et le mot **"aisthesia"** signifie *"la sensation"*. L'anesthésie générale est un outil indispensable dans la chirurgie médicale d'aujourd'hui. Par exemple, on a signalé qu'aux Etats-Unis plus de 21 millions de patients et en Amérique du Nord autour de 40 millions de patients reçoivent chaque année l'anesthésie générale pour la chirurgie. Cependant, malgré la l'utilisation répandue de l'anesthésie générale dans la médicale pratique d'aujourd'hui, son mécanisme sous-jacente précise est encore inconnu.

Les anesthésiques généraux incluent un grand nombre de médicaments, qui, sans eux, la clinique de chirurgie moderne n'auraient pas été possibles. En 1772, Joseph Priestley a découvert le protoxyde d'azote, également connu sous le nom de gaz hilarant. Quelques années plus tard, Humphry Davy a commencé à expérimenter avec du protoxyde d'azote. En 1844, le dentiste Horace Wells pour la première fois a utilisé le protoxyde d'azote comme anesthésique pendant un traitement chirurgical dentaire d'un patient. Cependant, l'anesthésique était inachevé et sa tentative était infructueuse. Après que Horace Wells ait sans succés utilisé le protoxyde d'azote comme anesthésique, William Morton s'est concentré sur la possibilitéé d'utiliser l'éther. En 1842, le médecin Crawford Williamson Long était le premier à utiliser l'éther comme une anesthésie générale au cours d'une intervention chirurgicale pour enlever une tumeur. Ses expériences, cependant, n'étaient pas enregistrées et le 16 Octobre 1846, la première démonstration publique et réussie de anesthésie par l'éther a été réalisée par William Thomas Green Morton au théâtre de l'Hôpital Général du Massachusetts. Bien que, ni l'éther ni le chloroforme est utilisé dans la chirurgie d'aujourd'hui, le protoxyde d'azote est l'un des anesthésiques les plus utilisés dans les centres dentaires et d'urgence. Depuis, beaucoup de médicaments anesthésiques comme les barbiturates, de thiopental, l'etomidate, le halothane, l'isoflurane, le sevoflurane, le ketamine, et le propofol ont été introduits en tant que médicaments anesthésiques. Le **Propofol**, une émulsion représenté par la formule 2,6-di-isopropylphénol est un agent hypnotique de courte durée d'action (en intraveineuse administré). Il est populaire parmi des patients en raison de son début et sa fin d'action sont relativement rapids, et aussi pour des effets antiémétiques. Ce travail est focalisé premierement sur les actions du mécanisme de cet agent, car il est largement utilisé dans les cliniques médicales et les études théoriques, et ses effets moléculaires est relativement bien compris.

Pendant la majeure partie du 20ème siècle, des anesthésiques ont été largement considerés pour fonctionner par la dissolution dans la membrane plasmique et la membrane plasmique lipide des neurones sont la cible d'action des agents anesthésiques. Autrement dit, les agents anesthésiques agissent par un mécanisme commun et non spécifique. Cependant , au cours des dernières années , des progrés significatifs ont été accomplis vers la compréhension de la façon dont les agents anesthésiques agir sur les neurones individuels (échelle microscopique). Un ensemble de preuves indique que les anesthésiques se lient directement aux protéines spécifiques, connus par récepteurs, et il n'y a pas un mécanisme d'action unique pour tous les agents anesthésiques. Parmi différents candidats, les canaux ligand-à déchenchements périodiques d'ion sont les cibles moléculaires le plus susceptibles pour les anesthésiques. Maintenant, il y a un accord général que les récepteurs de **GABA** comme neurotransmetteur inhibitrice principale dans le CNS jouent un rôle central dans les actions des médicaments anesthésiques. Il est largement admis que le $\mathrm{GABA_A}$, ou Récepteur $\mathrm{GABA_A}$ est une cible primaire pour anesthésiques. Les anesthésiques prolongent la durée ouverture du canal de chlorure aux récepteurs $\mathrm{GABA_A}$ et donc la fonction de cet objectif est améliorée par l'action d'anesthésiques. En raison des effets moléculaires des anesthésiques, pendant la transition à l'anesthésie, les changements spécifiques dans les données de l'imagerie du cerveau comme les modèles **EEG** peuvent être observées expérimentalement. Pour la concentration clinical de propofol ces changements caractéristiques compris ont augmenté l'activité dans les bandes de fréquence delta (0.5-4 Hz) et alpha (8-13 Hz) sur la région frontal, mais ils ont augmenté l'activité du **delta** et ils ont diminué l'activité de **l'alpha** sur la région occipital . Une question importante qui se pose est de savoir comment les actions anesthésiques sur le échelle microscopique d'un seul neurone pourrait entraîner des changements dans l'EEG et le comportement qui peut être observé à l'échelle macroscopique. Un des objectifs principaux de cette thèse est de répondre cette question importante en établissant un lien entre les deux échelles.

Aujourd'hui, l'anesthésie générale fonctionne bien dans la plupart des cas, mais il est certainement pas sans risque. Environ une personne sur 13000 patients meurent des accidents liés à l'anesthésie, et environ un ou deux patients sur 1000 cas peut prendre la conscience même en recevant une anesthésie générale. D'une manière générale, la procédure de l'anesthésie est principalement basé sur l'expérience des anesthésistes et il dépend fortement de l'etat de santé général des patients. Autrement dit, ça se fait en fonction des réponses cliniques des patients individuels. Dans la salle d'opération, les anesthésistes surveillent les réactions physiologiques ainsi que les activités électriques du cerveau pour adapter la concentration anesthésique constamment pour contrôler la profondeur de l'anesthésie. Les signes cliniques et physiologiques comme la pression artérielle, la fréquence cardiaque ou des mouvements involontaires peuvent être affectés par l'administration d'autres médicaments et peuvent donc être difficiles à interpréter en pratique. En revanche, l'enregistrement des effets anesthésiques dans les signaux EEG fournit une évaluation plus sûr de l'etat de conscience d'un patient pendant l'administration d'agents anesthṡiques. En conséquence, plusieurs paramèètres de surveillance à la base d'EEG ont été largement utilisés pour l'estimation de la profondeur de l'anesthésie. Selon les informations d'EEG, les indicateurs comme l'indice BIS, la fréquence de bord spectrale (SEF50 ou SEF95) et la fréquence médiane ont été dessiné pour déterminer quantitativement la profondeur de l'anesthésie. Pourtant, le fait d'estimer la profondeur d'anesthésie est toujours un domaine difficile dans la recherche d'anesthésie. Une compréhension approfondie des mécanismes sous-jacents d'anesthésie est crucial pour améliorer les méthodes de surveillance. La **modélisation mathématique** des activités électriques du cerveau offrent une direction prometteuse pour explorer la validité des hypothèses sur les mécanismes de l'anesthésie, et en général, sur les mécanismes sous-jacents des activités du cerveau pendant différents états fonctionnels.

La modélisation des activités du cerveau peut être effectuée dans les échelles différentes des neurones isolés aux populations de neurones. Pour révéler les actions moléculaires des anesthésiques au niveau microscopique, nous pouvons considérer les modèles qui décrivent la dynamique de la neurones isolés. Par contre, la simulation de l'activité de même une petite région du cerveau par la modélisation biophysique détaillée des synapses et des neurones impulsionnels est très coûteux en calcul. Par exemple, un réseau neuronal réaliste comme une corticale colonne a un grand nombre de neurones (à l'ordre de $10^4 - 10^8$ neurones) tandis que chaque neurone peut être connecté synaptiquement avec les autres $10^4 - 10^5$. De plus, la topologie physiologique des réseaux neuronaux réels est plutôt inconnu. Il faut noter que connecter les phénomènes comportementaux qui sont observés aux échelles macroscopiques aux éléments individuels de ces grands ensembles est aussi extrêmement difficile. En revanche, la plupart des coarsescale observables comme les données EEG reflètent l'activité globale d'une grande population de neurones. Cet aspect nous permet de simuler avec succès les signaux empiriques d'EEG par une approximation de **champ moyen**. Les détails de neurones individuels comme potentiels d'action et la dynamique des canaux ioniques n'apparaissent pas explicitement dans les modèles de champ moyennes mais ils sont considérés indirectement dans la description. L'objectif général de modèles de champ moyen est de décrire les propriétés moyennes de population de neurones dans des petites parcelles spatiales et de courtes fenêtres du temps, grâce à un ensemble d'équations différentielles ou d'équations d'intégrale-différentielles. Cette approche typiquement considère l'ensemble d'excitateur et inhibiteur des neurones, qui incorpore les éléments de relation entre les neurones excitateurs et les synapses inhibitrices. Un facteur commun à toutes les versions de modèles de champ moyen est que la moyenne potentiel électrochimique de membrane et les taux de la moyenne cadence de tir sont liés les uns aux autres par une fonction sigmoïde.

Au cours des dernières décennies, les modèles de champ moyen ont été largement utilisé pour reproduire les signaux EEG. Les résultats de la simulation de ces modéles grossiers montrent une correspondance remarquable avec les observations empiriques. Cette description a reussit dans la reproduction des principales caractéristiques des ondes electric du cerveau observés chez les humains lors de différents états fonctionnels du cerveau tels que les états de sommeil, et l'état de l'anesthésie. Il est important de noter que les modéles de champ moyen considèrent populations de neurones sur un niveau spatiale mésoscopique (des centaines de micrométres). Un tel modéle mésoscopique nous permet de combler les différentes échelles spatiales dans le cerveau, de l'échelle microscopique des neurones individuels à l'échelle macroscopique, à-dire le niveau des enregistrements EEG / MEG. Aujourd'hui, il existe une compréhension raisonnable sur les mécanismes moléculaires d'actions anesthésiques. Cependant, comment les effets microscopiques sur les sites de récepteurs peuvent être liés à des changements spècifiques dans observables macroscopiques tels que les données EEG est mal compris. Le présent travail utilise des modéles de champ moyen de fournir un lien entre les effets des anesthésiques sur les neurones simples et leur impact sur l'activité globale des populations de neurones enregistrés par les techniques de neuroimagerie.

Dans les derniȉes décennies, de nombreux travaux ont été focalisée sur l'étude des effets moléculaires des agents anesthésiques. L'étude des modèles de population de neurones sous l'effet des anesthésiques a été déclenché par le travail de Steyn-Ross et al. (1999), qui a proposé un modéle de macrocolonne corticale qui a reçu stimuli stochastiques externes de régions sous-corticales. Depuis lors, de nombreux modèles mathématiques au niveau de la population et le niveau de neurone unique ont été proposées pour comprendre les mécanismes anesthésie générale sous-jacente. La plupart des études théoriques précédents ont porté sur la dynamique de neurones corticaux. Cependant, plusieurs éléments de preuve indiquent que le thalamus et les circuits thalamo-cortical sont des sites cibles pour les important anesthésiques généraux. Bien que **le cortex** est connu comme étant la source de l'activité électrique spontanée du cerveau, **le thalamus** agit à la fois pour la porte d'entrée sensorielle dans le cortex et le site de réaction à partir de cellules corticales. Il a été démontré que le thalamus est au centre de traitement et de transmission de la quasi-totalité de l'information sensorielle qui atteint finalement le cortex. En outre, il existe des preuves montrant que l'accumulation des circuits **thalamo-corticale** impliquent cruciale dans la formation de sommeil, les activités physiologiques normales, le traitement de conscience et inconscience induite anesthésique. Selon ces résultats, nous utilisons un modéle constitué de cortex et le thalamus pour faire emerger plus précise des mécanismes physiologiques. Le présent travail considè re un modè le de champ moyen du systè me thalamo-cortical pour comprendre les mécanismes responsables pour les changements spécifiques qui sont observés au cours de la sédation avec l'anesthesique propofol dans les schèmas EEG. Le modèle comprend populations corticales excitateurs et inhibiteurs qui sont reliés par des synapses aux populations réticulaire et les neurones relais thalamiques par fibres axonales retardées. Le modè le prend en compte l'effet anesthésique au recepteurs inhibitrice GABAergique **synaptique** et les récepteurs **extra-synaptiques** situés dans populations de neurones thalamiques et corticales.

Bien qu'il soit connu que le cortex, le thalamus, et les boucle thalamo-corticales de rétroaction contribuent aux oscillations EEG, le rôle précis de chaque structure à la dynamique de l'EEG est inconnue. Par la manipulation de la topologie du système, nous pouvons obtenir une compréhension plus profonde sur les mécanismes responsables de la génération des rythmes EEG. En particulier, nous nous concentrons sur les bandes de fréquence de delta et alpha, puisque les etats au cours modifiés de l'excitation, des changements caractéristiques peuvent être observées dans ces bandes de fréquences. En outre, nous nous efforçons d'étudier le rôle de l'inhibition synaptique et extra-synaptic dans le cortex et le thalamus dans la génération des caractéristiques de l'EEG enregistrées pendant sédation par propofol. Par exemple, nous pouvons négliger l'effet de propofol dans les cellules corticales et de se concentrer seulement sur l'effet de propofol dans les neurones thalamiques. Cette simplification souligne l'importance du thalamus et affaiblit l'impact du cortex des effets neuronaux principaux sous anesthésie. Comme les récepteurs $\mathrm{GABA_A}$ créent plus de la transmission synaptique inhibitrice (en dehors de récepteurs $GABA_B$ qui ne sont pas inclus dans le modèle), nous supposons que toutes les transmissions synaptiques inhibitrices sont amenés par des récepteurs GABA. Il a été observé expérimentalement que le propofol augmente la constante de temps de décroissance des synapses GABA, et donc augmente le transfert de charge totale dans ces synapses, mais pas celle de synapses excitateurs. Il est intéressant de propofol qu'il a été montré avoir un effet négligeable sur les récepteurs synaptiques d'amplitude dans les neurones corticaux, mais il augmente nettement l'amplitude, le temps de décroissance, et le transfert de charge des recepteurs $\mathrm{GABA_A}$ postsynaptiques inhibitrice évoqués dans les neurones de relais dans le complexe ventrobasal. Nous modèlisons les effets de propofol mentionnés dans un accord très étroit avec les observations empiriques. Ensuite, nous cherchons à répondre à la question importante la façon dont ces effets de propofol sur les récepteurs GABA conduisent à des changements spécifiques observées dans **la puissance spectrique**. En outre, nous nous efforçons d'étudier comment l'effet du propofol anesthésique sur récepteurs GABAergiques extra-synaptiques peut modifier l'activité de la population de neurones et les signaux EEG.

La modélisation mathématique est une tâche essentielle dans l'étude de la biologie des systm̀es. L'objectif de la modélisation est de construire des formulations mathématiques qui décrivent quantitativement le comportement dynamique du systè me à l'étude. Pour atteindre cet objectif, nous devons d'abord une formulation de modéle de réussite qui devrait être en mesure de reproduire les fonctions spécifiques observées dans les données expérimentales, au moins qualitativement. Cette tâche est appelée *identification de structure*. La tâche suivante est **l'estimation des paramètres**. Après l'identification du modèle, nous devons déterminer les paramètres inconnus du modèle. Comme la dynamique du modèle dépend des valeurs des paramètres du modèle, reproduisant certaines caractéristiques des mesures expérimentales nécessite la sélection d'un appropriée set des paramètres inconnus. Bien que certains des paramètres de modèle peut être mesurée directement dans les expériences, la majorité des paramètres doit être estimée à partir de mesures expérimentales. Par conséquent, l'estimation des paramètres dire identification des paramètres inconnus du modèle èq partir d'observations expérimentales est l'une des principales étapes de l'élaboration de modèles mathématiques. Néanmoins, trouver un ensemble de paramètres du modèle qui correspond précisément aux données enregistrées est une tâche extrêmement difficile, surtout pour les modl̀es dynamiques non linéaires avec de nombreux paramt̀res et de contraintes.

Dans les derniéres années, une attention considérable a été accordée aux **algorithmes d' optimisation**. Par conséquent, plusieurs algorithmes d'optimisation ont été proposées et appliquées avec succés dans divers domaines scientifiques. Une des approches réussies pour les paramètres du modèle d'estimation est en utilisant des techniques d'optimisation. Dans cette approche, le problème paramètre de l'inférence est transformé à un problème fonctionnel d'optimisation, à savoir, en minimisant une fonction de remise en forme qui est définie par la discordance entre les données simulées et les données mesurées. En fait, la dynamique de la majorité des systèmes biologiques sont décrits par des équations différentielles plutôt que des fonctions algébriques explicites. En outre, les systémes biologiques sont souvent soumis à des stimuli externes bruites et les perturbations environnementales. Ainsi, nous nous concentrons sur l'estimation des paramètres de systèmes dont la dynamique sont régies par des équations différentielles ordinaires ou stochastiques retard. À l'élaboration finale de cette thèse, nous nous efforçons de répondre à la tâche de l'estimation des paramètres des modèles qui sont décrit par un ensemble de (**EDO ou DDE**) de données stochastiques mesurées. Dans cette étude, trois études sont étudiés en utilisant différents algorithmes d'optimisation, y compris la descente de gradient recherche locale et des méthodes de recherche globale stochastiques. La performance des méthodes d'optimisation est ensuite comparée à déterminer quel algorithme de recherche est plus approprié pour chacun des estimations des paramètres considérés du problème. Pour évaluer la performance de ces algorithmes deux études portant sur un ensemble de données pseudo-expérimentales appelées in silico problème d'estimation de paramètres sont etudiés: un oscillateur stochastique harmonique amortie, et une équation stochastique linéaire retardé différentiel, ce qui pose un problème d'optimisation unimodale et multimodal. Dans la troisième étude, un modèle thalamo-corticale est adapté au spectre de puissance des enregistrements EEG (une optimization de paramètre in vivo). Comme l'analyse du spectre de puissance est valable seulement si l'état de repos du système est stable, nous cherchons les conditions qui garantissent **la stabilité du système**. Les conditions d'inégalité dérivés réduisent l'espace paramètre de recherche et ainsi facilitent énormement la tâche d'estimation non linéaire. Nous montrons que le modèle proposé convient très bien à la puissance des spectres EEG, en particulier pour les pics spectraux de puissance observée en bandes de fréquence delta et alpha.

Un autre défi pour les problèmes d'estimation des paramètres est la possibilité d'identifier des estimations, à savoir, si les paramètres du modèle peuvent être déterminés uniquement par les données expérimentales fournies. Cette mission est appelée identifiabilité pratique. Nous employons différentes méthodes pour résoudre ce problème. Les régions de confiance des estimations sont tracées et la corrélation et les matrices de la sensibilité sont analysées pour examiner la fiabilité des estimations dans chaque étude.

En résumé, dans cette thèse, nous nous efforçons de toucher à une question importante: quel est le mécanisme sous-jacent du sédation par propofol? Pour répondre à cette question en utilisant une approche de modélisation, basée sur les questions mentionnées ci-dessus, nous devons adresser ces questions: comment nous pouvons lier les actions anesthésiques sur les cibles moléculaires de leur impact sur les observables macroscopiques tels que les signaux EEG? Quel est le rôle du cortex, le thalamus et circuits thalamo-corticale dans la génération des rythmes de l'EEG en bande de fréquence delta et alpha ? Étant donné un ensemble d'équations différentielles couplées et un ensemble de données expérimentales, comment nous pouvons identifier les paramètres modèle inconnu ? Ces questions soulèvent une question générale: Qu'est-ce que contestent l'approche modeling de révèler les mécanismes sous-jacents du système à l'étude.

Cette thése se compose de cinq chapitres. Les chapitres 1 et 2 présentent les éléments physiologiques et mathématiques fondamentales que nous devons effectuer pour les études analytiques et numériques. Par la suite, les résultats des travaux sont donnés dans les chapitres 3-5. Ces derniéres sections sont organisées en deux grandes parties. La premiére partie est consacrée à la modélisation mathématique et informatique du problème, qui est présentés dans les chapitres 3 et 4. Dans la deuxième partie, décrit dans le chapitre 5, nous utilisons une approche axée sur les données à acquèrir de nouvelles connaissances sur les mécanismes de la système à l'étude. Dans la suite, nous présentons chaque chapitre dans plus de détails.

Le chapitre 1 résume les connaissances actuelles sur les mécanismes neuronaux que les anesthésiques induisent pendant une anesthésie générale, du niveau de neurone unique aux observations macroscopiques. Le chapitre commence par la définition clinique et les composants de l'anesthésie générale. Nous introduisons ensuite brièvement les agents anesthésiques les plus couramment utilisés dans la pratique médicale d'aujourd'hui et les études cliniques en cours. Par la suite, les informations disponibles sur les mécanismes d'action des anesthésiques au niveau du neurone unique et leurs cibles moléculaires est examiné. Il est trè s important d'étudier l'action moléculaire des anesthésiques car il nous permet à identifier quelles structures du cerveau sont des cibles essentielles pour anesthésiques et à son tour jouent un rôle majeur dans l'induction des états altérés de l'excitation. Aprés cette partie, nous résumons les effets de propofol sur les signaux EEG, qui peuvent être surveillés experimentalement pour suivre les états du cerveau sous anesthésie. La majeure partie du travail dans cet élaboration vise à relier l'action anesthésique au niveau du neurone unique à leurs effets sur les observables macroscopiques tels que les données EEG. Enfin, dans la dernière section, nous présentons brièvement les hypothéses actuelles sur les mécanismes sous-jacents les changements observés associés à l'induction et l'entretien de l'anesthésie.

Le chapitre 2 est consacré aux outils mathématiques essentiels, qui sont la base pour la recherche présenté dans les chapitres suivants. Dans ce chapitre, nous décrivons d'abord les DDE, et nous nous concentrons sur leur analyse de la stabilité dans les cadres numériques et analytique. L'étude des DDEs est important car la dynamique de nombreux systèmes physiques et biologiques sont caractérisés par des DDEs. En particulier, nous sommes intéressés aux DDEs comme les modèles de champ moyen utilisées dans ce travail sont régies par un ensemble de DDEs couplés. La derniére section se concentre sur les modèles de population de neurones. Nous décrivons brièvement les modèles de champs de neurones, qui nous permettent de simuler avec succès les ondes cérébrales électriques dans une approche physiologique précise. Enfin, deux modèles de champs de neurones bien établies en reproduisant les caractéristiques EEG pertinents au cours des différentes activités cérébrales sont présentés: un mod'ele moyen développé par Peter Robinson et ses coll'egues (appelée modèle Robinson) et un modèle de champ neuronal étendue basée sur les travaux de Axel Hutt (appelé mod'ele Hutt), qui sera utilisé dans les chapitres 3 et 4, respectivement.

Chapitre 3 met l'accent sur le rôle des récepteurs extra-synaptiques dans le cadre de l'anesthésie. Dans ce chapitre, nous examinons d'abord brièvement la littérature sur les récepteurs extra-synaptiques et de leur affinité pour les médicaments anesthésiques. Ensuite, les effets anesthésique de propofol sur les récepteurs synaptiques et récepteurs extra-synaptiques localisé dans les populations de neurones corticales et thalamique sont modélisés. Par la suite, nous montrons comment les caractèristiques spécifiques observées dans le spectre de puissance EEG frontale au cours de sédation par propofol peuvent être reproduits en incorporant un modèle de population de neurones avec les effets anesthésiques sur récepteurs GABAergiques extra-synaptiques. Enfin, l'origine des pics de puissance en bande de fréquence delta et en bande de fréquence alpha est discuté brièvement. Dans le chapitre suivante, l'origine des activités delta et alpha observées en EEG spectrale de puissance est étudiée plus en détail.

Dans le chapitre 4, nous nous efforçons de comprendre les mécanismes qui sous-tendent les changements spécifiques observèes dans les rythmes de l'EEG frontaux et occipitaux pendant la sedation par propofol. Le modèle de la population de neurones utilisé dans ce chapitre est analysé en détails pour révèler l'origine des pics de puissance spectrales en bande delta et alpha. Dans ce chapitre, nous proposons un modèle thalamo-cortical réduit, qui est encore suffisant pour reproduire les changements observés dans les rythmes EEG. En outre, la faible dimension de ce modèle nous permet d'étudier le rôle des états du système de repos, le modèle sous-circuits et les populations de neurones dans un schéma analytique. Dans le dernier chapitre, le modèle proposé est adapté sur le spectre de puissance de l'EEG à quantifier à quel point ses prédictions sont aux observations expérimentales.

Le chapitre 5 est consacré à l'estimation des paramètres (problème inverse), à savoir, l'inférence de types valeurs de paramètres à partir d'observations expérimentales. Dans ce chapitre, nous résolvons les problèmes inverses considérés en minimisant l'écart entre la sortie simulée et les données mesurées. Finalement, nous appliquons des algorithmes d'optimisation de différents, comme Levenberg-Marquardt (LM), Particle Swarm Optimization (PSO), Differential Evolution (DE), Monte-Carlo Markov Chain (MCMC) et Simulated Annealing (SA). La performance de ces algorithmes est comparée dans le cas des problèmes d'optimisation unimodales et multimodales. En outre, dans chacun de l'étude considéré, la précision des estimations est évaluée en traçant les régions de confiance et par l'analyse de la sensibilité et de matrices de corrélation.

Les résultats obtenus dans cette thseè sont basés sur les données expérimentales qui ont été mis à disposition par Prof. Jamie Sleigh (Université d'Auckland, Nouvelle-Zélande).

1

Neuroscience of general anesthesia

Contents

Abstract

Although general anesthesia is commonly used in medical care for patients undergoing surgery, its precise underlying mechanisms remain to be elucidated. There are, however, several hypotheses that have been advanced to explain how general anesthesia occurs. A wide variety of drugs are used in modern anesthetic practice and for various hypnotic agents, during the transition from awake to anesthesia condition, specific changes in brain imaging data such as EEG can be observed experimentally. However, the mechanisms responsible for these characteristic changes are still unknown. This chapter begins with a clinical definition for general anesthesia. Then, the experimental findings that reveal the molecular mechanisms of anesthetic actions are summarized. Subsequently, we present the action of anesthetics on macroscopic brain observables such as EEG signals. Finally, a brief summary of the current hypotheses on the mechanisms by which anesthetics cause general anesthesia is provided.

1.1 General anesthesia

General anesthesia is a reversible medical procedure that is commonly induced by the administration of a combination of anesthetic agents to induce amnesia (partial or total loss of memory), sedation (reduction in the level of arousal and motor activity), hypnosis (loss of consciousness) and immobility (loss of motor reflexes) in patients. There are differing definitions of general anesthesia, but phenomena such as analgesia (loose of response to pain), muscle relaxation and anxiolysis should be included, in addition to the most obvious effect of loss of consciousness [10]. The reversibility along with the stability of physiological systems including the autonomic, cardiovascular, respiratory, and thermo-regulatory systems are the most important aspect of general anesthesia which distinguish this drug-controlled condition from persistent vegetative state, brain death or other type of irreversible unresponsiveness [17, 65]. It is important to point out that sometimes sedation is used as a synonym for hypnosis (LOC) or it refers to as incomplete hypnosis. However, there are recent evidences showing that sedative and hypnotic states are produced by distinct mechanisms [10]. Sedation is accompanied by slurred speech and decrease in anxiety, stress, irritability, and excitement, whereas LOC is defined as loss of the ability for patient to respond to verbal commands or mild shaking [10]. Typically, sedation occurs before LOC which appears at higher anesthetic concentrations. General anesthesia is widely used in today's medical surgery. For instance, it has been estimated that in the United States, around 100,000 patients per day receive general anesthesia for surgical procedures [1]. In the last decades, general anesthesia has attracted theoretical researchers and there have been a large number of efforts to reveal how the anesthetics create and sustain the state of general anesthesia. However, the precise mechanisms underlying the induction of, depth of, or recovery from anesthesia are not yet fully understood. In the following section, we briefly introduce the anesthetic agents that are most commonly used in surgical procedures and clinical studies. Subsequently, a brief review of the current knowledge on the mechanisms of action of general anesthetics and the relevant molecular targets is provided.

1.2 General anesthetics

General anesthetics include a large number of drugs which without them, modern medicine, especially surgery, would not have been possible. Nitrous oxide (N_2O), also known as laughing gas, was discovered in 1772 but its anesthetic properties was discovered in 1844 [3]. At about the same time (1840s), ether and chloroform were used as an effective surgical anesthetic [3]. In 1846, the first successful public demonstration of anesthesia was performed by ether at theatre of the Massachusetts General Hospital [3]. Whereas, neither ether nor chloroform is used in today's surgery, nitrous oxide is one of the most widely used anesthetics in dentistry and emergency centers. However, since 1980s, the use of nitrous oxide has been declined. Later, barbiturates was synthesized in 1864 and used as general anesthetic in 1903. Thiopental was introduced around 1935. Etomidate and halothane were found to have anesthetic properties in the 1950s and 1960s, respectively. Enflurane and isoflurane have been used since 1970s. Propofol was introduced in the mid- 1980s, and Sevoflurane and Desflurane was first used in 1990s [3].

General anesthetics can be divided into two categories: inhalation (volatile) and intravenous anesthetics [10]. The inhalation anesthetics such as Halothane, Enflurane, Isoflurane, Nitrous oxide, Sevoflurane, Desflurane enter the body through the lungs. The inhalation anesthetics are used usually together with intravenous agents since they are low-potency compounds [10]. Intravenous anesthetics which are more potent than inhalation agents include Ketamine, Thiopental (a Barbiturate), Methohexital, Etomidate, and Propofol. For more detailed discussion about different anesthetic agents see Refs. [66, 3, 67], and the references therein.

Propofol, an emulsion formulation of 2,6-di-isopropylphenol, is a short-acting, intravenously administered hypnotic agent; and is in widespread use for sedation and general anesthesia because of its relatively fast onset and offset, and anti-emetic effects [4]. Due to the widespread use of propofol in clinical medicine and theoretical studies, beside its relatively well-understood molecular effects, the present work is primarily focussed on the action mechanism of this agent.

1.3 Anesthetics effects on single neurons (microscopic level)

1.3.1 Molecular targets of general anesthetics

Identifying the target sites of anesthetic agents is crucial to understand the precise mechanisms of general anesthesia. Understanding the neuronal mechanisms of general anesthesia provide us with the neurobiological basis to elucidate the mechanisms of consciousness, which is one of the greatest unanswered questions in neuroscience. In recent years, significant progress has been made in the understanding of how general anesthetics act at the molecular level. Although the exact mechanisms governing anesthesia are still unclear, it is thought to be induced by enhancement of inhibitory neurotransmission or inhibition of excitatory neurotransmission. Here, some aspects of current knowledge on the molecular level effects of general anesthetics are briefly reviewed.

Over 100 years ago, the first theory of anesthesia was suggested by Meyer and Overton [5, 6]. They found a positive correlation between lipid solubility and anesthetic potency. The Meyer-Overton correlation led to the lipid hypothesis of general anesthesia, which states that the lipid cell membrane of neurons are the action target of anesthetic agents and they act by dissolving in the cell membrane [5, 6]. In other words, anesthetic agents act through a common and nonspecific mechanism [7, 10]. However, several lines of evidence indicate that general anesthetics interact directly with specific target sites instead of a nonspecific interactions with the lipid cell membrane [8, 11, 12]. It is now generally accepted that anesthetics directly bind to specific targets and there is not a single mechanism of action for all anesthetic agents [9]. Until now, many molecular targets and neuronal transmission pathways have been identified to contribute to general anesthesia. According to experimental findings, the most likely molecular targets are ligand-gated ion channels including $\mathrm{GABA_A}$ receptors, Glycine receptors, nicotinic and muscarinic Ach receptors, 5-HT3 (5-hydroxytryptamine, type 3) receptors, AMPA (α-amino-3-hydroxy-5-methyl-4-isoxazole propionic acid), NMDA (N-methyl-Daspartate) and kainate receptors [10, 9]. Moreover, some other ion channels such as potassium and sodium channels, and hyperpolarization activated cyclic nucleotide (HCN) channels are also involved in general anesthesia [13]. As it is shown in Fig. 1.1, these targets are differentially sensitive to various anesthetics. The most known anesthetic target is the $\mathrm{GABA_A}$ receptors [2]. Although anesthetics bind to a wide variety of receptors, there is accumulating evidence showing that $\mathrm{GABA_A}$ receptor is the major molecular target for the action of many anesthetic drugs in the brain [15, 16]. Propofol, our anesthetic of interest, binds to both $\mathrm{GABA_A}$ and glutamergic receptors, however, it has much larger effect on $\mathrm{GABA_A}$ receptors as compared to its effect on AMPA and NMDA receptors.

The GABA system induces inhibition in the CNS by generating inhibitory postsynaptic currents (IPSCs) [66]. GABA receptors are known as the major inhibitory neurotransmitter receptors in the mammalian brain, where one-third of all synapses are GABAergic [68, 14]. Activation of GABA receptors results in hyperpolarization of the cell membrane and suppression of the excitability of the neurons. GABA receptors belong to the family of ligand-gated ion channels which are found at both synaptic and extra-synaptic sites [69, 70, 71]. There are two classes of GABA receptors: $\mathrm{GABA_A}$ and $\mathrm{GABA_B}$ [72]. Whereas $\mathrm{GABA_A}$ receptors generate fast and transient postsynaptic currents by Cl^- influx, $\mathrm{GABA_B}$ receptors produce slower and more complex responses, which involve G proteins and second messengers [73].

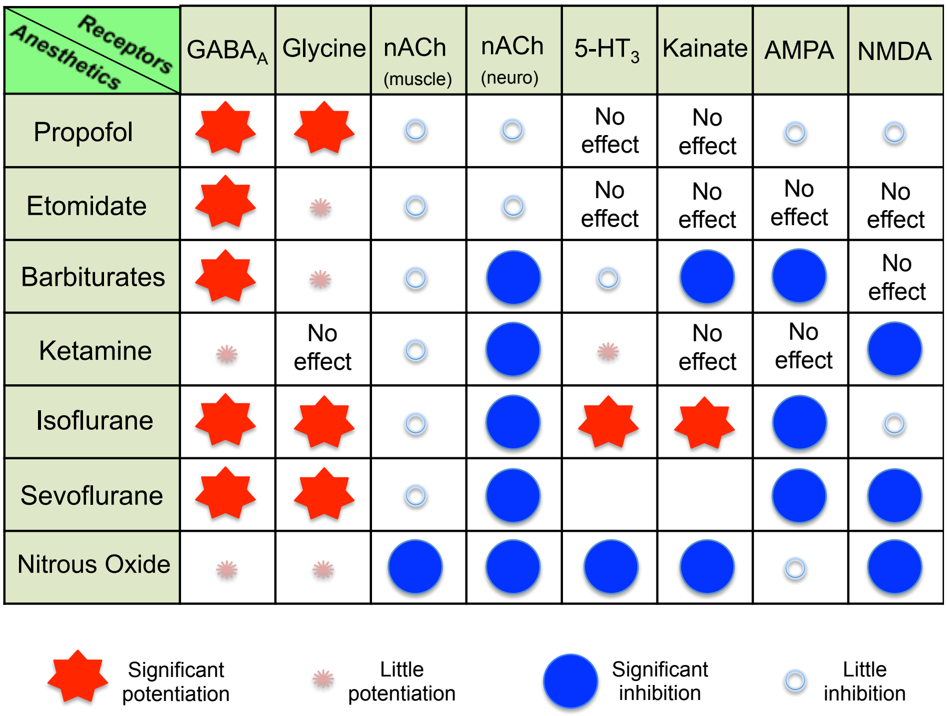

Receptors Anesthetics	$GABA_A$	Glycine	nACh (muscle)	nACh (neuro)	$5\text{-}HT_3$	Kainate	AMPA	NMDA
Propofol	★	★	○	○	No effect	No effect	○	○
Etomidate	★	✱	○	○	No effect	No effect	No effect	No effect
Barbiturates	★	✱	○	●	○	●	●	No effect
Ketamine	✱	No effect	○	●	✱	No effect	No effect	●
Isoflurane	★	★	○	●	★	★	●	○
Sevoflurane	★	★	○	●			●	●
Nitrous Oxide	✱	✱	●	●	●	●	○	●

★ Significant potentiation
✱ Little potentiation
● Significant inhibition
○ Little inhibition

Fig. 1.1. Ligand-gated ion channels as the most probable target sites for the action of current clinical anesthetics. In the figure, a large red or blue spot indicates significant potentiation or inhibition, respectively; a small light red or blue spot indicates little potentiation or inhibition, respectively. The data is taken from Refs. [10, 13].

As mentioned above, there is a general agreement that $GABA_A$ receptors are important target sites in mediating the inhibition during administration of many general anesthetics [16]. In particular, propofol produces the state of unconsciousness by acting on the $GABA_A$ receptors. The experimental observations indicate that propofol increases the decay time constant of $GABA_A$ synapses, and hence increases the total charge transfer in these synapses [9], as shown schematically in Fig. 1.2. It is important to point out that $GABA_A$ receptors are also found outside the synapse, and the tonic inhibitory currents generated by the extra-synaptic $GABA_A$ receptors are also potentiated by general anesthetics [74, 75]. See chapter 3 for more details on anesthetics effects on extra-synaptic receptors.

1.3.2 Neuroanatomical targets of general anesthetics

It is important to note that general anesthetics act on certain brain areas since anesthetic agents selectively interact with molecular targets and the target sites are specifically distributed among different brain regions. The experimental observations demonstrate that the cortex, thalamus, hypothalamus, reticular activating system (RAS), brainstem and spinal cord are the most critical targets for anesthetic action. There is strong evidence indicating that immobility is primarily produced by depressing spinal neurons whereas sedation, amnesia and unconsciousness are related to anesthetic actions on neurons in the brain [10]. Due to the functions of aforementioned brain areas, they play a significant role in drug induced general anesthesia; cortex as the most modern part of the brain responsible for high-level cognitive functions; thalamus, which contributes to arousal regulation, as a relay station that gates sensory inputs to the cortex; hypothalamus as a

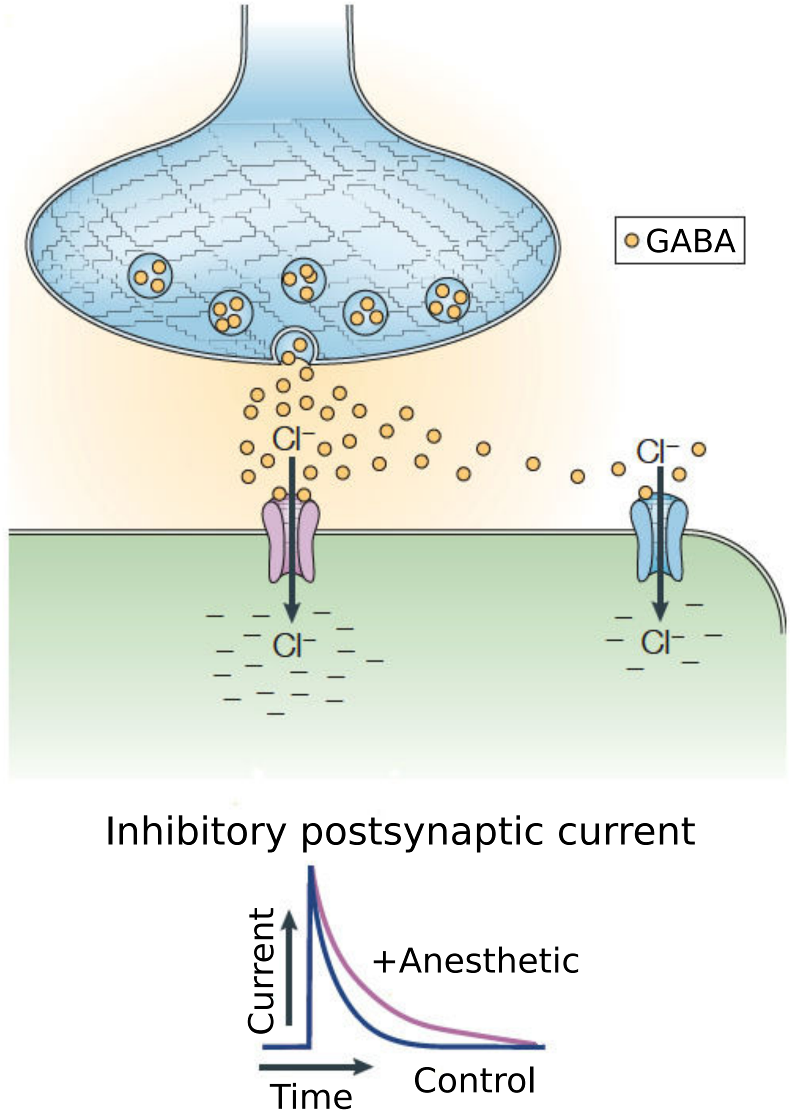

Fig. 1.2. Synaptic and extra-synaptic activation of GABA$_\mathrm{A}$ receptors. GABA$_\mathrm{A}$ receptors are activated by the release of GABA into the synaptic cleft due to arriving of action potentials. Synaptic receptors which are sensitive to GABA at mmol concentration produce fast inhibitory postsynaptic currents (IPSCs), whereas extra-synaptic receptors can be activated by low concentrations of GABA (at μmol order) and generate slower tonic inhibitory currents [16]. Propofol increases the decay time constant of the inhibitory GABA$_\mathrm{A}$ responses by prolonging the duration of channel opening. This leads to an increase in the total charge transfer in these synapses. The figure is taken from Ref. [10].

wake-sleep regulatory system; reticular activating system (RAS), which connects the brainstem to the cortex, as the ascending and descending neuronal pathways responsible for regulating arousal and sleep-wake transitions; brainstem, which forms the connection between the brain and the spinal cord, as a pivotal site for maintaining consciousness and regulating the sleep cycle [46]. However, it is not precisely clear which brain regions play a major role in the induction of different stages of anesthesia. For instance, Rudolph & Antkowiak have reported that at sedative concentrations, propofol affect cortical neurons whereas the subcortical areas are influenced by higher concentrations [10]. Accordingly, they have proposed a linear correlation between propofol plasma concentration and anesthetic depth, however, recent studies have shown that even at sedative concentrations, propofol significantly decreases the excitability of spinal neurons. In other study, it has been demonstrated that propofol effects are initiated via subcortical mechanisms, rather than in the neocortex [76]. Furthermore, whether the hypnosis is induced by drug effects on the cerebral cortex, thalamus, or subthalamic areas is still under debate [45, 77, 78]. Despite such debates over the exact role of brain regions at different anesthesia levels, an enormous body of evidence indicates that two main brain structures affected by anesthetic agents are the cortex and the thalamus (see Ref. [12] and the references therein). In particular, these brain regions have been identified to be the predominant candidates for general anesthetic to produce sedation and hypnosis, since at clinically relevant concentrations, they are strongly suppressed by various anesthetic agents [9, 10]. Taken together, appealing understanding has been obtained from functional neuroimaging and electrophysiological techniques, but due to the complexity of arousal system and the structural diversity of anesthetic agents, the precise role of each brain structure in induction of altered states of arousal is unknown.

Although anesthetics may act on several brain regions, the cortex and the thalamus (thalamocortical and cortico-thalamic loops) are highly sensitive targets for propofol [79, 48]. Most of the previous theoretical studies on anesthetic effects have considered a purely cortical model or they have explained the observed features during anesthesia by a cortico-thalamic model consider both thalamic and cortical anesthetic actions [24, 39, 23, 28, 35]. There is ample evidence showing that anesthetics potentiate functions of cortical inhibitory neurons [80, 47]. Importantly, the scalp EEG represents the neural activity of thousands or millions of spatially oriented pyramidal neurons of the cortex [22]. Moreover, a large body of evidence supports the importance of thalamus in the generation of specific oscillations observed experimentally during anesthesia state [81, 9]. The thalamus receives many inputs from and projects onto the cortex. According to these findings, we have focussed on the anesthetic effects on cortex and thalamus. The model used in the present work includes cortex and thalamus to reach more precise elucidation of physiological mechanisms. The details of the model is presented in the subsequent chapter. The propofol actions on GABAregic receptors within cortex and thalamus are modelized at the beginning of chapter 3. In the section that follows, the anesthetic effects on the brain imaging data such as EEG signal are summarized.

1.4 Anesthetics effects on EEG signals (macroscopic level)

Functional neuroimaging techniques such as positron emission tomography (PET), functional magnetic resonance imaging (fMRI), along with electroencephalography (EEG) have proven to be powerful tools in unraveling the neural mechanisms that underlie the human brain dynamics. Since metabolic activities in the brain are reflected in the patterns recorded by neuroimaging methods, these techniques can be employed to monitor different alterations in functional state of the brain such as transition to general anesthesia and altered states of arousal [18, 19]. Especially

EEG, which provides direct measurement of cognitive processing that take place in cortical brain area shed some more light on the mechanisms underlying the changes associated with induction and maintenance of anesthesia [82, 83].

Anesthetic studies using functional brain imaging provide evidence that different anesthetic agents cause distinct patterns in EEG oscillations. However, general anesthesia induced by various anesthetics is accompanied by some common features in EEG rhythms. The low amplitude $\alpha-$oscillations in the EEG rhythms predominate during wakefulness, whereas high amplitude $\delta-$waves are the hallmark of anesthesia onset. Most anesthetics (except Ketamine) decrease the frequency and increase the amplitude of EEG rhythms in a dose-dependent manner. This includes volatile agents, propofol, barbiturates, benzodiazepines and narcotics. As the dose of anesthetics is slowly increased, high-amplitude, low-frequency oscillations appear in EEG patterns. At or beyond the point at which consciousness is lost, the slow EEG rhythms are more increased, and an increase in EEG spectral power within $\beta-$frequency band is observed, that is sometimes called *beta buzz.* Further increasing the dose of anesthetics causes the so called burst suppression, which is characteristic of deep anesthesia. As the state of general anesthesia deepens, the time duration between suppression periods lengthens gradually until at the level of deep coma, the bursts are disappeared and EEG displays a continuous flat (isoelectric) line [17]. According to these findings, the EEG signatures related to increasing concentrations of anesthetics can be used to assess the depth of anesthesia.

Here we only summarize the propofol effects on EEG signals. The effects of other anesthetics on brain imaging data are described in [17, 12]. It has been reported that clinically relevant concentrations of propofol cause specific changes in electroencephalogram (EEG) rhythms of healthy adult humans. Up to sedative concentrations, these observations include an increase in power in the $\alpha-$ and $\delta-$ frequency bands over the frontal head region, accompanied by decreased $\alpha-$activity, and an increase in $\delta-$activity over the occipital sites [81, 84, 85, 86]. The frontal enhancement and occipital attenuation of $\alpha-$activity is commonly termed *anteriorization.* It has been shown that in deeper sedation, propofol attenuates posterior $\alpha-$ power and increases frontal β and total power [18, 87], and is associated with a frontal increase in $\alpha-$, $\delta-$, and $\theta-$power. With the loss of consciousness frontal power further increases across all frequency bands [87]. The frequency bands are defined in the intervals (0-4Hz) for delta, (4-8Hz) for theta, (8-13Hz) for alpha and (13-30Hz) for beta power.

Moreover, it has been observed that for many anesthetic agents such as thiopental, propofol, sevoflurane, etomidate, except for midazolam, during the transition from consciousness to unconsciousness, the EEG shows biphasic effects in amplitude: an initial increase of the spectral power followed by a decrease at higher concentrations [88, 89].

According to the aforementioned findings, substantial insights have been achieved into the molecular and cellular mechanisms of action of most anesthetic agents [90, 13]. However, how the anesthetic actions at single neuron level (microscopic scale) could lead to specific changes in EEG and behavior that can be observed at macroscopic scales, is an important question in medicine and neuroscience. To address this question, it is necessary to establish a bridge between the two scales. A well-tried method to link these two levels of brain dynamics is using the mean-field approach to characterize the activity of large populations of neurons at an intermediate mesoscopic scale [20, 91, 27]. The EEG represents the neural activity of thousands or millions of spatially oriented pyramidal neurons of the cortex [22]. By virtue of this large number of neurons, it is reasonable physiologically to model EEG by considering spatiotemporal neural activity of populations using a mean-field approximation [21, 92, 93, 29, 30, 23, 94, 95]. A large number of previous theoretical studies on anesthetic effects apply a mean-field model to explain various features in EEG data recorded during general anesthesia [31, 24, 38, 39, 40, 41, 25, 35, 28]. These theoretical studies are based on various extensions of the model of Liley *et al.* [96, 97], Wilson & Cowan [98], and Amari [99], including excitatory and inhibitory neurons and synapses. The following chapter concentrates on the neural population models and the mean field approximation.

1.5 Current theories of general anesthesia

A unifying theory that explains a common mechanism that underlies the anesthetic-induced unconsciousness for different hypnotic agent is still lacking. However, in recent decades, several theories have been advanced to understand the neural mechanisms by which general anesthetics cause unconsciousness when a patient receives high dose of anesthetics. In the following, current hypotheses on the neural mechanisms underlying anesthetic-induced unconsciousness are briefly reviewed.

An initial hypothesis to explain how general anesthetics produce unconsciousness was a global depression in the brain activities. The positron emission tomograohy (PET) data has shown that the administration of anesthetic propofol causes a global reduction in cerebral blood flow when LOC occurs [100, 101, 102]. This theory was reinforced by other observations demonstrating that brain metabolism and EEG activity are reduced by many different anesthetic drugs. However, several brain imaging studies have shown that certain regions are more deactivated than others and all anesthetics do not suppress global cerebral metabolism [9, 45]. For instance, propofol and volatile anesthetics preferentially reduce the regional brain activity in the thalamus, the precuneus and the posterior cingulate cortex, the cuneus and the frontoparietal cortex, whereas ketamin increases the activity in the thalamus, anterior cingulate cortex and the frontal cortex [9, 12]. The varying degrees of deactivation during LOC indicate a regional differences in anesthetic actions rather than a global brain suppression [100]. Therefore, the simple global depression theory during LOC can not explain the full characterization of effects of anesthetic agents. Taken together, the global brain activity is not necessarily a reliable predictor for assessing the level of consciousness [103, 104].

Another hypothesis for the mechanisms of drug-induced LOC is that anesthetics activate a thalamo-cortical switch during transition into unconsciousness. The theory of thalamic switch of consciousness is based on a series of convergent evidences showing that suppression of regional thalamic and midbrain reticular formation activity is a common feature in both inhaled and intravenous anesthesia. According to this theory, hyperpolarizing of thalamo-cortical cells increases the inhibition on excitatory thalamic neurons which in turn reduces the thalamo-cortical output to the cortex [44]. Thus, a thalamic block of somatosensory information results in the cortex being functionally disconnected from receiving sensory information [105, 106]. The theory suggests that LOC induced by different anesthetic agents is associated with a switch in thalamo-cortical cell from tonic-firing to burst-firing pattern [44, 107]. The shift in thalamo-cortical cell firing pattern is concomitant with the transition in the EEG pattern from low voltage, fast activity to high voltage, slow activity [44]. However, this Off-switch model has been challenged by the evidences showing that thalamus is activated by ketamin and all the anesthetic agents do not have a same activation/deactivation pattern [12]. In addition, the role of thalamus in induction of unconsciousness is still under debate. In several studies using brain imaging techniques, the deactivation of the thalamus has been identified during anesthetic induced unconsciousness [9]. However, there is strong evidence that indicates a more complex role for the thalamus beyond a basic reduction in signaling during LOC [108]. Many studies have also implicated an important role for the thalamus in producing EEG signatures associated with the altered states of arousal [81]. Currently it is unknown that the thalamus is inactivated directly or indirectly due to the cortical suppression. Therefore, it remains to be elucidated whether the thalamus switch can control consciousness, or the reduced thalamic activity is a secondary effect due to a decrease in excitatory feedback from the cortex [13].

Another hypothesis assumes that consciousness depends on integration of information within the thalamo-cortical system. The Information Integration Theory of Consciousness (IITC) suggests that anesthetics induce unconsciousness by preventing the brain to integrate the information [13, 109]. In this theory, information is defined as a large repertoire of the brain states whereas their availability to the system describe the integration. Thus, reducing of repertoire of brain states (decreasing the information) or interrupting of communication between brain states (decreasing the integration) results in a reduced level of consciousness [13, 110]. Taken together, according to IITC, the transition into unconsciousness is associated with a significant reduction in the capacity of the brain to integrate information. However, the exact mechanism of these effects is yet unclear.

As mentioned in the previous section, during altered states of arousal, specific changes in EEG patterns can be observed experimentally. Although it is not precisely clear yet how these certain changes in EEG rhythms occur, there have been many efforts to understand the underlying mechanisms leading to such EEG-level phenomena. For instance, a large number of studies have used mean field models to reveal how the EEG signatures during general anesthesia are related to anesthetic binding at specific receptor sites. Most of these theoretical studies have pointed out the importance of anesthetic-induced cortical inhibition considering [35], or neglecting [24, 39, 40, 41, 28] the feedback loop to the thalamus.

The first continuum model for the response of the cerebral cortex to a general anesthetic agent was proposed by Steyn-Ross and colleagues [38, 39, 40]. They have posited that loss and return of consciousness is related to a first-order phase transition in brain dynamics with a hysteresis separation between jump points. In their model, at a critical anesthetic dose correspond to the point of LOC an abrupt transition occurs from an activated high-firing state to a quiescent low-activity state, whereas ROC is described by a transition from down to the up state at a lower drug concentration than LOC. Although their studies have not produced the resting-state $\alpha-$band oscillations, they reproduced successfully the biphasic behavior in the EEG power spectrum, as it is observed for many anesthetic drugs during both induction and recovery from anesthesia [89, 88]. In contrast, the model of Liley *et al.* [31, 24] showed that the biphasic effect can be generated without requiring a phase transition between distinct neural states. Their model predict a continuous transition of electrical fluctuations in the cortex, implying that the loss and the return of consciousness occur at the same level of anesthetic concentration. Molaee-Ardekani *et al.* [41] advanced the models of Steyn-Ross *et al.* and Bojak & Liley by adding slow voltage dependent mechanisms on excitatory firing rate dynamics. In their mean field model, the firing rate of excitatory population was redefined to be also a function of the slow ionic mechanism. This modification results in an alternation in neural activities between two levels of activity referred to as up and down states, which reflects the high amplitude, low frequency delta activity in EEG signals observed during anesthesia. Their results show a good qualitative agreement with EEG signals recorded from children undergoing anesthesia with the agent desflurane. Hutt & Longtin [28] have developed a neural field model which is able to distinct response functions at excitatory and inhibitory synapses in contrast to previous models that have only considered the dynamics of a single synapse. Moreover, their model incorporates the activity transmission along axonal trees. They have shown that the biphasic power surges can occur in both case of transition; a first-order phase transition, or a smoothly continuous transition. Recently, Hutt [111] proposed a linear neural population model that explains the anesthetic-induced power increase in neural activity by an oscillatory instability in the model dynamics. The analytical tractability of the model allows exploration of conditions under which the power peak shifts to larger frequencies as observed in experiments.

Taken together, the findings of the mentioned studies emphasize the importance of neural field theories in elucidating the neurophysiological mechanisms that underlie the observed data during different behavioral states. In particular, this approach allows us to bridge the scales between molecular action at neural receptors (microscopic level) and neural population activity (macroscopic level).

Other modeling efforts have used conductance based models to explain how the EEG signatures occur in the transition from baseline to anesthetic levels. Ching *et al.* [81] have developed a thalamo-cortical model based on single neuron dynamics that suggests the importance of the thalamus in rhythmic activity in the frontal EEG. They have shown that synchronous frontal $\alpha-$activity in the EEG is the result of recruitment of some subset of the thalamic network into the cortical rhythm. This is in contrast to the theory of thalamic deactivation during general anesthesia. A recent study of Vijayan *et al.* [112] suggests that reduction in hyperpolarization-activated current ($\mathrm{I_h}$) silences bursting of a subset of thalamo-cortical cells leading to suppression of occipital $\alpha-$activity. Their work indicated that increased GABAergic inhibition onto thalamo-cortical cells resulted in an $\alpha-$ resonance that is reinforced by reciprocal cortico-thalamic feedback, and hence leads to the emergence of frontal $\alpha-$activity. Using a network of single neurons, other experimental features observed during general anesthesia such as paradoxical excitation [113], burst suppression [114], or cortical spindles [115] have been also described successfully. Note that whereas these works focus on the details of biophysical aspects such as action potential and membrane currents, the mean field approach provides a physiologically more accurate description of electrocortical activity.

In summary, the theoretical studies point out that mathematical approach can be used to gain insight into the mechanisms underlying EEG oscillation during different states of arousal. For review of recent works in modeling anesthesia see Refs. [116, 25, 108]. In the following chapter, we present neural population models of EEG activity that are able to reproduce the specific changes in EEG rhythms during general anesthesia in close agreement with the experimental observations. Furthermore, these models allows us to elucidate how the molecular actions of anesthetics at the microscopic scale has an impact on macroscopic observables as recorded by neuroimaging techniques.

1.6 Conclusion

Our current knowledge indicates that anesthetics act by binding to specific target sites. Among different ligand-gated ion channels as the most likely molecular sites for anesthetic actions, the GABA receptor is one of the most important anesthetic targets. Moreover, during the altered states of arousal, specific changes in brain imaging data such as EEG patterns can be observed experimentally. Numerous studies provide convincing evidence that the potentiation of GABAergic receptors in cortical and thalamic neurons seems to play a crucial role in emerging the EEG signatures during states of decreased arousal. According to previous theoretical studies, mathematical modelings, in particular mean field models provide deeper insights into mechanisms that underlie the clinical and neurophysiological features of general anesthesia.

2

Studying neural population models of EEG activity

Contents

Abstract

Mathematical modeling plays a central role in understanding the mechanisms underlying a complex system. In the modeling framework, differential equations are well established to describe the principles that govern the dynamics of the system under study. The present chapter provides the essential mathematical tools, which are the basis for the future research described in the following chapters. In particular, we focus on ordinary and delay differential equations since they are widely used to characterize the dynamics of many physical and biological systems. The first section of this chapter aims to illustrate the dynamics of a stochastic damped harmonic oscillator. In the subsequent section, the delay differential equations as well as their stability analysis are discussed. Furthermore, it is shown how one can compute the power spectrum of a set of stochastic delay differential equations by the aid of Green's function method. Finally, in the last section the neural population models used in this thesis are described. It will be shown how using neural field models, the macroscopic behavior emerging from the interaction of neural populations can be described in close agreement with the experimental observations.

2.1 Damped harmonic oscillator

It is well know that many oscillatory motions in various physical and biological systems can be described by the classical simple harmonic oscillator (SHO) given by

$$m\frac{d^2x}{dt^2} = -kx, \tag{2.1}$$

where k and m denotes the oscillator's spring constant and mass, respectively [117]. Since the SHO is neither driven nor damped by any external force, the system oscillates sinusoidally with a constant amplitude and a frequency of $f_0 = \omega_0/2\pi$, where $\omega_0 = \sqrt{k/m}$ is the resonant angular frequency of the system [117]. However, in many real-world systems, the oscillations are damped by the resistive or fractional forces. When the damping force depends linearly on the velocity of the oscillator ($F_c = -cdx/dt$), the time evolution of the object is given by [118]

$$\frac{d^2x}{dt^2} + \gamma\frac{dx}{dt} + \omega_0^2 x = 0, \tag{2.2}$$

where $\gamma = c/m > 0$ is a velocity-dependent constant which determines the strength of damping in the system [119]. When the damping constant γ is small ($\gamma < 2\omega_0$), the system is *under-damped* and oscillates at the shifted resonance frequency $\omega_d = \sqrt{\omega_0^2 - \gamma^2/4}$ with an amplitude that decays exponentially (ω_d illustrates the observable frequency of the oscillator). If $\gamma = 0$, $\omega_d = \omega_0$, the system re-casts to the SHO given by Eq. (2.1). When the damping constant γ is large ($\gamma > 2\omega_0$), the system is *over-damped* and returns to the steady state without oscillating. For a value of γ between under- and over-damped characteristic values ($\gamma = 2\omega_0$), the system is *critically damped* in which it returns to the steady state as quickly as possible without oscillating [120].

The dynamics of a damped harmonic oscillator driven by a random stochastic force can be described by the following stochastic differential equation [121]

$$\frac{d^2x}{dt^2} + \gamma\frac{dx}{dt} + \omega_0^2 x = \xi(t), \tag{2.3}$$

where ω_0 illustrates the intrinsic (undamped) angular frequency of the oscillator, γ denotes the damping coefficient, and $\xi(t)$ is Gaussian white noise, i.e., with zero mean and a δ correlation in time

$$\langle \xi(t) \rangle = 0, \quad \langle \xi(t)\xi(t') \rangle = 2\kappa\delta(t - t'), \tag{2.4}$$

where $\langle . \rangle$ denotes the ensemble average and κ is the intensity of the uncorrelated driving noise [122, 123].

Applying the Wiener-Khinchin theorem which states that the power spectral density of a stationary process is the Fourier transform of its autocorrelation, yields the following formula for the power spectrum of stochastic damped harmonic oscillator [124, 125]

$$P(\omega) = \frac{2\kappa}{\sqrt{2\pi}} \frac{1}{(\omega^2 - \omega_0^2)^2 + \gamma^2\omega^2}, \tag{2.5}$$

where has one maximum at $\omega_{max} = \sqrt{\omega_0^2 - \gamma^2/2}$.

The effect of damping coefficient on dynamics of damped harmonic oscillator are shown in Fig. 2.1. In this figure, the power spectra (panel **A**) and the time-series (panel **B**) are illustrated for different values of damping constant. It can be observed that when $\gamma = 0$, the system oscillates with a constant amplitude and shows a sharp spectral peak at the natural frequency of $f_0 = \omega_0/2\pi$. For a small value of damping coefficient (e.g., $\gamma = 0.5$ Hz) the system oscillates with an exponentially decreasing amplitude i.e., the oscillator enters in the under-damped regime. When the damping coefficient is large (e.g., $\gamma = 15$ Hz) the system is over-damped and decays to the steady state without oscillating. In this case, no peak can be seen in the corresponding power spectrum.

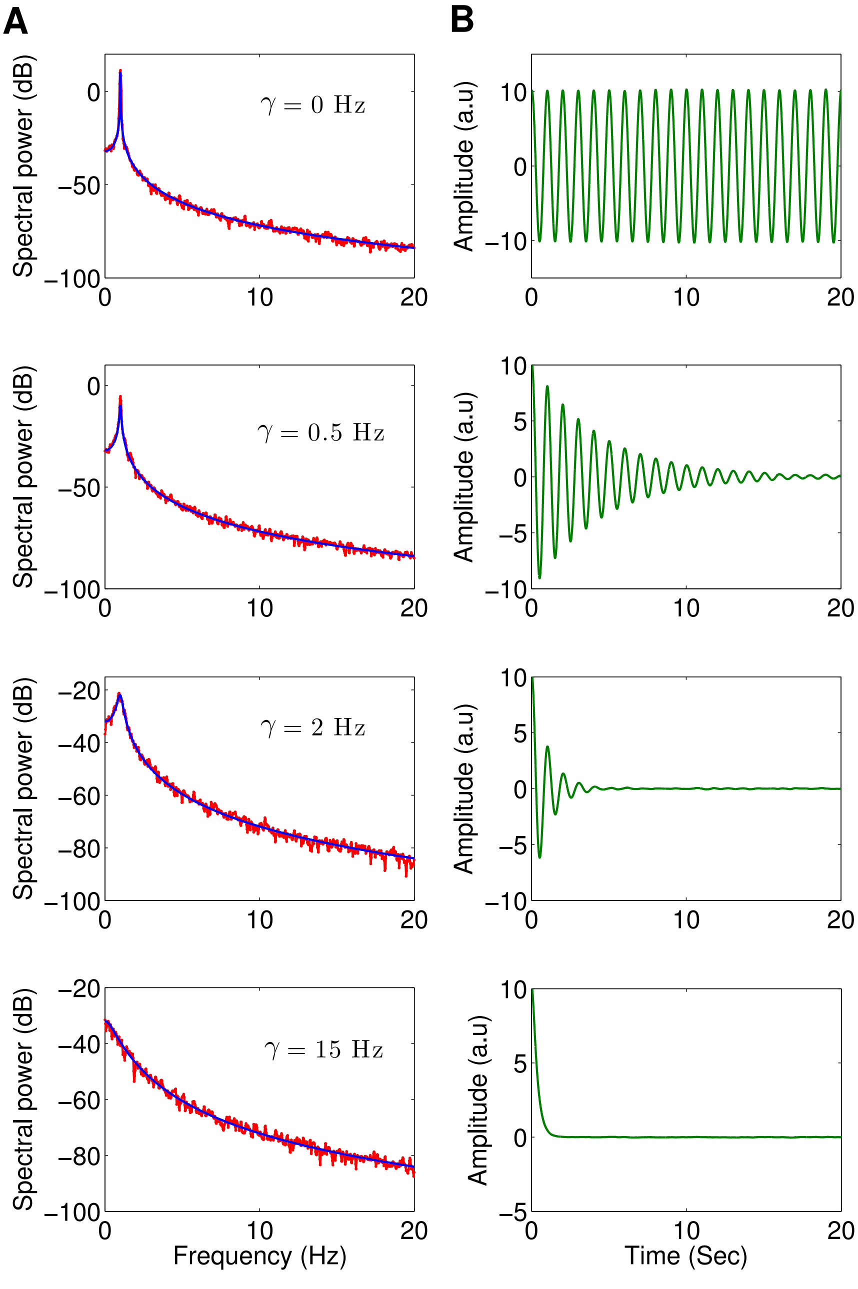

Figure 2.1. Dynamics of damped harmonic oscillator driven by a random stochastic force. The panel (**A**) shows the theoretical and numerical power spectra in blue and red, respectively, for different values of damping coefficients; $\gamma = 0, 0.5, 2, 15$ Hz. The corresponding simulated time series are presented in panel (**B**). For smaller values of damping coefficients, the power spectral peak is sharper whereas for large value of γ, there is no peak in the computed spectrum. The intrinsic angular frequency of the oscillator is chosen as $\omega_0 = 2\pi$, thus $f_0 = 1Hz$.

2.2 Linear delay differential equations

Delays or lags occur in many physical and biological systems, due to the limited processing speeds between non-local elements. In neuroscience, the finite propagation speed of action potentials along axonal branches, or in more general terms, the finite-time interaction between two elements in a spatially extended system is associated with a time delay. In this context, it is important to study the dynamics of differential equations with delay because most of the models describing the activity of a large population of neurons are governed by a set of coupled delay differential equations. In the current study, the time delays are treated as a constant in the system equations.

The dynamic of systems with time delay can be described by Delay Differential Equations (DDEs), also known as difference differential equations, which are a special class of differential equations that the rate of changes in the system depends on its past history. Time-delay systems and their applications can be found in many different scientific areas such as control theory, electronic circuits, nonlinear optics and lasers, neuroscience, networks and communication and so on [126, 127]. It has been extensively recognized that delays play a crucial role in mathematical modeling of real-world systems and explaining their dynamical properties. For instance, it has been shown that the delay values can determine the existence, stability and periodicity of the solutions [128, 129, 130, 131, 132, 133, 134, 135], the bifurcations of equilibria [136, 137, 138, 139], and the synchronization in such systems [140, 141, 142, 143, 144, 145].

In general, the mathematical formulation of a linear DDE is given by

$$\begin{cases} \dfrac{d\boldsymbol{Y}(t)}{dt} = \boldsymbol{A}\boldsymbol{Y}(t) + \boldsymbol{B}\boldsymbol{Y}(t-\tau), \qquad t \geq 0, \\ \\ \boldsymbol{Y}(t) = \boldsymbol{\phi}(t), \quad t \in [-\tau, 0], \end{cases} \tag{2.6}$$

where $\boldsymbol{Y}$ is an $N \times 1$ activity variable vector, $\boldsymbol{A}$ and $\boldsymbol{B}$ are constant quadratic matrices of order N, $\tau > 0$ denotes the time-delay, and $\boldsymbol{\phi}(t)$ is a continuous function that defines the initial condition [146]. Although a large number of studies have been devoted to obtain the exact stability conditions for these equations, finding analytical solutions for a wide class of DDEs remains as an open problem [147, 148, 149, 150, 151]. The DDEs are often solved using numerical methods such as the Euler or Runge-Kutta method [146, 152], by employing a Lambert function [153, 154], the discretization of the solution operator as implemented in the software package DDE-BIFTOOL [155, 156, 157], or by discretizating the infinitesimal generator as implemented in the software package TRACE-DDE [158, 159].

2.2.1 Stability of delay differential equations

The solution of a DDE is asymptotically stable if and only if all the roots of the characteristic equation referred to as the characteristic roots have negative real parts. The system is called unstable if there exists a root with positive real part. For an ordinary differential equation the characteristic function is a polynomial and the well-known Routh-Hurwitz criterion can be used to determine the negativity of the real parts of characteristic roots and thus the stability of the solution [160, 161, 162]. However, the characteristic functions for DDEs are not ordinary polynomial, instead, they are named as transcendental equation or exponential polynomials or quasi-polynomials, which the number of their roots can be countably infinite [163].

Assuming a solution of Eq. (2.6) takes the form of $\boldsymbol{Y}(t) = \boldsymbol{C}e^{\lambda t}$, where $\lambda \in \mathbb{C}$, yields the following *characteristic equation*

$$det\left(\lambda\boldsymbol{I} - \boldsymbol{A} - \boldsymbol{B}e^{-\lambda\tau}\right) = 0, \tag{2.7}$$

where $\mathbf{I}$ is an $N \times N$ identity matrix. This equation can be written as

$$P(\lambda) + e^{-\lambda\tau}Q(\lambda) = 0, \tag{2.8}$$

where and $P(\lambda)$ and $Q(\lambda)$ are polynomial in λ. This transcendental equation is known to have an infinite number of complex roots which, in general, cannot be expressed explicitly in terms of elementary functions. It is well-known that the system is asymptotically stable if and only if all the characteristic roots have negative real parts, i.e., $Re(\lambda < 0)$. Many approaches have been taken to determine the stability of the transcendental equations, however, in general no closed-form solution for Eq. (2.8) is available [164]. An analytic approach to obtain the solution of linear systems of DDEs is based on the concept of the Lambert function. Every function $W(x)$ that satisfies $W(x)e^{W(x)} = x$ is called a Lambert function [165]. The lamber function, $W(x)$ has an infinite number of branches $W_k(x)$, where $k \in -\infty, ..., -1, 0, 1, ...\infty$. It has been shown that the solution of Eq. (2.6) in terms of the Lambert function is given by [153, 166]

$$\boldsymbol{Y}(t) = \sum_{k=-\infty}^{k=-\infty} \boldsymbol{C_k} e^{\left(\frac{1}{\tau}\boldsymbol{W_k}(\boldsymbol{B}\tau e^{-\boldsymbol{A}\tau}) + \boldsymbol{A}\right)\tau}, \tag{2.9}$$

where the $\boldsymbol{C_k}$ is an $N \times 1$ coefficient matrix computed from the initial condition. Moreover, the stability of the system can be determined by using the principal branch of the Lambert function as

$$\lambda\boldsymbol{I} = \frac{1}{\tau}\boldsymbol{W_0}(\boldsymbol{B}\tau e^{-\boldsymbol{A}\tau}) + \boldsymbol{A}. \tag{2.10}$$

It is important to note that this solution is not valid for any kind of DDEs. The solution obtained by a matrix Lamber function is valid if and only if the matrices A and B are simultaneously triangularizable (in a particular condition, matrices A and B commute, i.e., $AB = BA$) [167, 154]. Using this approach, the analytic explicit formula for the scalar problem, i.e., when $\mathbf{A} = a_0$, $\mathbf{B} = b_0 \in \mathbb{C}$ is given by $\lambda = \frac{1}{\tau}\boldsymbol{W}_k(b\tau e^{-a\tau}) + a$, where $k \in \mathbb{Z}$ is the branch index. The characteristic roots for a scalar DDE using Lambert function W(x) can be evaluated in Matlab with the following commands

```
lambda = lambertw(k,b*tau*exp(-a*tau))/tau+a,
```

where *tau* indicates the time delay.

A robust numerical algorithm to obtain characteristic roots of transcendental equations is spectral discretization of the infinitesimal generator. In this method, the characteristic roots can be computed approximately from the eigenvalues of a matrix. It is known that a DDE can be rewritten as a hyperbolic partial differential equation (PDE) with interrelated boundary conditions. The operator corresponding to the boundary values is the so-called infinitesimal generator, and its spectrum is equal with the solutions of the characteristic equation. Thus, the eigenvalues of a matrix resulting from a sufficiently fine discretization of the PDE will approximate the solutions of the characteristic equation. The approach based on the discretization of the PDE-representation was used in [168]. Similar ideas proved to be successful in [158, 169], by applying a spectral discretization scheme based on the Chebyshev nodes as implemented in the software package TRACE-DDE [159]. The method can be implemented in three lines of code as:

```
Nod=100; N=length(A);
D=-cheb(Nod-1)*2/tau;
lambda=eig([kron(D(1:Nod-1,:),eye(N));[B,zeros(N,(Nod-2)*N), A]])
```

where "Nod" denotes the discretization nodes and "N" is the size of the equation. The code above uses the function cheb.m, which returns a Chebyshev differentiation matrix. This function is publicly available in [170].

In the following we employ a robust analytical approach to investigate the stability of DDEs. This method treats the length of time delay as a bifurcation parameter to seek whether or not varying the delay length can change the stability characteristics of a steady state. A bifurcation occurs if by increasing the delay, a steady state becomes unstable i.e., the characteristic roots λ traverse the imaginary axis. According to this approach, finding a delay value which induces instability in the system re-casts to the problem of finding real positive roots of a polynomial. The transcendental equations given by Eq. (2.8) can be rewritten as

$$\sum_{n=0}^{N} a_n \lambda^n + e^{-\lambda\tau} \sum_{n=0}^{M} b_n \lambda^n = 0, \tag{2.11}$$

where $N > 0$ and $M > 0$ denotes the degree of polynomials $P(\lambda)$ and $Q(\lambda)$, respectively, and a_n and b_n are constant coefficients. First we investigate the conditions under which the system is stable in the absence of delay ($\tau = 0$) i.e., when all the roots of the polynomial $P(\lambda) + Q(\lambda)$ have negative real parts. Then we investigate whether a bifurcation can occur as a result of the introduction of delay, i.e., a root transitions from having negative to having positive real parts. By inserting a purely imaginary root as $i\omega$, where $\omega \in \mathbb{R}$, into Eq. (2.8) we obtain

$$P(i\omega) + e^{-i\omega\tau} Q(\omega) = 0, \tag{2.12}$$

and after separating the real and imaginary parts, and writing the exponential in terms of trigonometric functions we get

$$\mathrm{Re}_{\mathrm{P}}(\omega) + i\,\mathrm{Im}_{\mathrm{P}}(\omega) + (\mathrm{Re}_{\mathrm{Q}}(\omega) + i\,\mathrm{Im}_{\mathrm{Q}}(\omega))(\cos(\omega) - i\sin(\omega)) = 0, \tag{2.13}$$

with

$$\begin{aligned}
\mathrm{Re}_{\mathrm{P}}(\omega) &= \sum_{n=0}^{N} (-1)^{n+1} a_{2n} \omega^{2n}, \\
\mathrm{Im}_{\mathrm{P}}(\omega) &= \sum_{n=0}^{N} (-1)^{n} a_{2n+1} \omega^{2n+1}, \\
\mathrm{Re}_{\mathrm{Q}}(\omega) &= \sum_{n=0}^{M} (-1)^{n+1} b_{2n} \omega^{2n}, \\
\mathrm{Im}_{\mathrm{Q}}(\omega) &= \sum_{n=0}^{M} (-1)^{n} b_{2n+1} \omega^{2n+1},
\end{aligned}$$

where Re_{P} and Re_{Q} are even polynomials of ω, while Im_{P} and Im_{Q} are odd polynomials. Since Eq. (2.13) must hold for both the real and imaginary parts, we obtain

$$\begin{aligned}
\mathrm{Re}_{\mathrm{P}}(\omega) + \mathrm{Re}_{\mathrm{Q}}(\omega)\cos(\omega\tau) + \mathrm{Im}_{\mathrm{Q}}(\omega)\sin(\omega\tau) = 0, \\
\mathrm{Im}_{\mathrm{P}}(\omega) - \mathrm{Re}_{\mathrm{Q}}(\omega)\sin(\omega\tau) + \mathrm{Im}_{\mathrm{Q}}(\omega)\cos(\omega\tau) = 0,
\end{aligned} \tag{2.14}$$

and by squaring each equation and summing the results we get

$$\mathrm{Re_P}^2(\omega) + \mathrm{Im_P}^2(\omega) = \mathrm{Re_Q}^2(\omega) + \mathrm{Im_Q}^2(\omega), \tag{2.15}$$

which is a delay-independent polynomial of degree $2N$. Since Eq. (2.15) is an even polynomial equation, it can be written as a N-th degree polynomial in terms of new variable $\Omega = \omega^2 \in \mathbb{R}$, as $\mathcal{P}(\Omega) = 0$. If all the real roots of polynomial $\mathcal{P}(\Omega)$ are negative, i.e., $\mathcal{P}$ has not any positive real root, there is no solution for Eq. (2.14) and therefore increasing τ does not lead to any change in the stability of the system. Conversely, if $\mathcal{P}(\Omega)$ has a positive real root, there is a critical value for delay (τ) that solves Eq. (2.14), and thus can cause a bifurcation.
This result can be summarized in the following theorem:

Theorem 1 (Forde & Nelson [171]) *Consider a system of delay differential equation $\dot{y}(t) = f(y(t), y(t-\tau))$ with $f : \mathbb{R}^n \times \mathbb{R}^n \to \mathbb{R}^n$, and a constant delay τ, where the associated characteristic equation is given by*

$$\sum_{n=0}^{N} a_n \lambda^n + e^{-\lambda\tau} \sum_{n=0}^{M} b_n \lambda^n = 0.$$

If the steady state is stable in the absence of delay i.e., $\tau = 0$, then with increasing delay values, there exists a critical delay $\tau^* > 0$ for which the steady state becomes unstable if and only if $\mathcal{P}(\Omega)$ given by

$$\left(\sum_n (-1)^n a_{2n} \Omega^n\right)^2 + \Omega \left(\sum_n (-1)^n a_{2n+1} \Omega^n\right)^2 = \left(\sum_n (-1)^n b_{2n} \Omega^n\right)^2 + \Omega \left(\sum_n (-1)^n b_{2n+1} \Omega^n\right)^2,$$

has a positive real root $\Omega^* = (\omega^*)^2$.

Thus, when the polynomial $\mathcal{P}(\Omega)$ has been derived, we must determine whether or not it has any positive real root. The roots of any second-order polynomial can be expressed explicitly by well-known quadratic formula. However, the general formula describing the roots of third and fourth degree polynomials are complicated. Nevertheless, to determine wether a polynomial has any positive real root or not, it is not necessary to compute the roots explicitly. Instead, it is sufficient merely to apply simpler approaches such as Routh-Hurwitz condition and Descartes' Rule of Signs. It is important to point out that Routh-Hurwitz condition is a method to determine whether or not a polynomial is stable. In other words, it determines if all of the roots of a polynomial are in the left half of the complex plane (the characteristic roots have negative real part). Thus, it is not an efficient method to determine whether or not a polynomial has any positive real roots. It is possible that a second-order polynomial has no positive real solution (it has a conjugate pair of roots with positive real part and non-zero imaginary part) but fails to satisfy the Routh-Hurwitz condition. For instance, for the polynomial $x^2 - 2x + 25 = 0$, whose roots are $1 \pm 2i\sqrt{6}$, the Routh-Hurwitz conditions are not satisfied, however, the polynomial has no positive real root. An appropriate approach to identify the possible number of positive real roots of a polynomial is Descartes' Rule of Signs. This method determines the maximum number of positive and negative real roots of a polynomial. More precisely, the rule states that the number of positive real roots is equal to the number of sign changes in the coefficients, modulo 2. Thus, if the number of sign changes is odd, a positive real root is guaranteed. If, however, the number of sign changes is even, the rule cannot distinguish between, for example, two roots and zero roots. In this situation, one must use a more general approach such as the so-called Sturm sequences. For a detailed discussion see Ref. [171].

Consider a scalar form of the linear DDEs given by Eq. (2.6), with $A = a$ and $B = b$, as real numbers. Setting a candidate solution in the form of $y(t) = Ce^{\lambda t}$ yields the following characteristic equation:

$$\lambda - a - be^{-\lambda\tau} = 0. \tag{2.16}$$

In the absence of delay we obtain

$$\lambda - a - b = 0,$$

in which it is stable if and only if $a+b < 0$. Inserting $\lambda = i\omega$ into Eq. (2.16) yields the polynomial $\mathcal{P}(\Omega)$ as

$$\Omega + a^2 - b^2 = 0.$$

Thus, $\mathcal{P}(\Omega)$ has not any positive real root if and only if $a^2 - b^2 > 0$. Taking these conditions together, a linear scalar DDE is stable if and only if $a+ \mid b \mid < 0$, or equivalently $a < b < -a$, which is independent of the delay values. Note that this condition is a *sufficient*, but not a *necessary* criterion for stability of linear systems. For instance, as it is shown in Fig. 2.2, all the characteristic roots of a linear system with $a = 0.5$, $b = -1$, and $\tau = 1$, have negative real parts, i.e., the system is stable. However, this point lies outside the region bounded by two lines $a + b = 0$ and $a - b = 0$. The exact stability condition for a scaler linear DDE is given by the following delay-dependent criterion

Theorem 2 (Hayes theorem [172]) *All roots of* $\lambda - a - be^{-\lambda\tau} = 0$*, have negative real parts if and only if*
if $b^2 - a^2 > 0$*, then:* $a + b < 0$*, and* $\sqrt{b^2 - a^2} < \frac{1}{\tau} arccos(-a/b)$,
if $b^2 - a^2 \leq 0$*, then:* $a + b < 0$ *(or equivalently* $-a < b < a$*).*

which comprises the delay-independent condition given by the cone $a+ \mid b \mid < 0$. This condition is depicted in the (a,b)-plane in Fig. 2.3 for $\tau = 1$, as compared to the delay-independent condition $a+ \mid b \mid < 0$. The shaded region shows the exact stability condition given by Theorem 2, whereas the hatched region displays the delay-independent condition given by Theorem 1. It can be seen that the delay-independent condition obtained by the presented approach provides a good approximation to the exact delay-dependent condition.

2.2.2 Power spectrum of delay differential equations

We close this section by computing the power spectrum of DDEs with the aid of of Green's function method. In general, a functional DDE can be written as

$$\hat{\boldsymbol{L}}(\partial/\partial t)\boldsymbol{X}(t) = \mathbf{F}(\boldsymbol{X}(t), \boldsymbol{X}(t-\tau)), \tag{2.17}$$

where $\boldsymbol{X}(t) \in \mathbb{R}^N$ is the activity variable vector, the diagonal matrix operator $\hat{\boldsymbol{L}}(\partial/\partial t) \in \mathbb{R}^{N\times N}$ includes the temporal operators, and $\mathbf{F} : \mathbb{R}^N \times \mathbb{R}^N \to \mathbb{R}^N$ denotes the nonlinear vector function at some resting state $\boldsymbol{X}_0 \in \mathbb{R}^N$, for instance, if $\hat{\boldsymbol{L}} = \mathbf{0}$, then $\mathbf{F}(\boldsymbol{X}_0, \boldsymbol{X}_0) = 0$, or if $\hat{\boldsymbol{L}} = \mathbf{1}$, then $\boldsymbol{X}_0 = \mathbf{F}(\boldsymbol{X}_0, \boldsymbol{X}_0)$. The system equations can be written as

$$\hat{\boldsymbol{L}}(\partial/\partial t)\boldsymbol{X}(t) = \boldsymbol{\Phi}(\boldsymbol{X}(t)) + \boldsymbol{\Psi}(\boldsymbol{X}(t-\tau)), \tag{2.18}$$

where those terms that have delays are separated from those terms without delays.
By adding an external input $\boldsymbol{I}(t)$ to the above system equation, we obtain

$$\hat{\boldsymbol{L}}(\partial/\partial t)\boldsymbol{X}(t) = \boldsymbol{\Phi}(\boldsymbol{X}(t)) + \boldsymbol{\Psi}(\boldsymbol{X}(t-\tau)) + \boldsymbol{I}(t), \tag{2.19}$$

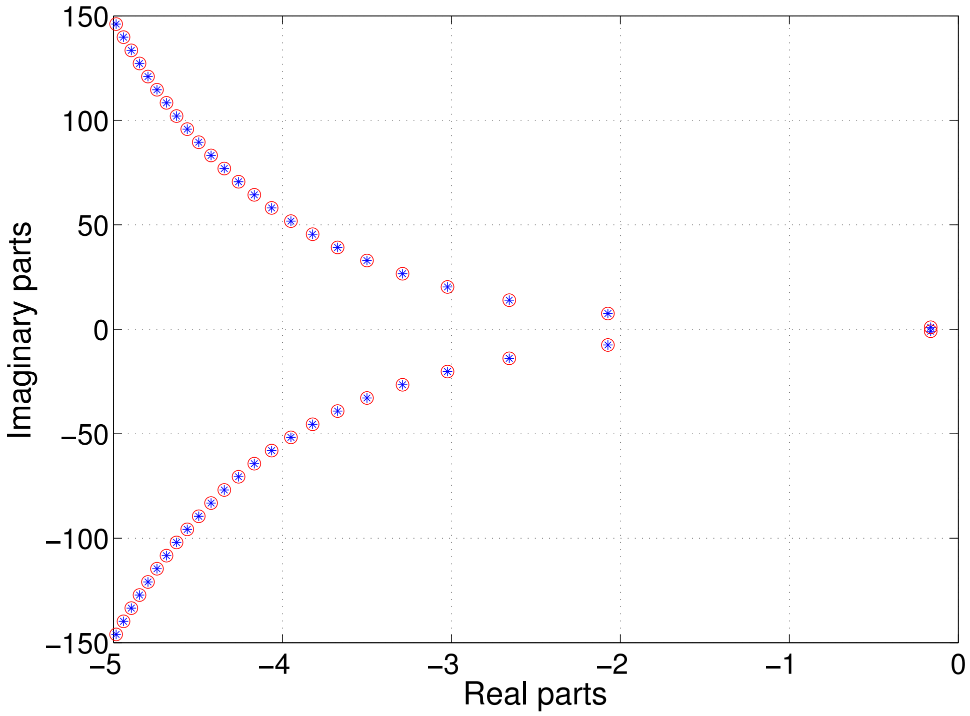

Fig. 2.2. Characteristic roots of a linear scalar DDE given by $\dot{y}(t) = ay(t) + by(t-\tau)$, where $a = 0.5$, $b = -1$, and $\tau = 1$. Since all the roots have negative real parts, the system is stable. The characteristic roots obtained by using Lambert function given by $\lambda = \frac{1}{\tau}\boldsymbol{W}_k(b\tau e^{-a\tau}) + a$ for $k \in -50, ..., 0, ..., 50$ are represented as open red circles, whereas the blue asterisks show the roots simulated by the spectral discretization of infinitesimal generator based on the Chebyshev nodes.

with $\boldsymbol{I}(t) = \boldsymbol{I}_0 + \boldsymbol{\xi}(t) \in \mathbb{R}^N$, where $\boldsymbol{I}_0 = (0, 0, ..., I_0, ..., 0)^\top$ denotes the mean value of external input, and $\boldsymbol{\xi}(t) = (0, 0, ..., \xi(t), ..., 0)^\top$ is a Gaussian white noise (c.f. Eq. (2.4)), which is projected onto the j-th element of the activity variable. The high index $\top$ denotes the transposed vector or matrix. Now, the resting state of the system i.e., $\boldsymbol{X}_0 \in \mathbb{R}^N$ can be obtain from $\boldsymbol{\Phi}(\boldsymbol{X}_0) + \boldsymbol{\Psi}(\boldsymbol{X}_0) + \boldsymbol{I}_0 = 0$ if $\hat{\boldsymbol{L}} = \boldsymbol{0}$ or $\boldsymbol{X}_0 = \boldsymbol{\Phi}(\boldsymbol{X}_0) + \boldsymbol{\Psi}(\boldsymbol{X}_0) + \boldsymbol{I}_0$ if $\hat{\boldsymbol{L}} = \boldsymbol{1}$. Linearizing this equation at resting state $\boldsymbol{X}_0$ yields the following linear stochastic DDE

$$\hat{\boldsymbol{L}}(\partial/\partial t)\boldsymbol{Y}(t) = \boldsymbol{A}\boldsymbol{Y}(t) + \boldsymbol{B}\boldsymbol{Y}(t-\tau) + \boldsymbol{\xi}(t), \tag{2.20}$$

where $\boldsymbol{Y}(t) = \boldsymbol{X}(t) - \boldsymbol{X}_0$, and $\boldsymbol{A}$, $\boldsymbol{B} \in \mathbb{R}^{N\times N}$ are constant quadratic matrices such that $\boldsymbol{A} \equiv \mathbf{J}_{\boldsymbol{\Phi}}(\boldsymbol{X}_{\mathbf{0}})$, and $\boldsymbol{B} \equiv \mathbf{J}_{\boldsymbol{\Psi}}(\boldsymbol{X}_{\mathbf{0}})$, where $\mathbf{J}_{\boldsymbol{\Phi}}(\boldsymbol{X}_0)$ and $\mathbf{J}_{\boldsymbol{\Psi}}(\boldsymbol{X}_0)$ are the Jacobian matrices for functions $\boldsymbol{\Phi}$ and $\boldsymbol{\Psi}$, respectively, computed at the fixed point $\boldsymbol{X}_0$.

The solution of Eq. (2.20) for $t \to \infty$ is

$$\boldsymbol{Y}(t) = \int_{-\infty}^{\infty} \boldsymbol{G}(t-t')\boldsymbol{\xi}(t')dt', \tag{2.21}$$

with the matrix Green's function $\boldsymbol{G} \in \mathbb{R}^{N\times N}$. Substituting Eq. (2.21) into Eq. (2.20) leads to

$$\hat{\boldsymbol{L}}(\partial/\partial t)\boldsymbol{G}(t) = \boldsymbol{A}\boldsymbol{G}(t) + \boldsymbol{B}\boldsymbol{G}(t-\tau) + \mathbf{1}\delta(t), \tag{2.22}$$

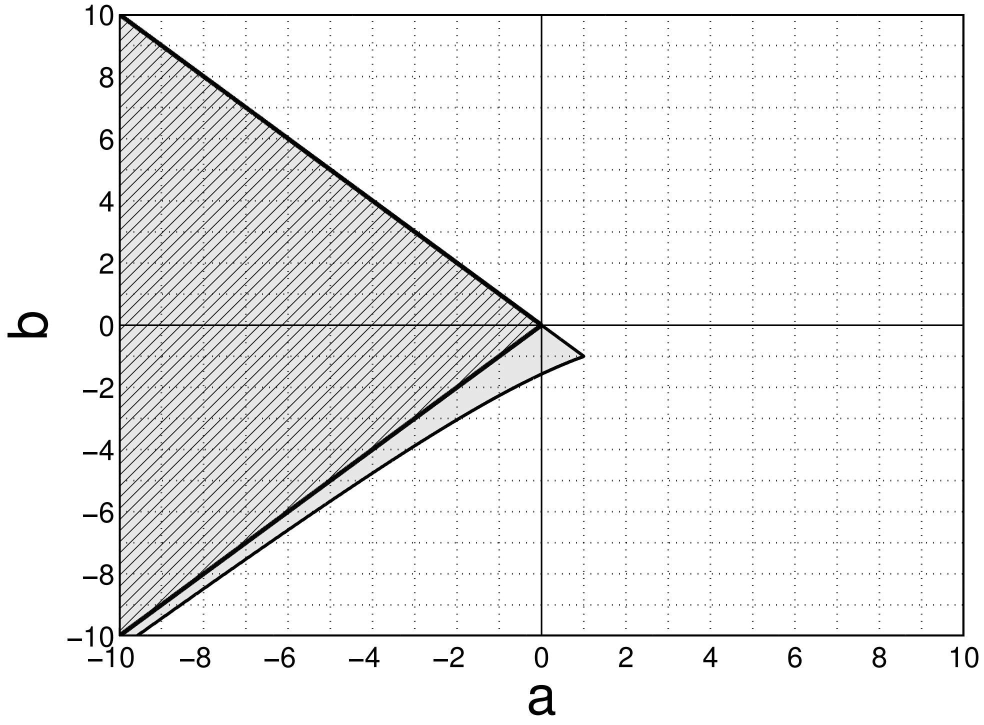

Fig. 2.3. The stability region for a linear scalar DDE given by $\dot{y}(t) = ay(t) + by(t-\tau)$, where $\tau = 1$. The shaded region presents the exact condition driven by Hayes theorem [172], which depends on the delay value (c.f. Theorem 2), whereas the hatched area shows the approximated condition given by the cone $a+ \mid b \mid < 0$, which is independent of the delay value (c.f. Theorem 1).

with the unitary matrix $\mathbf{1} \in \mathbb{R}^{N\times N}$, where the Dirac delta function $\delta(t)$ is given by

$$\delta(t) = \frac{1}{2\pi}\int_{-\infty}^{\infty} e^{-i\omega t} d\omega, \tag{2.23}$$

where ω denotes complex angular frequency. In addition, it can be shown that

$$\hat{\boldsymbol{L}}\left(\frac{\partial}{\partial t}\right) e^{i\omega t} = \hat{\boldsymbol{L}}(\omega) e^{i\omega t} \tag{2.24}$$

Applying the Fourier transform

$$\boldsymbol{G}(t) = \frac{1}{\sqrt{2\pi}}\int_{-\infty}^{\infty} \tilde{\boldsymbol{G}}(\omega) e^{i\omega t} d\omega, \tag{2.25}$$

and substituting Eq. (2.23)-(2.25) into Eq. (2.22) yields

$$\int_{-\infty}^{\infty} \hat{\boldsymbol{L}}\tilde{\boldsymbol{G}}(\omega) e^{i\omega t} d\omega - \int_{-\infty}^{\infty} \boldsymbol{A}\tilde{\boldsymbol{G}}(\omega) e^{i\omega t} d\omega - \int_{-\infty}^{\infty} \boldsymbol{B}\tilde{\boldsymbol{G}}(\omega) e^{i\omega (t-\tau)} d\omega = \frac{1}{\sqrt{2\pi}}\int_{-\infty}^{\infty} e^{i\omega t} d\omega,$$

thus, the Fourier transform of the Green's function of system can be written as

$$\tilde{\boldsymbol{G}}(\omega) = \frac{1}{\sqrt{2\pi}}\left[\boldsymbol{L}(\omega) - \boldsymbol{A} - \boldsymbol{B}e^{-i\omega\tau}\right]^{-1}. \tag{2.26}$$

The power spectral density matrix $\boldsymbol{P}(\omega)$ of $\boldsymbol{Y}(t)$ is the Fourier transform of the auto-correlation function matrix $\langle \boldsymbol{Y}(t)^t \boldsymbol{Y}(t-T) \rangle$ (Wiener-Khinchine Theorem) leading to [111]

$$\boldsymbol{P}(\omega) = 2\kappa\sqrt{2\pi}\tilde{\boldsymbol{G}}(\omega)\tilde{\boldsymbol{G}}^{\top}(-\omega).$$

Finally, by virtue of the specific choice of external input to the j-th element of the activity variable, the power spectrum of i-th element just depends on one matrix component of the matrix Green's function by

$$P_i(\omega) = 2\kappa\sqrt{2\pi}\tilde{G}_{i,j}(\omega)\tilde{G}_{i,j}(-\omega) = 2\kappa\sqrt{2\pi}\left|\tilde{G}_{i,j}(\omega)\right|^2. \tag{2.27}$$

Applying this approach to a first order scalar linear DDE with additive Gaussian white noise given by

$$\frac{dy(t)}{dt} = ay(t) + by(t-\tau) + \xi(t), \tag{2.28}$$

yields the following Fourier transform of the Green's function

$$\tilde{G}(\omega) = \frac{1}{\sqrt{2\pi}}\left(i\omega - a - be^{-i\omega\tau}\right)^{-1}, \tag{2.29}$$

and consequently, the power spectrum is

$$P(\omega) = \frac{2\kappa}{\sqrt{2\pi}}\frac{1}{(a + b\cos(\omega\tau))^2 + (\omega + b\sin(\omega\tau))^2}. \tag{2.30}$$

2.3 Neural population models

In this section we first describe mean-field approximation in order to model the activity of large populations of neurons. Subsequently, a brief review of two well-established neural field models for reproducing the EEG oscillations is provided: 1) Robinson model [173, 174, 23], which includes excitatory and inhibitory cortical populations that are synaptically connected to thalamic reticular and relay neuron populations by delayed thalamo-cortical axonal fibers. The model is able to reproduce various features in EEG data recorded during different brain activities. 2) A neural population model based on a recently developed neural field model of anesthetic action (Hutt & Longtin) [28]. This model has a same topological configuration as Robinson model, however, it distinguishes excitatory and inhibitory synapses. Both models are based on the models of Wilson & Cowan [98], and Amari [99], which involve averages of synaptic and neuronal activities over a population in small spatial patches and short time windows.

2.3.1 Neural field models

The oscillatory activities generated by thousands or millions of synchronized neurons at the macroscopic level can be measured by the EEG recordings. A large body of evidence has revealed that the brain activities across different behavioral states such as wakefulness, non-REM and REM sleep, anesthesia and deep coma have their own distinct rhythmic EEG patterns [175, 29, 30, 173, 176, 177, 17, 19, 83]. In other words, the EEG observables and the behavioral states are highly correlated such that the rhythmic pattern of traces in an EEG recording reflects the state of the brain activity. In particular, neuroimaging studies have extensively shown that during the transition from wakefulness to loss of consciousness, the characteristic features in EEG power spectra can be used to track the level of consciousness [85, 178, 19, 18, 81, 179, 82].

It is generally assumed that the scalp-recorded EEG signals represent the aggregate synaptic activity of large numbers of vertically oriented pyramidal cells [22]. Complete understanding of the mechanisms underlying the generation of EEG rhythmic patterns requires the detailed biophysical modeling of synapses and spiking neurons. However, the physiological topology of real neuronal networks are rather unknown in details. Moreover, the detailed simulation of a small realistic neural network is very computationally expensive. For instance, a small-scale neural network such as a cortical column comprises a huge number of neurons (on the order of 10^4-10^8 neurons), while each of them being synaptically connected to other 10^4-10^5 neurons [20]. Relating the behavioral phenomena that are observed at the macroscopic scales to the individual elements of such large ensembles is also extremely challenging. Indeed, most of the coarse-scale observables such as EEG reflect the overall activity of a large population of neurons. This aspect allows us to successfully simulate the empirical EEG signals by mean-field approximations [180, 21, 181, 96, 92, 29, 30, 23, 182, 183]. Through a set of differential equations or integral-differential equations, these models describe the average properties of neural ensembles, such as mean voltage or mean firing rate whilst their output variables can be strongly linked to macroscopic experimental quantities such as Local Field Potentials (LFPs) and EEG [97, 20, 184, 185, 26, 94]. Moreover, this description considers ensembles of excitatory and inhibitory neurons, which incorporates the connection elements between neurons as excitatory and inhibitory synapses. The coupling strengths, synaptic response functions, dendritic dynamics, nonlinear somatic firing rates, and transmission delays in axonal propagation related to non-local interactions are other important components of the mean-field models [186, 187, 93, 28].

The mathematical formulation of neural population activity have been triggered by the work of Wilson & Cowan [98], and Amari [99]. Since then, many mean-field models have been proposed especially for describing cortical population dynamics [96, 97, 24, 188, 174, 173, 28]. These works consider the cortex as a two-dimensional sheet of tissue with negligible thickness. They also incorporate the interactions between excitatory and inhibitory neural populations which are connected through excitatory and inhibitory synapses. Such models at an intermediate mesoscopic level allows us to bridge the various spatial scales in the brain, from the microscopic scale of single neurons to the macroscopic scale i.e., the level of EEG/MEG recordings [20, 27].

In general, modeling of neural activity using mean-field approximation can be divided into two classes: neural field and neural mass models. The neural field models consider the neural populations as recurrent networks of densely packed neurons, while the average is taken over a small spatial patch on the millimeter scale and a short time window on the scale of few milliseconds. In this kind of description, the quantity characterizing neural activity such as average membrane potential of a neural population evolves over both space and time. Thus, the spatiotemporal evolution of coarse-grained state variables is described in such models. Moreover, the coupling of neuronal populations are associated with spatial parameters.

Neural field models can be simplified to the neural mass models [189]. For instance, it has been extensively shown that the EEG can be described in a good approximation by spatially constant neural population activity [29, 30, 23, 35, 36, 37]. Indeed, the neural mass models are particular case of neural field models, since in this description the neural populations are assumed to be located at a single point and the neural states are characterized by functions of time only [190]. Therefore, the main difference between neural field and neural mass models is that the former explicitly incorporate the spatial extension whereas it is neglected in the later description.

In recent decades, neural field and neural mass models have been extensively employed to explain different brain activities from local field potentials (LFP) to EEG/MEG signals [191, 192, 193, 194, 195, 196, 197, 95]. In particular, these models have been widely used to generate the EEG alpha oscillations [180, 198, 199, 182, 33, 200, 201]. Alpha-band oscillations are predominate oscillations in EEG brain signals recorded from occipital head region during wakeful relaxation with closed eyes whereas it is reduced with open eyes, drowsiness and sleep [202, 203]. It has been shown that the simulation results of such coarse-grained models display remarkably close agreement with the empirical observations in resting state brain dynamics [32, 204, 205, 206, 207]. Furthermore, these approaches have been proven to be successful in reproducing key features of electrical brain waves during sleep states [208, 209], general anesthesia condition [39, 40, 210, 24, 25, 28, 35, 211, 36, 37], and human epileptic seizures [23, 212, 213, 214, 31, 215, 176, 216, 217]. Other studies have also been reported that these type of modeling approaches are appropriate to describe brain dynamics in neurological disorders and cognitive tasks [218, 219, 220, 221, 222, 223, 224, 225].

In the following, before describing two neural field models that have been found to reproduce very well the characteristic features of spectra and evoked responses observed empirically, we first briefly present the role of thalamo-cortical circuits in the brain activities, because the body of models used in this thesis are based on the thalamo-cortical neural populations.

2.3.2 Thalamo-cortical circuits

It is known that the cortex, the thalamus, and the thalamo-cortical feedback loops contribute in the EEG oscillations. However, the precise role of each structure to the dynamics of EEG is unknown. While the macroscopic cortical activities are directly reflected in EEG data, the thalamus acts as both the gate for sensory input to the cortex and the site for feedback from cortical cells [226]. It has been shown that the specific changes in EEG patterns during the brain transition states can be determined by neural activities of the cortex, the thalamus and the interactions between them [35, 36, 37]. Therefore, a population-level model of thalamo-cortical system is a plausible candidate for investigating the mechanisms responsible for the various features observed in EEG data [186, 29, 30, 23, 91, 227].

In the last years, a large number of studies using mean-field models have been devoted to understand how EEG recordings are related to underlying brain activity [228, 23, 24, 176, 229, 35]. However, the exact neurobiological mechanisms that generate the EEG oscillatory signatures along with its relation to behavioral states remain to be fully understood. It has been shown that depend on the functional state of the brain, thalamo-cortical circuits are involved in generating different spontaneous oscillatory patterns such as oscillatory tonic and burst firing, across a wide range of frequencies from slow and spindle rhythms to gamma-frequency band [230, 228, 231, 232]. The reciprocal thalamo-cortical loops has been proposed to be responsible for normal EEG oscillations during wake and sleep states [233]. Other researches illustrate that the thalamo-cortical circuits crucially involve in the formation of sleep, normal physiologic activities [234, 235, 236], consciousness processing and anesthetic-induced unconsciousness [237, 44, 81, 238, 239], processing of sensory information [240, 241, 242], attention regulation [243, 244, 245, 246], and also synchronization of cortical activity [247, 248, 249, 250, 251, 252]. There are further evidences showing that a change in these circuits can impair consciousness and induces spike-and-slow wave discharges (SWD), which are essential features of the absence seizures [253, 254, 230, 228, 255]. It has also been reported that mediating of T-type calcium channels and HCN-channels, which could influence the excitation/inhibition balance in these circuits play an important role in regulating thalamo-cortical rhythmicity and absence seizures [233, 256, 236]. In addition, clinical studies have revealed that enhancing oscillations in the thalamo-cortical loops could lead to epileptic seizures [257].

2.3.3 Robinson model

In the 1990's David Liley and Jim Wright started developing partial differential equation models for neural population activity [96, 97]. Their works have inspired other teams, e.g., Peter Robinson and colleagues, who developed a similar neural model which has been proven to be very successful in reproducing key features of EEG signals recorded during different behavioral states such as sleep [29, 34], anesthesia [35, 36], and seizures [176, 258].

The model incorporates key anatomic connectivities within the cortex, within the thalamus, and between these structures: cortical, thalamic, cortico-thalamic and thalamo-cortical pathways. In addition, the model is furnished with synaptic and dendritic dynamics, nonlinearity of the firing response, and finite axonal transmission speeds [259].

The body of the model is based on a population-level description of a single thalamo-cortical module [173, 29] comprising four populations of neurons, namely excitatory (E) and inhibitory (I) cortical population, a population built of thalamo-cortical relay neurons (S) and of thalamic reticular neurons (R), as shown in Fig. 2.4. This model is based on the original idea of Lopes da Silva et al., stating that the α-rhythm represents the noisy thalamic input signal band-pass filtered by feedback-connected cortical and thalamic neural populations [180]. The details of the model and the nominal parameter values are taken from the previous works [29, 30, 23]. Here we just briefly describe the key concepts of the model. The average soma membrane potential denoted by V_a, for $a = E, I, S, R$ is modeled by

$$V_a(t) = \sum_{b=E,I,R,S} h_b(t) \otimes \nu_{ab}\phi_b(t - \tau_{ab}), \tag{2.31}$$

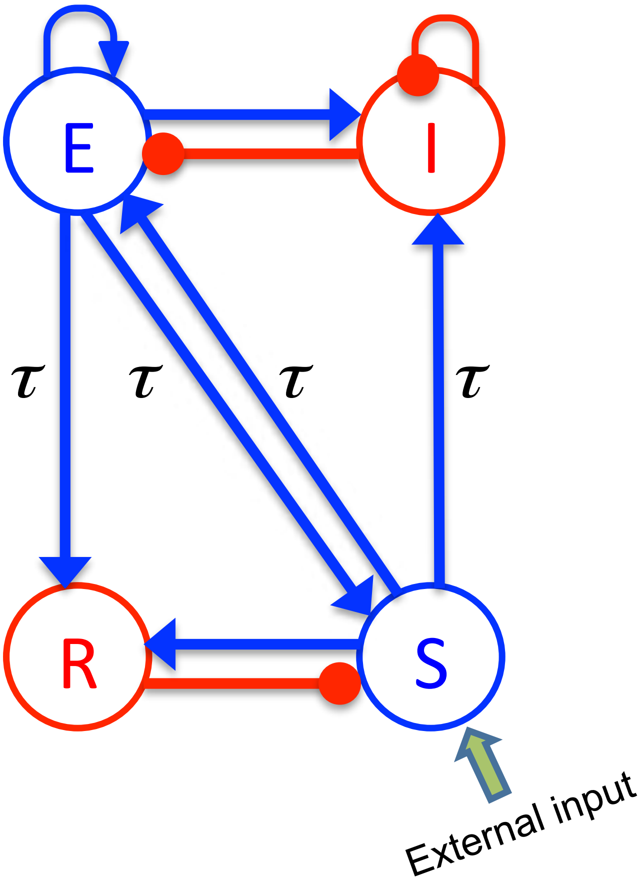

Fig. 2.4. Schematic diagram of Robinson model [29, 30, 23]. The blue arrows indicate excitatory connections while the red connections ending in filled circles denote inhibitory connections. The symbols E, I, S, and R denote the excitatory and inhibitory cortical neurons, thalamo-cortical relay, and thalamic reticular neurons, respectively. Moreover, the thalamo-cortical and cortico-thalamic connections exhibit the same nonzero time delay τ.

where $\otimes$ represents the temporal convolution, and $h_b(t)$ denotes the mean synaptic response function defined by

$$h_b(t) = \frac{\alpha\beta_b}{\alpha - \beta_b}\left(e^{-\beta_b t} - e^{-\alpha t}\right), \tag{2.32}$$

where α and β_b (with units Hz) are the synaptic rise and decay rates of the synaptic response functions, respectively. The synaptic decay rates and synaptic response functions depend on the source neurons of type b only and are independent of the target neurons. In the following, the subscript b in β_b is dropped for the simplicity reasons. The model assumes identical excitatory synaptic receptors with constant rise and decay rate. Inhibitory synaptic receptors are also assumed to exhibit identical constant rise and decay rates. This strong approximation is taken from a previous study [35] to be able to compare our results, while preliminary studies with more realistic parameters show similar results (not shown).

The constants ν_{ab} are the strengths of the connections from population of type b to population of type a (in mVs). More precisely, $\nu_{ab} = N_{ab}s_b$, where N_{ab} is the mean number of synapses from neurons of type b to type a, and s_b is the strength of the response to a unit signal from neurons of type b. Moreover, ϕ_b is the average firing rate of the population b (in Hz). The connections between cortex and thalamus are associated with a same non-zero time delay, $\tau_{ab} = \tau$, while the delay term is assumed to be zero within the cortex and within the thalamus [91, 229].

By virtue of long-range axonal projections of excitatory cortical neurons and by assuming the spatially-homogeneous dynamics on the cortex, the average firing rate ϕ_E obeys the damped oscillator equation

$$D\phi_E = S(V_E), \tag{2.33}$$

where the operator D is defined as

$$D = \left(\frac{1}{\gamma}\frac{\partial}{\partial t} + 1\right)^2, \tag{2.34}$$

and γ is the cortical damping rate. Note that it is assumed that ϕ_E is approximately proportional to the EEG. Moreover, the spatial spread of activity is very fast in other populations and the activity variable can be approximated by a sigmoidal function as $\phi_b = S(V_b)$, for $b = I, S, R$. The previous studies have considered a standard sigmoid formulation for the neuronal activation function $S(V_a)$

$$S(V_a) = \frac{S_a^{max}}{1 + \exp(-(V_a - \theta_a)/\sigma_a)}, \tag{2.35}$$

where S_a^{max} denotes the maximum population firing rate, θ_a indicates the mean firing threshold of neurons, and σ_a is related to the standard deviation of firing thresholds in population of type a. More precisely, $\sigma_a\sqrt{3}/\pi$ is the standard deviation of the threshold distribution in the neural population. The transfer function defined by Eq. (2.35) takes into account the distribution of firing thresholds of the neurons in the population [98] and the more similar the firing thresholds in the neural populations the smaller σ and the steeper the sigmoidal function.

Conversely to the original model [29, 30, 23], we use a more realistic transfer function derived from properties of type I-neurons given by [260]

$$S(V_a) = Sig(V_a, 0) - Sig(V_a, \rho), \tag{2.36}$$

with

$$Sig(V_a, \rho) = \frac{S_a^{max}}{2}\left(1 + \text{erf}\left(\frac{V_a - \theta_a - \rho\sigma_a^2}{\sqrt{2}\sigma_a}\right)\right) e^{-\rho(V_a - \theta_a) + \rho^2\sigma_a^2/2}, \tag{2.37}$$

where the parameter $\rho < \infty$ reflects the properties of type I-neurons. Note that $\rho \to \infty$ yields the standard formulation assuming McCulloch-Pitts neurons [261], with $Sig(V, \rho \to \infty) = 0$. In contrast to the standard sigmoid function (2.35), the novel transfer function (2.36) is not anti-symmetric to its inflection point anymore [261], and exhibits a larger nonlinear gain (slope) for large potentials $V > \theta$ compared to small potentials $V < \theta$, as illustrated in Fig. 2.5. This asymmetry results from the firing properties of type-I neurons, see Refs. [260, 261] for more details. Typically the sigmoidal shape of the transfer function leads to multiple resting states and its asymmetry gives the resting states that are closer to the θ. In this context, we mention another previous transfer function proposed by Freeman [262] to take into account an average sub-threshold value of sodium channels.

The external input to the system is considered as a non-specific input to thalamo-cortical relay neurons as

$$\phi_N = \langle\phi_N\rangle + \sqrt{2\kappa}\xi(t), \tag{2.38}$$

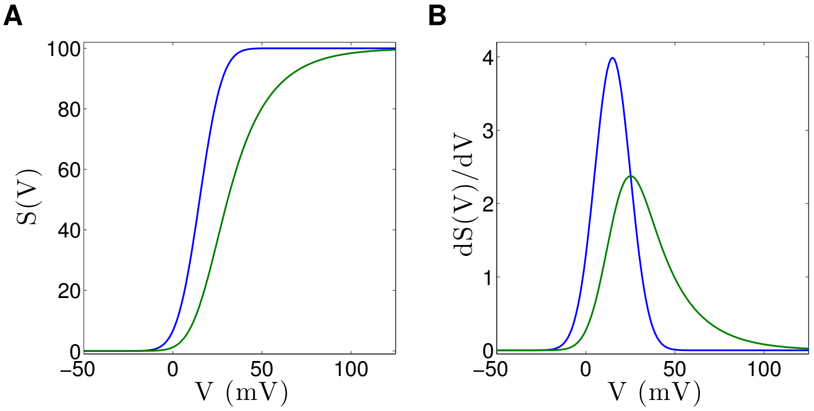

Fig. 2.5. The novel population firing rate $S(V)$ taken from Eq. (2.36) and the corresponding nonlinear gain $dS(V)/dV$ in comparison to the well-known sigmoid function $Sig(V, 0)$. Panel (A) illustrates the mean firing rate functions and panel (B) presents the corresponding nonlinear gains for the standard population firing rate (blue lines) and the novel transfer function (green lines). Parameters are $S^{max} = 100$ Hz, $\theta = 15$ mV, $\sigma = 10$ mV, $\rho = 0.05$ mV^{-1}.

where $\langle\phi_N\rangle$ indicates its mean value and $\xi(t)$ is a zero average Gaussian uncorrelated noise and κ is the noise intensity.

In the following, we aim to derive a formula for modeling the experimentally observed EEG power spectrum. It is important to point out that the theoretical power spectrum characterizes small fluctuations about the resting state of the system. Thus, we first need to determine the system resting state. The resting state of Eqs. (2.31) defined by $dV_a(t)/dt = 0$ obey

$$\begin{aligned}
V_E^* &= \nu_{ee}S(V_E^*) + \nu_{ei}S(V_I^*) + \nu_{es}S(V_S^*),\\
V_I^* &= \nu_{ie}S(V_E^*) + \nu_{ii}S(V_I^*) + \nu_{is}S(V_S^*),\\
V_S^* &= \nu_{se}S(V_E^*) + \nu_{sr}S(V_R^*) + \langle\phi_N\rangle,\\
V_R^* &= \nu_{re}S(V_E^*) + \nu_{rs}S(V_S^*),
\end{aligned} \tag{2.39}$$

where V_a^* denotes the resting state value of V_a for $a = E, I, S, R$. Moreover Eq. (2.33) gives $\phi_E^* = S(V_E^*)$. Applying a temporal operator $\hat{L} = \dfrac{\partial^2}{\alpha\beta\partial t^2} + (\dfrac{1}{\alpha} + \dfrac{1}{\beta})\dfrac{\partial}{\partial t} + 1$ on the left-hand side of Eqs. (2.31), the system equations convert to a set of coupled stochastic DDEs

$$\hat{L}V_a(t) = \sum_{b=E,I,R,S} \nu_{ab}\phi_b(t - \tau_{ab}). \tag{2.40}$$

Subsequently, we linearize Eqs. (2.40) about the resting state $\boldsymbol{X}_0 = (V_E^*, V_I^*, V_S^*, V_R^*)^\top$ and write them in a general matrix form of a linear DDE as

$$\hat{\boldsymbol{L}}(\partial/\partial t)\boldsymbol{Y}(t) = \boldsymbol{A}\boldsymbol{Y}(t) + \boldsymbol{B}\boldsymbol{Y}(t-\tau) + \boldsymbol{\xi}(t), \tag{2.41}$$

where

$$\boldsymbol{Y}(t) = \begin{pmatrix} \phi_E(t) - \phi_E^* \\ V_I(t) - V_I^* \\ V_S(t) - V_S^* \\ V_R(t) - V_R^* \end{pmatrix}, \quad \hat{\boldsymbol{L}} = \begin{pmatrix} \tilde{L}\frac{\tilde{D}}{K_{11}} & 0 & 0 & 0 \\ 0 & \tilde{L} & 0 & 0 \\ 0 & 0 & \tilde{L} & 0 \\ 0 & 0 & 0 & \tilde{L} \end{pmatrix},$$

$$\boldsymbol{A} = \begin{pmatrix} K_1 & K_2 & 0 & 0 \\ K_4 & K_5 & 0 & 0 \\ 0 & 0 & 0 & K_8 \\ 0 & 0 & K_{10} & 0 \end{pmatrix}, \quad \boldsymbol{B} = \begin{pmatrix} 0 & 0 & K_3 & 0 \\ 0 & 0 & K_6 & 0 \\ K_7 & 0 & 0 & 0 \\ K_9 & 0 & 0 & 0 \end{pmatrix}, \quad \boldsymbol{\xi}(t) = \begin{pmatrix} 0 \\ 0 \\ \sqrt{2\kappa}\xi(t) \\ 0 \end{pmatrix}, \tag{2.42}$$

with $\tilde{L} = (1 + i\omega/\alpha)(1 + i\omega/\beta)$, $\tilde{D} = (1 + i\omega/\gamma)^2$, and

$$\begin{aligned} K_1 = \nu_{ee}\ , K_2 = \nu_{ei}\frac{\partial S_I[V]}{\partial V}\ |_{V=V_I^*}\ ,\ K_3 = \nu_{es}\frac{\partial S_S[V]}{\partial V}\ |_{V=V_S^*}, \\ K_4 = \nu_{ie}\ ,\ K_5 = \nu_{ii}\frac{\partial S_I[V]}{\partial V}\ |_{V=V_I^*}\ ,\ K_6 = \nu_{is}\frac{\partial S_S[V]}{\partial V}\ |_{V=V_S^*}, \\ K_7 = \nu_{se}\ ,\ K_8 = \nu_{sr}\frac{\partial S_R[V]}{\partial V}\ |_{V=V_R^*}\ ,\ K_9 = \nu_{re}, \\ K_{10} = \nu_{rs}\frac{\partial S_S[V]}{\partial V}\ |_{V=V_S^*}\ ,\ K_{11} = \frac{\partial S[V]}{\partial V}\ |_{V=V_E^*}\ . \end{aligned}$$

As mentioned in the previous section, according to Wiener-Khinchine theorem, the power spectral density matrix $\boldsymbol{P}(\omega)$ of $\boldsymbol{Y}(t)$ is the Fourier transform of the auto-correlation function matrix $\langle \boldsymbol{Y}(t)^t \boldsymbol{Y}(t-T)\rangle$ leading to

$$\boldsymbol{P}(\omega) = 2\kappa\sqrt{2\pi}\tilde{\boldsymbol{G}}(\omega)\tilde{\boldsymbol{G}}^\top(-\omega), \tag{2.43}$$

where $\tilde{\boldsymbol{G}}(\omega)$ is the Fourier transform of the matrix Green's function and the high index $\top$ denotes the transposed matrix [111].

Following [22, 29, 30], it is assumed that the activity of excitatory cortical neurons generates the EEG, and by virtue of the specific choice of external input to thalamo-cortical relay neurons, the power spectrum of the EEG is related to the Green's function of linear deviations about the resting state by [111]

$$P_E(\omega) = 2\kappa\sqrt{2\pi}\left|\tilde{G}_{1,3}(\omega)\right|^2, \tag{2.44}$$

where

$$\begin{aligned} \tilde{\boldsymbol{G}}(\omega) &= \frac{1}{\sqrt{2\pi}}[\hat{\boldsymbol{L}} - \boldsymbol{A} - \boldsymbol{B}e^{-i\omega\tau}]^{-1} \\ &= \frac{1}{\sqrt{2\pi}}\begin{bmatrix} \tilde{L}\frac{\tilde{D}}{K_{11}} - K_1 & -K_2 & -K_3e^{-i\omega\tau} & 0 \\ -K_4 & \tilde{L} - K_5 & -K_6 & 0 \\ -K_7e^{-i\omega\tau} & 0 & \tilde{L} & -K_8 \\ -K_9e^{-i\omega\tau} & 0 & -K_{10} & \tilde{L} \end{bmatrix}^{-1}. \end{aligned} \tag{2.45}$$

It is important to note that the power spectrum analysis is valid only if the system resting states are stable and hence the fluctuations do not diverge. We have taken care of this additional condition and all given parameters guarantee the existence and stability of the resting states.

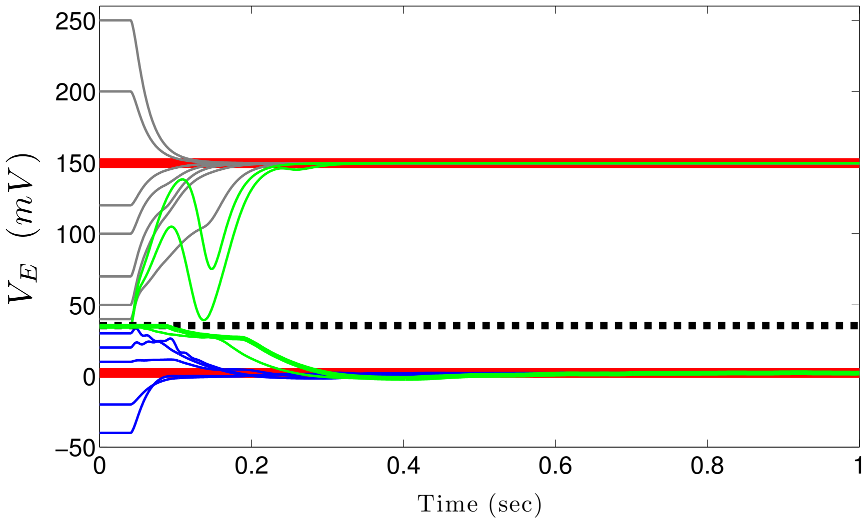

Fig. 2.6. Time evolution of membrane potential of cortical pyramidal neurons V_E governed by Eq. (2.31) simulated with the parameter set displayed in Table 2.1. The numerical simulations are started with different initial values for the system variables. The solid red lines indicate the stable resting states whereas the dashed black line shows the unstable solution. The gray and blues trajectories converge to the larger and smaller stable resting state, respectively, since they are initialized in the basin of attraction of the respective solution. The green trajectories started on the unstable resting state head toward one of the stable solutions.

To investigate the stability of the system resting states, we neglect the external input, since in a first approximation, the stability of a linear system does not depend on the external input [111]. For nominal model parameters listed in Table 2.1, three resting states given by $X_{01} = [2.95, 2.95, 1.84, 4.61]$, $X_{02} = [35.80, 35.80, 25.34, 99.30]$, $X_{03} = [149.57, 149.57, 100.99, 149.92]$ have been obtained, where $X_{01} < X_{02} < X_{03}$. Then, by inserting the ansatz $\boldsymbol{Y}(t) = \boldsymbol{C}e^{\lambda t}$ into Eq. (2.41) we arrive at the following characteristic equation

$$det\left(\lambda\boldsymbol{I} - \boldsymbol{A} - \boldsymbol{B}e^{-\lambda\tau}\right) = 0, \tag{2.46}$$

where the roots of this equation determine the stability of system resting states. Our analysis reveals that X_{01} and X_{03} are linearly stable, whereas X_{02} is unstable. The number and stability of the resting states can be confirmed by iterative numerical scheme with different initial guess values. For instance, the membrane potential's time series of cortical pyramidal neurons V_E with different initial values for the system state variables are displayed in Fig. 2.6. It can be observed that there exists three resting states in which the smaller and larger solutions are stable whereas the middle one is unstable. This result demonstrates that the above values calculated by *fsolve* function in MATLAB are correct.

Now we can compute the model power spectrum by linearizing the system equations around the stable resting states. The theoretical power spectra governed by Eq. (2.44) are displayed in Fig.2.7. The information about contribution of each frequency band to the EEG signals is often presented as a power spectrum with frequency on the x axis and power estimated by amplitude squared on the y axis. From panel **A**, we observed that the spectral power obtained by linearizing the equations about the smaller resting state, i.e., X_{01} reproduces the important human EEG features such as the alpha and beta peaks at frequencies $f \approx 1/(2\tau)$, $2/(2\tau)$, respectively, and

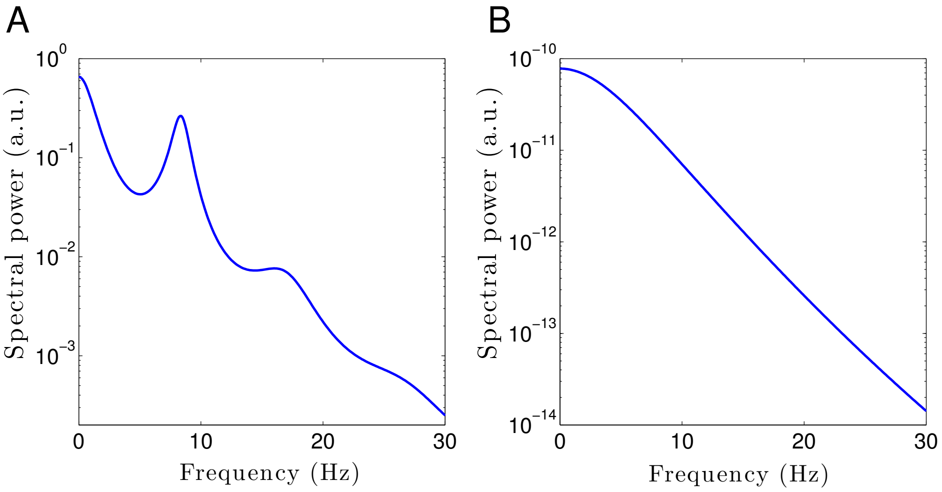

Fig. 2.7. Power spectra of ϕ_E computed from linearization about different resting states (c.f. Eq. (2.44)). (**A**) The spectral power density obtained by linearizing system equations around the smaller resting state reproduces specific human EEG features. (**B**) No peak can be observed when the spectrum is computed by linearization about the larger resting state.

the asymptotic low- and high-frequency behaviors [200]. However, no peak can be seen in the spectrum resulting from the linearization around the larger solution X_{03} (c.f. panel **B**).

2.3.4 A thalamo-cortical model to reproduce the EEG rhythms

In this section we consider a thalamo-cortical neuronal population model based on the work of Hutt & Longtin [28], which extends previous cortical models [173, 174, 23] by distinguishing the excitatory and inhibitory synapses. The model consists of a network of four populations of neurons: cortical pyramidal neurons (E), cortical inhibitory neurons (I), thalamo-cortical relay neurons (S) and thalamic reticular nucleus (R), as shown schematically in Fig. 2.8. Note that in this model the connection from population S to I is neglected for simplicity reasons. In addition, the long-range propagation of the signals has been considered by the connection between cortex and thalamus associated with a constant time delay and the model closely follows [229, 91] showing that long connections between cortico-cortical populations through white matter are not necessary to describe experimental EEG dynamics.

The underlying model considers an ensemble of neurons on a mesoscopic scale which includes two types of neurons, namely excitatory and inhibitory cells [28]. The connection elements between neurons are excitatory and inhibitory chemical synapses in which both types of synapses may occur on dendritic branches of both cell types. The present model considers AMPA/NMDA and GABA$_\mathrm{A}$ synaptic receptors and assumes spatially extended populations of both neuron types.

In the following the key concepts of the model are described and we derive a formula for the EEG power spectrum. Let us consider spatially extended populations of excitatory and inhibitory neurons on the order of a few hundred micrometers. Assume that the neural population of type a receives the incoming firing rates $P_e(x,t)$ and $P_i(x,t)$ at spatial location x and time t, which

Table 2.1. Model parameters, their symbols, and nominal values in Robinson model [23].

Parameter	Symbol	Nominal value
Maximum firing-rate of all populations	S^{max}	250 Hz
Mean firing threshold of all populations	θ	15 mV
Firing rate variance of all populations	σ	10 mV
Type-I population effect constant of all populations	ρ	0.08 mV^{-1}
Synaptic rise rate	α	200 s^{-1}
Synaptic decay rate	β	50 s^{-1}
Synaptic strength from E to E neurons	ν_{ee}	1.2 mVs
Synaptic strength from E to I neurons	ν_{ie}	1.2 mVs
Synaptic strength from E to S neurons	ν_{se}	1.2 mVs
Synaptic strength from E to R neurons	ν_{re}	0.4 mVs
Synaptic strength from I to I neurons	ν_{ii}	-1.8 mVs
Synaptic strength from I to E neurons	ν_{ei}	-1.8 mVs
Synaptic strength from S to E neurons	ν_{es}	1.2 mVs
Synaptic strength from S to I neurons	ν_{is}	1.2 mVs
Synaptic strength from S to R neurons	v_{rs}	0.2 mVs
Synaptic strength from R to S neurons	ν_{sr}	-0.8 mVs
Mean value of external input	$\langle\phi_N\rangle$	1 mV
Intensity of external noise	κ	0.1 mV
Cortical damping rate	γ	150 s^{-1}
Transmission delay between cortex and thalamus	τ	40 ms

are originated from excitatory and inhibitory cells (or terminate at excitatory and inhibitory synapses), respectively. Then, presynaptic population firing rates arrived at excitatory (e) or inhibitory (i) synapses convert to the mean excitatory and inhibitory postsynaptic potentials $V_a^e(t)$ and $V_a^i(t)$, respectively, by the convolution

$$V^{e,i}(x,t) = \int_{-\infty}^{t} h_{e,i}(t-t')P_{e,i}(x,t')dt', \tag{2.47}$$

where the functions $h_e(t)$ and $h_i(t)$ indicate the synaptic response function of excitatory and inhibitory synapses, respectively,

$$h_e(t) = a_e\frac{\alpha_e\beta_e}{\beta_e-\alpha_e}\left(e^{-\alpha_e t}-e^{-\beta_e t}\right), \quad h_i(t) = a_i\frac{\alpha_i\beta_i}{\beta_i-\alpha_i}\left(e^{-\alpha_i t}-e^{-\beta_i t}\right), \tag{2.48}$$

where $1/\alpha_e$ and $1/\alpha_i$ are the characteristic rise times of the response function for excitatory and inhibitory synapses, respectively, and $1/\beta_e$ and $1/\beta_i$ are the corresponding characteristic decay times. In general, the dynamics of the synapses can be different to each other, but here for simplicity reasons, it is assumed that all excitatory synapses on excitatory and inhibitory neurons are identical, which however is possible to be distinguished easily by increasing the number of model equations (same holds for inhibitory synapses). Moreover, the parameters a_e and a_i stand for the average synaptic gains i.e., the level of excitation and inhibition, respectively. Note that the mean excitatory and inhibitory charge transfers through the synaptic cleft denoted by $\rho_{e,i}$ are equal to the time integral $\rho_{e,i} = \int_0^\infty h_{e,i}(t)dt$, where $\rho_e = a_e$ and $\rho_i = a_i$.

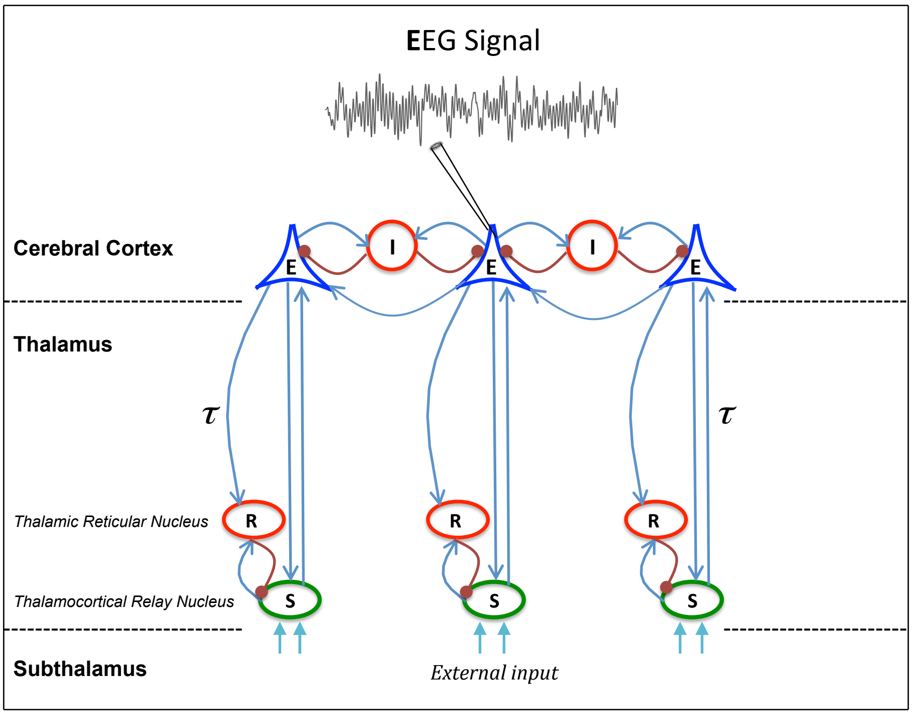

Fig. 2.8. Schematic of the thalamo-cortical model. The blue arrows indicate excitatory connections and the red connections with filled circle ends represent inhibitory connections. The model consists of four types of neural populations, namely, cortical excitatory and inhibitory neurons, thalamo-cortical relay, and thalamic reticular neurons denoted by E, I, S, and R, respectively. Furthermore, the connections between cortex and thalamus are associated with the same nonzero time delay τ.

Following [29, 23, 263], the integral equations (2.47) may be formulated as differential equations

$$\hat{L}_e V^e(x,t) = a_e P_e(x,t), \quad \hat{L}_i V^i(x,t) = a_i P_i(x,t), \tag{2.49}$$

with

$$\begin{aligned} \hat{L}_e(\partial/\partial t) &= \frac{1}{\alpha_e \beta_e} \frac{\partial^2}{\partial t^2} + \left(\frac{1}{\alpha_e} + \frac{1}{\beta_e} \right) \frac{\partial}{\partial t} + 1, \\ \hat{L}_i(\partial/\partial t) &= \frac{1}{\alpha_i \beta_i} \frac{\partial^2}{\partial t^2} + \left(\frac{1}{\alpha_i} + \frac{1}{\beta_i} \right) \frac{\partial}{\partial t} + 1. \end{aligned} \tag{2.50}$$

In more general mathematical terms, $h_{e,i}(t)$ are the Green's functions for the temporal operators $\hat{L}_{e,i}$ with $\hat{L}_{e,i} h_{e,i}(t) = \delta(t)$, where $\delta(t)$ represents the Dirac delta-function.

Moreover, in each neural population, the mean population firing rates $P_{e,i}$ which depend on the effective mean potential can be approximated by a sigmoidal function. We identify the mean population firing rates with the transfer function $S(V)$ defined by Eq. (2.36). In the following, the mean firing rate function in the cortex $S_C[\cdot]$ is considered to be different with the thalamic firing rate function $S_T[\cdot]$, while for the simplicity reasons, it is identical in the cortex and for relay and the reticular populations.

External input to the system originates from other neural populations and is considered as a non-specific input to relay neurons:

$$I(x,t) = I_0 + \xi(x,t), \tag{2.51}$$

where I_0 indicates its mean value and $\xi(x,t)$ is a Gaussian white noise with

$$\langle \xi(x,t) \rangle = 0, \quad \langle \xi(x,t)\xi(x',t') \rangle = 2\kappa\delta(t-t')\delta(x-x'), \tag{2.52}$$

where $\langle . \rangle$ denotes the ensemble average and κ is the intensity of the driving noise.

First, let us formulate the equations describing the excitatory and inhibitory postsynaptic potentials (PSPs) of both excitatory and inhibitory cell types. The mean potentials V_a^c, evoked at excitatory ($c = e$) and inhibitory ($c = i$) synapses, for $a \in \{E, I, R, S\}$ in the cortical pyramidal neurons (E), cortical inhibitory neurons (I), the thalamo-cortical relay neurons (S) and thalamic reticular neurons (R) obey

$$\begin{aligned}
\hat{L}_e V_E^e(x,t) &= K_{EE}(x) * S_C\left[V_E^e(x,t) - V_E^i(x,t)\right] + \\
&\quad K_{ES}(x) * S_T\left[V_S^e(x,t-\tau) - V_S^i(x,t-\tau)\right], \\
\hat{L}_i V_E^i(x,t) &= K_{EI}(x) * S_C\left[V_I^e(x,t) - V_I^i(x,t)\right], \\
\hat{L}_e V_I^e(x,t) &= K_{IE}(x) * S_C\left[V_E^e(x,t) - V_E^i(x,t)\right], \\
\hat{L}_i V_I^i(x,t) &= K_{II}(x) * S_C\left[V_I^e(x,t) - V_I^i(x,t)\right], \\
\hat{L}_e V_S^e(x,t) &= K_{SE}(x) * S_C\left[V_E^e(x,t-\tau) - V_E^i(x,t-\tau)\right] + I(x,t), \\
\hat{L}_i V_S^i(x,t) &= K_{SR}(x) * S_T\left[V_R^e(x,t)\right], \\
\hat{L}_e V_R^e(x,t) &= K_{RE}(x) * S_C\left[V_E^e(x,t-\tau) - V_E^i(x,t-\tau)\right] + \\
&\quad K_{RS}(x) * S_T\left[V_S^e(x,t) - V_S^i(x,t)\right],
\end{aligned} \tag{2.53}$$

where the parameter τ denotes the transmission time delay between cortex and thalamus, and $K_{ab}(x) * S[V(x,t)] = \int_\Omega K_{ab}(x-y)S[V(y,t)]dy$. The spatial kernel functions $K_{ab}(x-y)$ reflect the synaptic connection strengths in population a originating from population b in the spatial domain Ω. According to previous studies, we assume that the EEG can be described in a good approximation by spatially constant neural population activity [29, 23], we choose $K_{ab}(x-y) = K_{ab}\delta(x-y)$ with the Dirac function $\delta(\cdot)$ and thereby $K_{ab}(x) * S[V(x,t)] = K_{ab}S[V(x,t)]$.

It should be noted that parameter V_a^c in the above equations indicates the *effective* potential, i.e., the deviation of the measured potential with respect to the rest potential. Furthermore, as mentioned in the previous section, the power spectrum is modeled by small fluctuations about the resting state of the system. Thus, it is necessary to first compute the system resting state. In the case of constant external input $I(t) = I_0$, the spatially-homogeneous resting state of Eqs. (2.53) can be obtained by setting to zero all time derivatives, i.e., $dV_a^{e,i}/dt = 0$, for $a \in \{E, I, S, R\}$ leading to

$$\begin{aligned}
&V_E^{*e} = K_{EE}S_C\left[V_E^{*e} - V_E^{*i}\right] + K_{ES}S_T[V_S^{*e} - V_S^{*i}], \\
&V_E^{*i} = f_C(p)K_{EI}S_C\left[V_I^{*e} - V_I^{*i}\right], \\
&V_I^{*e} = K_{IE}S_C\left[V_E^{*e} - V_E^{*i}\right], \\
&V_I^{*i} = K_{II}S_C\left[V_I^{*e} - V_I^{*i}\right], \\
&V_S^{*e} = K_{SE}S_C\left[V_E^{*e} - V_E^{*i}\right] + I_0, \\
&V_S^{*i} = f_T(p)K_{SR}S_T\left[V_R^{*e}\right], \\
&V_R^{*e} = K_{RE}S_C\left[V_E^{*e} - V_E^{*i}\right] + K_{RS}S_T\left[V_S^{*e} - V_S^{*i}\right].
\end{aligned} \tag{2.54}$$

By linearizing Eqs. (2.53) about the resting state $\boldsymbol{X}_0 = (V_E^{*e}, V_E^{*i}, V_I^{*e}, V_I^{*i}, V_S^{*e}, V_S^{*i}, V_R^{*e})^\top$ obtained from Eqs. (2.54), we can write them in a general matrix form of a linear DDE as follows

$$\hat{\boldsymbol{L}}(\partial/\partial t)\boldsymbol{Y}(t) = \boldsymbol{A}\boldsymbol{Y}(t) + \boldsymbol{B}\boldsymbol{Y}(t-\tau) + \boldsymbol{\xi}(t), \tag{2.55}$$

where $\boldsymbol{Y}(t) \in \mathbb{R}^N$ denotes the small deviations from the system resting states, and the diagonal matrix operator $\hat{\boldsymbol{L}}(\partial/\partial t) \in \mathbb{R}^{N\times N}$ includes all temporal operators $\hat{L}_{e,i}$. Moreover, $\boldsymbol{\xi}(t) \in \mathbb{R}^N$ denotes the input Gaussian white noise to the system and $\boldsymbol{A}$, $\boldsymbol{B} \in \mathbb{R}^{N\times N}$ are constant matrices where N is the system dimension (here N=7). The solution of Eqs. (2.55) for $t \to \infty$ is

$$\boldsymbol{Y}(t) = \int_{-\infty}^{\infty} \boldsymbol{G}(t-t')\boldsymbol{\xi}(t')dt', \tag{2.56}$$

with the matrix Green's function $\boldsymbol{G} \in \mathbb{R}^{N\times N}$. Substituting Eq. (2.56) into Eq. (2.55) leads to

$$\hat{\boldsymbol{L}}(\partial/\partial t)\boldsymbol{G}(t) = \boldsymbol{A}\boldsymbol{G}(t) + \boldsymbol{B}\boldsymbol{G}(t-\tau) + \boldsymbol{1}\delta(t), \tag{2.57}$$

with the unitary matrix $\boldsymbol{1} \in \mathbb{R}^{N\times N}$. Then the Fourier transform of the matrix Green's function

$$\tilde{\boldsymbol{G}}(\nu) = \frac{1}{\sqrt{2\pi}}\left[\boldsymbol{L}(\nu) - \boldsymbol{A} - \boldsymbol{B}e^{-2\pi i\nu\tau}\right]^{-1}, \tag{2.58}$$

and as mentioned previously, the Wiener-Khinchine theorem defines the power spectral density matrix to

$$\boldsymbol{P}(\nu) = 2\kappa\sqrt{2\pi}\tilde{\boldsymbol{G}}(\nu)\tilde{\boldsymbol{G}}^\top(-\nu),$$

where the high index $\top$ denotes the transposed vector or matrix. Essentially, we assume that the EEG is generated by the activity of pyramidal cortical cells. By virtue of the specific choice of external input to relay neurons, the power spectrum of the EEG just depends on one matrix component of the Green's function by

$$P_E(\nu) = 2\kappa\sqrt{2\pi}\left|\tilde{G}_{1,5}(\nu)\right|^2. \tag{2.59}$$

In detail, we find

$$\begin{aligned}\boldsymbol{Y}(t) = (&V_E^e(t) - V_E^{*e}, V_E^i(t) - V_E^{*i}, V_I^e(t) - V_I^{*e}, V_I^i(t) - V_I^{*i},\\ &V_S^e(t) - V_S^{*e}, V_S^i(t) - V_S^{*i}, V_R^e(t) - V_R^{*e})^\top,\end{aligned}$$

$\boldsymbol{\xi}(t) = (0, 0, 0, 0, \sqrt{2\kappa}\xi(t), 0, 0)^\top$, and the diagonal matrix $\hat{\boldsymbol{L}}(\partial/\partial t)$ with the entries $\hat{L}_{1,1} = \hat{L}_{3,3} = \hat{L}_{5,5} = \hat{L}_{7,7} = \hat{L}_e(\nu)$, and $\hat{L}_{2,2} = \hat{L}_{4,4} = \hat{L}_{6,6} = \hat{L}_i(\nu)$, and

$$\boldsymbol{A} = \begin{pmatrix} K_1 & -K_1 & 0 & 0 & 0 & 0 & 0 \\ 0 & 0 & K_3 & -K_3 & 0 & 0 & 0 \\ K_4 & -K_4 & 0 & 0 & 0 & 0 & 0 \\ 0 & 0 & K_5 & -K_5 & 0 & 0 & 0 \\ 0 & 0 & 0 & 0 & 0 & 0 & 0 \\ 0 & 0 & K_5 & -K_5 & 0 & 0 & K_7 \\ 0 & 0 & 0 & 0 & K_9 & -K_9 & 0 \end{pmatrix}, \boldsymbol{B} = \begin{pmatrix} 0 & 0 & 0 & 0 & K_2 & -K_2 & 0 \\ 0 & 0 & 0 & 0 & 0 & 0 & 0 \\ 0 & 0 & 0 & 0 & 0 & 0 & 0 \\ 0 & 0 & 0 & 0 & 0 & 0 & 0 \\ K_6 & -K_6 & 0 & 0 & 0 & 0 & 0 \\ 0 & 0 & 0 & 0 & 0 & 0 & 0 \\ K_8 & -K_8 & 0 & 0 & 0 & 0 & 0 \end{pmatrix},$$

with

$$
\begin{aligned}
\hat{L}_e(\nu) &= \left(1+\frac{2\pi i\nu}{\alpha_e}\right)\left(1+\frac{2\pi i\nu}{\beta_e}\right), & \hat{L}_i(\nu) &= \left(1+\frac{2\pi i\nu}{\alpha_i}\right)\left(1+\frac{2\pi i\nu}{\beta_i}\right),\\
K_1 &= K_{EE}\frac{dS_C[V]}{dV}\,|_{V=(V_E^{*e}-V_E^{*i})}, & K_2 &= K_{ES}\frac{dS_T[V]}{dV}\,|_{V=(V_S^{*e}-V_S^{*i})},\\
K_3 &= K_{EI}\frac{dS_C[V]}{dV}\,|_{V=(V_I^{*e}-V_I^{*i})}, & K_4 &= K_{IE}\frac{dS_C[V]}{dV}\,|_{V=(V_E^{*e}-V_E^{*i})},\\
K_5 &= K_{II}\frac{dS_C[V]}{dV}\,|_{V=(V_I^{*e}-V_I^{*i})}, & K_6 &= K_{SE}\frac{dS_C[V]}{dV}\,|_{V=(V_E^{*e}-V_E^{*i})},\\
K_7 &= K_{SR}\frac{dS_T[V]}{dV}\,|_{V=V_R^{*e}}, & K_8 &= K_{RE}\frac{dS_C[V]}{dV}\,|_{V=(V_E^{*e}-V_E^{*i})},\\
K_9 &= K_{RS}\frac{dS_T[V]}{dV}\,|_{V=(V_S^{*e}-V_S^{*i})},
\end{aligned}
$$

$$
\tilde{\boldsymbol{G}}(\nu) = \frac{1}{\sqrt{2\pi}}\begin{bmatrix}
\hat{L}_e(\nu)-K_1 & K_1 & 0 & 0 & -K_2e^{-2\pi i\nu\tau} & K_2e^{-2\pi i\nu\tau} & 0\\
0 & \hat{L}_i(\nu) & -K_3 & K_3 & 0 & 0 & 0\\
-K_4 & K_4 & \hat{L}_e(\nu) & 0 & 0 & 0 & 0\\
0 & 0 & -K_5 & \hat{L}_i(\nu)+K_5 & 0 & 0 & 0\\
-K_6e^{-2\pi i\nu\tau} & K_6e^{-2\pi i\nu\tau} & 0 & 0 & \hat{L}_e(\nu) & 0 & 0\\
0 & 0 & 0 & 0 & 0 & \hat{L}_i(\nu) & -K_7\\
-K_8e^{-2\pi i\nu\tau} & K_8e^{-2\pi i\nu\tau} & 0 & 0 & -K_9 & K_9 & \hat{L}_e(\nu)
\end{bmatrix}^{-1}. \quad (2.60)
$$

Note that the constants $K_i,\ i=1,\ldots,9$ are proportional to the nonlinear gain $dS(V)/dV$ computed at the system stationary state.

It is important to point out that in the notation that has been presented in this section, the strengths of connections denoted by K_{ab} are positive constants, in contrast to Robinson model which the connections originated from inhibitory populations (ν_{ii}, ν_{ei}, ν_{sr}) should have negative values. Moreover, the model does not consider explicitly the spatially extended dendritic branches, however, one can easily consider a damped wave equation for the axonal propagation in the cortex. Considering an identical synaptic response function for excitatory and inhibitory synapses i.e., $\alpha_e=\alpha_i$, $\beta_e=\beta_i$, accompanied by $K_{ii}=-\nu_{ii}$, $K_{ei}=-\nu_{ei}$, $K_{sr}=-\nu_{sr}$, the system equations given by Eqs. (2.53) simplify to the equations in Robinson model.

In the subsequent chapters, we employ the presented neural population models to reproduce the specific features of EEG rhythms observed in general anesthesia. It is shown how the modeling approach shed some more light on the neural mechanisms underlying the EEG recordings during behavioral state changes such as the transition from awake condition to anesthetic-induced sedation.

2.4 Conclusion

The thalamo-cortical circuits play an important role in generating the EEG patterns during different states of brain functioning. Moreover, since most of the brain imaging data such as EEG signals reflect the overall activity of a large population of neurons, mean-field models provide a physiologically more accurate description of such macroscopic scale observables. Therefore, a population-level model of thalamo-cortical system is a plausible candidate for investigating the mechanisms responsible for the various features observed in EEG data during different brain functional states.

3

Modeling the anesthetic action on synaptic and extra-synaptic receptors

Contents

Abstract

The role of extra-synaptic receptors in the regulation of excitation and inhibition in the brain has attracted increasing attention. Because activity in the extra-synaptic receptors plays a role in regulating the level of excitation and inhibition in the brain, they may be important in determining the level of consciousness. In the present chapter, we first review briefly the literature on extra-synaptic GABA and NMDA receptors and their affinity to anesthetic drugs. Then the effects of anesthetic propofol on synaptic and extra-synaptic receptors located in cortical and thalamic neural populations are modelized. In this chapter, we show how the effect of the anesthetic drug propofol on GABAergic extra-synaptic receptors results in changes in neural population activity and the EEG signals. Our results indicate that increased tonic inhibition in cortical inhibitory neurons cause a dramatic increase in the power of both $\delta-$ and $\alpha-$ bands. Conversely, the effects of increased tonic inhibition in cortical excitatory neurons and thalamic

relay neurons have the opposite effect and decrease the power in these bands. The increased $\delta-$activity is in accord with observed data for deepening propofol anesthesia; but is absolutely dependent on the inclusion of extra-synaptic (tonic) GABA action in the model.

3.1 Function of extra-synaptic receptors

In recent years, a large amount of experimental literature has revealed characteristic spectral signal changes in electroencephalographic data (EEG) and Local Field Potentials (LFPs) during general anesthesia [18, 82, 179, 86, 264]. Besides the experimental studies, several theoretical neural models have been proposed to explain certain EEG signal features observed during anesthesia [81, 114, 113, 116, 38, 215, 265, 25, 266, 31, 260]. Although these studies may incorporate realistic neurobiological details of the brains' network topology and neuronal function, they have simplified dramatically the anesthetic action by considering only synaptic excitatory and inhibitory receptors. Most of the previous studies describing the EEG spectral power during general anesthesia have considered the effects of anesthetics only on the synaptic receptors in purely cortical or thalamo-cortical neural populations. However, there is a growing amount of experimental research that has revealed the importance of extra-synaptic receptors (ESR) for neural interactions in general [267, 268], and for anesthesia especially, see Refs. [261, 269, 13] and the references therein. To elucidate the role of ESR in the context of anesthesia, one approach might be to do a theoretical study of a realistic neural population model which reproduces the characteristic signal features observed in EEG. To perform such a theoretical study, it is necessary to incorporate physiological properties of ESRs into neural population models. The present chapter aims to point out the role of anesthetic effects on ESRs in explaining experimental EEG power spectra.

As mentioned in chapter 1, GABA receptors are a large and important class of ionotropic receptors. These receptors are located in the neuron's membrane and respond to the neurotransmitter GABA by opening Cl^- channels and inducing an inward hyperpolarising membrane current. This response may either be: phasic at synaptic receptors or, tonic at ESR which lie distant from synaptic terminals [270, 271, 272, 273, 269, 274]. The phasic response evolves on a time scale of $10 - 200$ ms whereas tonic response evolves on a much longer time scale [275, 276].

The precise biochemical origin of tonic inhibition is still heavily debated [277, 278]. A rather simple and intuitive model explains the tonic current as a spillover of excess neurotransmitters from synapses. This is due to incomplete GABA uptake by nearby synaptic GABA_A-receptors. The remaining neurotransmitter is thus able to diffuse to more distant GABA_A-receptors via extracellular space [277, 273, 279, 280]. This spillover may explain the longer time scale of tonic responses found experimentally. In addition, this explanation implies that even small concentrations of neurotransmitters are sufficient to generate tonic activity because of the high sensitivity of ESRs.

The effect of extra-synaptic receptors on the dendritic activity has not attracted much attention. This may because there are only a relatively small number of such receptors as compared to synaptic receptors [281, 277]. Moreover, only recently have experimental studies been able to classify and localize different sub-types of GABA_A receptors [273, 277]. GABA_A receptors are pentameric ligand-gated ion channels and it has been found that $\delta-$sub units of GABA_A receptors occur exclusively at ESRs [269, 277, 282, 283, 284]. This indicates a specific role of these receptors for the neural information processing in general with specific implications in diseases [267] and consciousness [281].

Tonic inhibition induced by extra-synaptic GABA_A-receptors represents a persistent increase in the cell membrane's conductance. On the single neuron level, this diminishes the membrane time constant and, consequently, reduces the size and duration of excitatory post-synaptic potentials propagating on the dendrite. Hence tonic inhibition reduces the excitability of the membrane and increases the effective firing threshold [277]. At the neural population level, extra-synaptic receptors affect the excitability of interneuron-pyramidal cell networks and thus modify network oscillations [272]. Kopanitsa [281] argues that the sustained spatially widespread tonic inhibition is energetically more effective for the system to diminish neural population activity than short-lasting local phasic inhibition, since lower neurotransmitter concentrations are sufficient. The critical factor in this mechanism is the the relatively high sensitivity of ESRs to modulations by anesthetic agents [277, 74, 270, 285]. The brain areas that have been shown to be affected by anesthetic-induced tonic inhibition are the hippocampus [286], brain stem [287], cerebellum [285], and the thalamus [269]. Since these areas are supposed to play a role in general anesthesia [13], ESRs may mediate clinical anesthetic effects, such as hypnosis and amnesia [288]. Thus it is reasonable to argue that GABA$_A$ ESRs set the background inhibition of neural populations and the brain network and mediate slow consciousness phenomena, such as loss of consciousness, sleep or arousal [281].

Converse to GABAergic receptors, NMDA receptors respond to the neurotransmitter glutamate by excitatory inward Na^+ and Ca^{2+} currents and K^+ outward currents. The response of NMDA receptors to glutamate depends on their spatial location with respect to synaptic terminals and the presence of co-agonists. A recent experimental study has revealed that the population of NMDA receptors, which are close to synaptic terminals, are primarily activated by the co-agonist d-serine in the presence of glutamate; while extra-synaptic NMDA receptors (more distant from the synaptic terminals) respond primarily to glutamate and the co-agonist glycine [289, 290]. D-serine and glycine are endogenous amino acids found naturally in the brain (d-serine is a derivative of glycine). Similar to GABAergic ESRs, it has been shown that there exists a significant ambient glutamate concentration which induces a tonic excitatory current [291, 292]. This current is evoked primarily at extra-synaptic NMDA receptors [293] and may be regulated by other cells, such as neighboring astrocytes [292, 294], which control glutamate uptake and also synthesize d-serine [295].

Commonly-used GABAergic anesthetic drugs directly modify the corresponding receptors. However various anesthetics are also known to affect the endogenous co-agonists of NMDA receptors [296, 289, 297]. Hence, the possible anesthetic effect on NMDA receptors is more complex and indirect than for GABAergic ESRs. There is a large class of NMDA receptor antagonists, that inhibit the excitatory action of NMDA receptors. These anesthetics induce so-called dissociative anesthesia [298] leading to amnesia and analgesia without depressing respiration, but also characterized by distorted perceptions of sight and sound and feelings of dissociation from the environment. An example of a dissociative anesthetic drug is the inhalational anesthetic xenon which - amongst other actions - binds primarily to the extra-synaptic glycine site of NMDA receptors [299] and attenuates long term potentiation present in the hippocampus by reducing extra-synaptic receptor currents [300].

To understand how the anesthetic effect of extra-synaptic receptor activity on the microscopic single neuron scale could lead to changes in EEG and behavior that can be observed at macroscopic scales, it is necessary to establish a bridge between the two scales. This bridge may be formulated as a dynamical theoretical model. As mentioned in the previous chapter, neural population models represent a good candidate for a dynamic description of neural activity at an intermediate mesoscopic scale [27, 301, 22]. For more details see section 2.3 of chapter 2. An increasing number of theoretical studies have used neural population models to describe signal features in LFPs and EEG observed during anesthesia [25, 116]. Most of these studies take into account anesthetic action on excitatory and/or inhibitory synapses [81, 31, 210, 28, 35] while few consider extra-synaptic receptors [302]. This link between the synaptic receptor properties in an ensemble of neurons and the average population dynamics is straight-forward, since classical neural population models already involve the average synaptic response function. The situation is different for extra-synaptic receptors, since their action is not incorporated into the classical models. A very recent work has filled this gap [260]. This theoretical work demonstrated a method to include mathematically extra-synaptic GABA$_A$ receptor action in neural population models; which enables researchers to study how changing anesthetic extra-synaptic receptor action modifies spectral features in the EEG, which might then be observed experimentally.

In the following section we first modelize the effects of anesthetic propofol on synaptic and extra-synaptic receptors located in cortical and thalamic neural populations. Subsequently we use the Robinson neural population model (c.f. section 2.3.3 of chapter 2) involving anesthetic synaptic inhibition; and then extend this model by including the effects of extra-synaptic GABAergic receptor action in the presence of the anesthetic drug propofol. With the help of this model, we demonstrate the role of extra-synaptic GABAergic inhibition, and the importance of tonic inhibition in the cortical inhibitory neuronal population, in explaining the frontal EEG power spectra recorded during propofol induced sedation.

3.2 Effect of propofol on cortical and thalamic neural populations

According to experimental results, it is now widely accepted that anesthetic agents act by binding directly to specific protein targets [3]. While it has been reported that many receptors and molecular targets contribute to general anesthesia, there is a general agreement that GABA$_\mathrm{A}$ receptors are important in mediating the inhibition during propofol administration [16]. It has been shown that propofol increases the decay time constant of GABA$_\mathrm{A}$ synapses, and hence increases the total charge transfer in these synapses [9]. Interestingly, Kitamura *et al.* [47] have shown experimentally that propofol has a negligible effect on the amplitude of synaptic response functions in cortical neurons, whereas it markedly increases amplitude, decay time, and thus charge transfer of GABA$_\mathrm{A}$ receptors of inhibitory synapses located in relay neurons in the thalamic ventrobasal complex [48]. Since GABA$_\mathrm{A}$ receptors mediate most of the inhibitory synaptic transmission, the present model assumes that the inhibitory synaptic transmission within cortex and thalamus are mediated by GABA$_\mathrm{A}$ receptors and GABA$_\mathrm{B}$ receptors are neglected.

In order to mimic the latter experimental findings, we assume that increasing propofol concentration decreases the decay rate of the inhibitory synaptic response function β_i by $\beta_i = \beta_i^0/p$ with $p \geq 1$ [38], where β_i^0 denotes the inhibitory decay rate in the absence of propofol. The factor p reflects the on-site concentration of propofol in the neural populations and $p = 1$ indicates the baseline condition. Increasing p leads to a decrease in the decay rate constant of inhibitory synapses and thereby an increase in the charge transfer in these synapses.

Consider the following synaptic response function for inhibitory synapses

$$h_i(t) = a_i f_j(p) \frac{\alpha_i \beta_i}{\alpha_i - \beta_i} \left(e^{-\beta_i t} - e^{-\alpha_i t} \right), \tag{3.1}$$

where $1/\alpha_i$ and $1/\beta_i$ are the characteristic rise and decay times of the inhibitory response function, respectively. The function $f_j(p)$ reflects the action of propofol on the GABAergic synaptic receptors and is proportional to the charge transfer in these receptors. From Fig. 2.4, afferents from thalamic (T) reticular neurons and cortical (C) inhibitory neurons terminate at GABAergic synaptic receptors, i.e., $j \in \{C, T\}$. In the following, the function f_j will be estimated from experimental data. Note that for simplicity reasons, here it is assumed that the decay rate of inhibitory synapses is identical in all neural populations under study. However, it is possible to be distinguished easily by increasing the number of model parameters. Based on the experimental findings, cortical inhibitory synapses retain their response amplitude while changing the anesthetics concentration [47, 28] leading to the relative increase of the charge transfer

$$f_C(p) = a_i \Gamma(\alpha_i, \beta_i^0)/\Gamma(\alpha_i, \beta_i), \tag{3.2}$$

with

$$\Gamma(\alpha, \beta) = \frac{\alpha\beta}{\alpha - \beta} \left[(\alpha/\beta)^{\frac{-\beta}{\alpha-\beta}} - (\alpha/\beta)^{\frac{-\alpha}{\alpha-\beta}} \right] ,$$

i.e., $\Gamma(\alpha_i, \beta_i) = h_i(t_0)$ is the peak amplitude of $h_i(t)$ at time $t_0 = \ln(\alpha_i/\beta_i)/(\alpha_i - \beta_i)$. This choice fixes the maximum of cortical response function to $h_C^{max} = a_i \Gamma(\alpha_i, \beta_i^0)$, which is independent of the action of propofol [35]. Conversely propofol increases the amplitude of evoked inhibitory post-synaptic currents in the ventrobasal relay neurons [79]. To take this effect into account the relative increase of the charge transfer in thalamic $\mathrm{GABA_A}$ receptors is

$$f_T(p) \approx a_i A_r(p) \Gamma(\alpha_i, \beta_i^0)/\Gamma(\alpha_i, \beta_i), \tag{3.3}$$

with the relative amplitude $A_r(p)$. This choice determines the maximum of thalamic response function to $h_T^{max} = a_i \Gamma(\alpha_i, \beta_i^0) A_r(p)$, i.e., the maximum response increases with $A_r(p)$ under the condition $A_r(1) = 1$. This choice is motivated by previous studies of cortical GABAergic synapses [35]. An optimal fit of A_r to experimental data yields $A_r(p) \approx 1.55 \ln(1.49 + 0.42 \exp(p)) \approx p^{0.42}$, cf. Fig. 3.1. The response functions $h_i(t)$ for cortical and thalamic receptors subject to the anesthetic concentration factor p are displayed in Fig. 3.2 illustrating the increasing response amplitude for thalamic receptors compared to the cortical receptors.

We point out that, by definition, the charge transfer in the respective receptors is proportional to $f_C(p)$ and $f_T(p)$. Since the charge transfer reflects the level of inhibition, the relation of thalamic to cortical inhibition

$$f_T/f_C \approx p^{0.42} > 1,$$

is an increasing function of p, i.e. the larger the anesthetic concentration the stronger is the anesthetic-induced thalamic inhibition compared to cortical inhibition.

Finally, we mention that the propofol concentrations in Fig. 3.1 are equivalent to the interval $[0; 0.53\mu\text{g/ml}]$ for a propofol molar mass of 178g. This concentration is the on-site concentration determined in the *in-vitro* experiment of Ying & Goldstein [79]. This concentration is not necessarily similar to the blood-plasma propofol concentrations in the experiments (c.f. Fig. 3.3) due to pharmaco-dynamic effects, e.g. caused by the blood-brain barrier. The uncertain relationship between on-site concentrations and blood plasma concentrations represents an uncertainty in the current model.

The GABAergic ESR tonic inhibition can be represented in the model as a constant shift of the firing threshold in neural population models [260]. For simplicity, we assume a linear relationship between the anesthetic concentration parameter p and the extra-synaptic threshold shift

$$\theta_a = \theta_0 + (p-1)k_a \tag{3.4}$$

with the mean firing threshold θ_0 (with unit mV) in the absence of propofol and the extra-synaptic anesthetic sensitivity $k_a > 0$. Here, $(p-1)k_a$ is the tonic inhibition induced by extra-synaptic

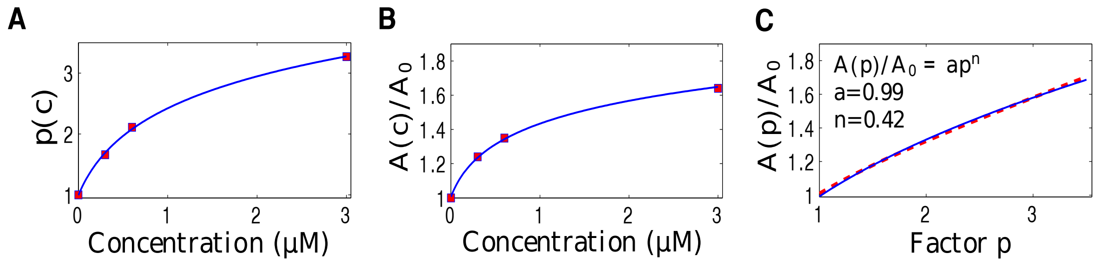

Fig. 3.1. Effect of propofol on thalamic GABA$_A$-receptors extracted from a previous experimental study [79, Fig. 5]. (**A**) The factor $p = \beta_i^0/\beta_i$ of evoked IPSCs in a relay neuron (taken from the experimentally measured normalized decay time) subject to the propofol on-site concentration c (red square) and the corresponding fitted function (blue line) $p(c) = k_1 \ln(k_2 + k_3 c)$. (**B**) The experimentally measured normalized amplitude $A(c)/A_0$ of evoked IPSCs subject to the propofol on-site concentration c (red square) and the corresponding fitted function (blue line) $A(c)/A_0 = k_4 \ln(k_5 + k_6 c)$. Here $A_0 = A(c = 0)$. (**C**) Since the constants $k_1, \ldots, k_6$ are fitted, $A_r(p) = A(p)/A_0 = k_4 \ln(k_7 + k_8 \exp(p/k_1))$ (red line) with $k_7 = k_5 - (k_2 k_6/k_3)$, and $k_8 = k_6/k_3$. An additional fit reveals $A(p)/A_0 \approx p^{0.42}$ (blue line).

action which depends linearly on the propofol concentration. Future experimental studies may motivate a more realistic relationship of threshold shift and the anesthetic concentration parameter. Summarizing, synaptic and extra-synaptic inhibition, and hence anesthetic action, is present in the cortical populations E and I and in the thalamic population of relay neurons S.

3.3 EEG acquisition and the experimental observations

We re-analysed previously-obtained experimental data from subjects that had been given a short propofol anesthetic. The details of the methods can be found in [303]. After obtaining regional ethical committee approval and written informed consent, five healthy subjects (mean age 27.7 yrs, four males) were included in the study. They were on no psychoactive drugs and had been starved for at least 6 hours prior to the study, and were monitored and managed as per the Australia and New Zealand College of Anaesthetists best practice guidelines. The induction consisted of an intravenous infusion of propofol at 1500 mg/hr until the subject no longer responded to verbal command (usually after about 5 minutes). At this point the propofol infusion was stopped and the subject allowed to recover spontaneously (typically after about 5 minutes). The estimated effect-site concentrations of propofol were calculated using standard population-based pharmacokinetic models.

The EEG was acquired using the Electrical Geodesics 128 channel Ag/AgCl electrode system (Eugene, CO, USA) referenced to Cz. Electrode impedances were below 30 KOhm (100 MOhm input impedance amplifier). The sampling frequency was 250 Hz, with a $0.1 - 100$ Hz analogue band pass filter, and A-D conversion was at 12 bits precision. The EEG data were re-referenced to a grand mean, and band-pass filtered using 3-rd order Butterworth filters $0.2 - 45$ Hz to eliminate line-noise. An additional Whittaker filter was applied to reduce movement and blink artifacts. The power in each frequency was obtained applying a short-time Fourier transform

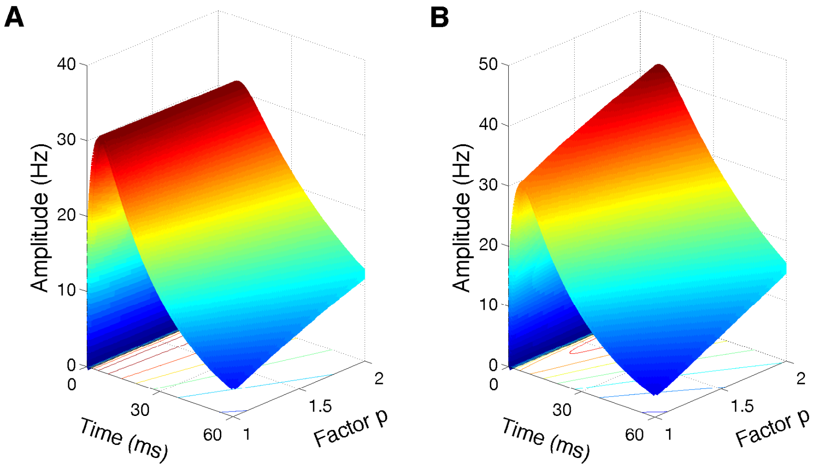

Fig. 3.2. The temporal synaptic response function of inhibitory GABA$_\text{A}$ synapses subject to the factor p. The factor p reflects the anesthetic propofol concentration. (**A**) The decay phase of the cortical response function $h_i(t)$ is prolonged at larger values of p, whereas the maximum height of $h_i(t)$ with (3.2) is constant. (**B**) The amplitude of $h_i(t)$ in thalamic receptors with (3.3), i.e. $A_r(p) \approx p^{0.42}$, increases as a function of p. Parameters are $\alpha_i = 400$ Hz and $\beta_i = 40$ Hz.

with a moving window of 60 sec and 54 sec overlap. The power spectra have been computed 1 min before infusion start ($t = 1$ min) and 5 min after infusion ($t = 5$ min). For visualization reasons, these power spectra at different time instances have been smoothed by a running average over frequencies with a 1 Hz window and a 0.017 Hz frequency step. Note that the experimental data presented in this chapter was recorded over frontal head regions.

Figure 3.3 illustrates how the EEG power spectrum depends on the concentration of propofol for a single subject. After starting the infusion at $t = 0$ min, the estimated propofol effect-site concentration increases gradually with time (Fig. 3.3**A**); resulting in increased power in the $\delta-$ and $\alpha-$frequency ranges (Fig. 3.3**B**). Over the period of the spectrogram the subject has become progressively more sedated; until a $t = 5$ min the subject no longer responds to verbal command but would still be responsive to nociceptive stimuli. Figure 3.3**C** shows the power spectra in the awake and sedation conditions. We observe a power enhancement primarily in the $\delta-$ and $\alpha-$frequency ranges.

3.4 Theoretical power spectrum

Consider the Robinson model as illustrated in section 2.3.3 of chapter 2. The mean membrane soma potentials V_a for $a = E, I, S, R$ are given by

$$V_a(t) = \sum_{b=E,I,R,S} h(t) \otimes \nu_{ab}\phi_b(t - \tau_{ab}), \tag{3.5}$$

where E, I, S, and R denote the cortical pyramidal and inhibitory populations, relay and reticular neurons, respectively, and $h(t)$ indicates the mean synaptic response function defined by

$$h(t) = \frac{\alpha\beta}{\alpha - \beta}\left(e^{-\beta t} - e^{-\alpha t}\right), \tag{3.6}$$

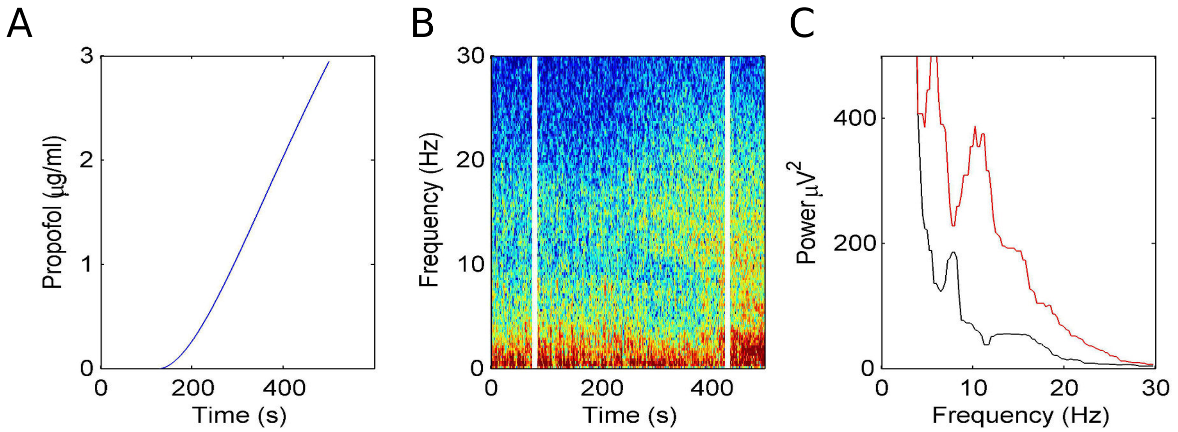

Fig. 3.3. Electroencephalographic data observed under anesthesia sedation in a single subject while increasing the propofol concentration. (**A**) Blood plasma concentration of propofol with respect to administration time. (**B**) Spectrogram of frontal EEG power. The vertical lines denote time windows well before the administration (left line) and at about 5min after the start of propofol infusion (right side); (**C**) Power spectra computed before the infusion of propofol (black) and 5 min after the start of infusion (red).

where α and β are the synaptic rise and decay rates of the synaptic response functions, respectively (in the absence of anesthetics). Considering the propofol effects mentioned earlier i.e., the decrease of decay rate of inhibitory synaptic response function by $\beta \rightarrow \beta/p$, the increase of charge transfer in cortical inhibitory transmissions $I \rightarrow E$ and $I \rightarrow I$ by $f_C(p)$, and the increase of charge transfer in thalamic inhibitory transmission $R \rightarrow S$ by $f_T(p)$, the system equations are given by

$$\begin{aligned}
&\hat{L}V_E(t) = \nu_{ee}\phi_E(t) + f_C(p)\nu_{ei}S(V_I(t)) + \nu_{es}S(V_S(t-\tau)),\\
&\hat{L}V_I(t) = \nu_{ie}\phi_E(t) + f_C(p)\nu_{ii}S(V_I(t)) + \nu_{is}S(V_S(t-\tau)),\\
&\hat{L}V_S(t) = \nu_{se}\phi_E(t-\tau) + f_T(p)\nu_{sr}S(V_R(t)) + \phi_N,\\
&\hat{L}V_R(t) = \nu_{re}\phi_E(t-\tau) + \nu_{rs}S(V_S(t)),\\
&D\phi_E(t) = S(V_E(t)),
\end{aligned} \tag{3.7}$$

where $\hat{L} = (1+\frac{1}{\alpha}\frac{\partial}{\partial t})(1+\frac{1}{\beta}\frac{\partial}{\partial t})$, and $D = (1+\frac{1}{\gamma}\frac{\partial}{\partial t})^2$. In addition, $\phi_N = \langle\phi_N\rangle + \sqrt{2\kappa}\xi(t)$ denotes the external input to the relay neurons. Here, the transfer functions $S(V_a)$ are identical in all neural populations and obey

$$S(V_a) = Sig(V_a, 0) - Sig(V_a, \rho), \tag{3.8}$$

with

$$Sig(V_a, \rho) = \frac{S_a^{max}}{2}\left(1 + \text{erf}\left(\frac{V_a - \theta_a - \rho\sigma_a^2}{\sqrt{2}\sigma_a}\right)\right) e^{-\rho(V_a-\theta_a)+\rho^2\sigma_a^2/2}, \tag{3.9}$$

The effect of propofol on extra-synaptic receptors is modeled by a linear shift in neural firing thresholds θ_a (c.f. Eq. (3.4)). Using the approach presented in the previous chapter, the EEG power spectrum is defined by

$$P_E(\omega) = 2\kappa\sqrt{2\pi}\left|\tilde{G}_{1,3}(\omega, p)\right|^2, \tag{3.10}$$

where

$$\tilde{\boldsymbol{G}}(\omega, p) \;=\; \frac{1}{\sqrt{2\pi}} \begin{bmatrix} \tilde{L}\frac{\tilde{D}}{K_{11}} - K_1 & -f_C(p)K_2 & -K_3 e^{-i\omega\tau} & 0 \\ -K_4 & \tilde{L} - f_C(p)K_5 & -K_6 & 0 \\ -K_7 e^{-i\omega\tau} & 0 & \tilde{L} & -f_C(p)K_8 \\ -K_9 e^{-i\omega\tau} & 0 & -K_{10} & \tilde{L} \end{bmatrix}^{-1} . \tag{3.11}$$

See section 2.3.3 of chapter 2 for definition of $\tilde{\boldsymbol{G}}$ elements.

We point out that the system resting states obtained from setting the time derivatives to zero in Eq. (3.7) depend on the anesthetic factor p, and the constants K_i for i=1,2,...,10 are evaluated at the resting state depending on p itself. Therefore, changing the factor p, changes the resting states, the corresponding nonlinear gains and consequently the system power spectrum.

3.5 Reproducing the experimental observations

In this section, we show that the model under study is able to reproduce the specific changes observed in frontal EEG data during the propofol-induced sedation. First we reproduce the results of Hindriks & van Putten [35], which suggest that the stronger synaptic inhibition within local cortical inhibitory neurons compare to other neuronal populations suffices to reproduce the experimental observations in frontal EEG oscillations during propofol anesthesia. Subsequently, we reproduce similar results by considering the propofol effects on extra-synaptic GABAergic receptors, while there are an identical synaptic inhibition in different neural populations.

3.5.1 The role of synaptic inhibition

Hindriks & van Putten [35] have considered different affinity of propofol for different neuron types, while it has been assumed that for inhibitory synaptic transmissions within the cortex and thalamus, propofol only decreases the decay rate of the GABA$_A$ receptors and does not influence their efficacy leading to

$$\begin{aligned} &\hat{L}V_E(t) = \nu_{ee}\phi_E(t) + f_C(p_1)\nu_{ei}S(V_I(t)) + \nu_{es}S(V_S(t-\tau)), \\ &\hat{L}V_I(t) = \nu_{ie}\phi_E(t) + f_C(p_2)\nu_{ii}S(V_I(t)) + \nu_{is}S(V_S(t-\tau)), \\ &\hat{L}V_S(t) = \nu_{se}\phi_E(t-\tau) + f_C(p_3)\nu_{sr}S(V_R(t)) + \phi_N, \\ &\hat{L}V_R(t) = \nu_{re}\phi_E(t-\tau) + \nu_{rs}S(V_S(t)), \\ &D\phi_E(t) = S(V_E(t)), \end{aligned} \tag{3.12}$$

where anesthetic factors p_1, p_2 and p_3 denote the propofol synaptic effect on cortical excitatory (E), cortical inhibitory (I), and thalamo-cortical relay neurons (S), respectively. It is important to point out that in the work of Hindriks & van Putten [35], the thalamic and cortical synaptic inhibition has been modeled by a same function $f_C(p)$ with different input factors p_1, p_2, and p_3. In addition, extra-synaptic inhibition was not modeled in their work.

Figure 3.4 shows the theoretical power spectrum P_E given by Eq. (3.10) in the baseline condition ($p = 1$) and after the administration of propofol $p > 1$ for two different relations of the anesthetic factors p_1, p_2 and p_3. At first we note that the spectra resemble well the spectrum obtained from experimental observations: increasing p_2 in a specific relation to the p_1 and p_3 yields increases in delta and theta power as well as more pronounced alpha oscillation with increased peak-frequency [304]. The dynamical analysis of the model [35] reveals three resonances in the baseline condition, including an oscillatory resonance corresponding to the peak in the

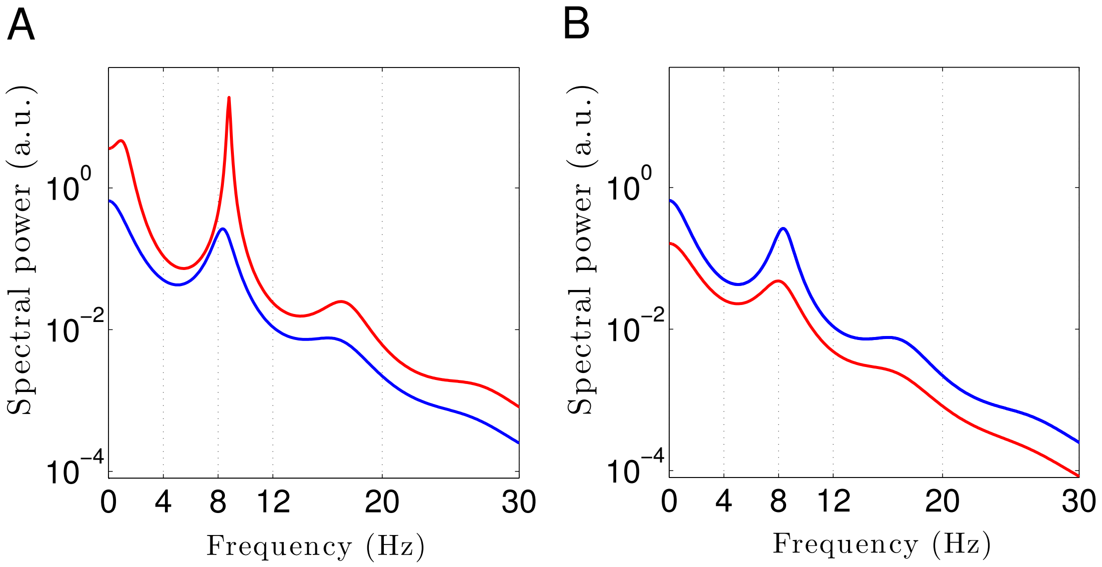

Fig. 3.4. Theoretical power spectrum of EEG in the baseline condition ($p_1 = p_2 = p_3 = 1$ encoded in blue lines) and in the anesthesia condition (red lines). (**A**) In anesthesia condition: $p_1 = p_3 = 1 + 0.3(p_2 - 1)$, and $p_2 = 1.125$ (**B**) In anesthesia condition: $p_1 = p_2 = p_3 = 1.125$.

alpha-band and a pair of zero-frequency resonances. Increasing the anesthetic concentration diminishes the damping rate of alpha resonances (and thus increases its magnitude) while its frequency increases. Hence increases in alpha power and its peak-frequency results from the approach of the system of an oscillatory instability [111]. Moreover, the two zero-frequency resonances collide and gradually increases in frequency leading to a magnitude increases in delta and theta power. For more details see [35].

Figure 3.5 illustrates how increasing the anesthetic concentration i.e., increasing the three factors p_1, p_2, and p_3 changes the stationary states and the corresponding gain function, dependent on the relation of these three factors. We observe that the nonlinear cortical gain denoted by $dS(V)/dV\ |_{V=V_E^*}$ may increase or decrease with increasing propofol dependent on the synapses that are modified, as shown in panels **B** and **D**, respectively. If the inhibition in cortical inhibitory neurons is stronger than other populations i.e., $p_2 > p_1$ and $p_2 > p_3$, then the nonlinear gain increases (Fig. 3.5**B**) reflecting an increased excitability and the power values increase as well (c.f. Fig. 3.4, red curve in panel **A**). In contrast, if the response of all three synapse types respond identically (as assumed in previous studies), then the nonlinear gain decreases (Fig. 3.5**D**) and the decreased excitability diminishes the power spectrum values (c.f. Fig. 3.4, red curve in panel **B**).

Moreover, the stationary states behave differently in the two cases, cf. Fig. 3.5**C** and **D**. Increasing (decreasing) the nonlinear gain is accompanied by an increasing (decreasing) value of the corresponding stationary state. It is also remarkable that in panel **C** the two lower stationary states collide to a single state whereas in panel **D** the two upper states collide. This difference indicates two fundamentally different mechanisms which may yield the different dynamics observed

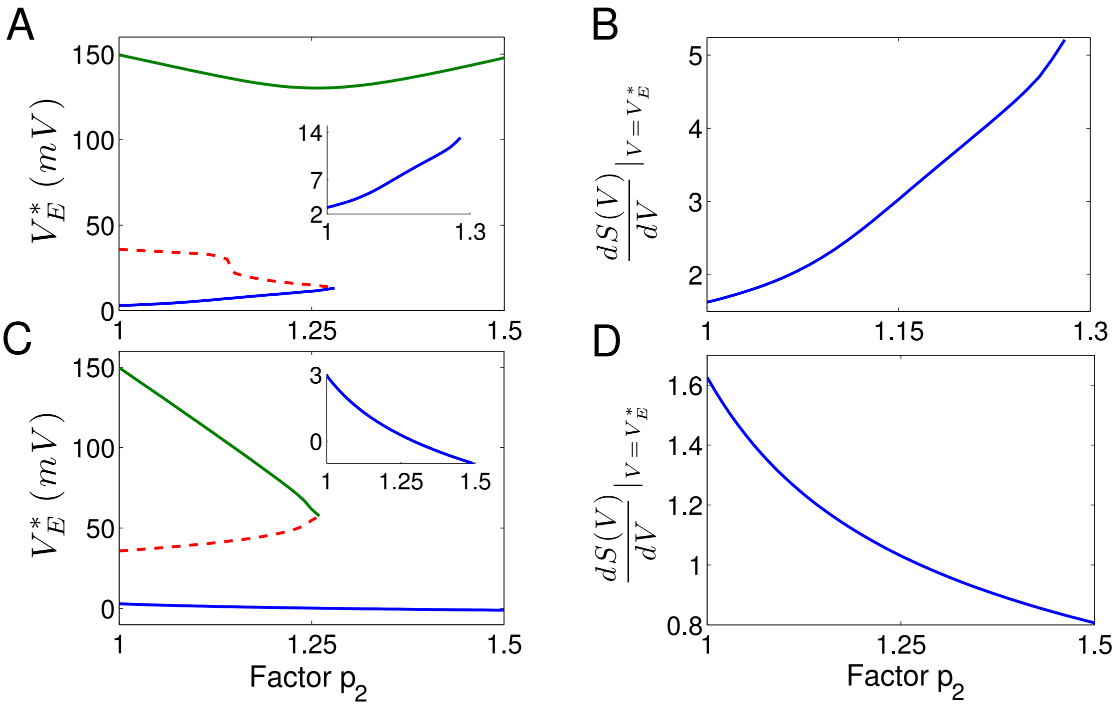

Fig. 3.5. The stationary states and the nonlinear gain dS/dV computed at the lowest stationary state of pyramidal neurons V_E^* subjected to the factor p_2. In panels (**A**) and (**B**) p_1=p_3= 1+0.3(p_2-1), whereas in panels (**C**) and (**D**) p_1=p_2= p_3. We observe three states in (**A**) and (**C**) for $p = 1$, where in panel (**A**) the two lower states collide and in panel (**C**) the two upper states collide. The center branches (dashed red lines) are linearly unstable, whereas the other branches are linearly stable. For illustration reasons, the lower branches are shown again in the insets.

in the power spectrum [259].

3.5.2 The role of extra-synaptic inhibition

In the following, to understand how propofol effects on ESRs might enhance $\delta-$ and $\alpha-$power, we examine the impact of adding tonic inhibition via extra-synaptic GABA$_A$ receptors [36]. This part of the work examines the effect of tonic inhibition (Eq. (3.4)) in various populations E, I, S on the power spectrum of neural activity in cortical excitatory neurons, i.e., population E.

Figure 3.6**A** shows the interaction between propofol and tonic inhibition in the cortical inhibitory neuronal population. If we set the tonic inhibition to zero (k_I = 0mV), we observe a decrease in spectral power as propofol concentrations increase (i.e., the power moves from the black line to the blue line in the figure). If we set the tonic inhibition to $(p-1) \cdot 15$ mV, we see the opposite effect - there is an increase of $\delta-$ and $\alpha-$power (black line to red line), with increasing propofol concentration.

Previous studies have indicated that extra-synaptic inhibition in thalamic relay neurons may control the level of inhibition in the brain [267]. However, Fig. 3.6**B** reveals that adding a non-zero tonic inhibition in the thalamic relay neurons causes a decrease in the spectral power, similar to the previous case of absent tonic inhibition in the inhibitory cortical neurons.

It is well-known that GABAergic anesthetics change the EEG from high frequency-low amplitude signals to low frequency-high amplitude signals [84, 87]. Figure 3.6**C** and **D** show simulated time series in the absence and presence of tonic inhibition in cortical inhibitory cells reproducing this experimental finding.

Our results elucidates that tonic inhibition in cortical interneurons and thalamic relay neurons affect the cortical power spectrum differently. This finding is similar to results of a previous computational neural population study of a cortico-thalamic feedback single-neuron model [302]. Figure 3.7 shows how the resting membrane potential (Fig. 3.7**A**) and the nonlinear gain (Fig. 3.7**B**) in the cortical excitatory population change with differing extra-synaptic anesthetic sensitivity in cortical inhibitory neurons (k_I) and in the thalamic relay neurons (k_S). We observe that both the resting potential and the nonlinear gain of cortical excitatory neurons increase when the cortical inhibitory extra-synaptic anesthetic sensitivity k_I increases, whereas resting potential and nonlinear gain of cortical excitatory neurons decrease when the extra-synaptic anesthetic sensitivity in thalamic relay neuron k_S increases. Since the nonlinear gain is proportional to the systems responsiveness to external stimuli, the power enhancement in population I may be explained by the augmented responsiveness of the cortical excitatory neurons. This responsiveness depends on the sub-circuit in which the neurons are involved. Since relay neurons are part of the thalamo-cortical feedback loop, while cortical inhibitory neurons contribute to the cortical loop, the cell types respond differently to the thalamic input. Essentially assuming tonic inhibition in the population of cortical excitatory neurons E, the study reveals a similar propofol concentration dependence of the power spectrum, the resting state potential and the nonlinear gain as for the thalamic tonic inhibition S. This shows the unique tonic inhibition effect in the cortical inhibitory neurons.

3.6 Induction of delta activity in EEG rhythms

In this section we aim to investigate how the spectral power peak in $\delta-$ frequency range changes with the level of tonic inhibition. The spectral power peaks exhibit a maximum of power, expressed mathematically as a local maximum of the function $P_E(f)$ where P_E denotes the EEG power spectrum (c.f. Eq. (3.10)). The local maximum at frequency f_0 is defined as $dP_E/df = 0$, $d^2P_E/df^2 < 0$ computed at f_0. If there is a local maximum of power in the $\delta-$ frequency range, then $\delta-$activity is present, whereas a missing local maximum in the $\delta-$frequency range indicates missing $\delta-$activity. Since the magnitude and frequency of power peaks change with the propofol concentration and extra-synaptic threshold, the concentration factor p and the extra-synaptic anesthetic sensitivity k_a are the parameters of the power spectrum, i.e. $P_E = P_E(p, k_a, f)$.

To illustrate the usefulness of this parametrization, let us assume a factor k_{a0} for which no $\delta-$power peak exists in the power spectrum $P_E(p, k_{a0}, f)$, and $k_{a1},\ k_{a1} > k_{a0}$ is the extra-synaptic anesthetic sensitivity leading to a spectral $\delta-$power peak in $P_E(p, k_{a1}, f)$, with $dP_E(p, k_{a1}, f_{max})$ $/df_{max} = 0$, where f_{max} is a frequency in the $\delta-$frequency range. Mathematically, then the continuity of all model functions and variables guarantee that there is a threshold for the emergence of $\delta-$activity at a certain extra-synaptic anesthetic sensitivity $k_{a,thr}$ with $k_{a0} \leq k_{a,thr} \leq k_{a1}$. Consequently, if a threshold extra-synaptic anesthetic sensitivity for $\delta-$activity exists, then the variation of model variables about this critical point guarantees the emergence of $\delta-$activity. This mathematical reasoning allows us to investigate conditions under which $\delta-$activity may emerge.

Figure 3.6 shows the power spectrum for single values of the extra-synaptic sensitivity k_I, for single values of the concentration factor p and fixed strength of self cortical inhibition ν_{ii}, while Fig. 3.7 gives more details on the role of extra-synaptic sensitivity for fixed values of

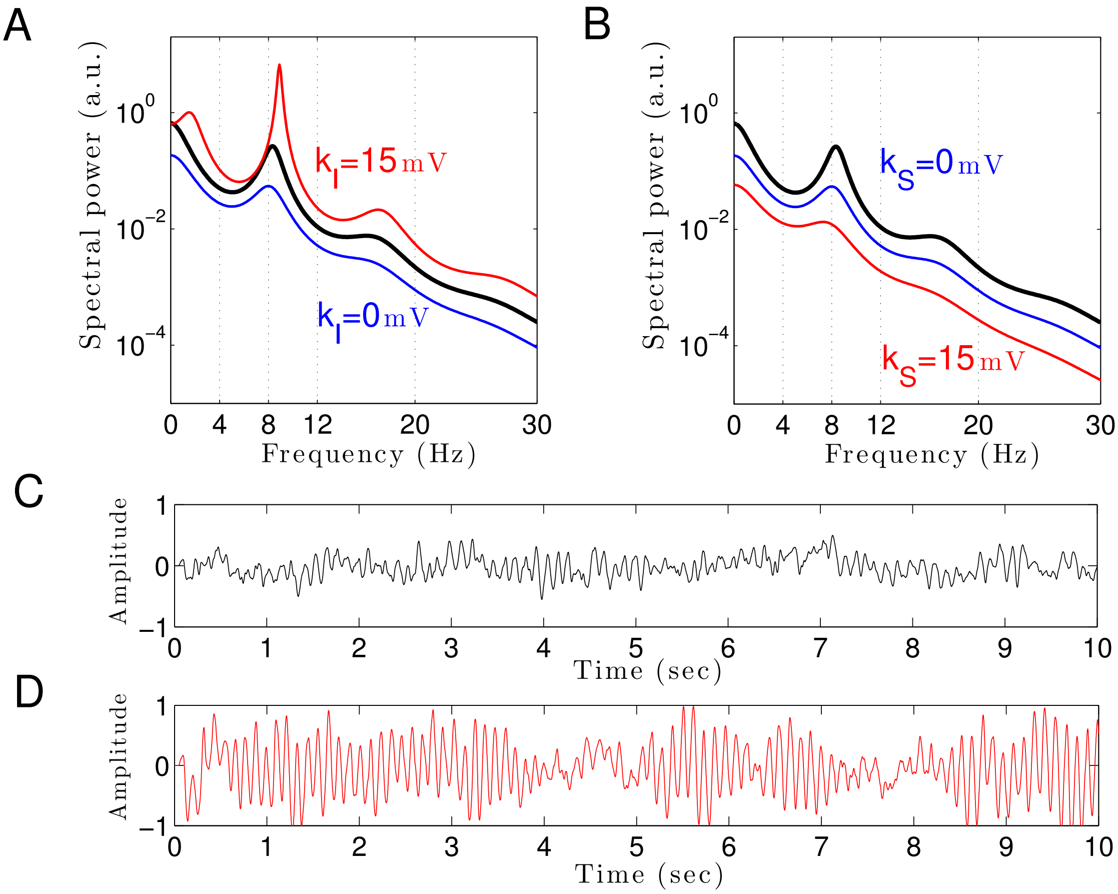

Fig. 3.6. The theoretical EEG power spectrum in the baseline and in the sedation condition with and without tonic inhibition in the cortical inhibitory neurons I in (**A**) and the thalamic relay neurons S in (**B**) and corresponding simulated EEG time-series. In (**A**) the administration of propofol without tonic inhibition (blue line) attenuates the power spectrum compared to the baseline condition (black line) while the tonic inhibition (red line) increases the global power and generates oscillatory activity in the $\delta-$frequency range. In (**B**) increasing the anesthetic concentration yields a global power decrease in the sedation condition without tonic inhibition (blue line) and a further power decrease in the presence of tonic inhibition (red line). In (**A**) and (**B**), the black lines indicate the EEG-spectral power in the baseline condition ($p = 1$), and the blue and red lines show the power spectrum in anesthesia condition ($p = 1.125$) in the absence ($k_a = 0$) and in the presence ($k_a = 15$ mV) of tonic inhibition, respectively. (**C**) The simulated EEG time-series in the absence of extra-synaptic effects, i.e. $k_E = k_I = k_S = 0$ mV. (**D**) The EEG time-series in the presence of extra-synaptic action in cortical inhibitory neurons with $k_I = 15$ mV, $k_E = k_S = 0$ mV. The tonic inhibition changes the EEGs from low-amplitude, high-frequency pattern to high-amplitude, low-frequency pattern. In addition, the strength of self cortical inhibition is $\nu_{ii} = -1.8$ mVs.

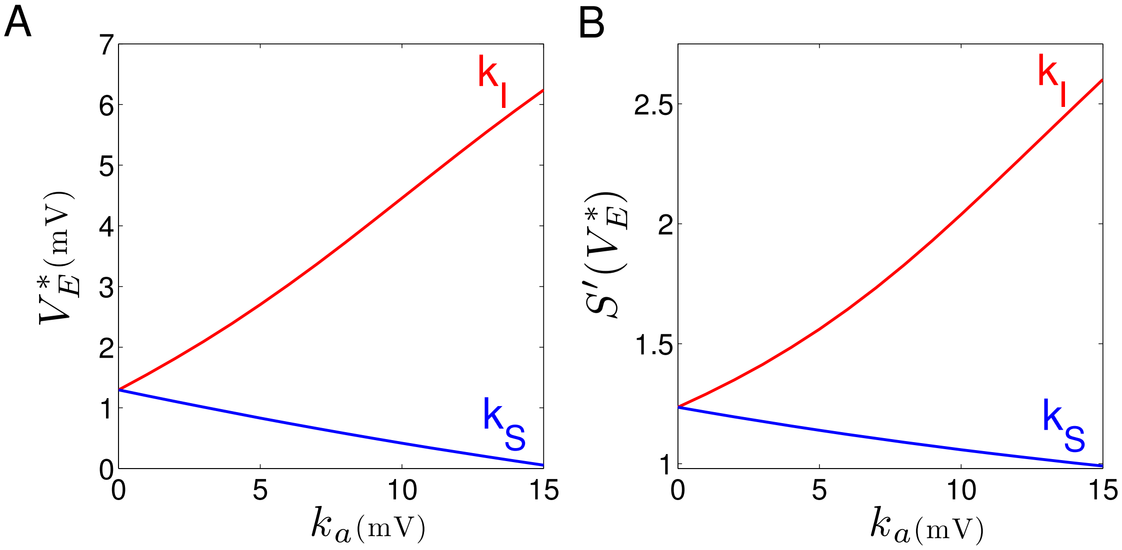

Fig. 3.7. Increasing the tonic inhibition (factor k_a for $a = I$ and S) affects the resting state of excitatory cortical neurons V_E^* (**A**) and the corresponding nonlinear cortical gain function (**B**). Here the anesthetic concentration factor is identical in the populations $a = E, I$ and S to ($p = 1.125$). In addition, the strength of self cortical inhibition is $\nu_{ii} = -1.8$ mVs.

the concentration factor p and fixed cortical self-inhibition. To understand better the interplay between tonic inhibition, synaptic inhibition and the strength of cortical self-inhibition, Fig. 3.8 shows the parameter pairs of synaptic inhibition p and the threshold of extra-synaptic sensitivity $k_{I,thr}$ at different self-inhibition levels, for which a peak in the $\delta-$frequency range emerges. Recall that the $k_{I,thr}$ is the critical (smallest) value of extra-synaptic sensitivity in cortical inhibitory neurons k_I, that lead to $dP_E/df = 0$, $d^2P_E/df^2 < 0$ computed at $f_{max} \in \delta-$range. Parameter values beyond the respective curves lead to $\delta-$activity power peaks.

We observe that for a chosen value of self cortical inhibition, by increasing the level of inhibition, the smaller value of $k_{I,thr}$ and thereby smaller tonic inhibition i.e., $(p-1) \cdot k_{I,thr}$ is required to induce the $\delta-$activity power peak, while the weaker the self cortical inhibition is the larger is the necessary extra-synaptic sensitivity or the synaptic inhibition to generate $\delta-$activity.

Even for vanishing self cortical inhibition ($\nu_{ii} = 0$), mathematical analysis (not shown) reveals that there is still a $\delta-$peak in the power spectrum for large enough synaptic or tonic inhibition (for p or k_I large enough). Moreover, Fig. 3.8 reveals a minimum tonic inhibition level (minimum value of k_I) beneath which no $\delta-$power peak emerges, irrespective of the level of synaptic inhibition (p). This result indicates a major role of tonic inhibition in the generation of $\delta-$activity, since it may support $\delta-$activity even if the synaptic inhibition level is not sufficient to support it.

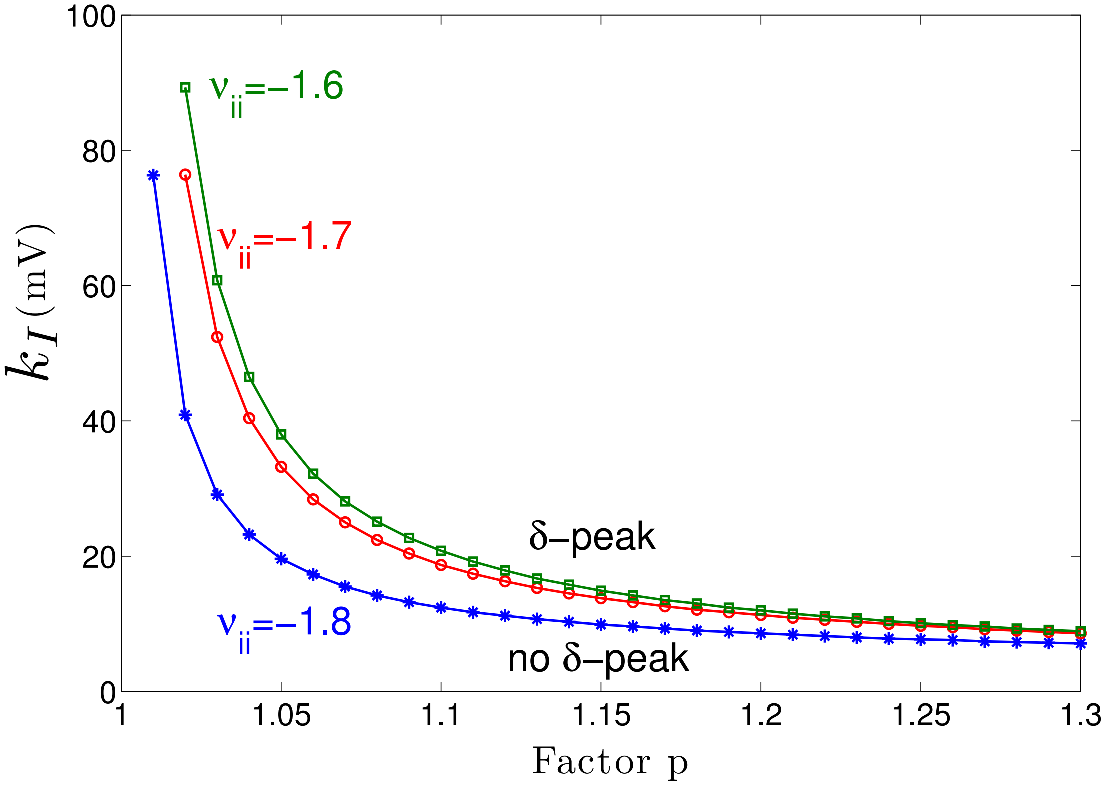

Fig. 3.8. Parameter space for $\delta-$power peak. The lines give the smallest (threshold) value of the extra-synaptic sensitivity $k_{I,thr}$ that induces $\delta-$ oscillations in the sedation condition with respect to the concentration factor p for different values of self-inhibitory connections ν_{ii}. The weaker the self cortical inhibition (the smaller $|\nu_{ii}|$), the higher the necessary level of propofol concentration (larger p) and the tonic inhibition (larger $(p-1) \cdot k_I$) to induce $\delta-$activity.

3.7 Discussion

In the sedation phase, for modest concentrations of propofol, the EEG power spectrum exhibits an increase in the $\delta-$ and $\alpha-$frequency ranges (Fig. 3.3) as found experimentally in the induction phase of propofol anesthesia [4]. One possible explanation for these phenomena is by postulating stronger GABAergic potentiation within cortical inhibitory neurons than within cortical pyramidal neurons (c.f. Fig. 3.4).

We hypothesize, that cortical GABAergic self inhibition plays a decisive role. Figure 3.6 reveals that the power surge in these frequency ranges might also result from extra-synaptic tonic inhibition active in cortical inhibitory neurons. Tonic inhibition increases the firing threshold and hence diminishes the output of inhibitory neurons to excitatory cortical neurons, which then allows increased excitation in the excitatory population and a power surge in the EEG. Conversely tonic inhibition in the thalamic relay cells does not induce power surge in EEG since augmented inhibition in the thalamic relay cells yields diminished excitation in cortical excitatory neurons, leading to a decrease in EEG power. This interpretation is corroborated by Fig. 3.7 which demonstrates augmented and diminished nonlinear gain in cortical excitatory neurons assuming tonic inhibition in inhibitory and thalamic relay population, respectively. This reflects enhanced and weakened response to the noisy thalamic external input, see Refs. [35, 111] for a similar line of argument.

Figure 3.6 clearly reveals the emergence of $\delta-$activity caused by extra-synaptic tonic inhibition which is affirmed by the existence of a minimum level of extra-synaptic inhibition shown in Fig. 3.8. Conversely, $\alpha-$activity appears to be much less sensitive to tonic inhibition since it is present for all tonic inhibition levels. One interpretation may be the generation of $\alpha-$activity by the cortico-thalamic feedback as hypothesized theoretically [33] while $\delta-$activity results from the cortical interaction of excitatory and inhibitory neurons. The exact origins of propofol-induced $\alpha-$ and $\delta-$activity are not known for certain. We find that the $\alpha-$ oscillations arise from thalamo-cortical resonances. These oscillations are commonly synchronous across widespread cortical regions and are not easily generated in isolated cortical tissue [305, 306]. This affirms the original model of Lopes da Silva *et al.* [180]. However, our model results are equivalent to results of other models describing $\alpha-$activity by purely cortical interactions. We are not aware of a methodology ruling out one or the other model and this is not the aim of the present work. Our work just reveals the additional possibility that the thalamus serves as a possible (indirect) source of $\alpha-$activity. Similarly, the origin of $\delta-$activity is not clear, but slow activity does increase at higher concentrations of propofol - which may be associated with decreasing $\alpha-$waves as observed during desflurane general anesthesia [307]. This is in keeping with $\delta-$waves becoming more pronounced as the cortico-thalamic systems becomes increasingly hyperpolarized. However there is a lot of variability between patients as regards the relative power of $\alpha-$ and $\delta-$activity during general anesthesia; which would suggest that the true explanation is more complex, and requires recognition of other factors such as the one presented in this paper - the influence of the propofol on extra-synaptic inhibition.

Although anesthetic action on synaptic and extra-synaptic GABAergic receptors is different, both actions diminish neural activity and hence increase inhibition. Figure 3.8 elucidates that strong enough extra-synaptic or synaptic inhibition induces $\delta-$activity. Hence, one may argue that the level of inhibition plays an important role while its origin, i.e. synaptic or extra-synaptic, plays a secondary role. This interpretation corroborates the idea of the balance of excitation and inhibition as the major mechanism in general anesthesia. This interpretation is in good accordance to previous experimental findings on the important role of the balance of excitation and inhibition in brain network under anesthesia [308, 309]. Such global concepts as excitation-inhibition balance are attractive to describe complex processes in general anesthesia. For instance, anesthetics alter arousal in several pathways, such as the cholinergic pathway [17] and the orexinergic pathway which has been identified to activate a complex functional network controlling, inter alia, the emergence from unconsciousness [310].

Our theoretical study considers the anesthetic propofol and its corresponding action at synaptic and extra-synaptic GABAergic receptors only, whereas it is known that propofol induces inhibition at various other receptors as well [13, 311], including minor effects on NMDA-receptors and voltage-gated potassium channels [13]. Propofol also potentiates glycine receptors which are are found all over the central nervous system and have a major role in regulating inhibition, e.g., in the brain stem [312].

Similar to extra-synaptic inhibition resulting from ambient GABA concentrations, the presence of ambient concentrations of glycine close to NMDA-receptors entails tonic depolarization. This tonic excitation diminishes the firing threshold of neurons and hence may counteract inhibition. The present work considers tonic inhibition only and neglects tonic excitation effect. Although it would be important to study tonic excitation effects, this additional study would exceed the major aim of the manuscript, namely demonstrating the fundamental effect of tonic anesthetic action.

In addition, by virtue of the focus on extra-synaptic action, the model proposed neglects known anesthetic effects on different receptors and ion channels, although they have been shown experimentally, e.g., [13, 313] and references therein, and theoretically [211] to affect EEG activity. Specifically, the latter work of Bojak *et al.* [211] considers anesthetic effects on hyperpolarization-activated cyclic nucleotide-gated potassium channel 1 (HCN1) subunits which, effectively, increase the mean firing threshold in neural populations and strongly resembles the tonic inhibition induced by extra-synaptic GABA-receptors.

The model network topology includes a single module of a closed thalamo-cortical feedback loop [314] comprising two thalamic nuclei and cortical excitatory and inhibitory neurons. This model represents a first approximation of brain networks since it neglects brain stem activity including the reticular activating system (RAS) [315], which has significant modulating effects on attention, arousal and consciousness. Future work will include structures of the brain stem, propofol action on glycine receptors, and will take into account the RAS - since its neural structures involved exhibit strong extra-synaptic inhibition [316, 317, 9]. The model also neglects the cholinergic pathway originating from the basal forebrain [318], which is known to co-regulate the level of consciousness [17].

Essentially, our theoretical model assumes population coding implying rate-coding response activity of neuron populations subjected to external thalamic noise. The model does not consider specific single neuron dynamics found experimentally under anesthetic conditions. For instance, it has been hypothesized that, at certain levels of anesthetic concentration, thalamic neurons switch their activity from tonic firing to bursting and induce loss of consciousness [44].

In spite of these limitations, our model reproduces qualitatively the action of propofol on EEG and reveals the possible impact of extra-synaptic GABAergic receptors on the EEG power. To our knowledge, the present work is the first to link extra-synaptic GABAergic action and experimental EEG. Future work will refine the model involving additional receptor action, e.g., tonic excitation caused by ambient glycine concentrations, and sub-cortical brain structures.

3.8 Conclusion

Our results demonstrate that the cortical GABAergic self inhibition plays a critical role in reproducing the characteristic features of frontal EEG rhythms observed experimentally during the propofol sedation. Tonic inhibition activated in cortical inhibitory neurons results in a power surge in the EEG. Conversely, the potentiation of extra-synaptic GABAergic inhibition in cortical excitatory neurons or thalamic relay cells diminishes the EEG power. Moreover, $\alpha-$activity appears to be less much sensitive to the tonic inhibition whereas the strong enough extra-synaptic or synaptic inhibition induces EEG $\delta-$activity as observed during propofol general anesthesia.

4

Modeling of EEG power spectrum over frontal and occipital regions during propofol sedation

Contents

Abstract

Increasing concentrations of the anesthetic agent propofol initially induces sedation before achieving full general anesthesia. As mentioned before, during this state of anesthesia, the observed specific changes in EEG rhythms comprise increased activity in the $\delta-$ ($0.5-4$ Hz) and $\alpha-$ ($8-13$ Hz) frequency bands over the frontal region, but increased $\delta-$ and decreased $\alpha-$activity over the occipital region. In this chapter we apply a thalamo-cortical neuronal population model to reproduce these certain changes in EEG spectral power during propofol-induced anesthesia sedation.

We show that the model reproduces the power spectrum features observed experimentally both in frontal and occipital electrodes. Moreover, a detailed analysis of the model indicates the importance of multiple resting states in brain activity. It is demonstrated that the $\alpha-$activity originates from the cortico-thalamic relay interaction, whereas the emergence of $\delta-$activity results from the full cortico-reticular-relay-cortical feedback loop with a prominent enforced thalamic reticular-relay interaction. The results of the present chapter suggest an important role for synaptic GABAergic receptors at relay neurons and, more generally, for the thalamus in the generation of both the $\delta-$ and the $\alpha-$ EEG patterns that are seen during propofol anesthesia sedation.

4.1 GABAergic inhibition in thalamic cells

In order to implement the anesthetic action in cortical and thalamic structures, a careful look at neural receptors and their response to anesthetic action is mandatory. Recent studies have revealed possible molecular sites and neuronal pathways for the action of the anesthetic propofol in the human brain. In vivo extracellular recordings have demonstrated that propofol suppresses field potentials in the rat thalamus and cortex [80]. Although some reports put emphasis on more prominent effects in the cortex, the cortical suppression may, in fact, be secondary to anesthetic action on projection neurons located elsewhere in the brain, especially in the thalamus. Also several lines of evidence indicate that thalamus and thalamic neuronal circuits might be important target-sites for the hypnotic effects of propofol [9, 42, 43]. Moreover, experimental observations strongly suggest that reticular thalamic neurons are a major source of inhibition to the relay neurons; and are thus a critical structure for the effect of propofol in thalamic circuits [319, 79]. These findings motivated us to more concentrate on the effect of propofol in thalamic neurons - in contrast to previous chapter. Based on these experimental observations, we first study a full model including anesthetic effects in cortical and thalamic populations at light sedation. Then, in order to form a hypothesis that the GABAergic inhibition in thalamic cells seems to play a crucial role in the generation of characteristic EEG patterns under propofol sedation, we neglect the anesthetic action in the cortex in a reduced model [37]. This assumption points out the importance of the thalamus for major neural effects under anesthesia sedation as well as simplifies the model under study, while later results shall reveal that the model is still adequate to reproduce the observed changes in EEG rhythms. The model aims to reproduce spectral features in light sedation, i.e. at low propofol concentrations. This anesthetic phase does not exhibit increased spectral power in the $\beta-$frequency band, that is sometimes called *beta buzz.*

In the present chapter, we provide evidence that thalamic GABAergic synaptic inhibition is one of the key actions inducing the characteristic changes in the $\delta-$ and $\alpha-$frequency ranges under propofol-induced sedation. Moreover, the detailed study of sub-circuits suggests the existence of two major cortico-thalamic sub-circuits that generate $\delta-$ and $\alpha-$spectral power peaks. To our best knowledge, this is the first neural population study that reproduces the EEG changes over frontal and occipital regions in the thalamo-cortical system.

In this chapter we use a neural population model based on the model of Hutt & Longtin [28], c.f. section 2.3.4 of chapter 2. The following section presents the model equations which takes into account anesthetic action at inhibitory GABAergic synaptic receptors in both cortical inhibitory neurons and thalamic relay cells. The anesthetic action of extra-synaptic GABAergic receptors are however neglected in the present chapter. Then, we demonstrate the simulation of power spectra of EEG in frontal and occipital electrodes and show that both the proposed full and reduced neural population model reproduce very well the characteristic spectral features in the $\delta-$ and $\alpha-$band subjected to the propofol concentration. The subsequent analysis of the model reveals the importance of multiple resting states and the presence of effective sub-circuits generating the spectral features in $\delta-$ and $\alpha-$frequency bands.

4.2 Theoretical power spectrum

Under the assumption of the spatial homogeneity, the mean potentials V_a^c, for $a \in \{E, I, R, S\}$ in the cortical pyramidal neurons (E), cortical inhibitory neurons (I), the thalamo-cortical relay neurons (S) and thalamic reticular neurons (R) shown in Fig. 2.8 obey

$$\begin{aligned}
\hat{L}_e V_E^e(t) &= K_{EE} S_C[V_E^e(t) - V_E^i(t)] + \\
&\quad K_{ES} S_T[V_S^e(t-\tau) - V_S^i(t-\tau)], \\
\hat{L}_i V_E^i(t) &= f_C(p) K_{EI} S_C[V_I^e(t) - V_I^i(t)], \\
\hat{L}_e V_I^e(t) &= K_{IE} S_C[V_E^e(t) - V_E^i(t)], \\
\hat{L}_i V_I^i(t) &= K_{II} S_C[V_I^e(t) - V_I^i(t)], \\
\hat{L}_e V_S^e(t) &= K_{SE} S_C[V_E^e(t-\tau) - V_E^i(t-\tau)] + I(t), \\
\hat{L}_i V_S^i(t) &= f_T(p) K_{SR} S_T[V_R^e(t)], \\
\hat{L}_e V_R^e(t) &= K_{RE} S_C[V_E^e(t-\tau) - V_E^i(t-\tau)] + \\
&\quad K_{RS} S_T[V_S^e(t) - V_S^i(t)],
\end{aligned} \tag{4.1}$$

evoked at excitatory ($c = e$) and inhibitory ($c = i$) synapses with

$$\begin{aligned}
\hat{L}_e(\partial/\partial t) &= \frac{1}{\alpha_e \beta_e} \frac{\partial^2}{\partial t^2} + \left(\frac{1}{\alpha_e} + \frac{1}{\beta_e} \right) \frac{\partial}{\partial t} + 1, \\
\hat{L}_i(\partial/\partial t) &= \frac{1}{\alpha_i \beta_i} \frac{\partial^2}{\partial t^2} + \left(\frac{1}{\alpha_i} + \frac{1}{\beta_i} \right) \frac{\partial}{\partial t} + 1,
\end{aligned} \tag{4.2}$$

where $1/\alpha_e$ and $1/\alpha_i$ are the characteristic rise times of the response function for excitatory and inhibitory synapses, respectively, and $1/\beta_e$ and $1/\beta_i$ are the corresponding characteristic decay times. Note that the propofol prolongs the decay phases only in inhibitory synapses, and thus $\beta_i \to \beta_i/p$, while other synaptic rates are unaffected by propofol. See section 3.2 for definition of functions $f_C(p)$, and $f_T(p)$. The external input to relay neurons is $I(t) = I_0 + \xi(t)$, where $\xi(t)$ is Gaussian uncorrelated noise. In addition, the parameter τ denotes the transmission time delay between cortex and thalamus. Here it is assumed that the mean firing rate function given by Eq. (2.36), in the cortex $S_C[\cdot]$ is different to the thalamic firing rate function $S_T[\cdot]$, while it is identical in the cortex and for relay and the reticular populations. The nominal values for two parameter sets are displayed in Table 4.1 in the absence of anesthetics.

It can be seen that the mean post-synaptic potentials in above equations do not depend on spatial locations and then obey the general delay differential equation system

$$\hat{\boldsymbol{L}}(\partial/\partial t, p)\boldsymbol{X}(t) = \mathbf{f}(\boldsymbol{X}(t), \boldsymbol{X}(t-\tau), p) + \boldsymbol{I}(t), \tag{4.3}$$

in which $\boldsymbol{X}(t) = (V_E^e, V_E^i, V_I^e, V_I^i, V_S^e, V_S^i, V_R^e)^\top \in \mathbb{R}^N$ is the activity variable vector with dimension N=7. The high index $\top$ denotes the transposed vector or matrix. The nonlinear vector

Table 4.1. Model parameters, their symbols, and nominal values for two parameter sets.

Parameter	Symbol	Nominal value (set I, set II)
Maximum firing-rate of cortical population	S_C^{max}	(130, 140) Hz
Maximum firing-rate of thalamic population	S_T^{max}	(100, 220) Hz
Mean firing threshold of cortical population	V_C^{th}	(25, 10) mV
Mean firing threshold of thalamic population	V_T^{th}	(25, 10) mV
Firing rate variance	σ	(10,12) mV
Type-I population effect constant	ρ	(0.05, 0.09) mV^{-1}
Excitatory synaptic rise rate	α_e	(500,500) s^{-1}
Excitatory synaptic decay rate	β_e	(50,50) s^{-1}
Inhibitory synaptic rise rate	α_i	(100,400) s^{-1}
Inhibitory synaptic decay rate	β_i	(10,40) s^{-1}
Excitatory synaptic gain	a_e	1 mVs
Inhibitory synaptic gain	a_i	1 mVs
Synaptic strength from E to E neurons	K_{EE}	(0.1, 0.1) mVs
Synaptic strength from E to I neurons	K_{IE}	(0.3, 0.2) mVs
Synaptic strength from E to S neurons	K_{SE}	(0.8, 0.2) mVs
Synaptic strength from E to R neurons	K_{RE}	(0.2, 0.5) mVs
Synaptic strength from I to I neurons	K_{II}	(0.2, 0.1) mVs
Synaptic strength from I to E neurons	K_{EI}	(0.6, 0.2) mVs
Synaptic strength from S to E neurons	K_{ES}	(0.8, 2.2) mVs
Synaptic strength from S to R neurons	K_{RS}	(0.1, 0.3) mVs
Synaptic strength from R to S neurons	K_{SR}	(0.8, 0.1) mVs
Constant external input	I_0	0.1 mV
Intensity of external thalamic noise	κ	0.5 mV
Transmission delay between cortex and thalamus	τ	40 ms

function $\mathbf{f} \in \mathbb{R}^N$ includes the nonlinear transfer functions and depend on the anesthetic factor p. The external input is written as $\boldsymbol{I}(t) = \boldsymbol{I}_0 + \boldsymbol{\xi}(t) \in \mathbb{R}^N$ with $\boldsymbol{I}_0 = (0,0,0,0,I_0,0,0)^\top$ and $\boldsymbol{\xi}(t) = (0,0,0,0,\xi(t),0,0)^\top$. The diagonal matrix operator $\hat{\boldsymbol{L}}(\partial/\partial t, p) \in \mathbb{R}^{N\times N}$ includes all temporal operators $\hat{L}_{e,i}$ and depends on the anesthetic factor p.

Assuming small random fluctuations $\xi(t)$, we define the resting state $\boldsymbol{X}_0 \in \mathbb{R}^N$ as a fixed point of Eq. (4.3), for which $\hat{\boldsymbol{L}} = \mathbf{1}$, and which is given by

$$\boldsymbol{X}_0 = \mathbf{f}(\boldsymbol{X}_0, \boldsymbol{X}_0, p) + \boldsymbol{I}_0. \tag{4.4}$$

We observe that the resting state depends on p and hence on the anesthetic concentration. The current model follows the standard assumption [22, 29, 23, 182, 320] that the electric dipol generating the EEG is modeled well by fluctuations of the dendritic currents about the resting state. Hence small deviations $\boldsymbol{Y}(t) \in \mathbb{R}^N$ from the resting state $\boldsymbol{X}_0$ generate the EEG and obey

$$\hat{\boldsymbol{L}}(\partial/\partial t, p)\boldsymbol{Y}(t) = \boldsymbol{A}(p)\boldsymbol{Y}(t) + \boldsymbol{B}(p)\boldsymbol{Y}(t-\tau) + \boldsymbol{\xi}(t), \tag{4.5}$$

where $\boldsymbol{A}(p)$, $\boldsymbol{B}(p) \in \mathbb{R}^{N\times N}$ are constant matrices. Following previous studies [22, 29, 23, 33, 173, 182], the EEG is generated by the population activity of pyramidal cortical cells V_E^e. Then, by virtue of the specific choice of external input to relay neurons, the power spectrum of the EEG at certain frequency ν reads [111]

$$P_E(\nu) = 2\kappa\sqrt{2\pi}\left|\tilde{G}_{1,5}(\nu, p)\right|^2, \tag{4.6}$$

where P_E just depends on one matrix component of $\tilde{\boldsymbol{G}}(\nu, p)$ given by

$$\tilde{\boldsymbol{G}}(\nu,p) = \frac{1}{\sqrt{2\pi}} \begin{bmatrix} \hat{L}_e(\nu) - K_1 & K_1 & 0 & 0 & -K_2 e^{-2\pi i\nu\tau} & K_2 e^{-2\pi i\nu\tau} & 0 \\ 0 & \hat{L}_i(\nu) & -f_C(p)K_3 & f_C(p)K_3 & 0 & 0 & 0 \\ -K_4 & K_4 & \hat{L}_e(\nu) & 0 & 0 & 0 & 0 \\ 0 & 0 & -K_5 & \hat{L}_i + K_5(\nu) & 0 & 0 & 0 \\ -K_6 e^{-2\pi i\nu\tau} & K_6 e^{-2\pi i\nu\tau} & 0 & 0 & \hat{L}_e(\nu) & 0 & 0 \\ 0 & 0 & 0 & 0 & 0 & \hat{L}_i(\nu,p) & -f_T(p)K_7 \\ -K_8 e^{-2\pi i\nu\tau} & K_8 e^{-2\pi i\nu\tau} & 0 & 0 & -K_9 & K_9 & \hat{L}_e(\nu) \end{bmatrix}^{-1} \tag{4.7}$$

See section 2.3.4 of chapter 2 for the definition of $\tilde{G}(\nu, p)$ elements. The matrix elements of $\tilde{G}_{1,5}(\nu, p)$ depend primarily on the level of excitation and inhibition in the various populations and on the nonlinear gains $dS_{T,C}[V]/dV$ computed at the resting state of the system. Since the resting state depends strongly on the anesthetic concentration factor p, in turn the nonlinear gains computed at the resting state depends on p as well.

4.3 Experimental power spectrum

An example of the time course of the progressive increase in propofol effect-site concentrations, and the changes in $\delta-$ and $\alpha-$power in each of the 11 para-midline electrodes are shown in Fig. 4.1**A** and **B** , respectively. Figure 4.1**C** shows the spectrogram of experimental EEG power averaged over frontal and occipital electrodes. The power spectra of frontal and occipital average EEG during the baseline phase and during sedation are shown in Fig. 4.1**D**. They show typical changes in EEG patterns; namely that the propofol resulted in a loss of the $\alpha-$rhythm (~ 10 Hz) in the occipital electrodes, but a gain in $\alpha-$ and $\beta-$power (peak frequency around 13 Hz) in the frontal leads ($p < 0.05$, t-test). There is a clear line of spatial delineation between the two modes of EEG response; most of the central and parietal electrodes are similar to the occipital pattern of response. Propofol also causes an increase in $\delta-$power in both frontal and occipital regions ($p < 0.05$, t-test). Figure 4.1**E** summarizes these results.

Figure 4.1**D** and **E** consider propofol concentrations which lead to sedation. In some patients, there is an increased activity in the frontal $\beta-$band which is seen at about 6 min in Fig. 4.1**C**. The alternations in higher frequencies are not specifically investigated in our model.

4.4 Power spectrum of full thalamo-cortical model

This section presents the results of the analytical study of the full model govern by equations presented in section 4.2.

Frontal spectrum

Figure 4.2 shows the EEG power spectrum (4.6) in the baseline condition (absence of propofol) and after the administration of propofol for certain parameters (parameter set I in Table 4.1). We observe an increase of power in the $\delta-$ and $\alpha-$frequency bands while increasing the propofol concentration accompanied by $\alpha-$activity shifted to higher frequencies (cf. Fig. 4.2**A**). These amplitude power changes bear a strong resemblance to the empirical observations in EEG power spectrum over the frontal region (cf. Fig. 4.2**B**). These results are confirmed by numerical simulations of the model.

To reveal the origin of the spectral EEG-changes with increasing concentration, we relate the maxima of spectral power to the roots of the characteristic equation of Eq. (4.5) $\lambda = \gamma + 2\pi i\nu$.

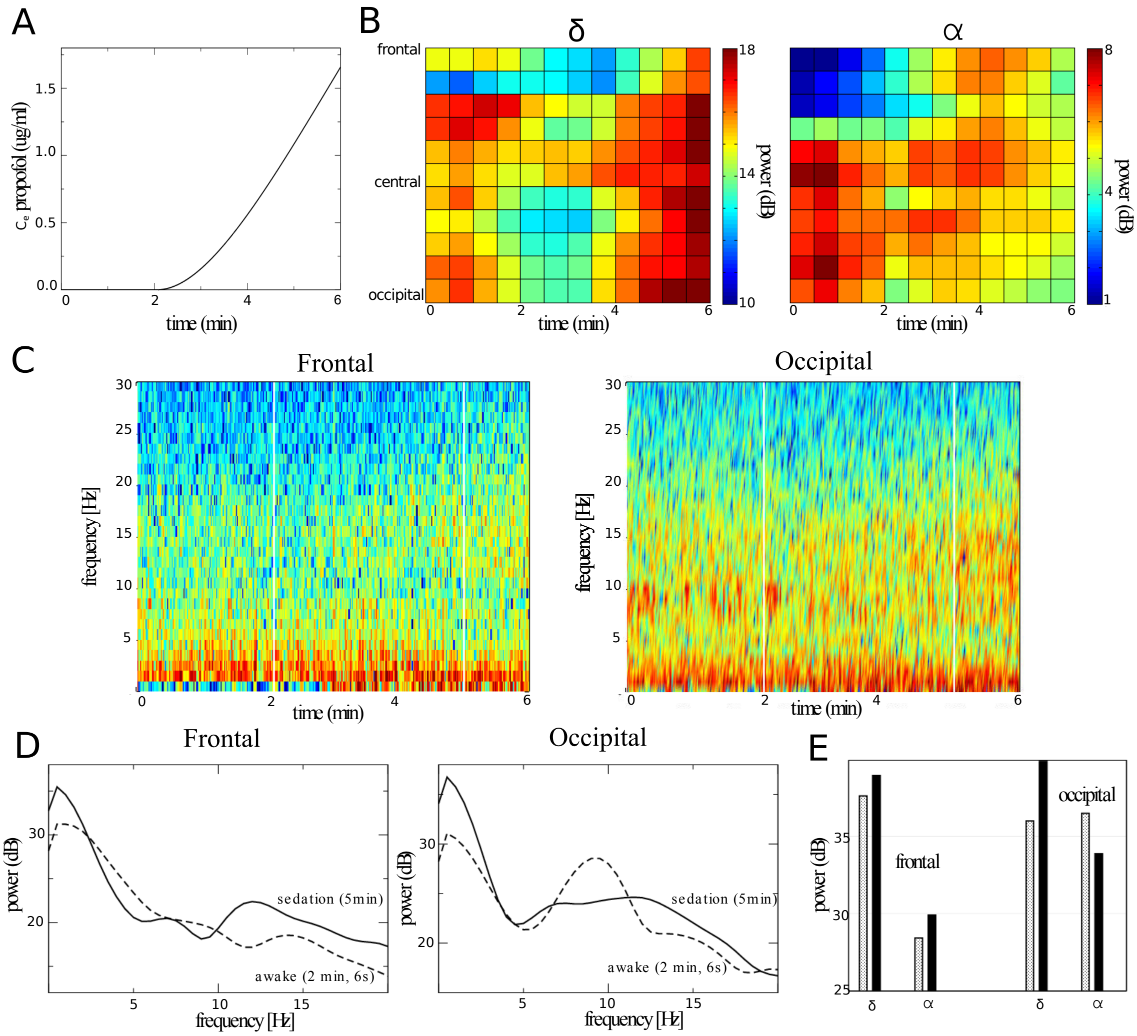

Fig. 4.1. Physiological and electroencephalographic data observed in a single subject while increasing the propofol concentration. (**A**) Blood plasma concentration of propofol with respect to administration time. Since average clinical propofol concentrations in sedation are around or smaller than 1μg/ml [321], the subject my leave the clinical sedation phase at about $t = 5$min. (**B**) Mean spectral power in the $\delta-$ and $\alpha-$frequency bands in single electrodes located along the scalp mid-line with respect to administration time. (**C**) Spectrogram of power averaged over four frontal (left) and four occipital (right) electrodes. The vertical white lines denote 2 sec-time windows at $t = 2$ min 6 sec and at $t = 5$ min. (**D**) Average power spectra over frontal (left) and occipital (right) electrodes during the baseline state (awake) and during sedation. The peak at about 2 Hz has been verified by modifying the sliding window duration of the power spectral density estimation technique. (**E**) Spectral power amplitude averaged over the $\delta-$ and $\alpha-$frequency bands in the frontal and occipital scalp. Grey and black color encodes awake and sedation, respectively.

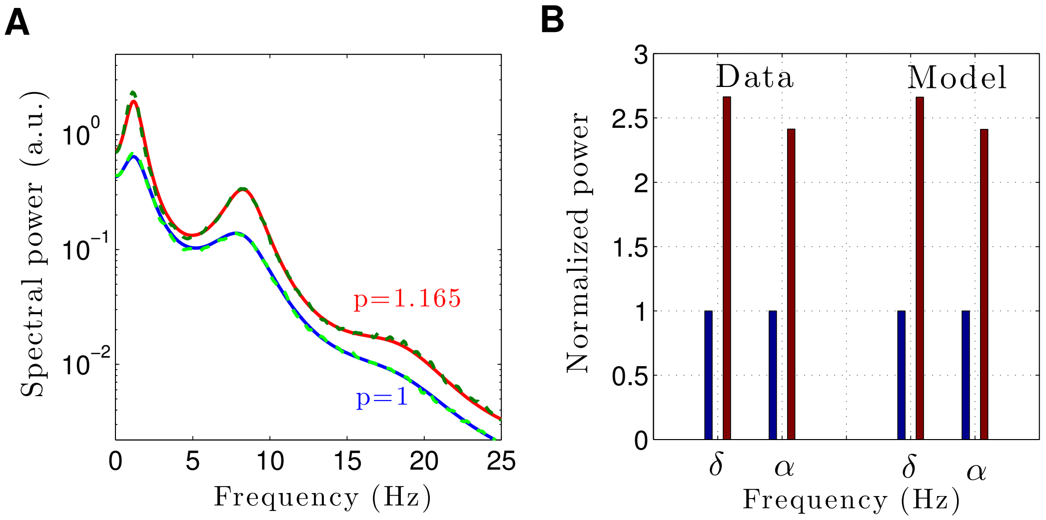

Fig. 4.2. The theoretical and experimental EEG-spectral power in the baseline and the sedation conditions. (**A**) The solid lines indicate the analytical solutions and the dashed lines show the numerical solutions of the model system for the control condition ($p = 1$) and under sedation ($p = 1.165$). (**B**) The normalized power amplitude of experimental data in frontal electrodes and the model over $\delta-$ and $\alpha-$band in the baseline condition (blue bars) and in the sedation condition (red bars). Parameters are taken from set I in Table 4.1, the spectrum is computed at the upper resting state of the system.

Figure 4.3 illustrates the damping rate γ and frequency ν of the roots in the $\delta-$ and $\alpha-$frequency ranges. While the power peak in $\alpha-$frequency range increases by the administration of propofol, the $\delta-$frequency is maintained for different propofol concentrations. Moreover, the damping rate of $\delta-$ and $\alpha-$activity increase with increasing anesthetic level and hence the power in the corresponding frequency band increases in accordance to standard spectral theory.

Occipital spectrum

For different parameters (set II in Table 4.1), Fig. 4.4 shows the model power spectrum resembling experimental activity observed in occipital EEG-electrodes. The power in the $\delta-$ frequency range increases and the $\alpha-$power decreases while increasing the anesthetic level (cf. Fig. 4.4**B**). Figure 4.5 presents the effect of increasing propofol concentration on damping rate and frequency of the model EEG in the $\delta-$ and $\alpha-$frequency ranges. It can be observed that as propofol concentration increases, the damping rate of $\delta-$activity increases whereas $\alpha-$damping rate decreases. This finding is consistent with enhanced $\delta-$ and attenuated $\alpha-$power observed experimentally. In addition, the frequency of the activity in both frequency bands increase very slightly.

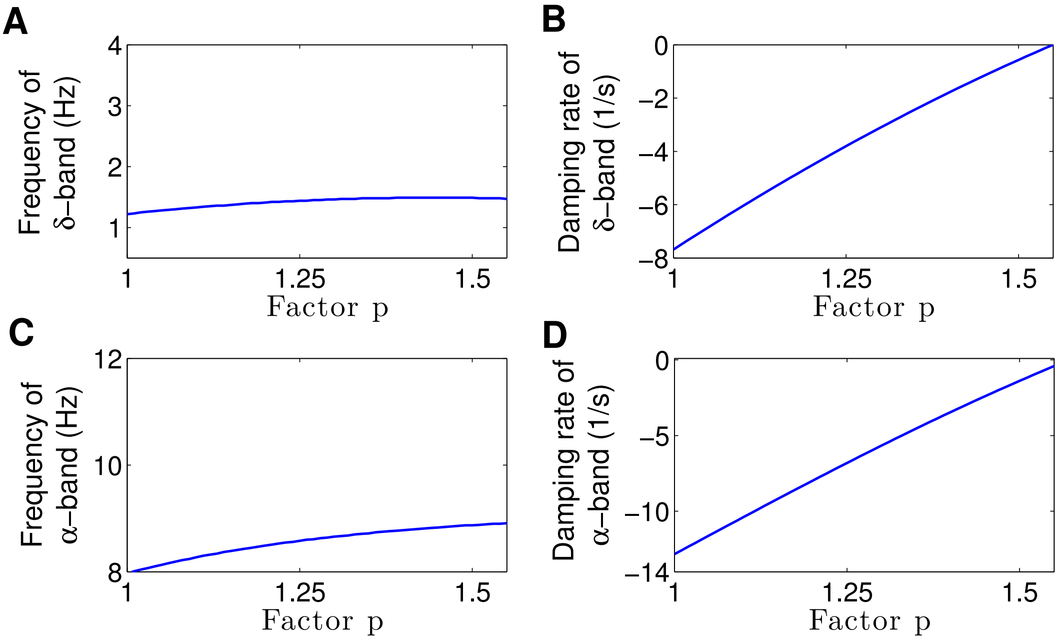

Fig. 4.3. Modulation of $\delta-$ and $\alpha-$activity in model over the frontal region. The panels show the frequency ν in the roots imaginary part which lie in the $\delta-$and $\alpha-$frequency ranges in panels (**A**) and (**C**), respectively. Panels (**B**) and (**D**) show the corresponding damping rates as a function of the anesthetic factor p. The factor p reflects the anesthetic propofol concentration.

Resting state and gain function

In the case of constant external input $I(t) = I_0$, the spatially-homogeneous resting states of Eqs. (4.1) can be obtained by $dV_a^{e,i}/dt = 0$, for $a \in \{E, I, S, R\}$ leading to

$$\begin{aligned}
V_E^{*e} &= K_{EE}S_C[V_E^{*e} - V_E^{*i}] + K_{ES}S_T[V_S^{*e} - V_S^{*i}],\\
V_E^{*i} &= f_C(p)K_{EI}S_C[V_I^{*e} - V_I^{*i}],\\
V_I^{*e} &= K_{IE}S_C[V_E^{*e} - V_E^{*i}],\\
V_I^{*i} &= K_{II}S_C[V_I^{*e} - V_I^{*i}],\\
V_S^{*e} &= K_{SE}S_C[V_E^{*e} - V_E^{*i}] + I_0,\\
V_S^{*i} &= f_T(p)K_{SR}S_T[V_R^{*e}],\\
V_R^{*e} &= K_{RE}S_C[V_E^{*e} - V_E^{*i}] + K_{RS}S_T[V_S^{*e} - V_S^{*i}].
\end{aligned} \tag{4.8}$$

Figure 4.6 presents the mean potential of pyramidal neurons in the resting state denoted by V_E^{*e}, and the corresponding nonlinear gain dependent on the propofol concentration for the two parameter sets considered in the previous section. We observe that three resting states may occur in the baseline condition, cf. Fig. 4.6**A** and **B**. Moreover, the upper and the center resting states collide at a critical value of p. Above this critical level, there exists a single resting state only at a low mean potential. The stability study of the resting states reveal that the upper and lower resting states are linearly stable, whereas the center resting state is unstable. This shows that the system may evolve either about the upper or the lower state, but never about the center resting state.

Since the spectral power depends heavily on the resting state and the nonlinear gain, the distinction between the upper and lower resting states is important to understand the power

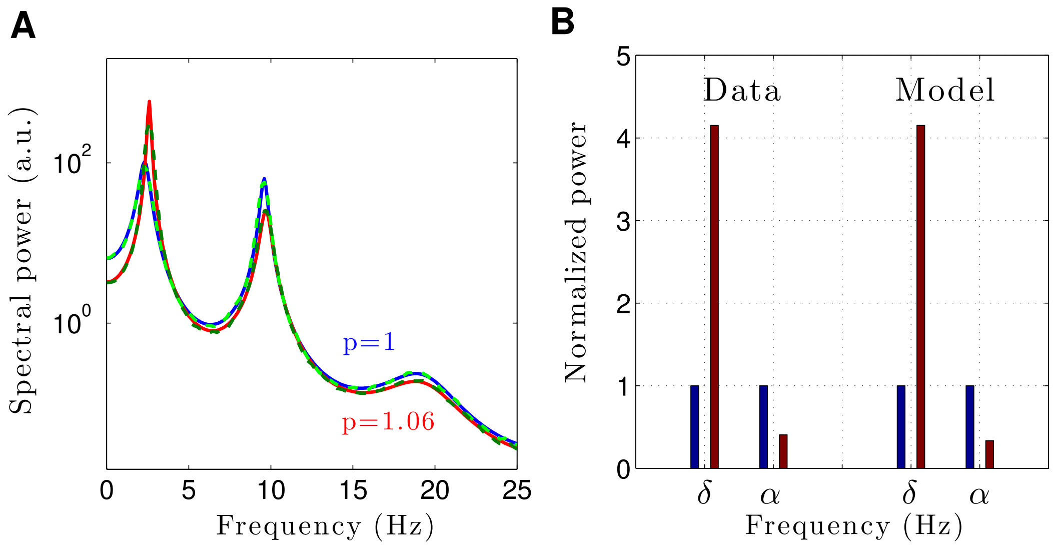

Fig. 4.4. The theoretical EEG-spectral power compared to the power observed experimentally in occipital EEG-electrodes in baseline and under sedation. (**A**) The solid and dashed lines indicate the analytical and numerical solutions, respectively, in the baseline ($p = 1$) and in the anesthesia sedation condition ($p = 1.06$). (**B**) The blue and red bars show the normalized power amplitude of experimental data in occipital electrodes and the model over $\delta-$ and $\alpha-$band in the baseline and anesthesia condition, respectively. Parameters are taken from set II in Table 4.1, the spectrum is computed at the lower resting state of the system.

changes shown in the previous section and in experiments. Increasing the anesthetic concentration decreases the mean potential of the upper resting state and, since the upper mean potential values are larger than the mean firing threshold and by virtue of the sigmoidal shape of the transfer function, decreasing V_E^{*e} on the upper resting state leads to an increase of the corresponding nonlinear gain function (Fig. 4.6**C** and **D**). Conversely increasing the anesthetic level on the lower resting state decreases the nonlinear gain.

Sub-circuits

The EEG results from the interactions of various neural populations which may be viewed as interacting sub-circuits [29, 23, 227]. According to the full model shown in Fig. 2.8 , we identity the sub-circuits $E \to S \to E$ (cortico-thalamic relay circuit), $E \to I \to E$ (intra-cortical circuit), $S \to R \to S$ (intra-thalamic circuit) and $E \to R \to S \to E$ (cortico-thalamic circuit). To reveal the relative contribution of these sub-circuits to the spectral power in the excitatory cortical population in certain frequency bands, we define the relative frequency response function from neurons of type b to neurons of type a

$$\psi_l(\nu, p) = \frac{|\eta_l(\nu, p)| - |\eta_l(\nu, p = 1)|}{|\eta_l(\nu, p = 1)|}, \tag{4.9}$$

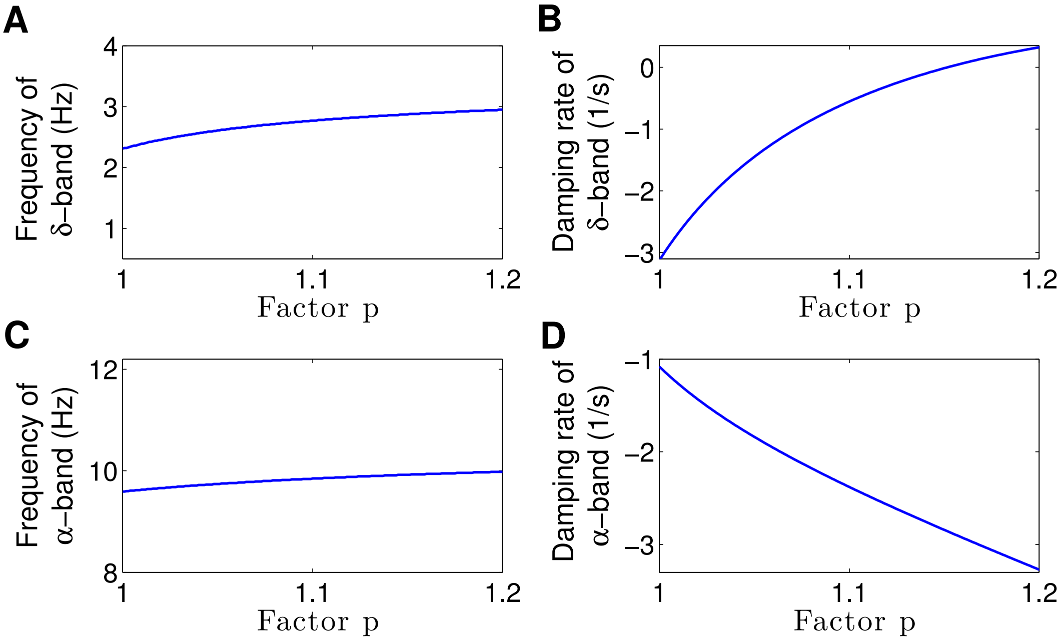

Fig. 4.5. Modulation of $\delta-$ and $\alpha-$activity in the model over occipital region. Shown are the frequency of $\delta-$and $\alpha-$oscillation in panels (**A**) and (**C**), respectively, and the corresponding damping rates in (**B**) and (**D**), respectively, as a function of the factor p. The factor p reflects the anesthetic propofol concentration.

where $l \in \{ese, eie, srs, esre\}$, $\eta_{ese} = \chi^e_{es}\chi^e_{se}$, $\eta_{eie} = \chi^i_{ei}\chi^e_{ie}$, $\eta_{srs} = \chi^i_{sr}\chi^e_{rs}$, and $\eta_{esre} = \chi^e_{es}\chi^i_{sr}\chi^e_{re}$, and

$$\begin{aligned}
\chi^{e,i}_{ab}(\nu, p) &= K_{ab}S'_{C,T}(V^{*e,i}_b)\phi^{e,i}(\nu, p)e^{-2\pi i\nu\tau} \quad \text{for } (a, b) \in \{(e, s), (s, e), (r, e)\}, \\
\chi^{e,i}_{ab}(\nu, p) &= K_{ab}S'_{C,T}(V^{*e,i}_b)\phi^{e,i}(\nu, p) \quad \text{otherwise.}
\end{aligned}$$

The relative frequency response function ψ_l defined in Eq. (4.9) is motivated by a similar measure defined by Hindriks & van Putten [35], but extends this previous definition by its frequency dependence. Here $S'_{C,T}(V^{*e,i}_b)$ are the nonlinear gains, i.e. the derivative of the mean firing rate function with respect to the voltages $V^{e,i}_b$ computed at the resting states $V^{*e,i}_b$. The term $e^{-2\pi i\nu\tau}$ denotes the phase shift due to the propagation delay between cortex and thalamus. Since it does not reflect any changes in our results, it can be neglected in the analysis. The functions $\phi^{e,i}$ are the Fourier transform of $h_{e,i}(t)$ and represent the synaptic frequency responses

$$\begin{aligned}
\phi^e(\nu, p) &= \left(1 + \frac{2\pi i\nu}{\alpha_e}\right)^{-1}\left(1 + \frac{2\pi i\nu}{\beta_e}\right)^{-1}, \\
\phi^i(\nu, p) &= f_j(p)\left(1 + \frac{2\pi i\nu}{\alpha_i}\right)^{-1}\left(1 + \frac{2\pi i\nu}{\beta_i}\right)^{-1}.
\end{aligned} \tag{4.10}$$

Increasing the factor p decreases the decay rate of synaptic inhibition β_i and increases the charge transfer $f_j(p)$. Hence the enhancement of inhibition leads to increased inhibitory synaptic frequency response function ϕ^i_{ab} given by Eq. (4.10). Moreover, the administration of propofol changes the resting states and consequently the nonlinear gain functions $S'_{C,T}(V^{*e,i}_b)$ which may increase or decrease.

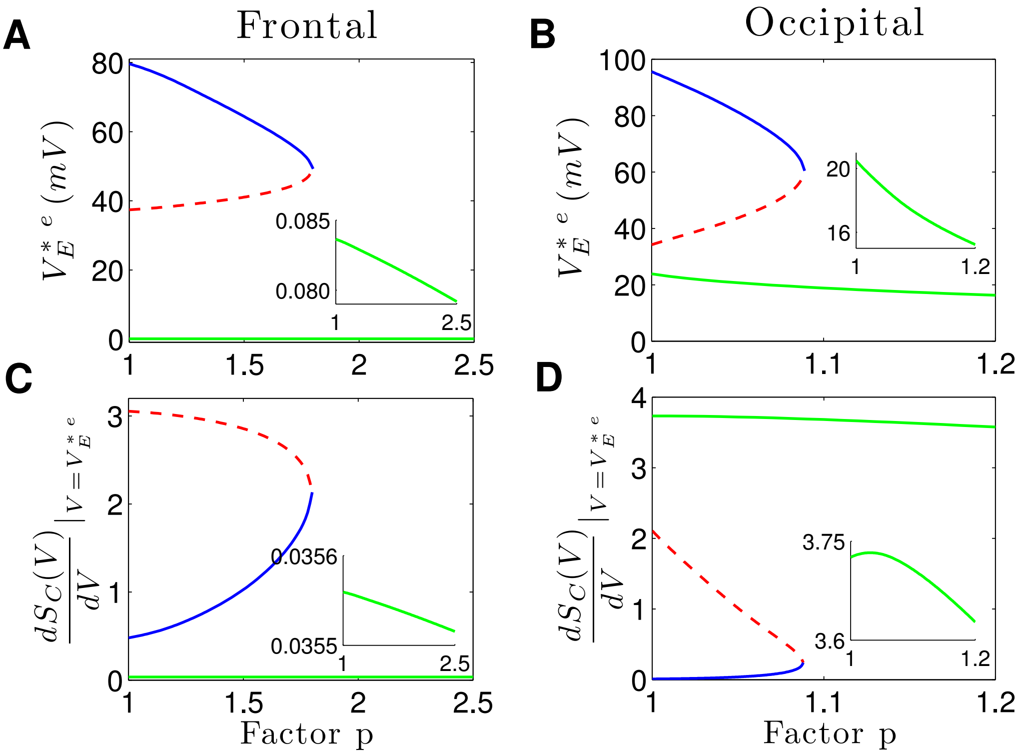

Fig. 4.6. The resting states of the system determined by Eq. (4.8) subject to the anesthetic level. The panels (**A**) and (**B**) show values of V_E^{*e} in the resting states for the two parameter sets I and II, respectively. Panels (**C**) and (**D**) present the corresponding nonlinear gain function dS_C/dV. The upper and lower stable branches are displayed respectively in solid blue and green lines whereas the middle unstable branches are encoded in dashed red lines. For illustration reasons, the lower branches are shown again in the insets. The factor p reflects the anesthetic propofol concentration.

Figure 4.7 illustrates the contribution of different anatomical loops $l \in \{ese, eie, srs, esre\}$ to the power spectrum at the upper and lower resting states of the system corresponding to the frontal and occipital regions, respectively.

In the upper resting state, increasing the propofol concentration increases the inhibitory synaptic frequency response function ϕ^i_{ab} (cf. Eq. (4.10)) as well as the nonlinear gain functions $S'_{C,T}(V_b^{*e,i})$ (cf. Fig. 4.6**C**). Hence, as observed in Fig. 4.7**A**, the relative frequency response function ψ_l in the $\delta-$ and $\alpha-$band increases for all loops. This affirms the enhancement of the power in $\delta-$ and $\alpha-$band observed over frontal electrodes.

At the lower resting state, increasing propofol concentrations increases the inhibitory synaptic frequency response function ϕ^i_{ab} but the nonlinear gain functions $S'_{C,T}(V_b^{*e,i})$ decrease (cf. Fig. 4.6**D**). As observed in Fig. 4.7**B**, since no inhibitory synapses are involved in the *ese* loop, ψ_{ese} decreases with a decreasing nonlinear gain function. This reveals an important role for the *ese* loop in the modulation of $\alpha-$activity which decreases by decreasing the gain function, in contrast to the upper resting state.

Within the *eie*, *srs* and *esre* loops, the nonlinear gains at the lower resting state decrease by an increase of the propofol concentration while the increase in the inhibitory charge transfer

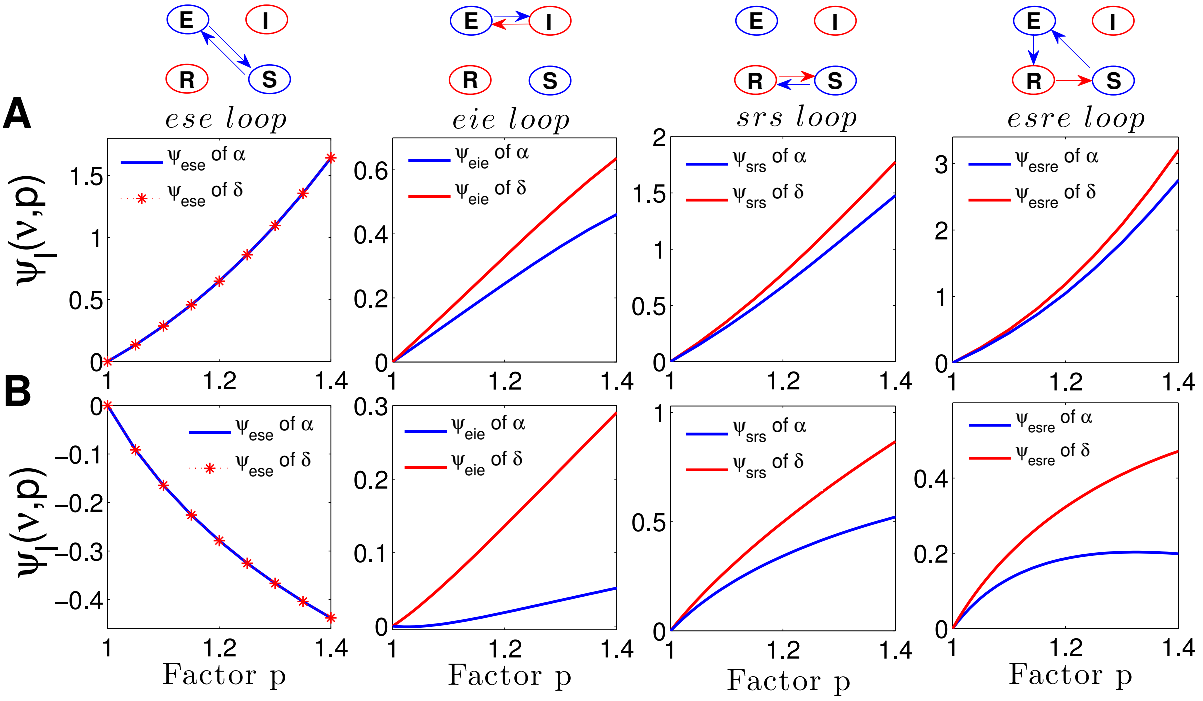

Fig. 4.7. The change of the relative frequency response function $\psi_l(\nu, p)$ defined by Eq. (4.9) in the $\delta-$ and $\alpha-$frequency bands within different anatomical loops of the thalamo-cortical system. The panels in (**A**) consider fluctuations about the upper resting state describing frontal EEG and panels in (**B**) give the results at the lower resting state describing occipital EEG. The factor p reflects the anesthetic propofol concentration.

more than compensates this decrease essentially leading to an increase in ψ_{eie} , ψ_{srs}, and ψ_{esre}. Consequently, in these loops the enhancement of inhibition plays a more substantial role than the gain function modulation.

4.5 Reduced thalamo-cortical model

The previous section considers both thalamic and cortical inhibition revealing their role in generating $\delta-$ and $\alpha-$activity. Specifically, cortical inhibition is strong and balances cortical excitation. In order to study the role of the intra-thalamic inhibition for the generation of characteristic EEG pattern under anesthesia sedation, we focus on the role of thalamic inhibition while neglecting inhibition within the cortex (although, of course, cortical inhibition is present in the brain) and refer to this model as *reduced model* in the following. This assumption simplifies the model under study, while the obtained results shall reveal that the reduced model is still adequate to reproduce observed changes in EEG rhythms within $\delta-$ and $\alpha-$activity bands. The results show clearly that thalamic inhibition balances cortical excitation as cortical inhibition does. Figure 4.8 shows the power spectra of EEG over frontal and occipital regions in the baseline and in the anesthetic conditions computed at the upper and lower resting states of the system. It turns out that the reduced model yields similar results compared to the full model (4.1), cf. Figs. 4.2 and 4.4.

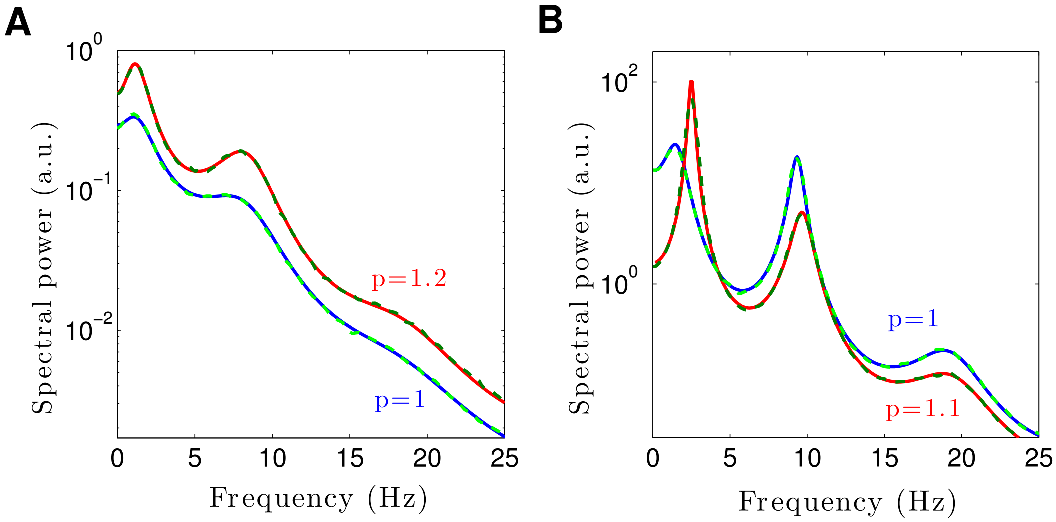

Fig. 4.8. The spectral power of EEG associated with the reduced thalamo-cortical model neglecting cortical inhibition in the baseline condition ($p = 1$) and under sedation ($p > 1$). The solid lines indicate the analytical solutions and the dashed lines show the numerical solutions of the model system. The panels show the spectrum computed at the upper and lower resting states in (**A**) and (**B**) reproducing the characteristics of experimental EEG spectra over the frontal and occipital regions, respectively. Parameters are taken from sets I, II in Table 4.1 while neglecting cortical inhibition.

4.5.1 The role of different populations and anatomical loops

To understand the role of different populations and the anatomical circuits of the reduced thalamo-cortical model, we study the contribution of PSPs to the power spectrum in the $\delta-$ and $\alpha-$ frequency bands over different brain areas. It is assumed that the system fluctuations about the resting state are a linear superposition of damped noisy oscillations whose frequencies are determined by the imaginary part of the characteristic roots of Eq. (4.5). We select a certain root and consider the fluctuations $\boldsymbol{Y}(t) = [y_1(t), y_2(t), y_3(t), y_4(t)]^\top$ with $y_n(t) = \hat{u}_n e^{\lambda t} + \hat{u}_n^* e^{\lambda^* t}$, $n = 1, \ldots, 4$. Here λ is the root and $\hat{u}_n$ is the $n-$th element of its eigenvector of the corresponding eigenvalue problem. Substituting the ansatz $\boldsymbol{Y}(t) = e^{\lambda t}\mathbf{u}$ with eigenfunction $\mathbf{u} = [u_E^e, u_S^e, u_S^i, u_R^e]^\top$ into Eqs. (4.5) yields

$$\begin{aligned}
\left(\frac{\lambda}{\alpha_e}+1\right)\left(\frac{\lambda}{\beta_e}+1\right)u_E^e &= K_2(u_S^e - u_S^i)e^{-\lambda\tau},\\
\left(\frac{\lambda}{\alpha_e}+1\right)\left(\frac{\lambda}{\beta_e}+1\right)u_S^e &= K_6 u_E^e e^{-\lambda\tau},\\
\left(\frac{\lambda}{\alpha_i}+1\right)\left(\frac{\lambda}{\beta_i}+1\right)u_S^i &= f_T(p)K_7 u_R^e,\\
\left(\frac{\lambda}{\alpha_e}+1\right)\left(\frac{\lambda}{\beta_e}+1\right)u_R^e &= K_8 u_E^e e^{-\lambda\tau} + K_9(u_S^e - u_S^i).
\end{aligned} \tag{4.11}$$

Now we can write all the elements of eigenfunction $\mathbf{u}$ in terms of the first element u_E^e as follows

$$\begin{aligned}
u_E^e &= u_1(\lambda)u_E^e,\\
u_S^e &= \left(\frac{K_6 e^{-\lambda\tau}}{(1+\frac{\lambda}{\alpha_e})(1+\frac{\lambda}{\beta_e})}\right)u_E^e \equiv u_2(\lambda)u_E^e,\\
u_S^i &= \left(\frac{K_6 e^{-\lambda\tau}}{(1+\frac{\lambda}{\alpha_e})(1+\frac{\lambda}{\beta_e})} - \frac{(1+\frac{\lambda}{\alpha_e})(1+\frac{\lambda}{\beta_e})}{K_2 e^{-\lambda\tau}}\right)u_E^e \equiv u_3(\lambda)u_E^e,\\
u_R^e &= \frac{(1+\frac{\lambda}{\alpha_i})(1+\frac{\lambda}{\beta_i})}{f_T(p)K_7}\left(\frac{K_6 e^{-\lambda\tau}}{(1+\frac{\lambda}{\alpha_e})(1+\frac{\lambda}{\beta_e})} - \frac{(1+\frac{\lambda}{\alpha_e})(1+\frac{\lambda}{\beta_e})}{K_2 e^{-\lambda\tau}}\right)u_E^e \equiv u_4(\lambda)u_E^e.
\end{aligned} \tag{4.12}$$

Then the associated normalized eigenfunction with known eigenvalue λ is $\hat{\mathbf{u}} = C\,(1, u_2(\lambda), u_3(\lambda), u_4(\lambda))^\top$, where $C = \dfrac{1}{\sqrt{1+u_2^2+u_3^2+u_4^2}}$. All elements of vector $\boldsymbol{Y}(t) = [y_1(t), y_2(t), y_3(t), y_4(t)]^\top$ can be written as $y_n(t) = \hat{u}_n e^{\lambda t} + \hat{u}_n^* e^{\lambda^* t}$ for $n = 1, ..., 4$. Here the superscript $*$ denotes the complex conjugate. Let $\lambda = \gamma + 2\pi i\nu$ and $\hat{u}_n = R_n + iI_n$, then $y_n(t)$ becomes

$$\begin{aligned}
y_n(t) &= (R_n + iI_n)e^{(\gamma+2\pi i\nu)t} + (R_n - iI_n)e^{(\gamma-2\pi i\nu)t}\\
&= 2e^{\gamma t}(R_n\cos(2\pi\nu t) - I_n\sin(2\pi\nu t)),
\end{aligned} \tag{4.13}$$

and for each root, the contribution of excitatory and inhibitory currents to power in a certain oscillation mode with root λ in population n can be defined by

$$w_n = \frac{\int_0^{2\pi} y_n^2(t)dt}{w_1 + w_2 + w_3 + w_4}. \tag{4.14}$$

Since characteristic roots are associated to certain frequency bands, w_n reflects the contribution of population n to the power spectrum in a certain frequency band. For instance, w_1 is the contribution of excitatory currents in cortical neurons, w_2 reflects the contribution of the excitatory currents in the relay neurons, w_3 the contribution of inhibitory currents in relay neurons and w_4 the contribution of excitatory currents in reticular neurons.

4.5.2 Frontal spectrum

Taking a closer look at the origin of the frontal EEG, Fig. 4.9**A** shows the spectral power of the system fluctuating about the upper resting state. It can be observed that under sedation (red line), the spectral power is well enhanced within the $\delta-$ and $\alpha-$band in comparison to the baseline condition (blue line). Moreover, the $\delta-$power peak emerges by increasing the concentration of propofol. Figure 4.9**B** and **C** give the relative contribution $\{w_n\}$ of the respective populations in the $\delta-$ and $\alpha-$frequency bands, respectively. They show that the mean postsynaptic potentials (PSPs) V_E^e, V_S^e and V_S^i contribute most to the $\delta-$activity while the excitatory PSPs involving in *ese* loop (i.e., V_E^e and V_S^e) generate the activity in $\alpha-$band.

To gain insight into the resting activity of the reduced model, we investigate the number of resting states of the system for possible combinations of different coupling connections. The

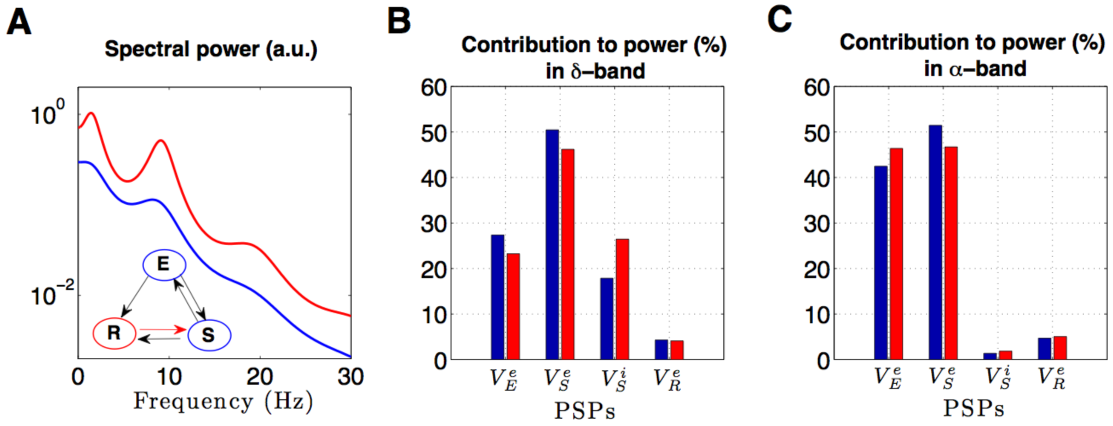

Fig. 4.9. The spectral power and the partial contributions in the brain areas describing activity in the frontal electrodes. (**A**) Power spectrum in the baseline ($p = 1$, blue) and sedation condition ($p = 1.3$, red). (**B**) Contributions w_n (cf. Eq. (4.14)) in $\delta-$band and (**C**) in the $\alpha-$band. The system fluctuates about the upper resting state of the system. Parameters are $\alpha_i = 200$, $\beta_i = 20$, and others are taken from set I in Table 4.1.

resting states of the reduced model obey

$$\begin{aligned} V_E^{*e} &= K_{ES} S_T[V_S^{*e} - V_S^{*i}], \\ V_S^{*e} &= K_{SE} S_C[V_E^{*e}] + I_0, \\ V_S^{*i} &= f_T(p) K_{SR} S_T[V_R^{*e}], \\ V_R^{*e} &= K_{RE} S_C[V_E^{*e}] + K_{RS} S_T[V_S^{*e} - V_S^{*i}]. \end{aligned} \tag{4.15}$$

By inserting these equations into each other

$$V_E^{*e} = K_{SE} S_T \left[K_{SE} S_C[V_E^{*e}] + I_0 - f_T(p) K_{SR} S_T[H[V_E^{*e}]] \right], \tag{4.16}$$

where $H[V_E^{*e}] \equiv K_{RE} S_C[V_E^{*e}] + \dfrac{K_{RS}}{K_{ES}} V_E^{*e}$. Thus the crossing points of V_E^{*e} and the right-hand side of Eq. (4.16), i.e.

$$Z[V_E^{*e}] \equiv K_{SE} S_T \left[K_{SE} S_C[V_E^{*e}] + I_0 - f_T(p) K_{SR} S_T[H[V_E^{*e}]] \right], \tag{4.17}$$

or equivalently, the solutions of equation

$$V_E^{*e} - Z[V_E^{*e}] = 0, \tag{4.18}$$

give the solutions V_E^{*e}. Since all the resting states $V_a^{*e,i}$ for $a \in \{E, R, S\}$ can be written as an implicit function of V_E^{*e}, the number of solutions of V_E^{*e}, i.e., the number of roots of Eq. (4.18), is identical to the number of resting states [186, 188, 33].

Figure 4.10 shows a graphical construction of Eq. (4.18) for various propofol concentrations. It can be seen that for $1 \leq p < 2.04$, there are three solutions, while for $p > 2.04$ there is a single one only. Moreover, increasing factor p from $p = 1$ yields a downshift in $V_E^{*e} - Z[V_E^{*e}]$ for large values of V_E^{*e} and thus the upper stable and unstable solutions approach each other, coalesce at the critical point $p = 2.04$, and finally disappear, whereas the lower stable solution remains more

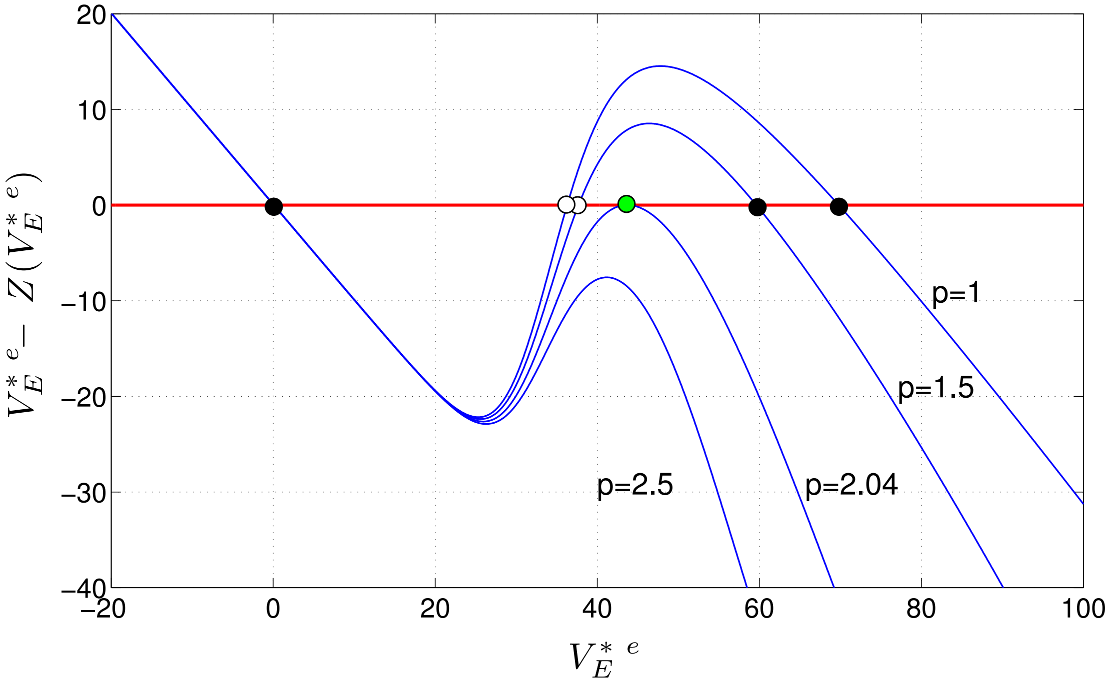

Figure 4.10. The number of system resting state. The blue curves represent the right-hand side of Eq. (4.18) subjected to various values of factor p. The intersection(s) of the blue curves and horizontal red line give the resting solution(s) V_E^{*e} correspond to the roots of Eq. (4.18). Filled and void circles denote stable and unstable solutions, respectively. At the critical value $p = 2.04$ there is a saddle node solution (green circle). Parameters are taken from set I in Table 4.1.

and less unaffected. This result show that for the constant external input I_0, the factor p plays as a control parameter that determines the number of system resting state.

Figure 4.11 represents the parameter space where the system exhibits single and triple resting solutions. It can be seen that the triple resting state occurs if the cortico-thalamic relay and relay-cortical connections are strong enough whereas the cortico-reticular and intra-thalamic connections are weak enough (cf. Fig. 4.11**H**,**I** and **J**). Moreover, cutting the connection between cortex and relay population leads to a single resting state independent of the other parameters.

4.5.3 Occipital spectrum

To investigate the occipital EEG in some more detail, we consider different topological configurations to study $\delta-$ and $\alpha-$activity. Figure 4.12 illustrates the power spectra and the relative contribution $\{w_n\}$, generated by different anatomical circuit configurations computed at the lower resting state of the system in the baseline and anesthetic conditions. At first, the plots reveal that the anesthetic state always exhibits a diminished $\alpha-$power compared to the baseline condition, when the thalamic inhibition is involved in the system.

Figure 4.12**A** (I) shows a system with the simplest topology including a reciprocal projection between cortical pyramidal neurons (E) and thalamo-cortical relay neurons (S) associated with a time delay (*ese* circuit). This cortico-thalamic relay loop generates $\alpha-$activity with a strong

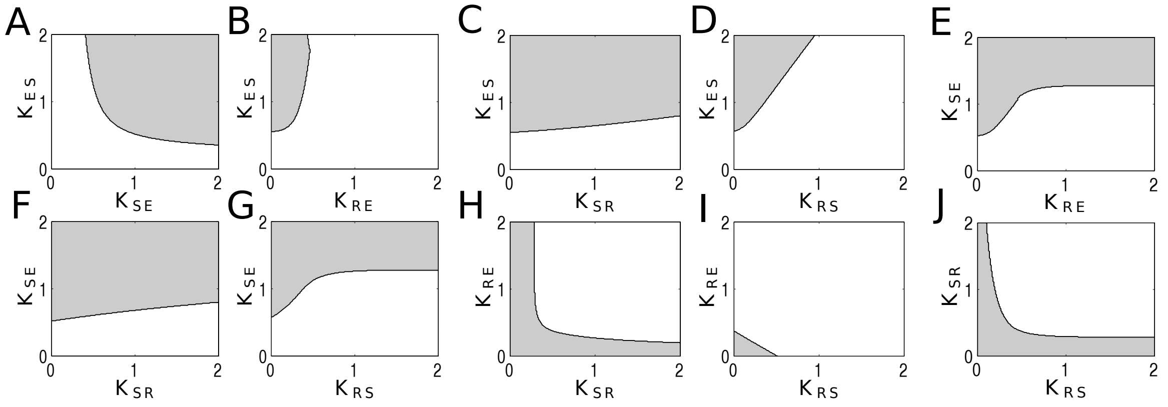

Fig. 4.11. Parameter space for different coupling connections. The shaded (unshaded) areas represent the parameter regions where the system exhibits triple (single) resting solutions. Parameters are taken from set I in Table 4.1.

power spectral peak at about 10 Hz, as illustrated in Fig. 4.12**B**. The circuit also generates activity in the $\delta-$band but no power spectral peak in this range. Figure 4.12**C** and **D** reveal that the spectral power is generated by the excitatory PSPs involving in this circuit, i.e., V_E^e and V_S^e. Since no inhibitory synapses are involved here, the resulting spectrum is independent of the anesthetic level.

Configurations (II) and (III) in Fig. 4.12**A** display the topology of the reduced model with the disrupted cortico-thalamic relay circuit. These configurations yield the loss of the prominent $\alpha-$peak that indicate the important role of *ese* loop in the generation of $\alpha-$activity. In configuration (II), we choose very small relay-cortical connection, because missing of this connection diminishes the power spectrum across the entire frequency bands (if $K_{ES} = 0$, then $P_E(\nu) = 0$). In configuration (III), removing the cortico-thalamic relay connection retains the *esre* and *srs* circuits in the system that yield a strong oscillation at about 3 Hz with the clear corresponding spectral peak. In addition, Fig. 4.12**C** and **D** show that the PSPs V_E^e, V_S^i and V_R^e involved in these circuits generate the activity in $\delta-$band.

Configuration (IV) demonstrates a system including the cortico-reticular, reticular-relay and relay-cortical connections (*esre* circuit). Similar to configuration (III), the resulting spectral power of this configuration exhibits a strong oscillation at about 3 Hz. Configurations (V) and (VI) illustrate the reduced model with a disrupted *esre* closed circuit. These configurations yield the loss of $\delta-$peak but a strong $\alpha-$power peak emerges, because the system comprises the *ese* circuit. This indicates the major contributions of *esre* and *srs* circuits to the generation of $\delta-$activity and the *ese* circuit to generation of $\alpha-$activity in the system.

To further reveal the role of *esre* and *srs* circuits in the generation of $\delta-$activity and the *ese* circuit in the generation of $\alpha-$activity, we investigate the effect of increasing connection strengths on the imaginary part (frequency) and real part (damping rate) of the characteristic root corresponding to the $\delta-$ and $\alpha-$activity, respectively. Figure 4.13 illustrates that the frequency and the damping rate of $\delta-$activity increase with increasing the cortico-reticular (K_{RE}), relay-cortical (K_{ES}) and intra-thalamic (K_{RS}, K_{SR}) connections indicating an increase of frequency and magnitude in the $\delta-$band. In a similar manner, Figure 4.14 shows that the frequency and the damping rate of $\alpha-$activity increase with increasing the cortico-thalamic relay (K_{SE}) and relay-cortical (K_{ES}) connections which demonstrate the increasing of frequency and mag-

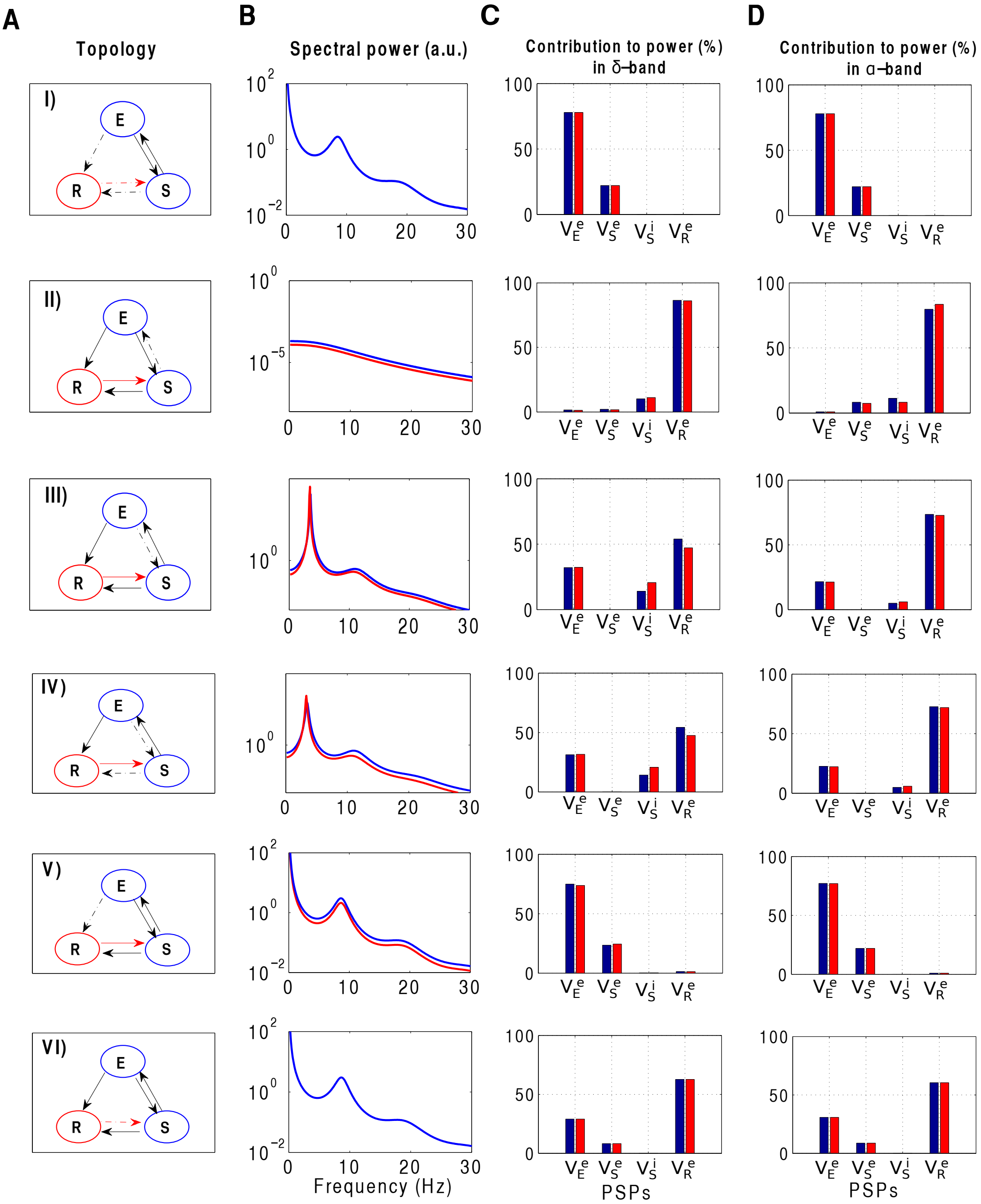

Fig. 4.12. Different topological configurations, their resulting spectral power and the contributions to power in the occipital electrodes. (**A**) Topology of the system. The solid and dashed arrows denote present and eliminated connections, respectively. (**B**) Spectral power in the baseline condition ($p = 1$, blue) and sedation condition ($p = 1.3$, red). (**C**) and (**D**) show contributions to power w_n (cf. Eq. (4.14)) in the $\delta-$band and $\alpha-$band, respectively. The systems fluctuate about the lower resting state of the system. Parameters are taken from set II in Table 4.1.

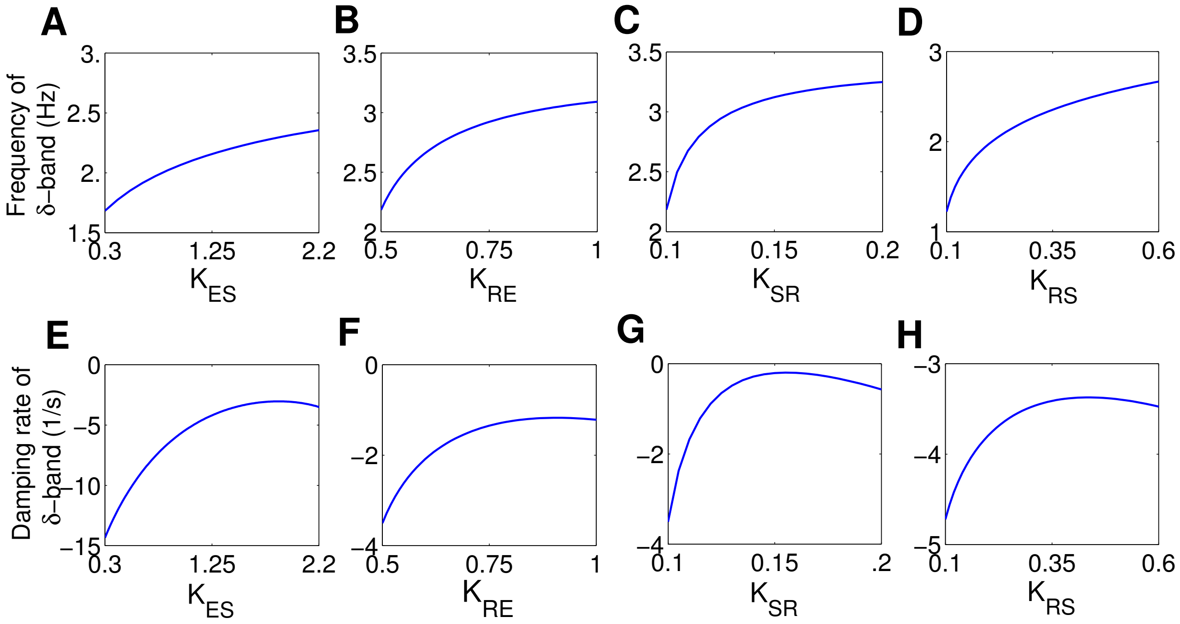

Fig. 4.13. Modulation of the frequency and the corresponding damping rate of $\delta-$activity by increase of coupling strengths in the *esre* and *srs* circuits. Parameters are taken from set II in Table 4.1.

nitude in the $\alpha-$band. An additional study (not shown) of the remaining connections, i.e., relay-cortical (K_{ES}) connection in the generating of $\delta-$activity and cortico-reticular (K_{RE}) and the intra-thalamic (K_{RS}, K_{SR}) connections in the generating of $\alpha-$activity, reveals a decreasing effect on the generation of $\delta-$ and $\alpha-$power, respectively. These results suggest the important role of *esre* and *srs* loops in the generation of $\delta-$activity and *ese* loop in the generation of $\alpha-$activity.

4.6 Discussion

4.6.1 Origin of spectral peaks

A large class of general anesthetics such as propofol act on inhibitory GABAergic synaptic receptors and hence enhance the inhibition in the neural populations. Accordingly one might expect that the stronger inhibition caused by propofol would reduce spectral power. The opposite is in fact the case; stronger inhibition induces a power surge in certain frequency bands. Figures 4.3 and 4.5 explain this power surge as an approach of the system dynamics to dynamical oscillatory instabilities. In the control condition the external random fluctuations from other cortical and non-cortical areas are well damped except for the $\alpha-$frequency band. The power surge of $\alpha-$activity indicates that the system is lying in the vicinity of an oscillatory instability point. The nonlinear instabilities analysis in large-scale neural activity have been demonstrated in [176] to explain the mechanisms underlying human generalized seizures. This explanation

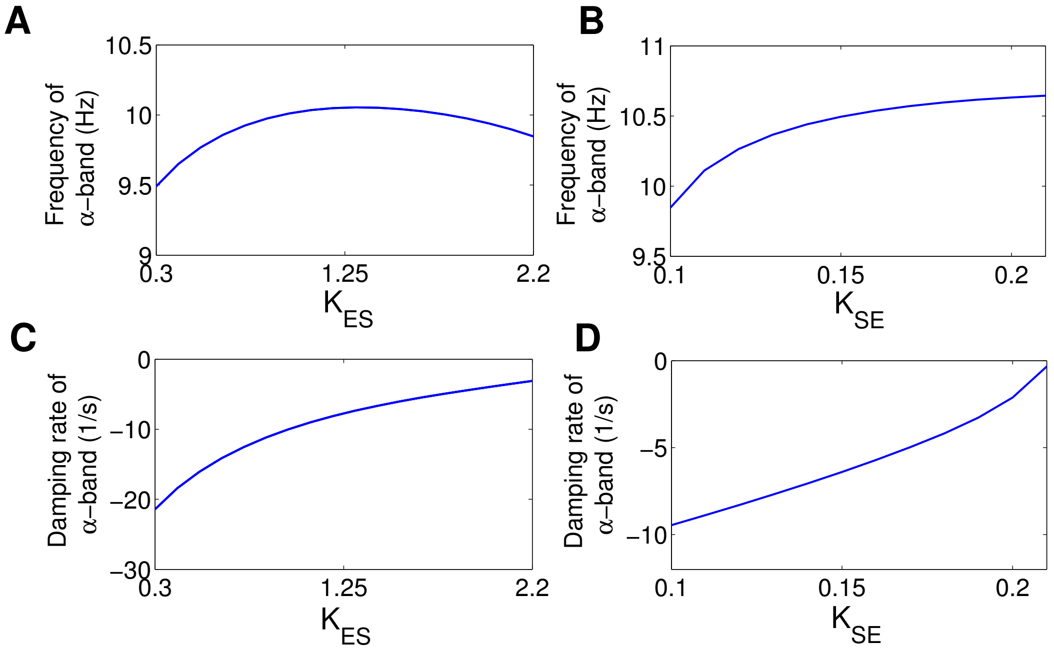

Fig. 4.14. Modulation of the frequency and corresponding damping rate of the $\alpha-$activity by increase of coupling strengths in the *ese* circuit. Parameters are taken from set II in Table 4.1.

is in line with other studies investigating the origin of $\alpha-$activity [29, 23, 91, 35, 111]. These models do not examine explicitly the effects of anesthetic-induced prolongation of the IPSP. In our study presented in this chapter, if the system is lying on the upper resting state, increasing the synaptic inhibition by increasing the anesthetic concentration moves the system closer to the instability point, decreasing the damping of external fluctuations, and hence leading to an increase of power as observed in Fig. 4.2 for frontal electrodes. In contrast, if the system is lying on the lower branch increased inhibition moves the system away from the oscillatory instability point and hence a resultant decrease in power as observed in occipital electrodes, cf. Fig. 4.4.

To explain the origin of the power surge in the $\delta-$frequency band, a slightly different mechanism comes into play since no spectral peak in the $\delta-$range is present in the control condition. Hence increased synaptic inhibition may not only move the system towards an already existing instability point, but actually also generates this instability point for increased inhibition. Figures 4.3 and 4.5 explain the origin of the power surge in the $\delta-$frequency band by the generation of an oscillatory instability at frequencies in the $\delta-$band. A more detailed analysis (cf. Fig. 4.9) reveals that the $\delta-$power surge is initiated at values $p > 1$, i.e., does not occur in the control condition ($p = 1$) but for increased anesthetic concentration only. Hence, the spectral power peak in the $\delta-$frequency band originates from the propofol-induced inhibition (c.f. Fig. 3.6).

Our model results both extend and contrast previous findings. To the best of our knowledge, the model is one of the first taking into account the explicit anesthetic action of propofol on thalamic GABAergic synaptic receptors. The model suggests an explanation for the observed changes in the EEG rhythms in the $\delta-$ and the $\alpha-$frequency bands and describes well the anteriorization of both the $\alpha-$ and $\delta-$rhythms, i.e., the distinct dynamics in both frontal and occipital cortical regions.

It seems likely that the observed characteristic changes in EEG rhythms are not just simply signatures of cortical inhibition. Our results show that the changes observed experimentally in EEG during sedation can be reproduced with and without inhibitory cortical neurons, cf. Fig 4.8. The neglect of cortical inhibition put emphasis on the effect of propofol on the inhibitory synaptic receptors in the thalamic cells as well as reducing the dimensionality of the model. By reducing the dimensionality of the mathematical model we are able to utilize their analytical tractability to obtain some inequality conditions for the stability of the resting states and even to gain further insights into the mechanisms responsible for the spectral features [111]. The application of analytical constraints on model parameters remains to be investigated in power spectral fitting methods, which it has the potential to improve previous work in fitting the model's predictions to experimental data [32, 34, 33]. This issue would be investigated in the following chapter.

Moreover, it is important to note that such a reduced model does not rule out other proposed models elucidating the mechanisms underlying the effects of anesthetic agents on brain dynamics. For instance, the findings in the previous chapter stressed the importance of cortical inhibitory neurons support the result obtained in this chapter; the increase of $\alpha-$power over frontal region can be caused by increase in the gain functions of thalamo-cortical network. Our results reveal that it is possible to replicate several observed EEG phenomena by modeling anesthetic action only in the thalamo-cortical loops. Several previous studies describing EEG spectra by a cortico-thalamic model consider both thalamic and cortical anesthetic action [81, 113, 35, 112] and point out the importance of cortical anesthetic action. Even purely cortical models [31, 215] may explain several spectral features observed in EEG under anesthesia. Most of the previous models are either rather complex with several tens of free parameters and hence many degrees of freedom permitting to fit the experimental data for a small subset of parameters [31, 215], or they identify specific single neuron mechanisms to be responsible for a certain anesthetic effect in macroscopic EEG, e.g., [81, 112, 113]. In contrast, our model is comparatively simple while proposing a major underlying mechanism: the activation of pre-defined oscillation modes whose amplitude and frequency depends on the level of synaptic inhibition.

The work presented in this study considers only light sedation, i.e., low propofol concentrations, far from those required for full surgical anesthesia. Some previous studies have investigated in detail the EEG power spectra at higher concentrations of propofol where additional characteristic features emerge, such as burst suppression [114], broad spatial EEG coherence [18, 19, 87, 82], strong spectral power in the $\beta-$band [113, 82], and functional fragmentation accompanied by a drop of population firing rate and increased spectral power at frequencies < 1 Hz [179]. For instance, Fig. 4.1C shows emerging $\beta-$activity well after light sedation that we consider in the present work. Our model does not explain these latter features, since they emerge for higher propofol concentrations and may result from fundamental changes in the interaction between neural structures, cf. [81] explaining the $\beta-$power surge by the interaction of two thalamo-cortical modules. To describe the features seen at high anesthetic concentration, it is necessary to incorporate more features of anesthetic actions on neural population than the effects considered in this study. Some of our preliminary simulations (not shown) demonstrate that, by assuming that anesthesia delays axonal transmission, the model used in this study is able to reproduce the $\beta-$power surge. However, this effect on the axonal transmission delay needs more experimental indication. Furthermore, recent studies have linked the low-frequency phase modulation of the $\alpha-$oscillation amplitudes to different states of unconsciousness [82, 322]. They have reported that two distinct patterns can be observed during propofol anesthesia. First, the trough-max pattern which appears at the transition into and out of unconsciousness. Second, the peak-max pattern which appears at profound unconsciousness. While these patterns can be used to track the states of unconsciousness, however, the mechanisms underlying these patterns remain to be understood. Such phase-amplitude modulation patterns are not visible in power spectral analysis and we postpone their discussion to later work since the corresponding discussion would exceed the major aim of the present work.

Our model describes very well the action of propofol on neural populations in the cortex and thalamus while the fundamental interactions of cortex, thalamus and other sub-cortical structures such as the brainstem and hippocampus are retained. In contrast, larger anesthetic concentrations may affect not only the activity in single populations but also the interaction between a larger set of neural structures. This effect on the inter-area interactions has been been quantified in several previous experimental studies and has been termed fragmentation or connectivity break-down [179, 83, 323].

4.6.2 Multiple resting states

Experimental EEG under propofol anesthesia shows an anteriorization in the $\delta-$ and $\alpha-$frequency bands, cf. Fig. 4.1 and [82, 18, 179]. The recent study of Vijayan *et al.* [112] is one of the first to explain the distinct evolution of spectral power. They suggest two distinct models for the anteriorization during propofol anesthesia: one for the frontal and one for the occipital EEG $\alpha-$activity; where the occipital cortico-thalamic connection exhibits an additional hyperpolarizing mechanism lowering the resting state population firing rate. Their model is based on simulations of small numbers of neurons, each with multiple specialized ion channels. The anteriorization is largely driven by a specialized subset of thalamic relay neurons that project only to the occipital cortex. The oscillatory activity of these neurons secondarily induce high- and low-activity resting states. In our study presented in this chapter, different systems with distinct parameter sets explain the spectral power of EEG associated with frontal and occipital head regions. In addition, our model extends the explanation of Vijayan *et al.* [112] by providing a more generic dynamical systems explanation for both the $\delta-$ and the $\alpha-$frequency bands, and emphasizes the importance of nonlinear gain functions in the corresponding resting states, rather than molecular scale ion channel activity. Our mathematical analysis of the power spectrum reveals that these gain functions are dependent on the resting potential values. Increasing nonlinear cortical gain functions induce a power surge in the $\alpha-$range, whereas decreasing nonlinear cortical gain functions diminish the $\alpha-$power. This is in line with the cortical activation hypothesis, which states that an increase or decrease in the firing rates of cortical pyramidal neurons leads to an increase or decrease in $\alpha-$activity, respectively [227, 32]. Since increases in the nonlinear gains occur at high activity-resting states only, while decreasing nonlinear gains are present in low activity-resting states (Fig. 4.6), our findings suggest the important role of multiple resting states at high and low population firing rates and affirms previous EEG modeling studies [40, 229, 91] pointing out the importance of multiple resting states to explain unstimulated EEG. This is affirmed by Fig. 4.11 illustrating that cutting the connections between cortex and relay population leads the loss of multiple states and consequently the destruction of realistic frontal population activity. In contrast, the evolution of the $\delta-$power is rather independent of the resting state, and increases for increasing propofol concentrations for both increasing and decreasing nonlinear gains. This strongly suggests that the $\alpha-$rhythm is fundamentally different from the $\delta-$rhythm.

4.6.3 Effective sub-circuits in the cortico-thalamic model

As argued before, the origin of the $\delta-$rhythm appears to be fundamentally different to the origin of $\alpha-$rhythm. A detailed analysis of the spectral contributions of the populations to $\delta-$ and $\alpha-$power, cf. Figs. 4.9 and 4.12, reveals that strong $\delta-$power occurs primarily when there is a strong connection between thalamic areas (*srs* loop) and from cortex to the reticular nucleus, reticular to relay nucleus and relay to cortex (*esre* loop), while strong $\alpha-$power is generated primarily by the cortico-thalamic relay circuit (*ese* loop). These results are based on an investigation of small deviations from the resting states in light sedation and are not directly related to nonlinear signal features observed in deeper anesthesia states, such as spindles.

Having identified these sub-circuits, their subsequent detailed analysis reveals that the frontal enhancement and occipital attenuation of $\alpha-$activity originates primarily from a (frontal) increase and (occipital) decrease in the nonlinear gain functions within the thalamo-cortical *ese* loop. In turn, this result supports the presence of multiple resting states derived in the earlier part of our analysis. Hence, we suggest that the phenomenon of anteriorization of $\alpha-$power results from fronto-occipital differences in the nonlinear gain functions in the cortico-thalamic relay circuit. The previous study of Vijayan *et al.* [112] on the anteriorization of $\alpha-$activity supports a similar idea. These results are also in agreement with the recent findings of Hindriks & van Putten [227]. They show that changes of transfer function properties and synaptic parameters, directly or indirectly, lead to changes in the gain functions by altering the values of the resting states of the system that cause the $\alpha-$response modulations. Their results affirm our hypothesis that the increase or decrease of $\alpha-$power spectrum depends profoundly on the the resting state values of the system and the corresponding nonlinear gain functions. This finding is well in line with previous modeling studies on the origin of occipital $\alpha-$activity in the absence of anesthesia explaining the amplitude modification by modified nonlinear gain changes.

The changes in the $\delta-$frequency band are explained by increases in the charge transfer within the inhibitory synapses what results to an increase of the frequency response function within the loops involving inhibitory neurons (such as *srs* and *esre* loops), which essentially enhances the $\delta-$power. This hypothesis on the interplay of nonlinear gain and synaptic inhibition has been briefly mentioned in a previous work Hutt [111].

In the present chapter, our analysis aimed to extract general interaction mechanism for the generation of spectral EEG characteristics. To this end, we employed a reductionist approach: starting from a complex model and reducing it step by step to find a neurophysiologically reasonable minimal model that explains as much experimental features as possible. The approach is motivated by the insight that general anesthesia is a macroscopic global and fundamental effect that occurs in all species of animals, even though they exhibit different detailed neural structures. Consequently, the underlying mechanism should be rather unspecific in biological detail but rather general in concept. We have identified elements of principal underlying mechanisms to explain $\delta-$ and $\alpha-$power observed during propofol anesthesia sedation in adult humans, namely the nonlinear population gain, the level of synaptic inhibition and the interaction of neural sub-circuits (or microcircuits). It appears that one of the most important properties of the sub-circuits is their ability to generate an oscillation. Since these elements promise to reflect underlying principles, they are rather independent of the choice of the anesthetic agent and may generalize to the larger class of anesthetic GABAergic [324], or volatile drugs [313].

Several previous modeling studies have explained the $\alpha-$rhythm by the delayed thalamo-cortical feedback [29, 23, 173, 204, 227], or by a cortical model, cf. [325, 326, 111]. At first glance these two explanations appear exclusive. However the underlying principle put forward in the present chapter is not contradictory to cortical and thalamo-cortical circuits since both represent oscillating sub-circuits. Previous cortical models have included feedback loops of excitatory and inhibitory populations and most thalamo-cortical feedback models oscillate due to delay, which is known to facilitate oscillations [30, 32]. Consequently, the $\alpha-$rhythm may originates from a general class of oscillating circuits. This interpretation is supported by the experimental findings that the brain is highly adaptive and brain areas may take over tasks of other areas as seen under general anesthesia [327], in sleep [328], or after brain injury [329].

Similarly, various sources and mechanisms have been proposed for EEG $\delta-$activity. Previous experimental studies suggest a cortical origin of $\delta-$waves under anesthesia [19] and point out the importance of the cortico-thalamic feedback in the generation of $\delta-$waves in anesthesia [83] and sleep [230, 330], while $\delta-$activity during sleep may also results from a connected network of thalamus, brainstem and different cortical areas [331]. In the present chapter, our model results point out the importance of the intra-thalamic feedback of reticular and relay populations as part of the thalamo-cortical feedback loop, which is in full line with the previous literature.

4.6.4 Model limitations

Our model concentrates on the effects of low concentrations of propofol, whereas higher anesthetic concentrations lead to additional spectral EEG features not captured by the current model, such as an increase in $\beta-$power just before loss of consciousness [82], or burst suppression patterns after loss of consciousness [114, 266]. To consider these effects, a future model will incorporate additional thalamo-cortical modules and nonlinear dynamics in thalamic populations. In addition, the model fitting with experimental data will reveal the optimal topology model that is able to reproduce the observed specific features in experimental data [332].

4.7 Conclusion

We would conclude that - using a model of cortico-thalamic loops - it is possible to replicate the different frontal and occipital changes in the $\alpha-$ and $\delta-$rhythms in the EEG, caused by modest concentrations of propofol. The $\alpha-$rhythm is primarily dependent on the cortico-thalamic relay interactions; dependent on the mean potential values of the resting states of the system, an increase or decrease in the gain functions within the thalamo-cortical circuits results in an increase or decrease in the spectral power in the $\alpha-$band, whereas the increased propofol inhibition acting via the thalamo-cortical loops is necessary for the increase in $\delta-$waves. This model also offers a plausible explanation of the eyes-closed occipital alpha rhythm.

5

Spectral power fitting using stochastic optimization algorithms

Contents

Abstract

Mathematical modeling is a powerful tool which enables researchers to describe the dynamics of complex systems. Starting with a robust model, since the model output depends on the model parameters, reproducing the experimental measurements requires selecting a good set of unknown parameters. However, inverse problem i.e., finding a set of model parameters that yields the best possible fits to the recording data is a very challenging problem. It has been extensively demonstrated that minimizing the error between the model prediction and the measured data as a nonlinear optimization problem has solved most of the parameter estimation problems. In this chapter, we apply different optimization algorithms namely Levenberg-Marquardt (LM), Particle Swarm Optimization (PSO), Differential Evolution (DE), Metropolis-Hastings (MH) and Simulated Annealing (SA) algorithms to solve the considered inverse problems. To evaluate the performance of these algorithms, two case studies are investigated: a stochastic damped harmonic oscillator, and a stochastic linear delay differential equation, which pose an unimodal and a multimodal optimization problem, respectively. Our results show that although in the case of unimodal problem, the LM algorithm converges to the minimum faster than the other algorithms, it fails to arrive at the global minimum when the case study poses a multimodal fitness function. In contrast, PSO and DE algorithms are computationally expensive due to the high number of function evaluations, however, they significantly outperform the other algorithms in finding the global solution. In third case study, a thalamo-cortical model is fitted to the power spectra of measured EEG data. We show that the proposed model fits very well to the EEG power spectra, particularly to the spectral peaks observed in delta and alpha frequency ranges. Moreover, for each case study we investigate the practical identifiability of the model parameters by plotting the confidence regions of the estimates and analyzing the correlation and sensitivity matrices.

In sum, using the framework presented in this study, given a set of coupled ordinary or delay differential equations subjected to additive noise, we are able to accurately estimate the independent model parameters while avoiding the computational costs due to numerical integration of the model equations.

5.1 Parameter estimation (inverse problem)

Although mathematical modeling plays a key role in describing the dynamics of complex systems, it still remains a challenging problem [49, 50, 51, 52]. In order to build a successful model formulation which allows us to reveal the mechanisms underlying a complex system, first we need to select a robust model whose output is consistent with our *a priori* available knowledge about the system dynamics [53, 54, 55]. The selected model should be able to reproduce, at least qualitatively, the most important features of the experimental observations. This task is referred to as *structure identification* [56, 57]. The subsequent task is *parameter estimation* [58, 59]. After the model identification, one needs to determine the unknown model parameters. Since the output of a model strongly depends on the values of its parameters, reproducing specific features of the experimental measurements requires selecting a suitable set of the unknown parameters. Therefore, parameter estimation is a very important component of the model developing procedure. Broadly speaking, given a set of experimental data and a particular mathematical model, the aim of parameter estimation (also known as inverse problem or model calibration) is to identify the unknown model parameters from the measurements for which substituting the estimated parameters in the model equations reproduces the experimental data in the best possible way [54]. Nevertheless, finding a set of model parameters which accurately fits the recorded data is an extremely difficult task, especially for nonlinear dynamic models with many parameters and constraints. Numerical integration of differential equations and finding the best solution in the entire of search domain (global minimum) are two major challenges in the parameter estimation problems [60].

In the past few years, considerable attention has been paid to optimization algorithms. Consequently, numerous optimization algorithms have been applied successfully in a wide range of scientific areas with different applications . It has been extensively demonstrated that minimizing a fitness function defined by the discrepancy between the model output and the measured data is able to solve most of the parameter estimation problems [333, 334, 335].

It is important to point out that there are various optimization algorithms for solving nonlinear optimization problems subject to nonlinear constraints, and no single method is the best for all problems or even for a broad class of problems [63]. The choice of optimization technique usually depends on the linearity or nonlinearity of the model and its constraints, the problem dimension, as well as the our a priori knowledge about the system. One must note that the most important criterion for choosing a proper search algorithm is the landscape of the fitness function, in which it poses a unimodal or multimodal optimization problem. In general, optimization algorithms can be divided into local and global search algorithms [336]. The search algorithms which do not get stuck in local minima are necessary to be exploited especially to solve parameter estimation problems in systems biology, because in this context multimodal (non-convex) optimization problems are more pervasive than unimodal problems [335, 337]. It has been extensively reported that for solving the inverse problems in biological systems, evolutionary algorithms (stochastic global search method) outperform the local search methods [61, 62, 54, 338]. In the present study, in order to solve the the considered estimation problems, we employ different optimization algorithms, namely Levenberg-Marquardt (LM) algorithm as a gradient descent local search method, Particle Swarm Optimization (PSO) and Differential Evolution (DE) algorithms as the stochastic global search methods, and Metropolis-Hastings (MH) and Simulated Annealing (SA) as the popular sampling methods belong to Monte Carlo Markov Chain (MCMC) algorithms, which are widely used in the Bayesian inference. Moreover, their performance is compared to determine which algorithm is more suitable for each of the parameter estimation problem considered in this study.

It is well known that the dynamics of a majority of biological systems can be described by a set of coupled Ordinary Differential Equations (ODEs), Partial Differential Equations (PDEs), or Delay Differential Equations (DDEs) [63]. Moreover, biological systems are often subject to external noise from signal stimuli and environmental perturbations. Thereby, in this chapter we focus on the parameter estimation of systems whose dynamics are governed by stochastic ODEs or DDEs rather than deterministic differential equations or explicit algebraic functions. More precisely, the parameter estimation problem in three case studies are investigated. As *in silico* parameter estimation problem, we estimate the parameters of a damped harmonic oscillator and those of a linear scalar delay differential equation, in the presence of additive noise, by fitting the model equations to a set of pseudo-experimental data. The first and second case studies pose an unimodal and a multimodal optimization problem, respectively. We show that in the unimodal case study, the LM method as a local search algorithm exhibits fast convergence to the only minimum of problem, whereas in the multimodal case study it easily gets stuck at a local minimum and thus is not able to find the global solution. In order to find the global minimum using LM algorithm, the algorithm has to be started with an initial guess in the vicinity of the solution. In contrast, PSO and DE algorithms usually require a high number of fitness function evaluations, which results in larger computational costs compared to local search algorithms. However, they significantly outperform the local search algorithms in converging to the global solution. In addition, the PSO algorithm has the advantage of being able to use the evaluated fitness functions to construct the confidence regions for the estimated parameters. In third case study, as *in vivo* parameter estimation problem, a thalamo-cortical model is fitted to the recorded EEG data in awake and anesthesia conditions. It is shown that the proposed model is able to fit very well to the spectral power peaks observed in the delta and alpha frequency ranges, whereas the more complex models with additional parameters do not exhibit satisfactory results.

After the parameter estimation, another challenge is the *identifiability* of the estimates [59, 64]. The identifiability analysis investigates whether the model parameters can be uniquely determined by the given experimental data [55]. For each carried out case study, we employ different methods to address this issue. The confidence regions of the estimates are plotted and the correlation and sensitivity matrices are analyzed to assess the accuracy of the estimates in each case study.

We also note that numerical integration of differential equations is a major time consuming problem for the parameter estimation of nonlinear dynamic systems [339]. In this chapter we aim to present a general framework for estimating the parameters of systems described by a set of stochastic ODEs or DDEs through fitting the model's spectrum to the measured data. In the proposed scheme, the power spectrum of the model equations is computed with the aid of Green's function method, which provides a great advantage in terms of optimization speed, because it allows us to avoid the numerical integration of model equations.

5.2 Optimization problem

5.2.1 Formulating an optimization problem

Many real-world processes in several scientific areas such as physics, chemistry, biology, bioinformatics, computer science, economics, and engineering involve optimization problems. Solutions of these problems are not account as correct or incorrect, but instead are rated in terms of quality. In general, the aim of solving an optimization problem is to find the best solution which maximizes or minimizes a real function referred to as fitness or objective function (also known as cost function), while satisfying some constraints. The optimal solution must be chosen from a set of candidate solutions known as the search space. In maximization, we search for a solution which has a greater or equal value of the objective function than any other solution, whereas in minimization we investigate the opposite: a solution which has a fitness function value smaller or equal than all the others. Therefore maximization of function f is equivalent to minimization of $-f$. Although both maximization and minimization occur in optimization problems, we can easily convert a maximization problem into a minimization problem, and vice versa. In this work, we choose to solve minimization problems.

An optimization problem subject to algebraic constraints and upper and lower bounds for the variables can be mathematically expressed as follows:

$$\begin{aligned}
&Given \quad f(\vec{x}) : \mathcal{S} \subseteq \mathbb{R}^N \to \mathbb{R} \\
&find \ \ \vec{x^*} \in \mathcal{S} : f(\vec{x^*}) \leq f(\vec{x}) \ \ (\forall \vec{x} \in \mathcal{S}) \\
&Subject\ to: \\
&h_i(\vec{x}) = 0 \qquad\quad i = 1, 2, ..., m \\
&g_i(\vec{x}) \leq 0 \qquad\quad i = 1, 2, ..., q \\
&\vec{x}_{lb} \leq \vec{x} \leq \vec{x}_{ub}
\end{aligned}$$

where $f(\vec{x})$ known as as objective function (fitness function or cost function) is the function being optimized, and $\vec{x}$ denotes a candidate solution. The candidate solutions can be described as a vector of N independent variables; $\vec{x} = [x_1, x_2, ..., x_N]^\top \in \mathcal{S} \subseteq \mathbb{R}^N$. The constraints represented by $h_i(\vec{x}) = 0$ are called equality constraints, and those represented by $g_i(\vec{x}) \leq 0$ are called inequality constraints. The equality and inequality constraints could be linear or nonlinear. The $\vec{x}_{lb}$ and $\vec{x}_{ub}$ indicate the lower and upper bounds to the candidate solutions, respectively. The domain $\mathcal{S} \subseteq \mathbb{R}^N$ is called the search space (or parameter space) which composes all the possible solutions known as a position, agent or particle. The parameter N is the dimensions of the search space, i.e. the number of variables or parameters involved in optimization problem. The output of the fitness function at each solution is a single scalar value which determines the goodness of that solution. A local minimum is a candidate solution which has a smaller value of the objective function than any other candidate solution in a particular region of the search space. The minimum $\vec{x^*} \in \mathbb{R}^N$ which has the smallest value of the objective function in the entire search space is called the global minimum. Mathematically, $\vec{x^*} \in \mathcal{S}$ is called a global minimum for the function f if

$$\forall \vec{x} \in \mathcal{S} : \quad f(\vec{x}^*) \leq f(\vec{x}). \tag{5.1}$$

5.2.2 Objective function

The most widely used criteria to evaluate the goodness of a model fit are the maximum likelihood estimation (MLE) and the least-squares estimation (LSE) [340, 334]. In MLE which was originally introduced by R.A. Fisher in 1912 [341], we search to obtain the parameter probability distributions that produce the observed data most likely [342]. In other words, the MLE assesses the quality of estimated parameters by maximizing the likelihood function (or equivalently the log-likelihood function which is easier to work mathematically). The likelihood function is the probability of obtaining the set of observed data, with a given set of parameter values. The set of values of the parameters which maximize the likelihood function is called the maximum likelihood estimator. Using LSE, we seek for a set of parameter values that provides the most closest model fit to the experimental data by minimizing the (weighted) sum of squared error (SSE) between the measured and the simulated data [343, 344]. Both approaches have been applied successfully in a wide variety of optimization problems while they have their advantages in the proper situations. The MLE method used in Bayesian paradigm is able to handle the noise in the system as well as the uncertainty in parameters, since it treats the parameters as random variables with a prior distribution [345]. Moreover, the MLE gives the whole probability distribution of the parameters rather than a single optimal values in LSE approach. However, the former method is more complex and more expensive in terms of computational cost than the latter method [56]. Especially, the MLE method used in the frequentist (classical) framework is more simpler, and is more suitable for high-dimensional models i.e., models with a large numbers of parameters [57]. Interestingly, if we assume that the experimental errors are independent and normally distributed (the measurement noise is uncorrelated with Gaussian distribution), the MLE is equivalent to LSE [346, 343]:

$$\underset{\boldsymbol{p}}{argmax}\ \Big\{\mathcal{P}(\boldsymbol{p})\Big\} = \underset{\boldsymbol{p}}{argmin}\ \Big\{\mathcal{E}(\boldsymbol{p})\Big\}, \tag{5.2}$$

where

$$\begin{aligned} \mathcal{P}(\boldsymbol{p})) &= ln\left(\prod_{i=1}^{N_y}\left(\frac{1}{2\pi\sigma_i^2}\right)^{\frac{1}{2}}\right) - \frac{1}{2}\left(\sum_{i=1}^{N}\left[\frac{\Big(Y_i(X_{data}) - \hat{Y}_i(X_{data},\boldsymbol{p})\Big)^2}{\sigma_i^2}\right]\right), & (5.3)\\ \mathcal{E}(\boldsymbol{p}) &= \sum_{i=1}^{N_y}\left[\frac{\Big(Y_i(X_{data}) - \hat{Y}_i(X_{data},\boldsymbol{p})\Big)^2}{\sigma_i^2}\right], & (5.4) \end{aligned}$$

where $\mathcal{E}(\boldsymbol{p})$ is the weighted least-squares cost function, $Y_i(X_{data})$ denotes the measured data in the i-th data point , $\hat{Y}_i(X_{data},\boldsymbol{p})$ represents the corresponding model prediction, $\boldsymbol{p}$ the parameter vector being estimated, σ_i are the measurement errors (the variance of the experimental fluctuations), and N_y is the number of sampling points of the observed data. If we assume that all variances σ_i^2 are equal, the Eq. (5.7) simplifies to the well-known chi-squared error criterion [347]

$$\chi^2 = \sum_{i=1}^{N_y}\Big(Y_i(X_{data}) - \hat{Y}_i(X_{data},\boldsymbol{p})\Big)^2. \tag{5.5}$$

In the results section, it is shown that if with the aid of standard chi-squared error criterion we were not able to fit a model to the spectral power peaks in certain frequency bands, we employ a modified chi-squared error criterion referred to as the biased weighting chi-squared function given by

$$\begin{aligned} \chi^2 = c_1\sum_{i=1}^{N_1}\Big(Y_i(X_{data}) - \hat{Y}_i(X_{data},\boldsymbol{p})\Big)^2 + c_2\sum_{i=N_1}^{N_2}\Big(Y_i(X_{data}) - \hat{Y}_i(X_{data},\boldsymbol{p})\Big)^2 + \\ c_3\sum_{i=N_2}^{N_3}\Big(Y_i(X_{data}) - \hat{Y}_i(X_{data},\boldsymbol{p})\Big)^2 + c_4\sum_{i=N_3}^{N_y}\Big(Y_i(X_{data}) - \hat{Y}_i(X_{data},\boldsymbol{p})\Big)^2, \end{aligned} \tag{5.6}$$

where c_1, c_2 c_3 and c_4 are manually chosen constants depending on the observed spectral peaks in each estimation problem. The constants N_1, N_2, and N_3 can be chosen in such a way that the intervals $[1, N_1]$, $[N_1, N_2]$, $[N_2, N_3]$ and $[N_3, N_y]$ contains the delta, theta, alpha and beta frequency bands, respectively. Then, a large values of c_i for $i = 1, 2, 3, 4$ forces the model output to be fitted with the observed spectral peaks within corresponding frequency ranges. It is trivial that $c_1 = c_2 = c_3 = 1$ yields the well-known chi-squared error criterion given by Eq. (5.5). To fit the model's power spectrum to the empirical data, we can take the logarithm of spectral power as $Y(X_{data})$, where X_{data} represents the frequency f in Hz, i.e., $\hat{Y}_i(X_{data}, \boldsymbol{p}) = log(\text{Power}_{model}(f_i, \boldsymbol{p}))$, where $\boldsymbol{p}$ contains all the unknown parameters to be estimated.

5.2.3 Types of optimization methods

Optimization methods can be broadly divided into two major groups known as local optimization methods and global optimization methods. Local optimization methods can be further subdivided into two categories. First, gradient based methods like Levenberg-Marquardt and Gauss-Newton algorithms, which involve the use of derivative information and thus cannot be applied to non-smooth problems. Second, direct search methods such as Needler-Mead simplex, Hooke-Jeeves and Downhill simplex algorithm, which involve the use of function evaluations only and do not need the derivative information. Local optimization methods are initialized with a predefined guess for the parameter values and in order to obtain satisfactory results one has to manually tune the initial parameters. These algorithms easily get trapped at a local minimum if they are not initialized close to the global minimum. Several studies have been reported that although the local search algorithms converge very rapidly on a solution, they fail to arrive at the global minimum when the objective function has several minima [61, 63, 54, 348]. To overcome such drawbacks, global optimization methods have been widely used for the solving of nonlinear optimization problems [64, 338, 57]. Global optimization methods need neither an initial guess for the parameters nor the gradient of the objective function. In general, these methods can be mainly classified as deterministic [349, 350], and stochastic approaches [351, 352, 353]. In contrast to deterministic methods which rely on the analytical properties of the problem, stochastic methods rest on probabilistic assumptions [354, 355]. Although stochastic methods can not guarantee the convergence to a global optimum, they particularly adapt better to black-box optimization problems (problems that pose no known structure as *a priori*) and the extremely ill-behaved functions since they do not calculate derivatives of the objective functions [356, 357, 358]. Stochastic methods are also usually faster and more efficient in locating a global minimum than deterministic methods [359, 360].

There are several kinds of stochastic global optimization methods, which are mostly based on biological or physical phenomena [361, 362]: Adaptive stochastic methods [363, 364, 365], Clustering methods [366, 367], Taboo Search, and Evolutionary algorithms (including Genetic algorithm, Evolutionary Programming, Evolution Strategies and swarm-based algorithms). Evolutionary algorithms (EAs) are stochastic search methods which incorporate a random search principle existing in natural systems including biological evolution (such as mating and mutation) and social swarming behavior of living organisms (such as birds flocking or fish schooling). Since EAs require many more fitness function evaluations, the high computational costs due to the function evaluations will in general lead to a slower convergence to the global solution. However, one can use parallelized algorithms to reduce the computational cost of the implementations while still finds a better solutions via EAs rather than using local search algorithms. Furthermore, their performance is independent of initial guesses for the model parameters. A large number of studies have been applied successfully different paradigms of EAs to solve inverse problems in various types of biological systems and their robustness have been reported extensively [368, 369, 370, 61, 63, 54, 371, 336]. In addition to the general advantages mentioned above, DE and PSO show better performance, faster convergence speed, and lower computational cost than other EAs [372, 373, 374]. In the following section the details of these methods are described, and we will see that they are simple to implement and have a few of parameters which require tuning. To sum up, although the EAs do not provide a guarantee for finding the global minimum, their robustness make them the best candidates for solving inverse problems in particular for multimodal (non-convex) problems.

5.3 Optimization algorithms

In this section, we briefly review the optimization algorithms employed in this work and then explore their performance by estimating the model parameters of the two case studies presented in section 5.5. First, we present a popular deterministic local optimization method known as Levenberg-Marquardt (LM) algorithm, which is a gradient-based method. In the results section, we show that the goodness of solutions obtained by this algorithm heavily depends on the initial conditions. Then, we present two robust global optimization methods known as Particle Swarm Optimization (PSO) and Differential Evolution (DE) algorithms which both are stochastic and derivative-free search methods. Finally, we explain two widely used Monte Carlo Markov Chain (MCMC) methods known as Metropolis-Hastings (MH) and Simulated Annealing (SA). For the two case studies (one unimodal and one multimodal optimization problem), we will compare performance of the mentioned algorithms. The outperformed algorithm is employed in parameter estimation of a thalamo-cortical model through the model's fitting to the EEG spectral power during awake and anesthesia conditions.

5.3.1 Levenberg-Marquardt algorithm (LM)

The Levenberg-Marquardt (LM) algorithm is a robust curve-fitting algorithm which is a combination of Gauss-Newton algorithm and gradient descent method (also known as steepest descent method). In the gradient descent method, the least squares function is minimized by updating the parameter values in the direction of the greatest decrease in error function i.e., the direction opposite to the gradient of fitness function. This algorithm exhibits a slow, but guaranteed convergence to a local minimum. In the Gauss Newton method, it is assumed that the least squares function is locally quadratic around the minimum. This method is very fast near a local minimum, however there is no guarantee of convergence to a minimum when the parameters are far from the solution. The LM algorithm incorporates the fast convergence of Gauss Newton algorithm and the stability of gradient descent algorithm. This method is simpler than Gauss Newton method since the Hessian does not need to be evaluated exactly, while it converges to the minimum faster than the gradient descent algorithm. When the current parameter values are far from a minimum, the LM algorithm behaves as gradient-descent method, thus converges to a local minimum. In contrast, when the parameters are close to a minimum, the LM algorithm acts like Gauss-Newton method, thus exhibits fast convergence to the solution.

Consider the sum of squared errors between the data points and the model prediction, referred to as the least squares function:

$$\begin{aligned} \mathcal{E}(\boldsymbol{p}) &= \sum_{i=1}^{N_y} \left[\frac{\Big(Y_i(X_{data}) - \hat{Y}_i(X_{data}, \boldsymbol{p})\Big)^2}{\sigma_i^2} \right], & (5.7) \\ &= \boldsymbol{r}^\top \boldsymbol{W} \boldsymbol{r}, & (5.8) \end{aligned}$$

with the residual vector defined by $\boldsymbol{r} = \sum_{i=1}^{N_y} \Big(Y_i(X_{data}) - \hat{Y}_i(X_{data}, \boldsymbol{p})\Big)^2$, where $Y_i(X_{data})$ indicates the measured data in the i-th data point from N_y sampling points, $\hat{Y}_i(X_{data}, \boldsymbol{p})$ represents the corresponding model prediction with model parameters $\boldsymbol{p}$, and $\boldsymbol{W}$ is a diagonal matrix with the elments of $W_{ii} = 1/\sigma_i^2$, where σ_i is uncertainty in the measurement.

In order to minimize the least squares function $\mathcal{E}(\boldsymbol{p})$, at each iteration step, the parameter vector $\boldsymbol{p}$ is updated to $\boldsymbol{p} + \boldsymbol{\delta}$, while $\boldsymbol{\delta}$ can be determined by linearizing the differentiable function

$\hat{Y}(X_{data}, \boldsymbol{p})$:

$$\hat{Y}(X_{data}, \boldsymbol{p} + \boldsymbol{\delta}) \approx \hat{Y}(X_{data}, \boldsymbol{p}) + J\boldsymbol{\delta}, \tag{5.9}$$

where $J(\boldsymbol{p}) = \dfrac{\partial \hat{Y}(X_{data}, \boldsymbol{p})}{\partial \boldsymbol{p}} |_{\boldsymbol{p}}$ is an $N_y \times N_p$ Jacobian matrix evaluated at $\boldsymbol{p}$. Substituting this approximation in the least squares function given by Eq. (5.7) yields:

$$\mathcal{E}(\boldsymbol{p} + \boldsymbol{\delta}) \approx (\boldsymbol{r} - J\boldsymbol{\delta})^{\top} \boldsymbol{W} (\boldsymbol{r} - J\boldsymbol{\delta}) . \tag{5.10}$$

Taking the derivative of $\mathcal{E}(\boldsymbol{p} + \boldsymbol{\delta})$ with respect to $\boldsymbol{\delta}$ and setting the result to zero gives the so-called *normal equations*

$$\boldsymbol{H}\boldsymbol{\delta} = \boldsymbol{J}^{\top}\boldsymbol{W}\boldsymbol{r}, \tag{5.11}$$

where $\boldsymbol{H} = \boldsymbol{J}^{\top}\boldsymbol{W}\boldsymbol{J}$ indicates an approximation to the Hessian function of $\frac{1}{2}\boldsymbol{r}^{\top}\boldsymbol{W}\boldsymbol{r}$ [375], so that this approximation leads to a rapid convergence. Note that $\boldsymbol{J}^{\top}\boldsymbol{W}\boldsymbol{r}$ is along the steepest descent direction, because the gradient of $\frac{1}{2}\boldsymbol{r}^{\top}\boldsymbol{W}\boldsymbol{r}$ is equal to $-\boldsymbol{J}^{\top}\boldsymbol{W}\boldsymbol{r}$ [376]. Levenberg added the (non-negative) damping factor λ to determine the trade-off between steepest descent and the quadratic approximation in the update rule [377], leading to the *augmented normal equations*

$$(\boldsymbol{H} + \lambda \boldsymbol{I})\, \boldsymbol{\delta} = \boldsymbol{J}^{\top}\boldsymbol{W}\boldsymbol{r}, \tag{5.12}$$

in which small value of damping factor λ results in a Gauss-Newton update, whereas large value of λ results in a gradient descent update. In general, the efficiency of LM algorithm depends on the choice of the damping factor. In a standard method suggested by Marquardt, at each iteration, the damping factor is adjusted according to whether the error function $\boldsymbol{r}$ increases or decreases. When the error function is decreased as a result of the update, then the damping factor λ is reduced by a fixed factor (for instance $L_{\downarrow}$), the parameters are updated and the process is repeated with a decreased damping factor. If an iteration gives insufficient decrease in the error function, damping factor λ increases a larger value (for instance with the factor $L_{\uparrow}$) and the process is repeated until a decrease in the error is found [378, 379]. The above algorithm has the disadvantage that if the value of λ is large, the Hessian matrix H is not used at all, which leads to a slow convergence in the direction of the small gradient. To remedy this shortcoming, Marquardt suggested to replace the identity matrix $\boldsymbol{I}$ with the diagonal of Hessian [380]

$$(\boldsymbol{H} + \lambda\, \mathrm{diag}(\boldsymbol{H}))\, \boldsymbol{\delta} = \boldsymbol{J}^{\top}\boldsymbol{W}\boldsymbol{r}. \tag{5.13}$$

In this manner, each component of the gradient is scaled according to the curvature. This results in a larger movement along the directions where the gradient is smaller. Taken together, given an initial guess, the LM algorithm iteratively moves the guess point towards a minimum with taking steps $\boldsymbol{\delta}$, which at each iteration, are computed from Eq. (5.13). The pseudo-code of the LM algorithm is shown in Algorithm 5.1. In Ref. [381], it has been suggested that the parameters $\lambda = 0.001$, $L_{\uparrow} = 11$, $L_{\downarrow} = 9$, and $\epsilon = 0.01$ have good convergence properties.

Algorithm 5.1 LM algorithm

```
Initialize with a parameter set $\vec{p}$ in the search space; $\vec{p} \in [\vec{lb}, \vec{up}]$.
while ($k <$ max evaluations)) do
  Compute $\boldsymbol{\delta}$ from $(\boldsymbol{H} + \lambda \operatorname{diag}(\boldsymbol{H}))\, \boldsymbol{\delta} = \boldsymbol{J}^\top \boldsymbol{W} \boldsymbol{r}$,
  $\vec{p}_{new} = \vec{p} + \boldsymbol{\delta}$
  Evaluate $\mathcal{E}(\vec{p}_{new})$, and $\rho = (\mathcal{E}(\vec{p}) - \mathcal{E}(\vec{p}_{new})) \,/\, \big(2\boldsymbol{\delta}^\top(\lambda\boldsymbol{\delta} + \boldsymbol{J}^\top \boldsymbol{W}\boldsymbol{r})\big)$,
  if $\rho \leq \epsilon$ then
    Update the parameters: $\vec{p} = \vec{p}_{new} + \boldsymbol{\delta}$
    Decrease the damping factor: $\lambda = \lambda / L_{\downarrow}$
  else
    Reject the increment $\boldsymbol{\delta}$; $\vec{p}_{new} = \vec{p}$
    Increase the damping factor: $\lambda = \lambda L_{\uparrow}$
  end if
end while
```

5.3.2 Particle Swarm Optimization (PSO)

Particle Swarm Optimization (PSO) is a population-based optimization method used to find the globally optimal solution of an optimization problem. The PSO algorithm utilizes a stochastic search method which is inspired by social behavior patterns of organisms that live and interact within a large group, such as a flock of birds or a school of fish. The work of Reeves [382], Reynolds [383], and some years later, Heppner and Grenander on the modeling of collective behavior of a flock of birds [384] inspired James Kennedy and Russell C. Eberhart (social-psychologist) to combine cognitive abilities with social interaction leading to the Particle Swarm Optimizer [385]. Since then, many researchers have proposed different variants of PSO to improve its performance [386, 387, 388, 389, 390, 391, 392, 393, 394, 395, 396].

During the past decades, the PSO algorithm and its variants have been applied successfully in different scientific fields to solve a wide variety of optimization problems. In particular, PSO as a global optimization technique has obtained significant popularity due to its robust searching mechanism, excellent convergence and simple implementation. It is important to point out that PSO requires neither derivative information nor good initial guesses for the model parameters. Thus, PSO makes its use appealing when the gradient of objective function is either unavailable (discontinuous objective function) or computationally expensive to obtain.

The PSO algorithm belongs to the larger class of evolutionary algorithms (EAs), thus it shares many common concepts with other evolutionary search method such as Genetic Algorithm (GA). For instance, PSO and GA are both population based which initialize with a population of random potential solutions. They evaluate the individuals by measuring their fitness values, and explore the search space iteratively for the optimum solution by updating the particles. However, in contrast to GA, PSO does not have genetic operators such as crossover and mutation. Furthermore, in PSO, candidate solutions known as particles, are evolved by cooperation and competition between each other, and they have memory which is the characteristic feature of the PSO algorithm. However, in GA the current population is the only memory available for the individuals.

The PSO method maintains a population of S particles called as swarm in which the position of each particle in the swarm can be regarded as a candidate solution to the optimization problem. In general, a particle (also known as an agent) is interconnected to other particles so that each particle can share the information with every other particle. The shared information contains the best location found so far by a particle itself and the best location achieved so far across the whole population. In a swarm, any particle has a position and a pseudo velocity. The initial position and velocity of particles are uniformly random values within the search space bounds. Then, at each iteration, the velocity of each particle is updated by the updating rule and is added to the particle's current position to move it to a new position. The current position of any particle through the search space depends on three terms: 1) Its previous position which is known as the inertia term. This term is the tend of particles to keep their current path. 2) Its best previous position obtained by the particle, itself in each iteration, which is called the cognitive aspect of PSO. This term is the attraction of particles towards the previously found personal best position. 3) The best position obtained by all particles in the whole swarm i.e., the best of personal best positions or the global best position, which is referred to as the social aspect of PSO. This term is the attraction towards the global best position of whole swarm.

The particle positions adjust by the updating rule to explore the search space in order to find the best global location. The equations of the updating rule for each particle in each dimension presented by Shi and Eberhart [386] is given by

$$\begin{aligned} \vec{v}_i(k+1) &= \omega(k)\vec{v}_i(k) + \phi_p[r_p(\vec{P}_i(k) - \vec{x}_i(k))] + \phi_g[r_g(\vec{G}(k) - \vec{x}_i(k))], \qquad (5.14) \\ \vec{x}_i(k+1) &= \vec{x}_i(k) + \vec{v}_i(k+1), \qquad (5.15) \end{aligned}$$

where the vectors $\vec{x}_i(k)$ and $\vec{v}_i(k)$ represent the position and velocity of th i-th particle, respectively, at the k-th iteration, with $i = 1, 2, ..., N$, where N is the size of the swarm, i.e., the number of individuals in the population. The vectors $\vec{x}_i(k)$ and $\vec{v}_i(k)$ are D-dimensional vectors where D is the dimension of the swarm, i.e., the number of parameters being optimized. Thus, $\vec{x}_i(k) = [x_{i,1}(k), x_{i,2}(k), ..., x_{i,D}(k)]$, and $\vec{v}_i(k) = [v_{i,1}(k), v_{i,2}(k), ..., v_{i,D}(k)]$, where $\vec{x}_i, \vec{v}_i \in \mathcal{S} \subseteq \mathbb{R}^D$, and $\mathcal{S}$ denotes the feasible space. Moreover, $\vec{P}_i$ denotes the personal best position found by particle i since initialization, and $\vec{G}$ is the global best position found in the search space by whole swarm up to the current iteration (the best of the personal bests). The parameter ω represents the inertia coefficient, whereas ϕ_p and ϕ_g indicate the cognitive and social acceleration coefficients, respectively. The parameters $r_{p,g}$ are uniformly distributed random numbers in the range [0,1], i.e., $r_{p,g} \in \mathcal{U}(0, 1)$.

Figure 1 shows the graphical search mechanism of the PSO algorithm in a two-dimensional search space. The new position $\vec{x}_i(k+1)$ is the sum of current $\vec{x}_i(k)$ position and the velocity $\vec{v}_i(k+1)$, where the new velocity $\vec{v}_i(k+1)$ is the sum of inertia, cognitive and social terms. It should be noted that if the search space is defined by the bounds $[\vec{lb}, \vec{up}]$, then the value of $\vec{x}_i$ is clamped to the range $[\vec{x}_{min} = \vec{lb}, \vec{x}_{max} = \vec{ub}]$ to prevent those particles that might leave the search space. The lower and upper boundaries of the search space are represented by $\vec{lb}$ and $\vec{ub}$, respectively. Typically, the particles move back to the boundary value if they exceeded the boundaries. In order to evaluate potential solutions, at each iteration, each candidate position is evaluated by its value of objective function. Then, the personal and the global best positions are updated by comparing their evaluated fitnesses against the previous ones. This process repeats until a predefined acceptable fitness level is achieved or a maximum number of fitness evaluations has been met. At this time, the last global best position found by the swarm returns as the global optimum. The algorithmic description of PSO method is illustrated in Algorithm 5.2.

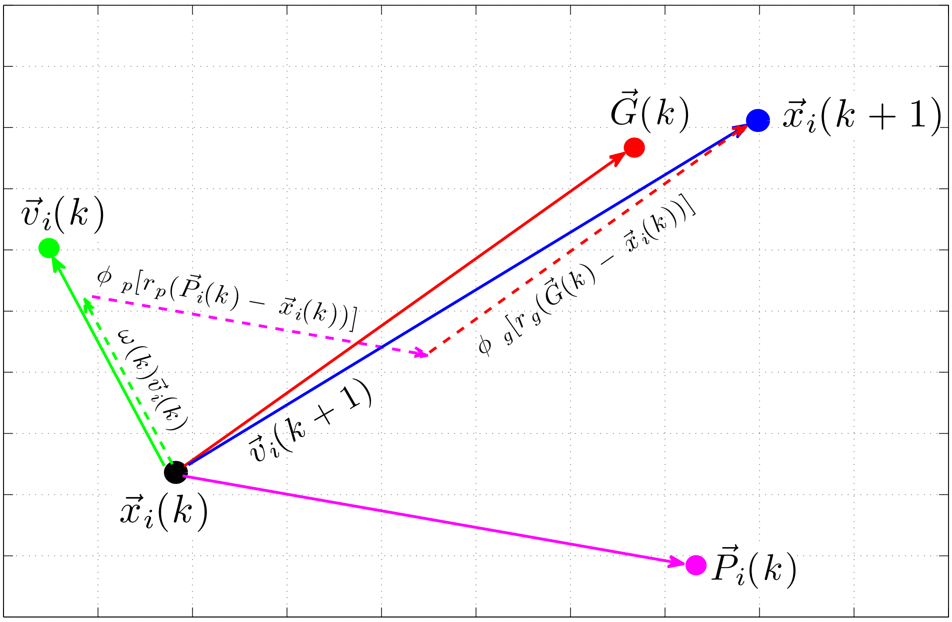

Fig. 5.1. Graphical representation of updating rule in PSO algorithm. The position and velocity of i-th particle in a swarm are adjusted by using the updating rule shown in Eqs. 5.14 and 5.15, respectively.

The PSO algorithm uses a few tuning parameters that affect its performance. A large number of studies have been invested to reveal the impact of the PSO parameters, namely the swarm size N, the inertia weight ω, and the acceleration coefficients ϕ_p and ϕ_g on the algorithm performance. According to several evidences, the PSO performance is sensitive to the values of these parameters. In the following, we briefly explain how the parameters can affect the PSO performance.

First, the number of particles in the swarm denoted by N heavily affects the convergence of the algorithm. It is expected that increasing the number of particles decreases the number of required iterations to converge, but an algorithm initialized by a large number of particles resembles a random search and needs more function evaluations at each iteration. In contrast, using a smaller number of particles requires more iterations to converge but fewer function evaluations. Since the optimization cost is usually dominated by the fitness function evaluations, choosing a smaller number of particles leads to a faster clock time. However, using too few of particles would results in insufficient exploration of the search space. Empirical studies have recommended that the swarm size should be larger than the dimensionality of the problem in order to avoid the premature convergence of the particles towards a non-optimal point [397, 398]. The most efficient reported values for the swarm size are between $N = 20$ to $N = 300$ particles [399].

The parameter ω (inertia coefficient) plays a crucial role in the PSO convergence. It has been reported that without the inertia term, the velocity of particles quickly explode to large values. Consequently, particles with large position updates would leave the search space boundaries [400, 401]. The inertia term was proposed by Shi and Eberhart to guarantee that the particles converge to a stable point in the search space [386, 388]. Note that a proper value of the parameter ω provides a balance between global exploration and local exploitation abilities. Exploration is the tendency to test new regions in the search space. In contrast, exploitation is

Algorithm 5.2 PSO algorithm

```
Initialize randomly the swarm; $\vec{x_i} \in \mathcal{U}(\vec{lb}, \vec{up})$, $\vec{v_i} \in \mathcal{U}(- \mid \vec{ub} - \vec{lb} \mid, \mid \vec{ub} - \vec{lb} \mid)$.
Set $\vec{P_i} = \vec{x_i}$ and identify $\vec{G}$ in the initial population.
while $(k < max\ evaluations)$ or $(best\ fitness > acceptable\ fitness)$ do
  for $i = 1$ to $N$ do
    Adjust the position and velocity of the particles according to
        $\vec{v}_i(k+1) = \omega(k)\vec{v}_i(k) + \phi_p[r_p(\vec{P}_i(k) - \vec{x}_i(k))] + \phi_g[r_g(\vec{G}(k) - \vec{x}_i(k))],$
        $\vec{x}_i(k+1) = \vec{x}_i(k) + \vec{v}_i(k+1).$
    Evaluate the swarm.
    if $\mathcal{E}(\vec{x_i}(k+1)) < \mathcal{E}(\vec{P_i}(k+1))$ then
      Update the personal best positions: $\vec{P_i}(k+1) = \vec{x_i}(k+1)$.
    end if
    if $\mathcal{E}(\vec{P}(k+1)) < \mathcal{E}(\vec{G_i}(k+1))$ then
      Update the global best position: $\vec{G}(k+1) = \vec{P_i}(k+1)$.
    end if
  end for
end while
```

the tendency to more concentrate in small regions of the search space around promising candidate solutions. In general, the larger values of inertial coefficient facilitates global exploration tendency of the swarm, whereas the smaller values promotes the local exploitation and result in a faster convergence to a solution [402]. The inertia term can be chosen as a constant value or as a linear decreasing function. It has been recommended to use the inertia weight as a linear decreasing function. This choice improves the initial exploration of the search space during the initial iterations whereas the exploitation is enhanced as the iteration count increases [386, 402]. In the present work, the inertia term is defined as a decreasing linear function of iteration index k

$$\omega(k) = \frac{\omega_{min} - \omega_{max}}{K}(k-1) + \omega_{max} \quad for \;\; k = 1, 2, ..., K \tag{5.16}$$

where K is the maximum number of iteration. The parameters ω_1 and ω_2 are

$$\begin{aligned} \omega_{max} &= 1 - \epsilon, \\ \omega_{min} &= \frac{\phi_p + \phi_g}{2} - 1 + \epsilon, \end{aligned} \tag{5.17}$$

with $\epsilon \ll 1$. The parameters ϕ_p and ϕ_g are responsible for the swarm behavior referred to as cognitive and social acceleration coefficients, respectively. These parameters control the cognitive aspect (movement the particles toward the personal best) and social aspect (movement the particles toward the global best position), respectively. The necessary and sufficient conditions for stability of the swarm are [403, 404]

$$\begin{aligned} &\phi_p + \phi_g < 4, \\ &\frac{\phi_p + \phi_g}{2} - 1 < \omega < 1, \end{aligned} \tag{5.18}$$

in which, these conditions guarantee the convergence to a stable equilibrium, however it might not be the global optimum [389, 403].

The reader is referred to Refs. [405, 406, 397] for a more detailed review of the PSO algorithm.

5.3.3 Differential evolution (DE)

Differential Evolution (DE) algorithm is a stochastic population-based optimization method which was originally introduced by Storn and Price in 1996 [407]. Similar to PSO, the DE algorithm belongs to the class of metaheuristic evolutionary algorithms. The DE maintains a population of individuals which evolve based on biology-inspired operations. As with other EAs, the algorithm does not require the gradient of the problem being optimized. Thus, it is not necessary that the optimization function to be a differentiable function. Moreover, the simplicity, fast convergence and using a few control parameters are the other important features of DE algorithm.

In DE, as it is presented in Algorithm 5.3, first a population of S agents is generated with uniformly distributed random positions which are constrained in the range $[\vec{lb},\vec{ub}]$. Then, a new generation is created from the current generation by using a certain mutation and crossover operations. At each iteration k, for each target agent $\vec{x_i} \in [1, N]$, three other agents $\vec{a_i}$, $\vec{b_i}$, and $\vec{c_i}$ are choosed randomly, for which they must be distinct from each other as well as the target agent $\vec{x_i}$. Then, a mutant agent is generated as $\vec{y_i}(k+1) = \vec{a_i}(k) + F(\vec{b_i}(k) - \vec{c_i}(k))$, where the positive factor $F \in [0, 2]$, known as the differential weight, is a control parameter for scaling the difference vectors. After the mutation phase, the crossover operation is applied to each pair of target agent $\vec{x_i}$ and its mutant agent $\vec{y_i}$ to generate a trial vector $\vec{u_i}$. For each dimension $j \in [1, D]$, the crossover is defined as

$$u_i(k+1, j) = \begin{cases} y_i(k+1, j) & \text{if } (j = R) \text{ or } (r < C_R) \\ x_i(k, j) & \text{else} \end{cases} \tag{5.19}$$

where user-specified constants $C_R \in [0, 1]$ is the crossover probability, and $R \in [1, D]$ is a randomly chosen index in the range $[1, D]$, where D is the dimensionality of the problem, and $r \in \mathcal{U}(0, 1)$ is a uniformly distributed random number in the range [0,1]. The mutation is continued until D crossover have been made. In fact, the trial agent $\vec{u_i}$ is the outcome of binary crossover of target agent $\vec{x}$ with its mutant agent $\vec{y_i} = \vec{a_i} + F(\vec{b_i} - \vec{c_i})$, by a crossover probability of $C_R \in [0, 1]$. Finally, the objective function values of the target and trial agents are evaluated to perform the selection operation as follow

$$x_i(k+1, j) = \begin{cases} u_i(k+1, j) & \text{if } \mathcal{E}(\vec{u_i}(k+1)) < \mathcal{E}(\vec{x_i}(k)) \\ x_i(k, j) & \text{otherwise} \end{cases} \tag{5.20}$$

Thus, if the trial agent $\vec{u}$ has smaller objective function value than the corresponding target agent $\vec{x}$, the target agent $\vec{x}$ is replaced with the trial agent $\vec{u}$, and it is admitted to enter the next generation. The process repeats until a predefined termination condition has been met i.e., once either a maximum number of iteration has been performed, or a sufficient fitness function has been achieved. At each iteration and during each operation if an element of a vector is found to exceed the the upper or lower limits it is reset to the violated boundary.

The DE algorithm has a few behavioral parameters which the choice of these parameters can significantly influence the optimization performance [408, 409]. In the past decade, many researchers have suggested various mutation and crossover strategies with different parameter settings [410]. In this work, we use the introduced control parameters by Pedersen [399], which

Algorithm 5.3 DE algorithm

```
Initialize randomly the swarm in the search space; $\vec{x_i} \in \mathcal{U}(\vec{lb}, \vec{up})$.
while ($k <$ max evaluations) and (best fitness $>$ acceptable fitness) do
  for $i = 1$ to $N$ do
    For each target agent $\vec{x_i}$ pick randomly three other distinct agents $\vec{a_i}$, $\vec{b_i}$ and $\vec{c_i}$, and generate a mutant agent $\vec{y_i}(k+1) = \vec{a_i}(k) + F(\vec{b_i}(k) - \vec{c_i}(k))$.
    For each pair of $\vec{x_i}$ and $\vec{y_i}$ generate a trial vector $\vec{u_i}$.
    Pick a random index $R \in [1, D]$.
    for $j = 1$ to $D$ do
      For each dimension $j \in [1, D]$ pick a uniformly distributed random numbers $r \in \mathcal{U}(0, 1)$, and compute the j'th element of the trial vector $\vec{u_i}$.
        $u_i(k+1, j) = \begin{cases} y_i(k+1, j) & \text{if } (j = R) \text{ or } (r < C_R) \\ x_i(k, j) & \text{else} \end{cases}$
    end for
    Evaluate the trial agent $\vec{u_i}$;
    if $\mathcal{E}(\vec{u_i}(k+1)) < \mathcal{E}(\vec{x_i}(k))$ then
      Update agent's position: $x_i(k+1, j) = u_i(k+1, j)$.
    else
      Keep the current state: $x_i(k+1, j) = x_i(k, j)$.
    end if
  end for
end while
```

have been obtained by the way of meta-optimization (the use of another overlying optimizer for finding good behavioral parameters) and result in a satisfactory optimization performance for various tested problems.

5.3.4 Metropolis-Hastings (MH)

In mathematical statistics, Monte Carlo Markov Chain (MCMC) algorithms are used for sampling from a probability distribution to construct a Markov chain, whose steady state distribution asymptotically approaches a desired distribution. In these algorithms, as the process of sampling proceeds, the distribution of samples more closely approximates the distribution of interest. The MCMC methods were primarily used for numerical calculating of the multi-dimensional integrals, then they have been widely employed for calculating the expectation or expected values of distributions. The term *Markov chain* refers to a sequence of stochastic states such that the transitions from one state to another depends only on the current state of the chain, neither on the previous nor the future states. An important property of Markov chains is that once the chain reaches to its steady state, the starting state of the chain no longer affects the chain states. In other words, the Markov chains converge to a stationary distribution independent of the starting point. The transition probability in a Markov chain i.e., the probability associated with state changes can be mathematically expressed as $P(x^{t+1} \mid x^t, x^{t-1}, ..., x^1) = P(x^{t+1} \mid x^t)$, with $x^{t+1} = x^t + \epsilon_t$, where $\epsilon_t \in \mathcal{N}(0, 1)$. This kind of memorylessness aspect of stochastic processes is called Markov property. A well-known Markov chain is the so-called *random walk* or drunkard's walk, which is a sequence of random steps in such a way that the transition probabilities depend solely on the current position.

In the following we will not explain the details of the MCMC methods, but we provide a brief description of the most popular MCMC algorithms and its use in parameter estimation problems. For more details of MCMC algorithms and related concepts see Refs. [411, 412]. In the past years several MCMC methods have been developed to draw samples from a distribution. However, the most commonly used MCMC method for obtaining a sequence of random samples from a probability distribution is Metropolis-Hastings (MH) algorithm [413, 414], especially when the number of dimensions is high. Since MH algorithm belongs to the class of MCMC methods, the sequence of samples generated by MH has the Markov property, i.e., the next sample value depends only on the current sample value. Consider we aim to compute the value of a function $f(x)$, which is proportional to the density of a desired stationary distribution $P(x)$, often referred to as the target distribution. In order to evaluate the target distribution $P(x)$, we need to construct a Markov chain with stationary distribution $P(x)$. To this end, at each iteration, a sample candidate is drawn from an arbitrary proposal distribution $Q(. \mid x^t)$, which determines the next sample value based on the current sample value. In other word, a trial transition to a candidate state x^* is proposed randomly from the present state x^t. Then, the candidate sample is either accepted or rejected with some probability α. In MH algorithm the acceptance probability is given by $\alpha = min\{1, \dfrac{P(x^*)Q(x^t \mid x^*)}{P(x^t)Q(x^* \mid x^t)}\}$, where $P(x^t)$ describes the probability of finding the system in state x^t, and $Q(x^* \mid x^t)$ denotes the probability of generating the candidate state x^* from the current state x^t. If the candidate sample is accepted, it will be used as the current sample in next iteration, i.e., the chain moves to the new proposed state. Otherwise, the rejected candidate sample is discarded and the current sample is re-used again for the next iteration until a candidate sample is accepted. In general, the proposal distribution can be non-symmetric i.e., the probability of transition to a new state may not be identical with the probability of reverse transition. However, in the widespread used Metropolis algorithm, a symmetric distribution function is considered for the proposal distribution, which yields to the simplified acceptance probability $\alpha = min\{1, \dfrac{P(x^*)}{P(x^t)}\}$. For instance, it is common that in the so-called Random walk Metropolis (REM) algorithm, a Gaussian function is considered as the proposal distribution.

Here we illustrate how one can constructs a target distribution by using the Random walk Metropolis (REM) algorithm. Figure 5.2 shows an example of producing a Cauchy target distribution with the probability density $P(x) = 1./(1 + (x - 2)^2$, by sampling from a Gaussian distribution. It is worth mentioning that in the MH method, we do not need to know the normalizing constant of the density or probability functions. In this example a single chain is generated by 50000 sampling drawn from $Q(x) = \dfrac{1}{\sqrt{2\pi}\sigma} exp\left(-\frac{1}{2}(\dfrac{x-\mu}{\sigma})^2\right)$, with $\sigma = .5$, as the proposal distribution (c.f. panel **A**). Moreover, it can be observed in panel **B** that as more samples are generated, the distribution of generated samples coincides better with the target distribution.

The most widely used application of MCMC techniques, in particular the MH algorithm, is points sampling in Bayesian paradigm in order to create a Markov chain on search space that approximates the posterior distribution. This sampling procedure results in the parameter estimates that maximize the posterior probability of the parameters given the observed data. The description of Bayesian inference is beyond the scope of the present work, for the details see Ref. [415]. Here, we briefly sketch the MH algorithm in order to minimize a sum of square error problem resulting in a single-point estimation, in contrast to maximizing the likelihood function in Bayesian approach which is a distribution-based inference. However, it should be

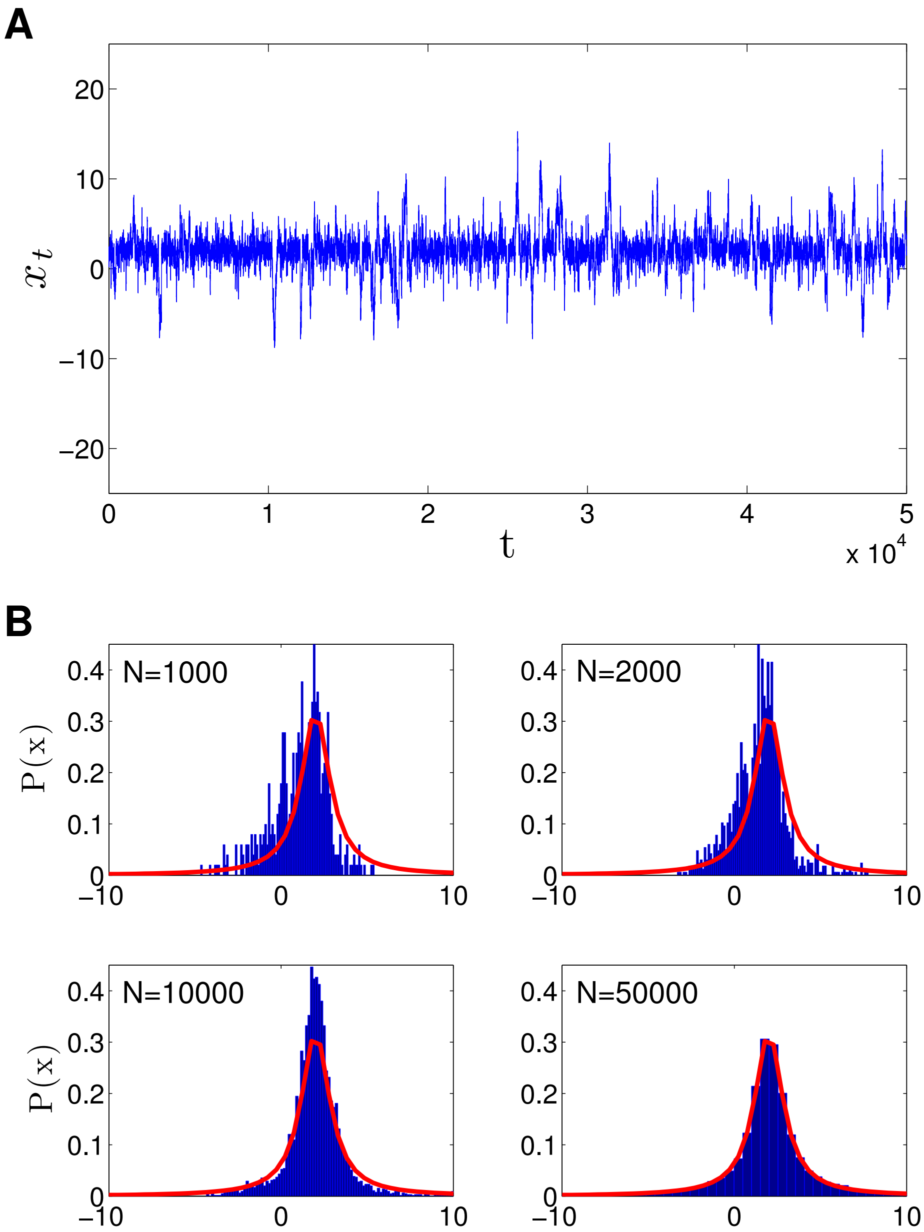

Fig. 5.2. Construction of a Cauchy target distribution $P(x) = 1./(1 + (x - 2)^2$, using Random walk Metropolis (REM) algorithm by sampling from a Gaussian distribution. (**A**) The sequence of 50000 samples as a Markov chain. (**B**) The histograms of N samples with different chain lengths, illustrated in blue bars. The red curves show the target distribution $P(x)$, which has a Cauchy shape with the mean centered at $x_0 = 2$. The histogram of samples at $N = 5000$ is in good agreement with the target distribution $P(x)$.

Algorithm 5.4 MH algorithm

```
Initialize with a state $\vec{x}$ in the search space; $\vec{x} \in \mathcal{U}(\vec{lb}, \vec{up})$.
while ($k < max\ evaluations$)) do
    Generate a new state $\vec{y}$, randomly.
    Evaluate $\Delta\mathcal{E} = \mathcal{E}(\vec{y}) - \mathcal{E}(\vec{x})$, and $P = exp(-\Delta\mathcal{E})$.
    Draw $r \in \mathcal{U}(0,1)$ and compute $a = min\{1, P\}$.
    if $r \leq a$ then
        Accept the new state and set it as the current state in the next iteration: $\vec{x}(k+1) = \vec{y}(k)$.
    else
        Reject the new state and maintain the current state: $\vec{x}(k+1) = \vec{x}(k)$.
    end if
end while
```

mentioned that if we assume additive Gaussian noise on the measurements, maximizing the log likelihood is equivalent to minimizing the sum of squared residuals between the model simulations and the experimental data. It is well-know that by employing an analogy between the model parameters and the states in a Markov chain, one can use the MH algorithm to minimize an objective function. In this method, a random walk through the search space is constructed which eventually converges towards a region of the state space where is the minimum of the sum of squared errors. As the pseudo-code of MH method is illustrated in Algorithm 5.4, first the algorithm starts with an initial state. Then, at each iteration, a trial move $\vec{y}$ is generated randomly from the current state $\vec{x}$. Due to the Markov property of the space exploration in MH algorithm, whether a trial step will be selected or rejected depends only on the fitness function values at current and the trial steps. This is in contrast to the PSO algorithm which a new movement in the search space depends to the fitness function of all the previous steps. The trial move is accepted with the probability $P = exp(-\Delta\mathcal{E})$, where $\Delta\mathcal{E} = \mathcal{E}(\vec{y}) - \mathcal{E}(\vec{x})$. In other words, the trial state is accepted if it has a objective function value less than current state. Otherwise, it is accepted with probability of $a \geq r$, where $a = min\{1, P\}$, and $r \in \mathcal{U}(0,1)$ is a random number drawn from a uniform distribution in the range $[0,1]$. If the trial state is accepted, the chain moves to new state and it will be used as the current state in the next iteration, whereas the rejected trial state is discarded and the process repeats with another trial state until a trial state is accepted.

5.3.5 Simulated Annealing (SA)

Simulated annealing (SA) is a generic probabilistic metaheuristic algorithm inspired by annealing process in metallurgy. Annealing is a metallurgic technique which is used to increase the crystal size of a metal with minimum defects by a procedure of heating, followed by slow cooling at a specific rate. By this technique, the metal achieves its most regular possible lattice configuration i.e., the ground state which has the minimum energy state. The SA method was introduced by Scott Kirkpatrick, C. Daniel Gelatt and Mario P. Vecchi [416], from adapting the MH algorithm under assuming an analogy between the solutions in optimization problems and the energy states in thermodynamic theorem. By virtue of this analogy, the goodness of a solution in SA algorithm is treated as the energy of a state in thermodynamic.

Although the SA method is quite robust for solving global optimization problems, it can be very slow in optimizing those problems that the objective function is expensive to compute. This is because the exploring of search space is accompanied by accepting a fraction of non-improving

Algorithm 5.5 SA algorithm

```
Initialize with a state $\vec{x}$ in the search space; $\vec{x} \in \mathcal{U}(\vec{lb}, \vec{up})$.
while ($k <$ max evaluations) or ($T < T_0$) do
    Generate a new state $\vec{y}$, randomly.
    Evaluate $\Delta\mathcal{E} = \mathcal{E}(\vec{y}) - \mathcal{E}(\vec{x})$, and $P = exp(\frac{-\Delta\mathcal{E}}{T_k})$.
    Draw $r \in \mathcal{U}(0,1)$ and compute $a = min\{1, P\}$.
    if $r \leq a$ then
        Accept the new state and set it as the current state in the next iteration: $\vec{x}(k+1) = \vec{y}(k)$.
    else
        Reject the new state and maintain the current state: $\vec{x}(k+1) = \vec{x}(k)$.
    end if
    Decrease $T_k$.
end while
```

solutions, which is a fundamental property of this method. Consider the current state of a system denoted by $\vec{x}$ with the fitness function of $\mathcal{E}(\vec{x})$ is updated to a candidate state $\vec{y}$ with the fitness function value $\mathcal{E}(\vec{y})$, through a random walk scheme. The new state is accepted if $\mathcal{E}(\vec{x}) < \mathcal{E}(\vec{y})$, whereas if $\mathcal{E}(\vec{x}) > \mathcal{E}(\vec{y})$, the new state is accepted with some probability. If the new state is accepted, it becomes as the current state and the process continues. Otherwise, if the new state is rejected another state is generated from the current one. This step is repeated until the system reaches a new acceptable state or a maximum number of iteration has been performed. The probability of accepting new state based on the Boltzmann distribution is $a = min\{1, P\}$, where $P = \exp(\frac{-\Delta\mathcal{E}}{T_k})$, and $\Delta\mathcal{E}$ is the difference between the fitness value of new and current states, and T_k is the temperature at iteration k. Once the acceptance probability is calculated, it will be compared to a random number drown from a uniform distribution in the range [0,1], i.e., $r \in \mathcal{U}(0,1)$. If the acceptance probability is larger than the random number, the new state is accepted, otherwise it is rejected. Compared to MH algorithm, in SA method the acceptance probability is cooled slowly over time.

The notion of slow cooling inspired by annealing technique is implemented in SA method as a slow decrease in the temperature. In general, the algorithm starts with a high temperature, and then the temperature is reduced slowly according to a cooling schedule. Starting with a high temperature leads to a high chance for accepting the worse solutions at the beginning of the optimization procedure. This facilitates the global exploration ability of the algorithm in order to avoid getting trapped by local optima early. As the temperature lowers, the acceptance probability decreases, which enhances the local exploitation ability. In other words, the algorithm concentrates on the most promising regions of the search space that may contain the optimum solution. Since the annealing schedule i.e., the manner in which temperature is decreased plays an essential role in the algorithm performance, many schedule has been suggested for decreasing the temperature in SA algorithm. A simplest cooling schedule is reducing temperature linearly or exponentially as the simulation proceeds. In this work, we consider the cooling schedule as a function of iteration index k given by $T_k = \alpha T_{k-1}$, with $\alpha = 0.001^{(1.0/(M-1.0))}$, where M is the maximum number of iterations. Taking this schedule, for the enough large value of maximum iterations, for instance $M = 1000$, the temperature starts from $T_0 = 10$ and gradually decreases to zero.

5.4 Precision of the estimates

Once the model's parameters have been estimated, it is necessary to determine the identifiability of the estimates. The identifiability analysis in general can be classified into two categories known as structural identifiability (*a priori identifiability*) and practical identifiability (*a posteriori identifiability*) [59, 417]. The structural identifiability is related to the model structure only and is independent of the quality and quantity of the measurements [418, 419]. Conversely, the practical identifiability is related to the experimental data and the noise measurements [420, 421, 422]. The *practical identifiability* analysis aims to determine whether the model's parameters can be uniquely estimated by the experimental data [421, 422, 423].

Although many technique have been developed to address the identifiability problems [424, 425, 418, 426, 427, 428, 429, 430, 431], analyzing the identifiability of parameters is still a very challenging problem, particularly in the case of large and highly non-linear models [432, 433]. In the following we describe the most widely used metrics for assessing the accuracy of estimates.

5.4.1 Confidence regions

Due to the noise in the measurements, the estimated parameters do not exactly coincide with the true parameter values. Therefore, there is a discrepancy between the true and the estimated values, which needs to be evaluated. A widely used method in statistical inference to assess the accuracy of the estimated parameters is constructing the confidence regions [434, 435]. A confidence region with the confidence level of $(1-\alpha)\%$ is a region around the estimated parameter in which contains the true parameter with a probability of $(1-\alpha)$. Since in linear models the sum of squares function is quadratic, the confidence regions for linear problems with Gaussian noise can be obtained exactly as the following ellipsoid [342]

$$(\boldsymbol{p}^* - \boldsymbol{p})^\top C_{lin}^{-1}(\boldsymbol{p}^* - \boldsymbol{p}) \leq N_p \mathcal{F}^{1-\alpha}_{N_P, N_y - N_p}, \tag{5.21}$$

which is centered at estimated parameter $\boldsymbol{p}^*$ with principal axes directed along the eigenvectors of C_{lin}^{-1}, where C_{lin} denotes the covariance matrix of the linear model, $\mathcal{F}$ is the Fisher distribution with N_p and $N_y - N_p$ degree of freedom, N_p and N_y are the number of model parameters and the total number of data points, respectively, $1-\alpha$ indicates the confidence level, and the high index $\top$ represents the transposed vector or matrix.

In contrast, in nonlinear models there is no exact theory for the evaluation of confidence regions [436, 54]. However, one can approximate the covariance matrix to extend Eq. (5.21) for nonlinear models leading to the following ellipsoid [437, 343]

$$(\boldsymbol{p}^* - \boldsymbol{p})^\top C_{approx}^{-1}(\boldsymbol{p}^* - \boldsymbol{p}) \leq N_p \mathcal{F}^{1-\alpha}_{N_P, N_y - N_p}, \tag{5.22}$$

where C_{approx} is an approximation of covariance matrix and it can be computed either the Fisher information matrix (represented by C_J), or by the Hessian matrix (represented by C_H) [436, 64]. Using Fisher matrix, the approximate covariance matrix is given by [438, 439, 440]

$$C_J = s^2 \left(J(\boldsymbol{p})^\top W J(\boldsymbol{p}) \right)^{-1}, \tag{5.23}$$

where $s^2 = \dfrac{\mathcal{E}(\hat{\boldsymbol{p}})}{N_y - N_p}$ is an unbiased approximation of the measurement variance, $J(\boldsymbol{p}) = \dfrac{\partial \hat{Y}(X_{data}, \boldsymbol{p})}{\partial \boldsymbol{p}} |_{\boldsymbol{p}^*}$ is an $N_y \times N_p$ matrix indicating the Jacobian matrix evaluated at $\boldsymbol{p}^*$, and

W is a weighting diagonal matrix with elements $w_{ii}^2 = 1/\sigma_{ii}^2$ in the principal diagonal. Consequently, by substituting Eq. (5.23) into Eq. (5.22), the confidence region obtained with Fisher matrix reads

$$(\boldsymbol{p}^* - \boldsymbol{p})^\top \left(J(\boldsymbol{p})^\top W J(\boldsymbol{p}) \right) (\boldsymbol{p}^* - \boldsymbol{p}) \leq N_p \frac{\mathcal{E}(\boldsymbol{p}^*)}{N_y - N_p} \mathcal{F}^{1-\alpha}_{N_P, N_y - N_p}. \tag{5.24}$$

In another approach, the approximate covariance matrix can be derived from the curvature of objective function through the Hessian matrix [436]

$$C_H = 2s^2 H(\boldsymbol{p})^{-1}, \tag{5.25}$$

where $H(\boldsymbol{p}) = \dfrac{\partial^2 \mathcal{E}(\boldsymbol{p})}{\partial \boldsymbol{p} \partial \boldsymbol{p}^\top} |_{\boldsymbol{p}^*}$, i.e. the Hessian matrix depends on the shape of objective function. Therefore, the confidence region based on Hessian matrix reads

$$(\boldsymbol{p}^* - \boldsymbol{p})^\top H(X_{data}, \boldsymbol{p})(\boldsymbol{p}^* - \boldsymbol{p}) \leq 2N_p \frac{\mathcal{E}(\boldsymbol{p}^*)}{N_y - N_p} \mathcal{F}^{1-\alpha}_{N_P, N_y - N_p}. \tag{5.26}$$

It has been shown that the estimation accuracy can be evaluated by comparing confidence regions obtained with the Hessian and the Fisher methods [436]. If both approaches yield the same confidence ellipsoids, the estimation converges to the true parameters. Otherwise, any discrepancy between them indicates an inaccurate estimation [436, 64].

Another way of constructing the confidence regions in non-linear models is known as the likelihood method. In this approach, an approximate confidence region is defined as all the parameter sets which satisfy [441]

$$\mathcal{E}(\boldsymbol{p}) \leq \mathcal{E}(\boldsymbol{p}^*) \left(1 + \frac{N_p}{N_y - N_p} \mathcal{F}^{1-\alpha}_{N_P, N_y - N_p} \right). \tag{5.27}$$

In general, the confidence regions constructed by this approach do not have to be elliptical. Furthermore, since the Eq. (5.27) does not depend on the linearization, the confidence regions obtained through the likelihood method are more precise than those computed through the approximate covariance matrix [442]. However, generating likelihood-based confidence regions requires a large number of function evaluations, which can be computationally expensive. Despite this fact, since minimizing an objective function with metaheuristic optimization algorithms like PSO is performed through function evaluations, using them is a well suitable way to obtain the likelihood confidence regions [443, 442]. In this work, we use PSO algorithm to compute the likelihood confidence regions which will be compared with those obtained through the covariance approximation.

5.4.2 Correlation analysis

Correlation matrix measures the possible interrelationship among the model parameters, which can be obtained from the covariance matrix. The correlation coefficient between the i-th and j-th parameter which can only take values between -1 and $+1$ is defined by [64, 54]

$$\begin{aligned} R_{ij} &= \frac{C_{ij}}{\sqrt{C_{ii} C_{jj}}}, \quad i \neq j \ , \\ R_{ij} &= 1, \qquad\qquad i = j \ , \end{aligned} \tag{5.28}$$

where C_{ij} is the covariance between the i-th and j-th parameter estimates. The correlation coefficient between two parameters indicates how the modification of model output due to the changes in one parameter can be taken place by proper changes in the other parameter [55].

It is important to notice that the correlation among parameters leads to non-identifiability problems [444, 64, 54]. The highly correlated parameters are not identifiable, because the influence of small changes in one parameter on the model output can be compensated by an appropriate change in the other parameter.

5.4.3 Sensitivity analysis

Sensitivity analysis is an appropriate way to identify which model parameters mostly contribute to variations in model output due to the changes in model input [445, 446]. Therefore, this method allows us to determine which model parameters are the key factors in controlling system behaviors [445]. A local sensitivity coefficient measures the influence of small changes in one model parameter on the model output, while the other parameters are held constant [447, 445, 446]. The $N_y \times N_p$ local sensitivity matrix is defined as the first-order partial derivatives of the model function with respect to each model parameter [448, 449]

$$S_{i,j} = \frac{\partial \hat{Y}_i(X_{data}, \boldsymbol{p})}{\partial p_j} \mid_{\boldsymbol{p}^*}, \tag{5.29}$$

where $i \in \{1, 2, ..., N_y\}$ and $j \in \{1, 2, ..., N_p\}$. Since Eq. (5.29) involves the use of Jacobian matrix, the local sensitivity coefficients can be defined by [448, 55]

$$\Gamma(p_j) = \mathcal{D}(J(\boldsymbol{p})^\top W J(\boldsymbol{p})), \tag{5.30}$$

where $\mathcal{D}$ denotes the main diagonal elements of a matrix. In addition, the local sensitivity matrix can be determined by computing the curvature of objective function through the Hessian matrix (second-order derivative) [346]

$$\Lambda(p_j) = \mathcal{D}(\frac{\partial^2 \mathcal{E}(\boldsymbol{p})}{\partial \boldsymbol{p} \partial \boldsymbol{p}^\top} \mid_{\boldsymbol{p}^*}). \tag{5.31}$$

The sensitivity analysis can shed light on the identifiability of model parameters. Making a small change in a very sensitive model parameter causes a strong response in the model output, which indicates that the parameter is more identifiable. On the contrary, a model parameter with low sensitivity is more difficult to being identified, because any modification in insensitive parameters has no influence on the model output [55]. The sensitivity analysis can be also a useful tool for model reduction techniques. For instance, a model can be simplified by either omitting the insensitive parameters or by fixing their values at some constants based on prior knowledge about the system dynamics [445, 421].

5.5 Case Studies

First, in order to illustrate the performance and capability of the parameter estimation method carried out in this work, we estimate the model parameters of two case studies; Case Study I) a stochastic damped harmonic oscillator, and Case Study II) a stochastic linear delay differential equation. For each case study we have generated *in silico* spectral data by a pseudo-experimental process, i.e., the spectral power data is generated artificially by adding noise to the output obtained by simulating the model equations with a set of pre-chosen parameters referred to as the *true*, or *nominal* values. Then, the confidence regions constructed by the approximate covariance matrix are compared with the likelihood confidence regions obtained by PSO algorithm. Moreover, identifiability analysis is performed through the sensitivity and correlation analyses for both case studies I and II to evaluate the reliability and accuracy of the estimates. Finally, we compare the performance of different optimization algorithms to determine which algorithm is more suitable for the *in vivo* parameter estimation problem considered in this work; Case Study III) estimating the unknown parameters of a thalamo-ocortical model by fitting the model power spectrum to the EEG spectral power recorded during awake and anesthesia conditions. All the computations in the present work were implemented in Matlab (http://www.mathworks.com) on a Mac OS X machine with 2.5 GHz Intel Core i5 processor and 12 GB of 1333 MHz DDR3 memory. The source codes needed to reproduce the presented results are available from the author on the request.

5.5.1 Case Study I: A stochastic damped harmonic oscillator

In Case Study I, we aim to estimate three unknown parameters of a noisy damped harmonic oscillator. The mathematical model of a damped harmonic oscillator driven by a random stochastic force can be formulated as [121]

$$\frac{d^2x}{dt^2} + \gamma\frac{dx}{dt} + \omega_0^2 x = \xi(t), \tag{5.32}$$

where ω_0 is the intrinsic angular frequency of the oscillator, and γ denotes the damping coefficient. The additive Gaussian white noise is represented by $\xi(t)$, which obeys

$$\langle\xi(t)\rangle = 0, \quad \langle\xi(t)\xi(t')\rangle = 2\kappa\delta(t-t'), \tag{5.33}$$

where κ is the intensity of the uncorrelated driving noise, and $\langle.\rangle$ denotes the ensemble average [122, 123]. Using the Wiener-Khinchin theorem, the power spectrum of the stochastic differential equation given by Eq. (5.32) reads [124, 125]

$$P(\omega) = \frac{2\kappa}{\sqrt{2\pi}}\frac{1}{(\omega^2-\omega_0^2)^2+\gamma^2\omega^2}, \tag{5.34}$$

where $\omega = 2\pi f$ denotes the angular frequency. It can be shown that the only maximum of $P(\omega)$ is located at $\omega_{max} = \sqrt{\omega_0^2 - \gamma^2/2}$, where $\omega_0 = 2\pi f_0$ is the resonant angular frequency of the system c.f. Fig. 2.1 of chapter 2. In this case study, the vector of unknown parameters to be estimated is $\boldsymbol{p_I} = (\kappa, \gamma, f_0)$, where all the parameters can only be greater than zero.

5.5.2 Case Study II: A stochastic linear delay differential equation

The considered inverse problem in Case Study II is to identify the unknown parameters of a linear delay differential equation which is driven by additive Gaussian white noise. Consider a

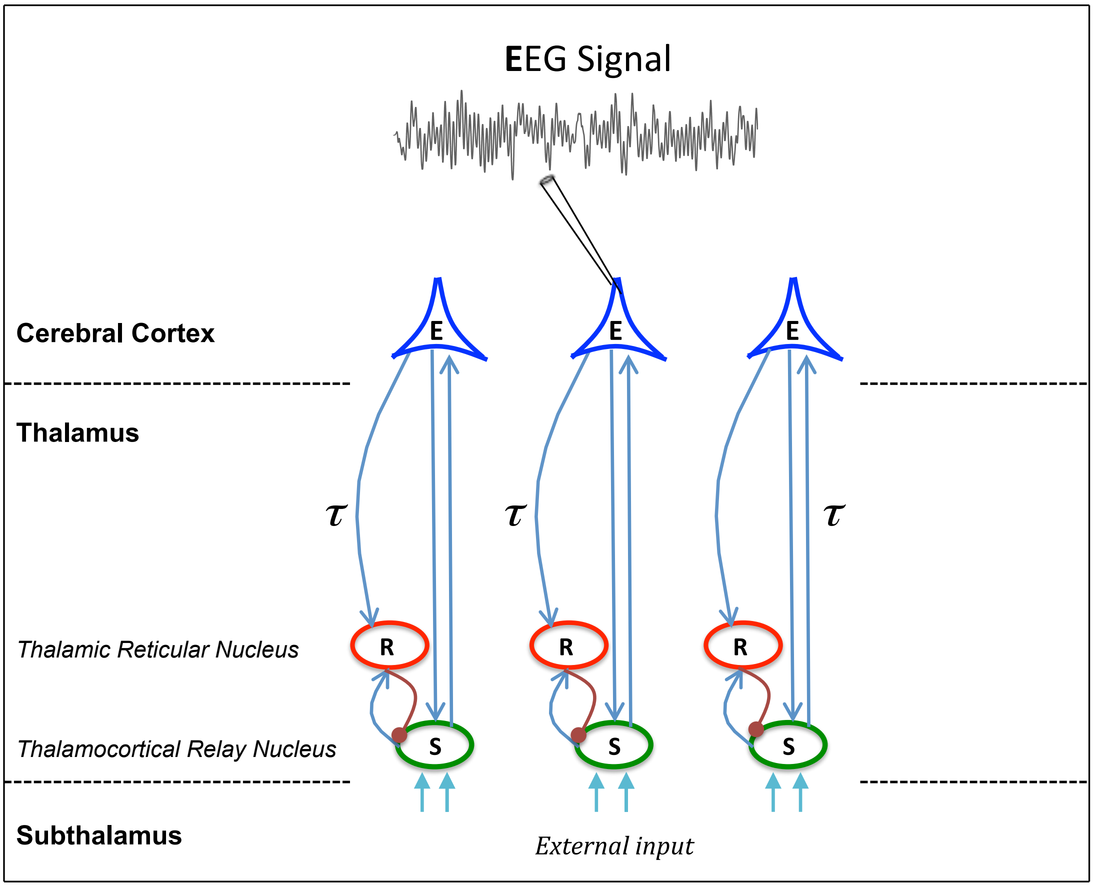

Fig. 5.3. Schematic diagram of the thalamo-cortical system. The excitatory connections (glutamatergic) are indicated with blue arrows, while the inhibitory connections (GABAergic) are represented by red lines with filled circle ends. The connections between cortical pyramidal neurons (E) and the thalamus consisting of thalamo-cortical relay neurons (S) and thalamic reticular nucleus (R) are associated with a constant time delay τ.

linear scalar delay differential equation in the presence of additive white noise given by

$$\frac{dy(t)}{dt} = ay(t) + by(t-\tau) + \xi(t). \tag{5.35}$$

The power spectrum of this equation is defined by the following equation

$$P(\omega) = \frac{2\kappa}{\sqrt{2\pi}} \frac{1}{(a + b\cos(\omega\tau))^2 + (\omega + b\sin(\omega\tau))^2}, \tag{5.36}$$

where κ is the intensity of the additive white noise with a Gaussian distribution represented by $\xi(t)$. In this case study the vector of unknown parameters to be estimated is $\boldsymbol{p}_{II} = (\kappa, a, b, \tau)$, where $\kappa > 0$, $\tau > 0$, and $a, b \in \mathbb{R}$.

5.5.3 Case Study III: A thalamo-cortical model reproducing the EEG rhythms

Case Study III aims to estimate the parameters of a neural mass model by fitting the power spectrum of the system to the recorded EEG data during awake and anesthesia conditions. To this end, we consider a well-tried thalamo-cortical neuronal population model developed by Robinson *et al.* [173, 174, 23], which is able to reproduce the characteristic spectral changes in EEG rhythms observed experimentally during different behavioral states such as wakefulness, slow-wave sleep, seizure and anesthesia conditions [186, 29, 176, 35, 36, 37]. In the following, the model equations is represented and then we derive the formula for EEG power spectrum which will be fitted to the empirical spectra. Consider the thalamo-cortical system shown schematically in Fig. 5.3. The model consists of a network of three populations of neurons: cortical pyramidal neurons (E), thalamo-cortical relay neurons (S) which both are excitatory glutamatergic neurons, and thalamic reticular nucleus (R) which is a thin shell of GABAergic cells surrounding the thalamus. The cortical pyramidal neurons (E) receive excitatory input from thalamo-cortical relay neurons (S) and project back to the same nuclei. This reciprocal long-range excitatory interaction would generates a positive feedback which is associated with a conduction delay τ. However, the incessant excitation in this loop is prevented by the interposed inhibition to thalamo-cortical relay neurons (S) which originates from thalamic reticular nucleus (R). The thalamic reticular nucleus (R) receive excitatory input from axon collaterals of the cortical pyramidal neurons (E) and thalamo-cortical relay neurons (S), which the former input is associated with a constant time delay τ [29, 229].

We denote the excitatory and inhibitory postsynaptic potentials (PSPs) in the model's neuronal populations by V_a^c, where $a \in \{E, R, S\}$ represents the pyramidal (E), relay (S), and reticular (R) neurons, respectively, and $c \in \{e, i\}$ indicates the excitatory and inhibitory synapses, respectively. The system dynamics are governed by the following set of coupled delay differential equations

$$\begin{aligned}
&\hat{L}_e V_E^e(t) = K_{ES} S_S[V_S^e(t-\tau) - V_S^i(t-\tau)],\\
&\hat{L}_e V_S^e(t) = K_{SE} S_E[V_E^e(t-\tau)] + I(t),\\
&\hat{L}_i V_S^i(t) = K_{SR} S_R[V_R^e(t)],\\
&\hat{L}_e V_R^e(t) = K_{RE} S_E[V_E^e(t-\tau)] + K_{RS} S_S[V_S^e(t) - V_S^i(t)],
\end{aligned} \tag{5.37}$$

where the parameters K_{ab} are the synaptic connection strengths in population a originating from population b and τ is the transmission time delay between cortex and thalamus. According to previous studies, we assume that the EEG can be described in a good approximation by spatially constant neural population activity [29, 23, 35, 36]. Thus, under the assumption of the spatial homogeneity, mean post-synaptic potentials in above equations do not depend on spatial locations. The parameters $S_a[.]$ describe the mean firing rate functions for neuronal populations $a \in \{E, R, S\}$, in which they are generally considered as a standard sigmoid function

$$S_a(V) = \frac{S_a^{max}}{1 + e^{-c(V - V_a^{th})}}, \tag{5.38}$$

where S_a^{max} is the maximum firing rate of population a, V_a^{th} indicates the mean firing threshold, and c denotes the slope of the sigmoid function at the inflexion-point V^{th}. The temporal operators $\hat{L}_{e,i}$ are given by

$$\begin{aligned}
\hat{L}_e(\partial/\partial t) &= \frac{1}{\alpha_e \beta_e} \frac{\partial^2}{\partial t^2} + (\frac{1}{\alpha_e} + \frac{1}{\beta_e}) \frac{\partial}{\partial t} + 1,\\
\hat{L}_i(\partial/\partial t) &= \frac{1}{\alpha_i \beta_i} \frac{\partial^2}{\partial t^2} + (\frac{1}{\alpha_i} + \frac{1}{\beta_i}) \frac{\partial}{\partial t} + 1.
\end{aligned} \tag{5.39}$$

with $\alpha_e > \beta_e$, and $\alpha_i > \beta_i$, where α_e and α_i indicate the synaptic rise rates of the response functions for excitatory and inhibitory synapses in s^{-1}, respectively, and β_e and β_i denote the corresponding decay rate constants. Moreover, the delay term, τ, is zero if both the sending and receiving populations are in the thalamus while for the thalamo-cortical or cortico-thalamic pathways, the delay term is nonzero.

Finally, since we assume that the EEG is generated by the activity of pyramidal cortical cells [22, 29, 30, 173, 182], and by virtue of the specific choice of external input to relay neurons, the power spectrum of the EEG just depends on one matrix component of the Green's function by

$$P_E(\omega) = 2\kappa\sqrt{2\pi}\left|\tilde{G}_{1,2}(\omega)\right|^2, \tag{5.40}$$

where

$$\tilde{G}_{1,2}(\omega) = \frac{-K_1\hat{L}_i e^{-i\omega\tau}}{\hat{L}_e(\hat{L}_e\hat{L}_i + C_2) + e^{-2i\omega\tau}(C_3 - C_1\hat{L}_i)}, \tag{5.41}$$

with $C_1 = K_1K_2$, $C_2 = K_3K_5$ and $C_3 = K_1K_3K_4$, and

$$\begin{aligned}
\hat{L}_e &= \left(1+\frac{i\omega}{\alpha_e}\right)\left(1+\frac{i\omega}{\beta_e}\right), & \hat{L}_i &= \left(1+\frac{i\omega}{\alpha_e}\right)\left(1+\frac{i\omega}{\beta_e}\right), \\
K_1 &= K_{ES}\frac{dS_S[V]}{dV}\,|_{V=(V_S^{*e}-V_S^{*i})}, & K_2 &= K_{SE}\frac{dS_E[V]}{dV}\,|_{V=V_E^{*e}}, \\
K_3 &= K_{SR}\frac{dS_R[V]}{dV}\,|_{V=V_R^{*e}}, & K_4 &= K_{RE}\frac{dS_E[V]}{dV}\,|_{V=V_E^{*e}}, \\
K_5 &= K_{RS}\frac{dS_S[V]}{dV}\,|_{V=(V_S^{*e}-V_S^{*i})}.
\end{aligned}$$

In the following, in a reasonable approximation we assume an instantaneous rise of the synaptic response function followed by an exponential decay i.e., $\alpha_e \gg \beta_e$, and $\alpha_i \gg \beta_i$. This approximation reduces the second-order temporal operators $\hat{L}_{e,i}$ given by Eq. (5.39) to the first-order operators $\hat{L}_e = 1 + i\omega/\beta_e$, and $\hat{L}_i = 1 + i\omega/\beta_i$. Using this approximation, the sixth-order characteristic equation (the denominator of $\tilde{G}_{1,2}$ given by Eq. (5.41)) simplifies to a third-order equation, which is more analytically tractable. It can be shown that this simplification does not affect the spectral power in the delta and alpha ranges. Moreover, it is widely accepted that anesthetic agent propofol prolongs the temporal decay phase of inhibitory synapses while the rise rates remain unaffected [28, 35].

Taken together, by fitting the power spectrum of EEG given by Eq. (5.40) to the empirical spectra, we are able to estimate seven model parameters, namely, the power normalization $D = \sqrt{2\kappa K_1}$, excitatory and inhibitory synaptic decay rates β_e, and β_i, axonal propagation delay τ, and the total loop gains C_1, C_2, and C_3. Therefore, in this case study the vector of unknown parameters to be estimated is $\boldsymbol{p}_{III} = (D, \tau, \beta_e, \beta_i, C_1, C_2, C_3)$, where based on the physiological limits, all the parameters are restricted to be positive. Furthermore, the response functions for the inhibitory synapses exhibit a longer characteristic rise and decay time constants than the excitatory synapses, thus $\alpha_e > \alpha_i$, and $\beta_e > \beta_i$ (Constraint I).

In the following, we derive more analytical conditions for the stability of the system which will be imposed over the chi-squared error function in spectral fitting problem. To this end, we employ the method described in Theorem 1 of chapter 2. We first probe the conditions for the stability of the system in the absence of time delay i.e., $\tau = 0$. Then, by increasing the delay value we investigate about whether or not there exists a critical delay for which the system becomes unstable. Since the power spectrum analysis is valid only if the resting state of the system is stable, we seek the conditions which guarantee that there exists no critical value for the time delay, i.e., the introduction of delay does not yield any bifurcation, thus the system remains stable. Now consider the denominator of the Fourier transform of the Green's function given by Eq. (5.41), which can be written in the following general form of transcendental equations

$$P(\lambda) + e^{-\lambda\tau} Q(\lambda) = 0, \tag{5.42}$$

where $P(\lambda)$ and $Q(\lambda)$ are polynomial in $\lambda = i\omega$, given by

$$\begin{aligned} P(\lambda) &= a_3\lambda^3 + a_2\lambda^2 + a_1\lambda + a_0, & (5.43)\\ Q(\lambda) &= b_2\lambda^2 + b_1\lambda + b_0, & (5.44)\end{aligned}$$

with

$$\begin{aligned} a_3 &= \frac{1}{\beta_e^2\beta_i}, & a_2 &= \frac{2}{\beta_e\beta_i} + \frac{1}{\beta_e^2}\ ,\\ a_1 &= \frac{C_2+2}{\beta_e} + \frac{1}{\beta_i}, & a_0 &= 1 + C2\ ,\\ b_2 &= 0\ , & b_1 &= -\frac{C_1}{\beta_i}\ ,\\ b_0 &= C_3 - C_1\ . \end{aligned}$$

In the absence of delay ($\tau = 0$), the characteristic equation described by Eq. (5.42) recast to the following polynomial

$$a_3\lambda^3 + a_2\lambda^2 + (a_1 + b_1)\lambda + (a_0 + b_0) = 0. \tag{5.45}$$

By Routh-Hurwitz conditions, this polynomial is stable if and only if

$$a_3 > 0\ , \quad a_2 > 0\ , \quad a_1 + b_1 > 0\ , \quad a_0 + b_0 > 0\ , \quad a_2(a_1 + b_1) - a_3(a_0 + b_0) > 0\ .$$

Thus, the non trivial conditions for the stability of the system in the absence of delay are

$$\begin{aligned} \beta_i(C_2+2) + \beta_e(1 - C_1) &> 0, & (5.46)\\ C_3 + C_2 - C_1 + 1 &> 0, & (5.47)\\ (2\beta_e + \beta_i)\left(\frac{C_2+2}{\beta_e} + \frac{1 - C_1}{\beta_i}\right) - (C_3 + C_2 - C_1 + 1) &> 0. & (5.48)\end{aligned}$$

Moreover, according to the Theorem 1 described in chapter 2, by squaring and summing the the real and imaginary parts of the polynomials $P(\lambda)$ and $Q(\lambda)$ while the exponential is defined in terms of trigonometric functions, one obtains

$$a_3^2\Omega^3 + (a_2^2 - 2a_3a_1)\Omega^2 + (a_1^2 - 2a_2a_0 - b_1^2)\Omega + (a_0^2 - b_0^2) = 0, \tag{5.49}$$

where $\Omega = \omega^2$. Since $a_3 > 0$,

$$\mathcal{P}(\Omega) = \Omega^3 + \xi_2\Omega^2 + \xi_1\Omega + \xi_0, \tag{5.50}$$

where

$$\begin{aligned} \xi_2 &= \frac{a_2^2 - 2a_3a_1}{a_3^2} = (2\beta_e + \beta_i)^2 - 2\left(\beta_2^2 + \beta_e\beta_i(C_2+2)\right),\\ \xi_1 &= \frac{a_1^2 - 2a_2a_0 - b_1^2}{a_3^2} = \left(\beta_e^2 + \beta_e\beta_i(C_2+2)\right)^2 - 2\beta_e^2\beta_i(2\beta_e + \beta_i)(C_2+1) - \beta_e^2C_1^2,\\ \xi_0 &= \frac{a_0^2 - b_0^2}{a_3^2} = (\beta_e^2\beta_i)^2\left((C_2+1)^2 - (C_3 - C_1)^2\right). \end{aligned}$$

Now we seek the conditions under which the polynomial $\mathcal{P}(\Omega)$ has no positive real root. In a simplest way, if all the coefficients of a polynomial are positive, the polynomial can not have any positive real roots. In this situation, if the discriminant of the above polynomial i.e., $\Delta = 18\xi_2\xi_1\xi_0 - 4\xi_2^3\xi_0 + \xi_2^2\xi_1^2 - 4\xi_1^3 - 27\xi_0^2$ will be zero or positive ($\Delta \geq 0$), all the three roots are real and negative. In another situation, the above polynomial can have one negative real root and two complex conjugate roots. By Descartes' rule of signs, it can be shown that if the lead coefficient of a third order polynomial is positive, one negative real root is guaranteed if and only if the constant coefficient is positive. Moreover, if the discriminant $\Delta < 0$, then the polynomial has one real root and two complex conjugate roots. Thus, $\Delta < 0$, and $\xi_0 > 0$, guarantee that we have one negative real root and two complex roots i.e., $\mathcal{P}(\Omega)$ has no any positive real roots. In summary, the following conditions gurantee that the the denominator of the Fourier transform of the Green's function given by Eq. (5.41) is stable in the absence of the delay, and the introduction of a time delay can not cause a bifurcation i.e., for $\tau \geq 0$ the reduced thalamo-cortical model exhibits stable oscillations:

$$\begin{aligned}
\beta_i(C_2+2) + \beta_e(1-C_1) &> 0, \quad \text{(Condition II)}\\
C_3 + C_2 - C_1 + 1 &> 0, \quad \text{(Condition III)}\\
(2\beta_e + \beta_i)\left(\frac{C_2+2}{\beta_e} + \frac{1-C_1}{\beta_i}\right) - (C_3 + C_2 - C_1 + 1) &> 0, \quad \text{(Condition IV)}\\
(\beta_e^2\beta_i)^2\left((C_2+1)^2 - (C_3 - C_1)^2\right) &> 0, \quad \text{(Condition V)}\\
\Delta < 0, \;\; or \;\; if \;\; \Delta \geq 0 \; then \; \xi_1, \xi_2 &> 0, \quad \text{(Condition VI)}
\end{aligned}$$

5.6 Results of the parameter estimation in Case Studies I, II, and III

In this section, we show how given a set of ODEs or DDEs subjected to the additive noise, one can estimate the unknown model's parameters. Due to the lack of experimental data, we first consider the parameter estimation problem designed with artificial data set in two case studies: Case Study I) a noisy damped harmonic oscillator (governed by a second order ODE). Case Study II) a stochastic linear delay differential equation (governed by a first order DDE). Starting from known parameter values allows us to asses the performance of different optimization algorithms in different estimation problems. Then, the tested estimation method is applied to the real experimental data set to estimate the parameters of a thalamo-cortical model described in Case Study III.

For Case Studies I and II, the power spectrum of the model is computed by substituting a set of nominal parameters into the model equations. Then, in order to generate a set of pseudo-experimental data, a zero mean Gaussian white noise with the standard deviation of σ, is added to the simulated noise-free data. Mathematically, the generated *in silico* data can be expressed as [336]

$$\Psi = \Phi + \sigma r \tag{5.51}$$

where Φ and Ψ denote the simulated noise-free data and the corresponding noisy data, respectively. The parameter r is a pseudo-random value drawn from standard Gaussian distribution (with zero mean and unit variance), which can be generated by MATLAB command *randn*. In the present work, the standard deviation of additive Gaussian white noise is set to $\sigma = 0.2$.

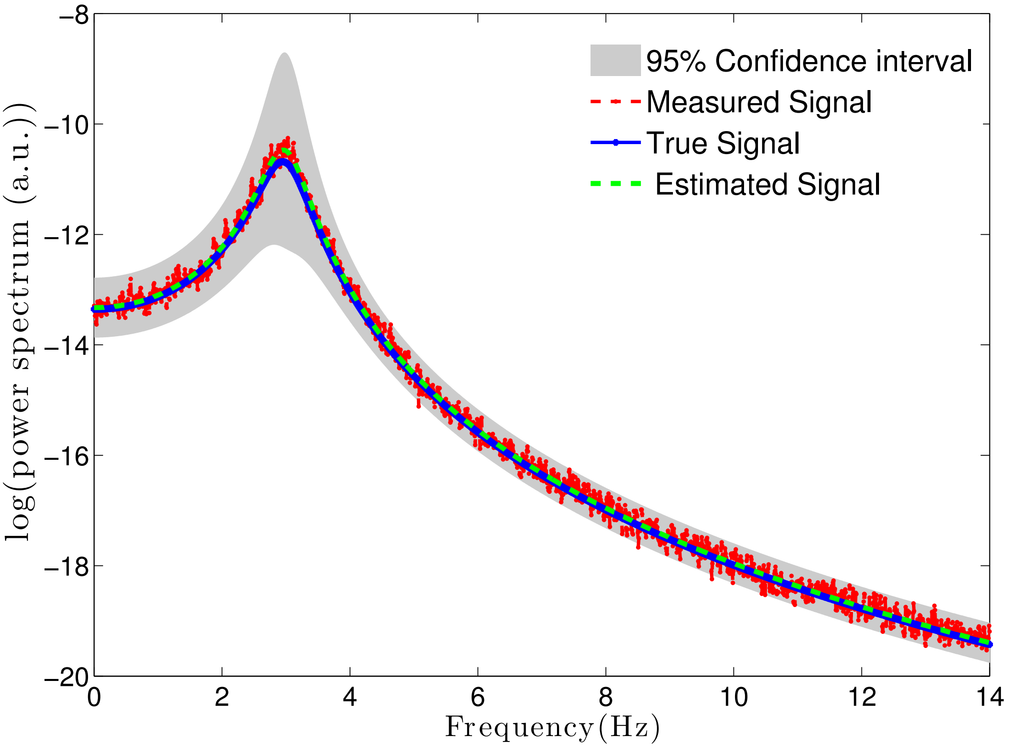

Figure 5.4. Estimating the parameters of a stochastic damped harmonic oscillator (Case Study I) from a set of noisy *in silico* data. Shown are the constructed power spectrum (*estimated signal*) versus the noise-free (*true signal*) and the noisy spectra (*measured signal*), encoded in dashed green, solid blue, and dashed red lines, respectively. In addition, the grey shaded area represents the 95% confidence interval. The true and estimated parameters are $\boldsymbol{p}_I^* = (\kappa, \gamma, f_0) = (0.103\ \text{mV}, 4.562\ \text{Hz}, 3.00\ \text{Hz})$, and $\boldsymbol{p}_I^* = (\kappa, \gamma, f_0) = (0.103\ \text{mV}, 4.562\ \text{Hz}, 3.00\ \text{Hz})$, respectively.

Case Study I deals with estimating the parameters of a stochastic damped harmonic oscillator by fitting the model's spectrum to a set of pseudo-experimental data. This estimation is shown in Fig. 5.4. In this figure, the estimated power spectrum (*estimated signal*) obtained by PSO algorithm is compared with the respective noise-free (*true signal*) and the noisy (*measured signal*) spectra. From the result, we observe that the estimated power spectrum is in very good agreement with the measured signal. The noise-free power spectrum was generated according to Eq. (5.34) with the true parameters $\boldsymbol{p}_I = (\kappa, \gamma, f_0) = (0.1\ \text{mV}, 5\ \text{Hz}, 3\ \text{Hz})$. White Gaussian noise with the standard deviation of $\sigma = 0.2$ was added to the true signal to generate the measured signal. Fitting this noisy data with PSO algorithm results in the estimated parameters $\boldsymbol{p}_I^* = (\kappa, \gamma, f_0) = (0.103\ \text{mV}, 4.562\ \text{Hz}, 3.00\ \text{Hz})$, which are very close to the true parameters $\boldsymbol{p}_I$. The estimated parameters $\boldsymbol{p}_I^*$ yield the best-fit value of $\mathcal{E}(\boldsymbol{p}_{\text{I}}^*) = 0.6554$.

Furthermore, the residuals between the measured and the simulated data in this case study are shown in Fig. 5.5. It can be seen that the residuals are uncorrelated. The lack of correlation between the residuals confirms that the estimation converges to the true parameters with sufficient accuracy.

It is worth pointing out that in this case study, by other optimization algorithms such as LM, DE, MH, and SA, we can obtain a similar estimation (not shown).

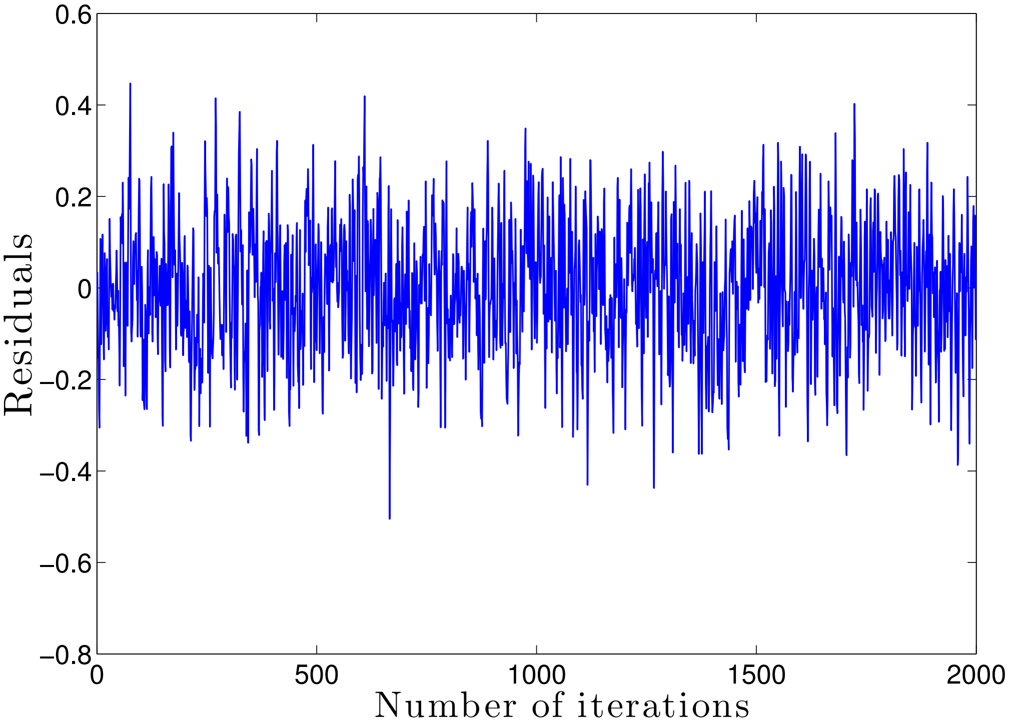

Figure 5.5. Residuals as a function of number iterations for Case Study I; power spectral fitting of a stochastic damped harmonic oscillator to a set of pseudo-experimental data.

Once the model parameters have been inferred, one can determine the uncertainties in the parameter estimations. Here, in order to check the accuracy of the estimation shown in Fig. 5.4, we plot the confidence regions of the calibrated parameters. Figure 5.6 illustrates the 95% elliptical and likelihood confidence regions for different pairs of parameter estimates in Case Study I. The elliptical confidence regions are obtained through the covariance matrix estimation, whereas the likelihood confidence regions are produced by PSO algorithm. In this case study, since $J(\boldsymbol{p}^*)^\top W J(\boldsymbol{p}^*) = 2H(\boldsymbol{p}^*)$, we observe that the covariance matrix approximated by Fisher Information Matrix (c.f. Eq. (5.24)) and Hessian matrix (c.f. Eq. (5.26)) are equal, which yields exactly the same elliptical confidence regions. Considering the conceptual difference of Hessian and FIM approaches in the derivative terms [436], the exact coincidence of the ellipsoids obtained by Hessian and FIM methods confirms that the accuracy in parameter estimations are well captured. Moreover, by comparing the likelihood confidence regions calculated via the PSO procedure (c.f. Eq. (5.27)) with the elliptical confidence regions, it is very clear that satisfied solutions can be obtained by using the PSO algorithm.

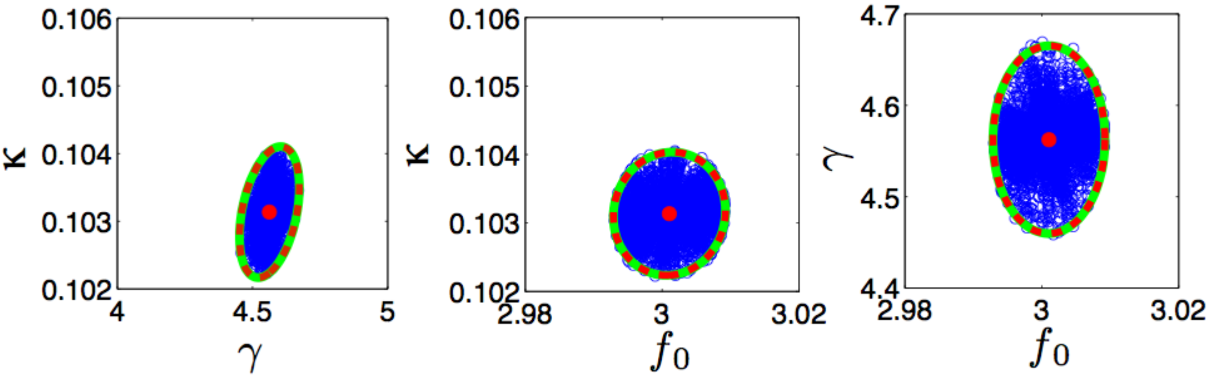

Figure 5.6. Comparison of 95% elliptical and likelihood confidence regions for different pairs of parameter estimates in Case Study I. The ellipsoids encoded in dashed red and green lines show the confidence regions obtained by approximating the covariance matrix through FIM and Hessian approaches, respectively. The regions constructed by the blue markers indicate the likelihood confidence regions produced by the PSO algorithm. The regions are centered at the optimal parameters $\boldsymbol{p}_I^* = (\kappa, \gamma, f_0) = (0.103 \text{ mV}, 4.562 \text{ Hz}, 3.00 \text{ Hz})$, which are illustrated by the filled red circles.

It was mentioned before that the parameter exploration in PSO algorithm is completely different with MH and SA algorithms (c.f. Sections 5.3.2, 5.3.4, and 5.3.5). Here we present a visual comparison of the way that parameters are estimated in these algorithms. In PSO, a population of particles evolves in the search space by cooperation and competition among themselves to find the global minimum. In this algorithm, the next position of each particle depends on its previous positions, as well as the positions of all the other particles. Figure 5.7 shows how the search space is explored in PSO algorithm by a swarm of 100 particles, i.e., with the swarm size of $S = 100$. It can be seen that initially the particles (blue markers) are uniformly distributed in the search space. Then, after a sufficient number of iterations, all the particles converge to the global minimum by attraction towards the global best position (red lines). It should be noted that the trajectory of the particles, at each iteration, determined by the combination of inertia (its previous position), cognitive (the best personal position) and social (the global best position) components not only one of them.

In the case of MH and SA algorithms, the search space is explored by Markov chains in such a way that the next step of the chains depends only on the current state of the chains. The trajectory of Markov chains constructed by MH and SA methods are plotted in Fig. 5.8. We observe that using MH (panel **A**), after a short transition, the chains oscillate around the true parameter values, whereas the chains constructed by SA (panel **B**) show fluctuations only at the beginning, since the algorithm was initiated with a high temperature value. As the temperature is reduced to zero, according the cooling schedule, the chains converge to the true parameter values with quickly decreasing the amplitude of chain oscillations.

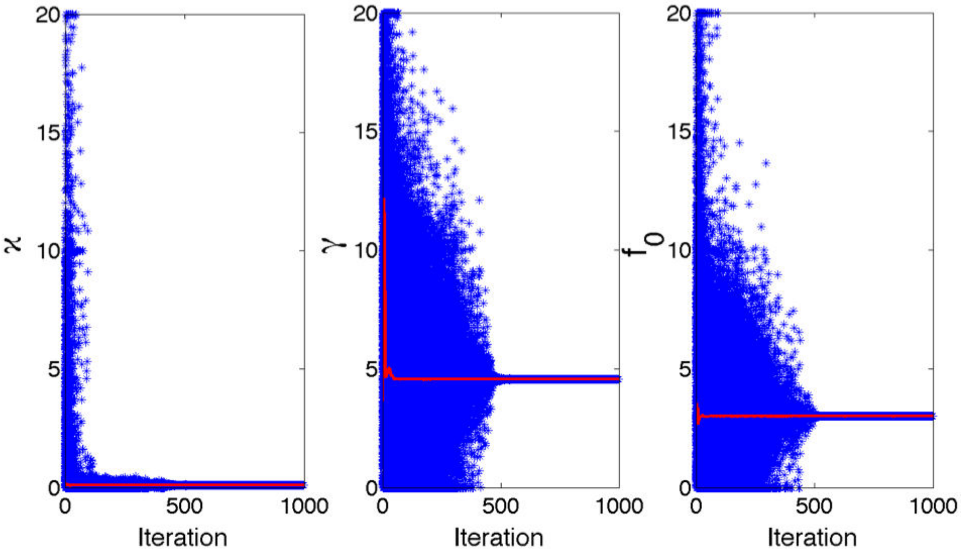

Figure 5.7. Trajectory of the particles in PSO algorithm used for estimating the parameters of a stochastic damped harmonic oscillator (Case Study I). The blue markers show the positions of different particles in the swarm, which converge to the trajectory of the global best particles illustrated in red lines.

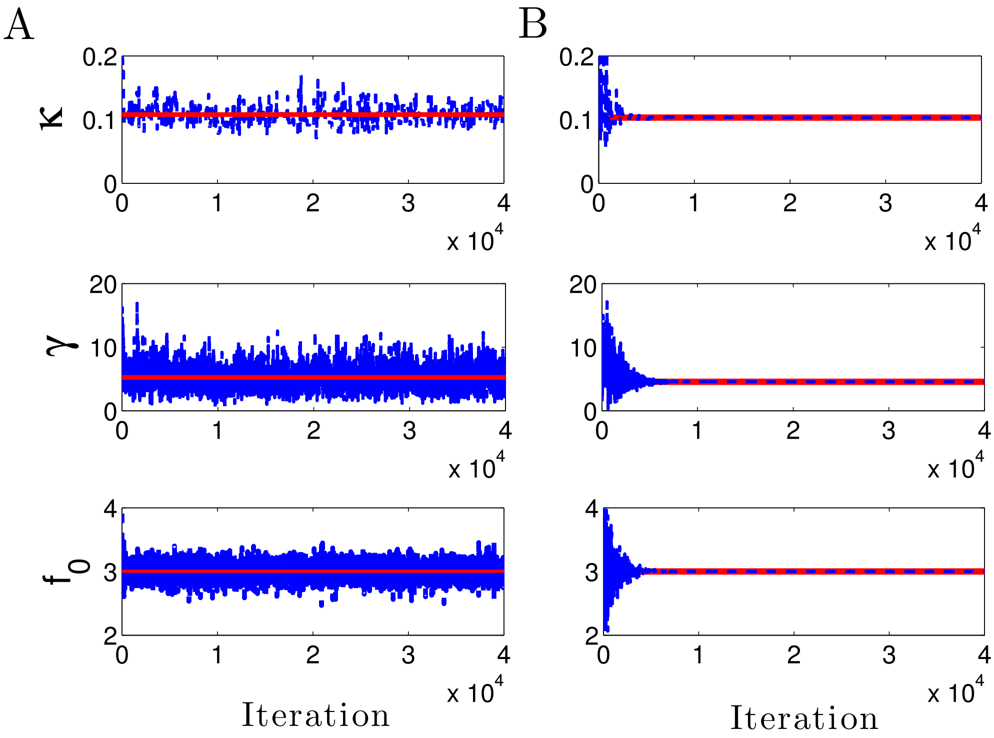

Figure 5.8. Evolution of Markov chains in the power spectral fitting of a stochastic damped harmonic oscillator (Case Study I) to a set of *in silico* data. The chains in panels (**A**) and (**B**) are obtained by MH and SA algorithms, respectively. The values of true parameters are illustrated in the red lines.

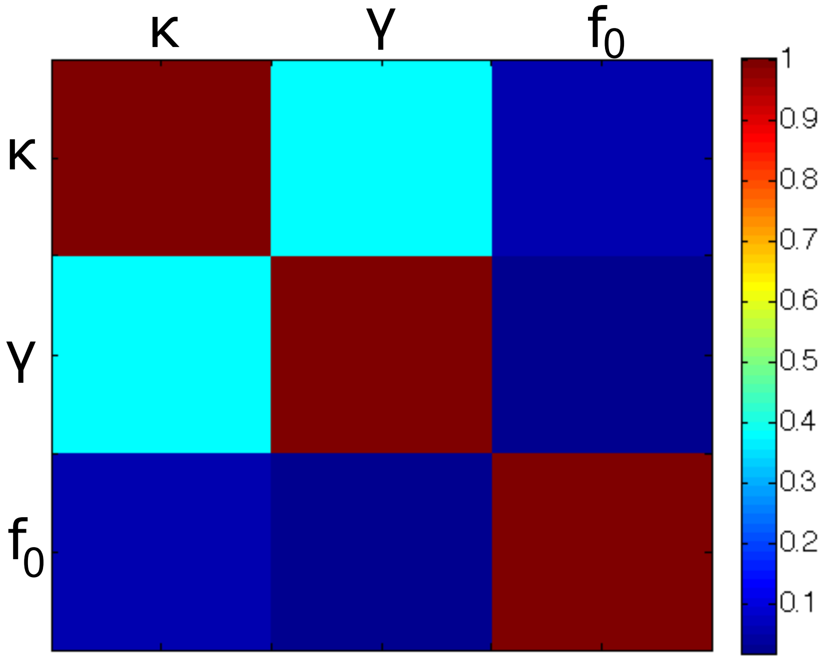

Figure 5.9. Correlation matrix in Case Study I; power spectral fitting of a stochastic damped harmonic oscillator to a set of pseudo-experimental data. The estimated parameters are κ, γ, and f_0.

An easy way to study the practical identifiability of an estimation is to plot the correlation matrix of the model parameters. Here, the local identifiability of the obtained estimations is evaluated based on the correlation analysis. Figure 5.9 displays the color plot of the correlation matrix according to Eq. (5.28), for Case Study I. In this figure, it can be observed that there is no element equals to ±1 out of the diagonal. The lack of correlation among the estimated parameters indicates that all the parameters are identifiable. Furthermore, the Fisher Information Matrix (FIM) is not singular for this estimation. These results indicate that the estimated parameters in this case study are captured adequately accurate.

Since the sensitivity analysis is a key tool of the local identifiability procedures, here, it is performed to evaluate the obtained estimations. In order to visualize the influence of a small parameter change on the model output we can plot the fitness function with respect to the model parameters over a range of values. Figure 5.10 illustrates the results of sensitivity analysis in Case Study I. In panels **A**, **B**, and **C**, the fitness function is plotted versus each model parameter, while other parameters are fixed at their nominal values $\boldsymbol{p}_I^*$. It can be observe that for each parameter, the estimated values given by $\boldsymbol{p}_I^* = (\kappa, \gamma, f_0) = (0.103 \text{ mV}, 4.562 \text{ Hz}, 3.00 \text{ Hz})$ are located at the minima of the fitness function (see the red squares). In addition, the sensitivity of the model measured through the Hessian matrix defined by Eq. (5.29) is shown in panel **D**. From this figure we can observe that the fitness function in panel **A** exhibits sharper valley around the optimal values compare to the others. This indicates that the fitness function in this case study is much more sensitive to the parameter κ than to the other parameters, in consistence with the sensitivity indices shown in panel **D**. In contrast, a very flat valley is observed in the region of parameter space near the minimum in panel **B**, which indicates a very low sensitivity to the the parameter γ, as illustrated in panel **D**. It is also worth mentioning that since in this case study $J(\boldsymbol{p}^*)^\top W J(\boldsymbol{p}^*) = 2H(\boldsymbol{p}^*)$, the sensitivity of the fitness function to the model parameters measured by Jacobian matrix given by Eq. (5.30) are qualitatively identical with those obtained through the Hessian Matrix (more precisely, $\Gamma(p_j) = 2\Lambda(p_j)$).

In Fig. 5.11, the inverse of fitness function normalized by its values at the estimates i.e., $\dfrac{1}{\mathcal{E}(\boldsymbol{p})/\mathcal{E}(\boldsymbol{p}^*)}$ is plotted for each model parameter (blue curves), while the other parameters are fixed at their estimated values $\boldsymbol{p}_I^*$. Since the minimum of fitness function for each model parameter is located at the estimated parameters $\boldsymbol{p}_I^*$, the normalized functions exhibit a maximum at the optimal values (see the filled green circles). In panels **A**, **B**, and **C**, each normalized fitness function is fitted with a Gaussian distribution (encoded in dashed red lines) with the mean value at the optimal values $\boldsymbol{p}_I^*$, and unknown standard deviation of σ. Then, to compare the sensitivity of the fitness function to the model parameters, the estimated standard deviations of the fitted distributions i.e., σ_κ, σ_γ, and σ_{f_0} are illustrated in panel **D**. It can be seen that, in consistence with the results shown in Fig. 5.10, the fitness function reveals a high sensitivity to the parameter κ compare to the other parameters, whereas it is less sensitive to the parameter γ than to the others.

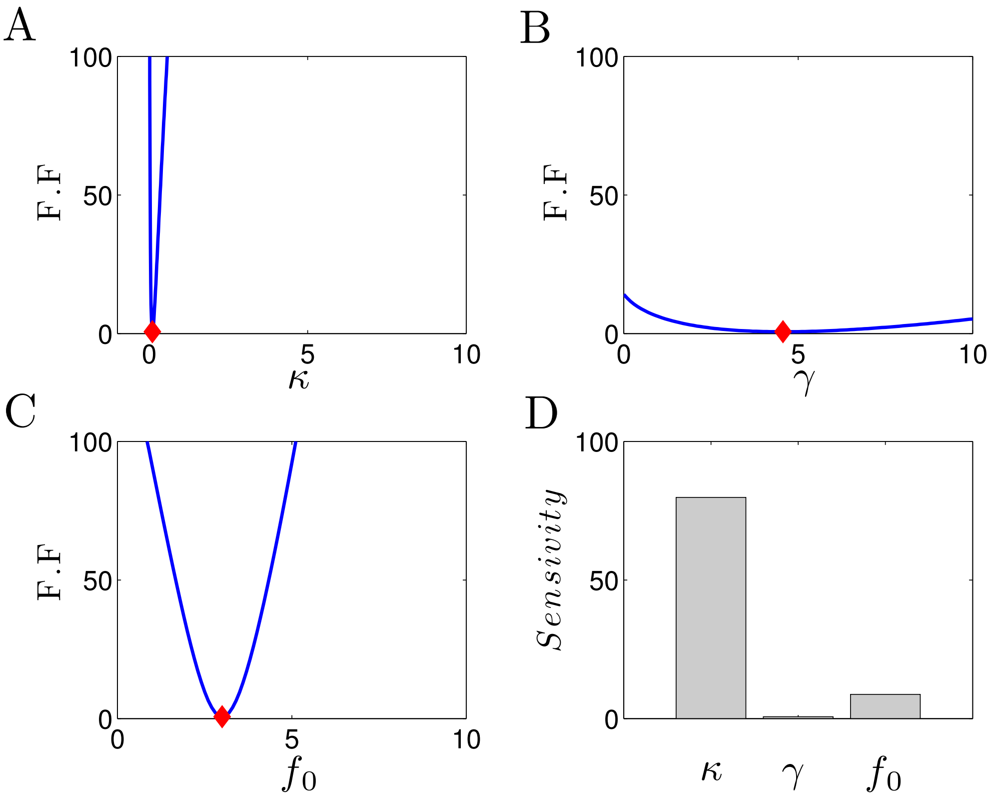

Figure 5.10. Sensitivity analysis in Case Study I; power spectral fitting of a stochastic damped harmonic oscillator to a set of *in silico* data. Panels (**A**), (**B**), and (**C**) show the plotted fitness function versus the model parameters κ, γ, and f_0, respectively. The red squares indicate the values of the estimated parameters $\boldsymbol{p}_I^* = (\kappa, \gamma, f_0) = (0.103 \text{ mV}, 4.562 \text{ Hz}, 3.00 \text{ Hz})$. Panel D illustrates the sensitivity of the fitness function to the model parameters measured through the Hessian matrix according to Eq. (5.29).

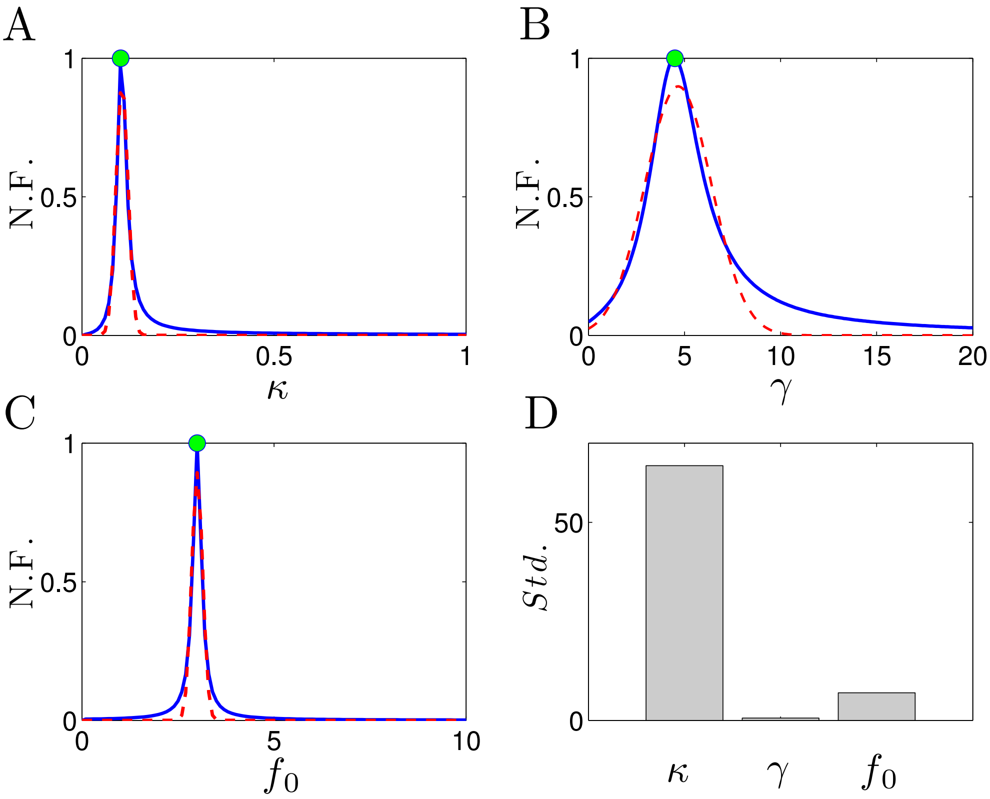

Figure 5.11. Sensitivity analysis measured through the fitting of a Gaussian distribution to the normalized fitness function, in Case Study I. In panels (**A**), (**B**), and (**C**) the blue lines show the normalized fitness function defined by $\frac{1}{\mathcal{E}(\boldsymbol{p})/\mathcal{E}(\boldsymbol{p}^*)}$ versus the model parameters κ, γ, and f_0, respectively. The filled green circles illustrate the values of the estimated parameters $\boldsymbol{p}_I^* = (\kappa, \gamma, f_0) = (0.103\ \text{mV}, 4.562\ \text{Hz}, 3.00\ \text{Hz})$. In each panel, a Gaussian distribution with the mean value at $\boldsymbol{p}_I^*$, and an unknown standard deviation of σ is fitted to the normalized fitness function (dashed red lines). (**D**) The estimated standard deviations of the fitted Gaussian distributions i.e., σ_κ, σ_γ, and σ_{f_0}.

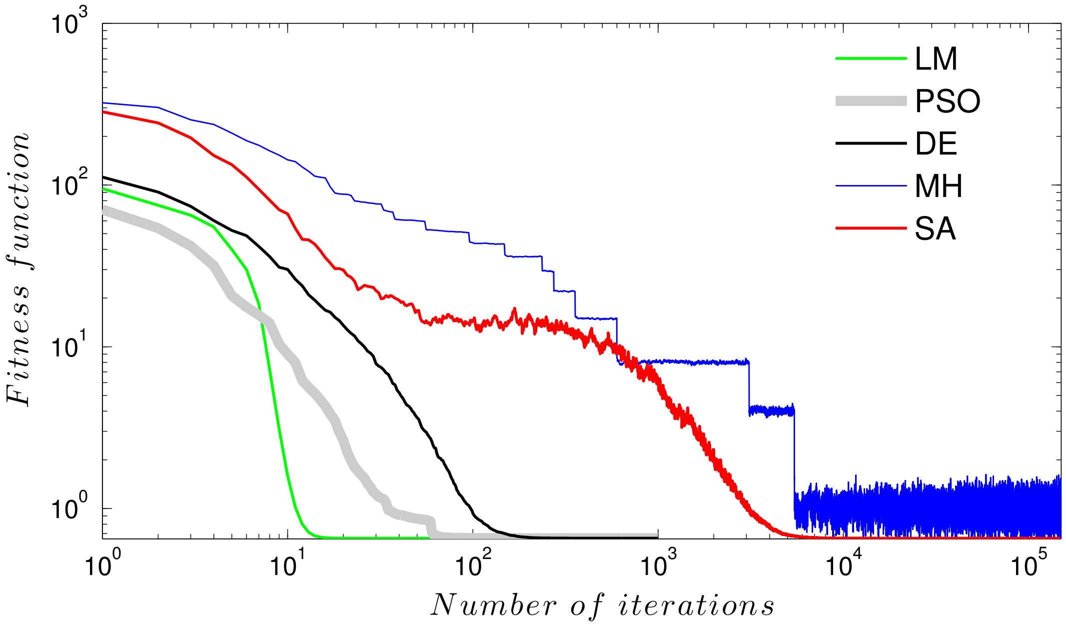

Figure 5.12. Convergence curves of several optimization algorithms used in Case Study I. The values of fitness function versus the number of iterations in a log-log scale, for different optimization algorithms namely LM, PSO, DE, MH, and SA are shown in green, thick gray, black, blue and red lines, respectively.

Here, in order to compare the convergence speed of different optimization methods carried out in Case Study I, we plot their convergence curves i.e., the fitness function values versus the iteration numbers. Figure 5.12 shows the convergence curve of LM, PSO, DE MH, and SA algorithms averaged over 100 runs. It can be observe that although the fitness function values in the all methods finally converge to a same minimum, the LM algorithm shows the fastest convergence speed than the other algorithms. The PSO method is the second fastest one, whereas the DE method has a faster convergence compare to the MH and SA algorithms. In addition, we observe that in SA algorithm, after a fluctuating period, when the temperature is reduced toward zero, the fitness function converge to the minimum value in a damping manner. In contrast, in MH method, the the fitness function keep oscillating around the minimum value.

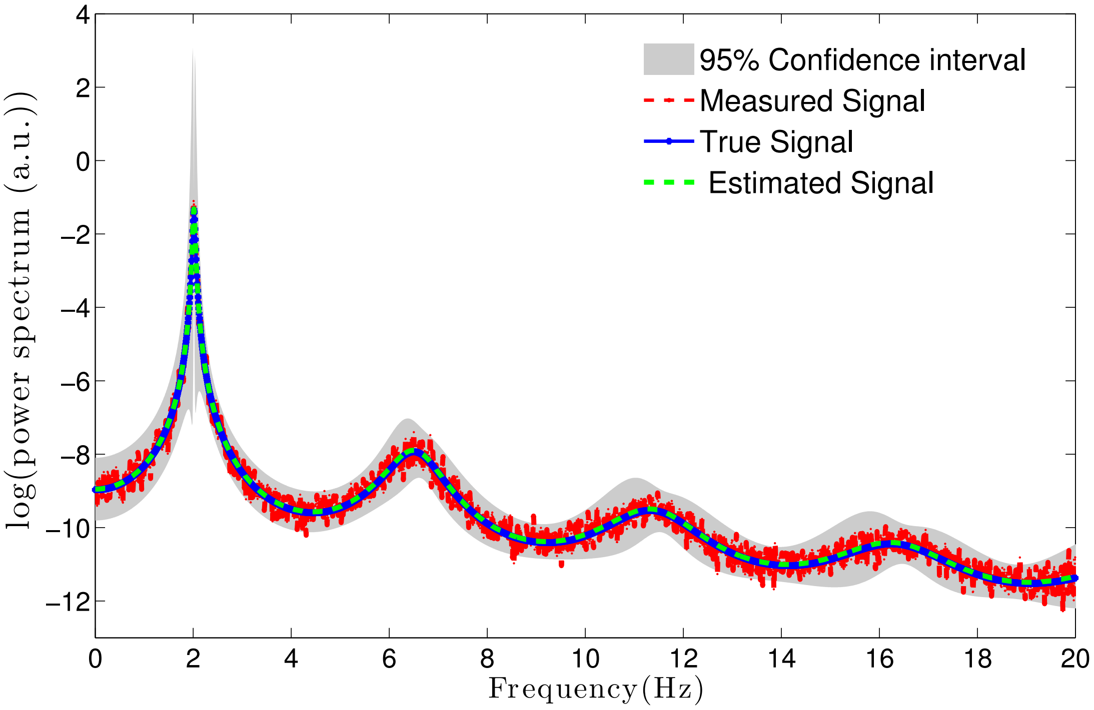

Figure 5.13. Estimating the parameter values of a stochastic linear delay differential equation (Case Study II) from a set of *in silico* data. Shown are the estimated power spectrum (dashed green line) versus the corresponding noise-free signal (blue line) and the noisy measured data (dashed red line). In addition, the grey shaded area represents the 95% confidence interval. The true and estimated parameters are $\boldsymbol{p}_{II} = (\kappa, a, b, \tau) = (0.1 \text{ mV}, -17.3, -21.32, 0.2)$, and $\boldsymbol{p}^*_{II} = (\kappa, a, b, \tau) = (0.103 \text{ mV}, -18.4, -21.49, 0.2)$, respectively.

In Case Study II, the power spectrum of a stochastic linear delay differential equation is fitted to a set of pseudo-experimental data. This case study poses a multimodal objective function, which is more challenging problem in optimization compare to Case Study I as an example of unimodal functions. Figure 5.13 demonstrates the estimated power spectrum from the respective noisy measured signal, which is obtained by the PSO algorithm. It can be seen that the constructed spectrum is very close to the true signal. Here, the noise-free power is obtained by substituting the true parameters $\boldsymbol{p}_{II} = (\kappa, a, b, \tau) = (0.1 \text{ mV}, -17.3, -21.32, 0.2)$ in Eq. (5.36). The fitted signal yields the optimal parameters $\boldsymbol{p}^*_{II} = (\kappa, a, b, \tau) = (0.103 \text{ mV}, -18.4, -21.49, 0.2)$, which allow us to reproduce almost exactly the measured signal. The fitness function of this estimation is $\mathcal{E}(\boldsymbol{p}^*_{\text{II}}) = 32.15$, which is the best value obtained through 100 runs.

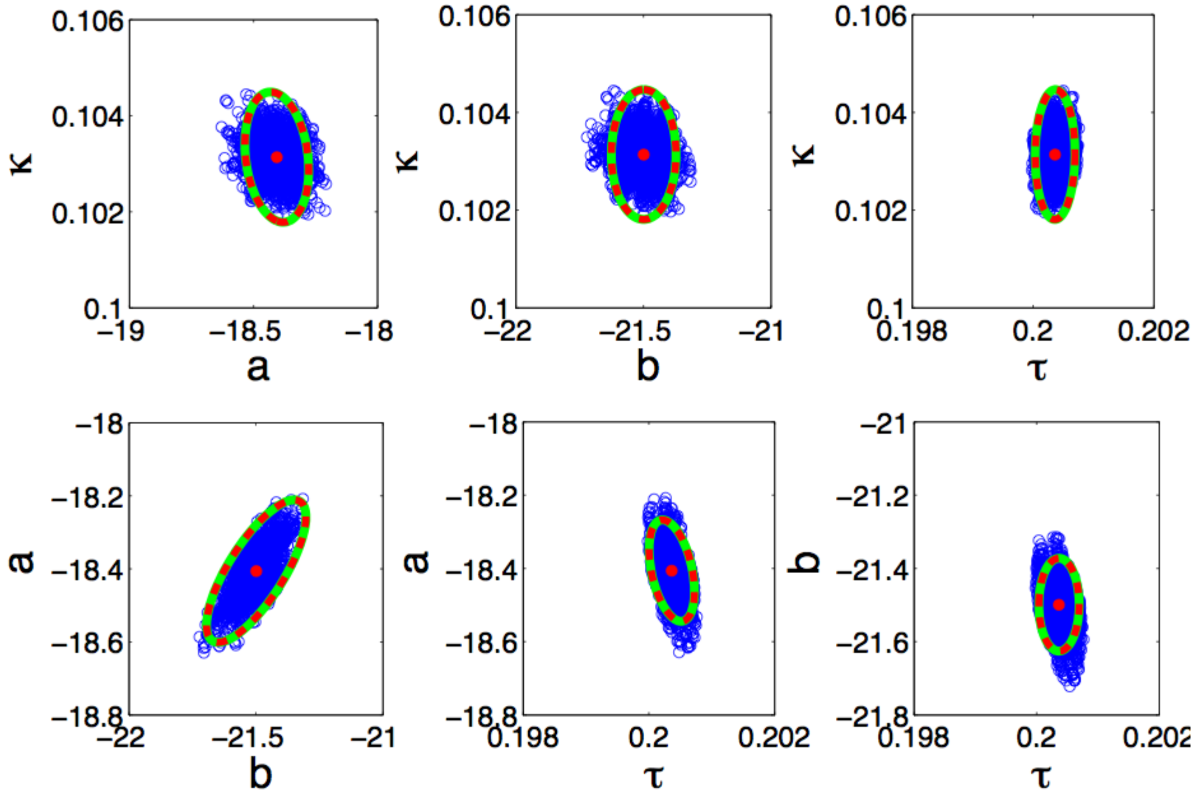

Figure 5.14. The elliptical and likelihood confidence regions at the 95% confidence level for each pair of the estimated parameters in Case Study II. The ellipsoids are calculated with FIM (in dashed red) and Hessian (in green) matrices, whereas the likelihood confidence regions (in blue) are produced by PSO algorithm. The estimated parameters $\boldsymbol{p}_{II}^{*} = (\kappa, a, b, \tau) = (0.103\,\mathrm{mV}, -18.4, -21.49, 0.2)$ encoded by filled red circles are located at the center of confidence regions.

Fig 5.14 displays the confidence regions for all possible pairs of the estimated parameters in Case Study II. Similar to Case Study I, the elliptical confidence regions are calculated by covariance matrix estimation according to Eqs. 5.24, and 5.26, whereas the likelihood confidence regions are provided by PSO method according to Eq. (5.27). It can be seen that the ellipsoids constructed with covariance matrix estimation using FIM or Hessian matrix coincide, because in this case study $J(\boldsymbol{p}^*)^\top W J(\boldsymbol{p}^*) = 2H(\boldsymbol{p}^*)$. However, comparing the elliptical and likelihood confidence regions, we observe that when one of the estimated parameters is either parameter a, or b, the regions evaluated based on covariance matrix are different from those computed through the PSO method.

In order to identify the origin of discrepancy between elliptical and likelihood confidence regions in Case Study II (c.f. Fig. 5.14, we investigate the correlation among the model parameters. In Fig. 5.15, we have plotted the correlation matrix of the model parameters in this case study. If two parameters are highly correlated, the change in the model output caused by a change in one parameter can be compensated by an appropriate change in the other parameter. This prevents the parameters from being uniquely identifiable. In other words, for a pair of correlated parameters there exist many combinations which give almost the same value of the fitness function. Based on the observation of Fig. 5.15, the parameters a and b are practically non-identifiable since they are highly correlated, whereas other pairs of parameters are uncorrelated. To overcome such problem, the pairs of correlated parameters must be removed analytically by introduction of new variables. In this case study, setting a candidate solution in the form of $y(t) = Ce^{\lambda t}$ yields the following nonlinear transcendental characteristic equation:

$$\lambda - a - be^{-\lambda\tau} = 0,$$

where, by inserting $\lambda = i\omega$, and separating the real and imaginary parts we obtain

$$\begin{aligned} a &= -b\cos(\omega\tau), \\ \omega &= -b\sin(\omega\tau), \end{aligned} \tag{5.52}$$

or equivalently,

$$\begin{aligned} a &= \omega/\tan(\omega\tau), \\ b &= -\omega/\sin(\omega\tau). \end{aligned} \tag{5.53}$$

where $\omega = 2\pi\Omega$. Thus, introducing the parameter Ω according to the above equations, leads to a model equation containing three unknown parameters: κ, Ω, τ, in which the plotted correlation matrix in this case reveal no correlation among the parameters (not shown). As it is shown in Fig. 5.16, using this set of uncorrelated parameters, the elliptical confidence regions coincide exactly with the likelihood-based regions. These results indicate a precise estimation with uniquely identifiable estimates. Here, to compute the confidence regions of the model parameters we employed the same approach as used in Fig. 5.14.

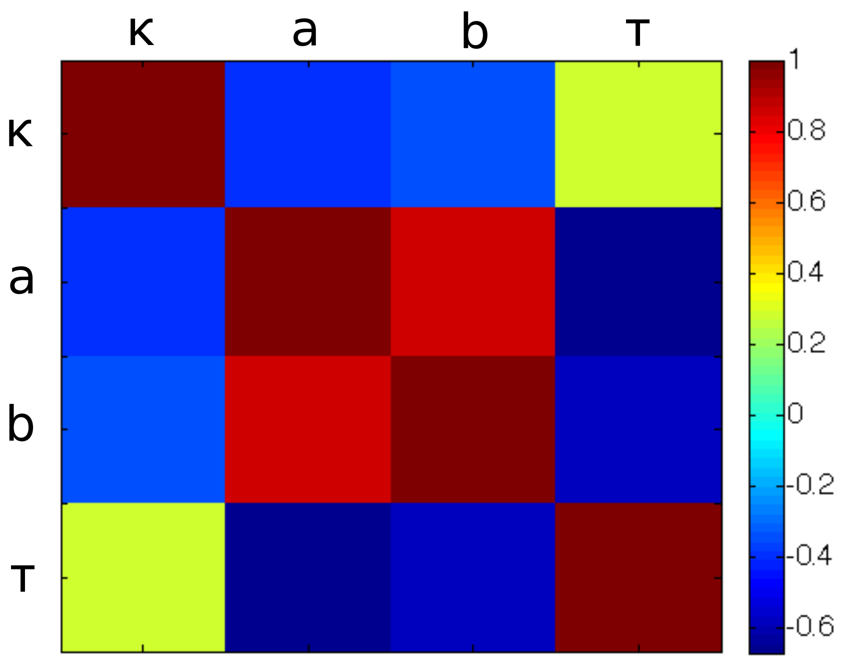

Figure 5.15. Correlation matrix in Case Study II; power spectral fitting of a stochastic linear delay differential equation to a set of noisy pseudo-experimental data. The estimated parameters are κ, a, b, and τ.

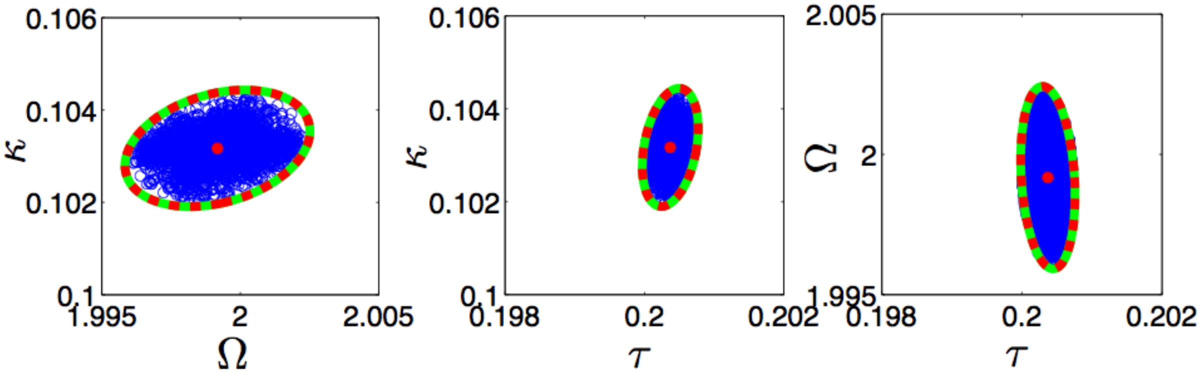

Figure 5.16. The elliptical and likelihood confidence regions in Case Study II with the uncorrelated parameters κ, Ω, and τ. The regions are centered at the estimated parameters $\boldsymbol{p}^*_{II} = (\kappa, \Omega, \tau) = (0.103 \text{ mV}, 1.99, 0.2)$, whereas the true parameters are $\boldsymbol{p}_{II} = (\kappa, \Omega, \tau) = (0.1 \text{ mV}, 2, 0.2)$.

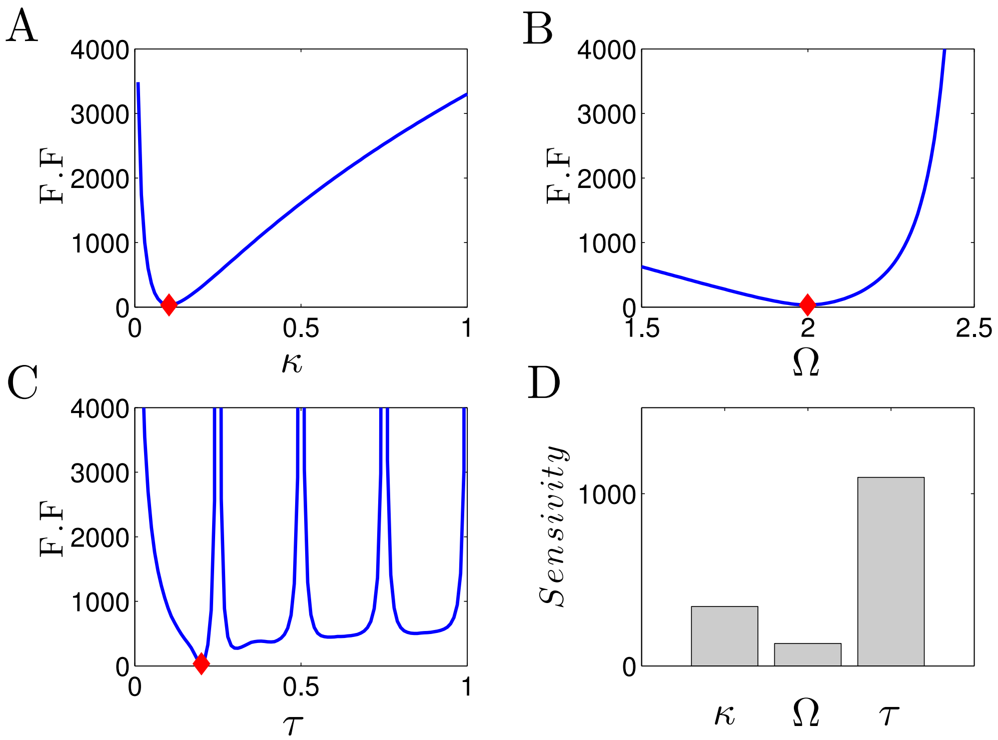

Figure 5.17. Sensitivity analysis in Case Study II; power spectral fitting of a stochastic linear delay differential equation to a set of *in silico* data. Panels (**A**), (**B**), and (**C**) show the plotted fitness function versus the model parameters κ, Ω, and τ, respectively. In each panel, the estimated parameters $\boldsymbol{p}_{II}^{*} = (\kappa, \Omega, \tau) = (0.103 \text{ mV}, 1.99, 0.2)$ are illustrated by the red squares. (**D**) The sensitivity of the fitness function to the model parameters measured through the Hessian matrix according to Eq. (5.29).

Here we investigate the sensitivity of the fitness function to the estimated parameters in Case Study II. In Fig. 5.17, the panels **A**, **B**, and **C** show the landscape of fitness function with respect to the parameters κ, Ω, and τ, respectively. It can be seen that the fitness function exhibits a sharp valley around the delay optimal values (c.f. panel **C**), while there are multiple local minima close to the global solution. In contrast, the fitness landscape is very flat around the optimal value of Ω compare to the other parameters (c.f. panel **B**). Moreover, panel **D** shows the sensitivity values measured by the Hessian matrix according to Eq. (5.29). We observe that in consistent with the plotted landscapes, the fitness function of this case study is much more sensitive to the delay values than to the other parameters, whereas it is less sensitive to the parameter Ω. In order to confirm these results, in Fig. 5.18, for each model parameter, we have plotted the normalized fitness function defined by $\frac{1}{\mathcal{E}(\boldsymbol{p})/\mathcal{E}(\boldsymbol{p}^{*})}$. In each panel **A**, **B**, and **C** a Gaussian distribution with the mean value located at the optimal values and an unknowing standard deviation of σ is fitted to the normalized fitness function. The values of the measured standard deviations are illustrated in panel **D**. It can be observed that in consistence with the sensitivity analysis shown in Fig. 5.17, the fitness function is more sensitive to parameter τ, whereas the parameter Ω has the lowest sensitivity index.

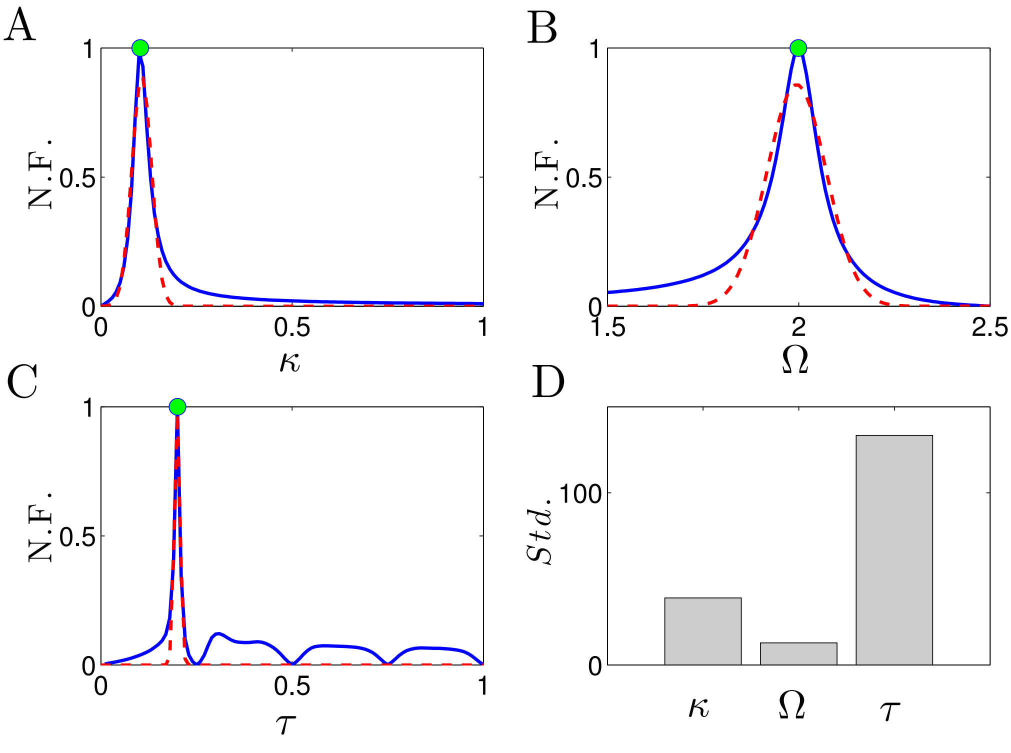

Figure 5.18. Sensitivity analysis measured by fitting a Gaussian distribution to the normalized fitness function in Case Study II. Panels (**A**), (**B**), and (**C**) show the normalized fitness function defined by $\frac{1}{\mathcal{E}(\boldsymbol{p})/\mathcal{E}(\boldsymbol{p}^*)}$ respect to the model parameters κ, Ω, and τ, respectively. The estimated parameters $\boldsymbol{p}_{II}^* = (\kappa, \Omega, \tau) = (0.103 \text{ mV}, 1.99, 0.2)$ are illustrated by the filled green circles. In each panel, a Gaussian distribution with the mean value at $\boldsymbol{p}_I^*$, and an unknowing standard deviation of σ is fitted to the normalized fitness function (dashed red lines). (**D**) The measured standard deviation of the fitted Gaussian distributions i.e., σ_κ, σ_Ω, and σ_τ.

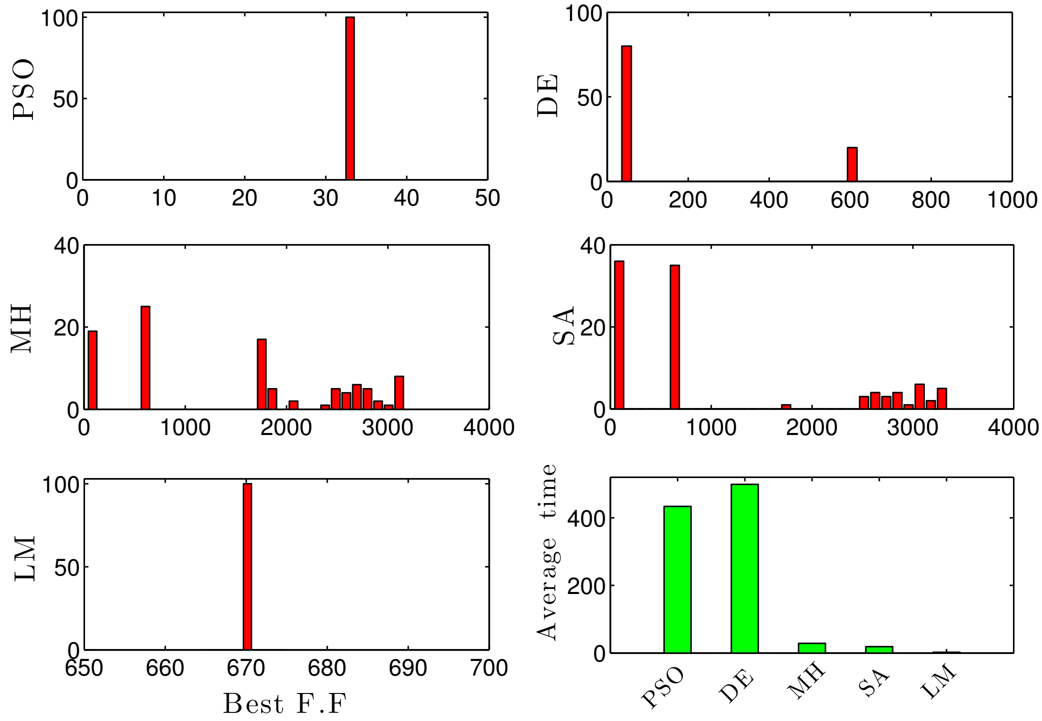

Figure 5.19. Comparing the performance of different optimization algorithms through 100 independent runs in Case Study II. The red bars indicate the histogram of obtained fitness function by the applied algorithm. The average of running time for the algorithms are shown by green bars. For clarity reasons, the results are also reported in Table 5.1.

Finally, for this case study, we compare the performance of different optimization algorithm presented in section 5.3, i.e., LM, PSO, DE, MH, and SA. For the sake of fair comparison, each optimization algorithm has been ran 100 times with each run executed for 10000 iterations. The initial guesses in the LM, MH, and SA algorithms were created randomly within the parameter search space to have an identical starting condition with the PSO and DE methods. The parameter search space was limited in the range [0,20] for each parameter. The results for 100 runs are reported in Fig. 5.19 and Table 5.1. Based on these results it can be observed that the PSO, DE, MH and SA methods succeeded in finding the global minimum in 100, 80, 18, and 33 times out of 100 runs, respectively, as indicated by the number of counts of the best fitness value in Table 5.1. However, the LM algorithm as a local optimization search method fails to arrive at the global minimum. If we compare these algorithms, the results obtained with the PSO and DE significantly outperformed the achieved results via LM, MH and SA algorithms. In addition, the PSO delivers better solutions than the DE method, and the SA algorithms outperform the MH method.

Furthermore, for each algorithm, the best value of fitness function, its mean value and the average of running time are listed in Table 5.1. According to these results, although LM method shows the fastest convergence speed, it can not find the global minimum since it get easily stuck at a local minimum. In contrast, although the PSO and DE methods reveal a high computational costs, they show very better performance in finding the better solutions. The simulation results show that although both the PSO and DE algorithms are competitive in finding the global minimum, the convergence speed of PSO is slightly better than the DE algorithm, and the SA algorithms is faster than the MH method.

Our findings, in agreement with the results in other reports, show that although the local search algorithms converge rapidly on a minimum, they can arrive at the global minimum only if the algorithm starts with an initial guess of the parameters at the vicinity of the global minimum.

Table 5.1. Comparing the results obtained by different optimization algorithms achieved from 100 independent runs in Case Study II. The best values of fitness function (minimum), the related counts, its minimum value and the average of computational time (in second) for each algorithm are illustated in the table.

Algorithm	Minimum	Counts	Mean	Compuational time (Sec)
PSO	32.15	100	33.15	433.83
DE	33.20	80	147.95	498.76
MH	37.77	18	1484.2	28.54
SA	33.50	33	1065.1	19.01
LM	670	100	670	2.31

The first two case studies were designed with the measured *in silico* data. In the following we identify the parameters of the third case study; estimating the parameters of a thalamo-cortical model described by a set of coupled stochastic delay differential equations through the model spectral fitting to the *in vivo* experimental data. This model which has been referred to it as a *reduced* thalamo-cortical model in [37], is able to reproduce the specific changes in EEG rhythms during the transition from awake state to anesthesia condition; increased activities in power spectrum of frontal EEG within delta $(0 - 4Hz)$ and alpha $(8 - 13)$ frequency bands, but increased delta and decreased alpha activities in EEG spectral power recorded over occipital head region. See section 5.5.3, for the details of the model.

In Fig. 5.20 the power spectrum of the model given by Eq. (5.40) is fitted to the power spectra of EEG recorded over frontal and occipital head regions during awake and anesthesia conditions. From the figure, it can be seen that a close prediction of the observed certain features in experimental data can been achieved by fitting the proposed model with the PSO algorithm.

It is important to point out that in most of the cases, by using a standard fitness function defined by the discrepancy between the models output and the measured data we are not able to fit the spectral power peak observed in delta frequency range (c.f. panels **A**, **B**, and **D**). However, since the delta peak is one of the most important observed specific EEG features, we employed a biased chi-squared function according to Eq. (5.6) in order to fit the model with the spectral power peak in this range. Taking a biased the fitness function with more weight value in delta frequency band the model output is forced to be fitted with the observed spectral power peaks. For instance, in panel **A**, we set $c_1 = 20$, $c_2 = 1$, $c_3 = 10$, $c_4 = 1$ to fit the model with the observed delta peak. It is trivial that $c_1 = c_2 = c_3 = c_4 = 1$ results in the standard chi-squared function (as used in panel **C**).

Fitting the spectral power given by Eq. (5.40) to the power spectrum of occipital EEG in awake state shown in Fig. 5.20**A** yields the estimates $\boldsymbol{p}^*_{III} = (27.02, 0.04, 69.10, 8.99, 0.68, 0.45, 0.13)$. Here, for this case study, we measure the sensitivity of the fitness function to the estimated parameters. Figure 5.21 presents the plotted fitness function versus the model parameters over a range of values while the other parameters are fixed at their estimated values. The sensitivity of the fitness function are also computed through the Hessian matrix according to Eq. (5.29). It can be seen that the fitness function in this case study is dramatically more sensitive to the delay values τ than to the other parameters. In this panel, since the sensitivity index for delay values is very large, we can not compare the other indices. For illustration reason, we have shown them in Fig. 5.22**A**. Moreover, for a comparison, the the sensitivity elements computed by fitting Gaussian distributions to the normalized fitness function for each model parameters are illustrated in 5.22**B**. In both panels, we observe that the fitness function is much more sensitive to the gain parameters C_1, C_2, and C_3 compare to the other parameters D, β_e, and β_i.

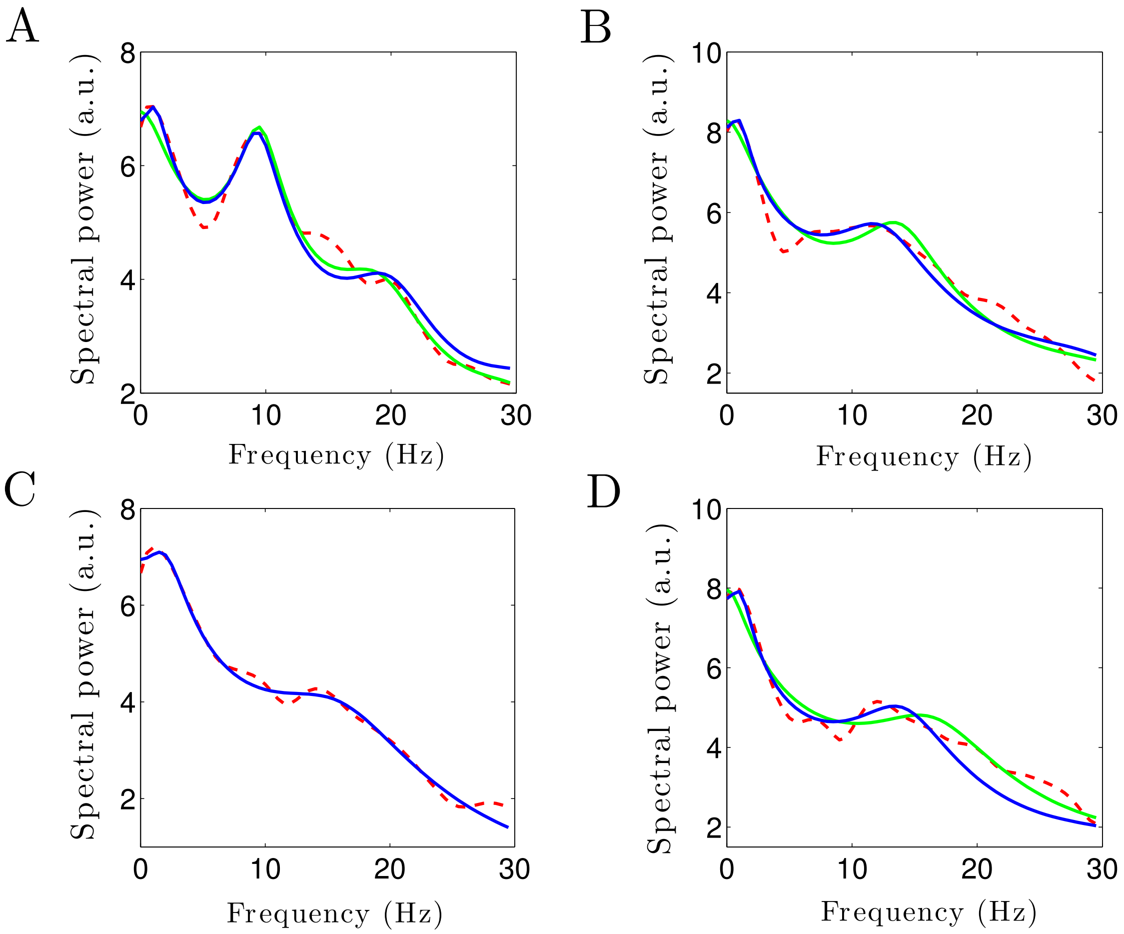

Figure 5.20. Fitting a *reduced* thalamo-cortical model to the EEG power spectra in awake and anesthesia conditions using PSO algorithm. The recorded EEG spectral power are shown by dashed red lines, whereas the fitted spectral power are encoded in the solid lines. Panels (**A**) and (**B**) illustrate the recorded EEG spectral power over occipital head region in awake and anesthesia conditions, respectively. The frontal EEG spectral power in awake and anesthesia conditions are displayed in panels (**C**) and (**D**), respectively. The fitted spectra using standard chi-squared function are illustrated by green lines whereas those obtained by the biased chi-squared function according to Eq. (5.6) are shown in blue lines.

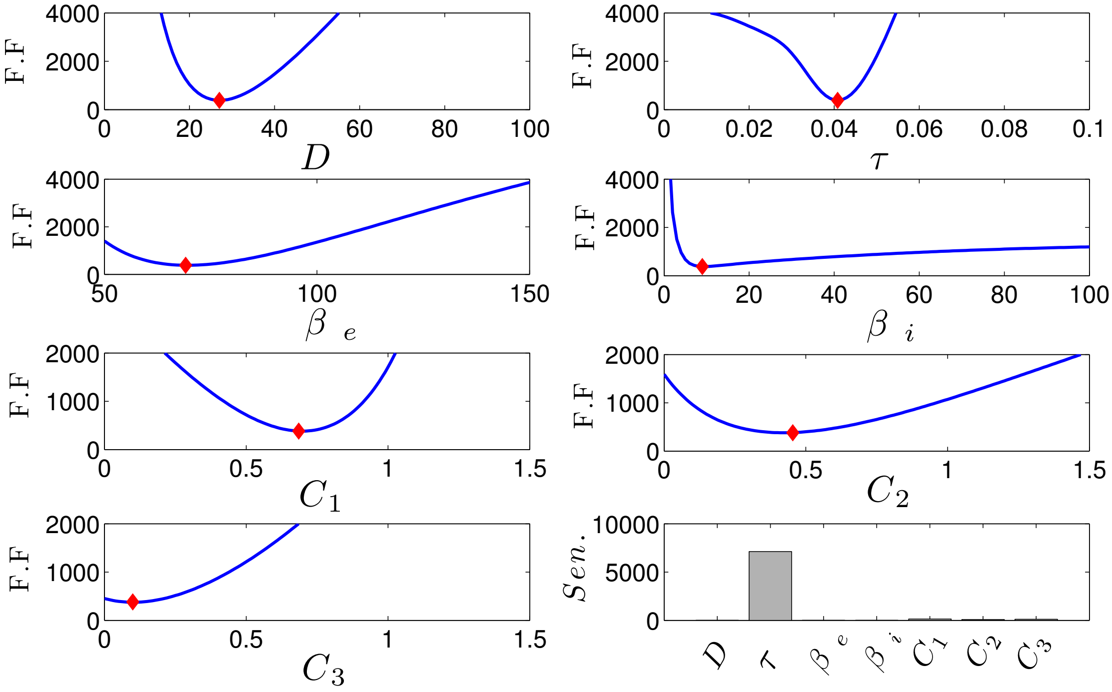

Figure 5.21. Sensitivity of fitness function in fitting a reduced thalamo-cortical model to the EEG spectral power. Shown are the plotted fitness function versus the model parameters $\boldsymbol{p}_{III} = (D, \tau, \beta_e, \beta_i, C_1, C_2, C_3)$. The estimated parameters $\boldsymbol{p}^*_{III} = (27.02, 0.04, 69.10, 8.99, 0.68, 0.45, 0.13)$ are illustrated by red squares. The lowest panel in right show the sensitivity of the fitness function to model parameters measured through the Hessian matrix.

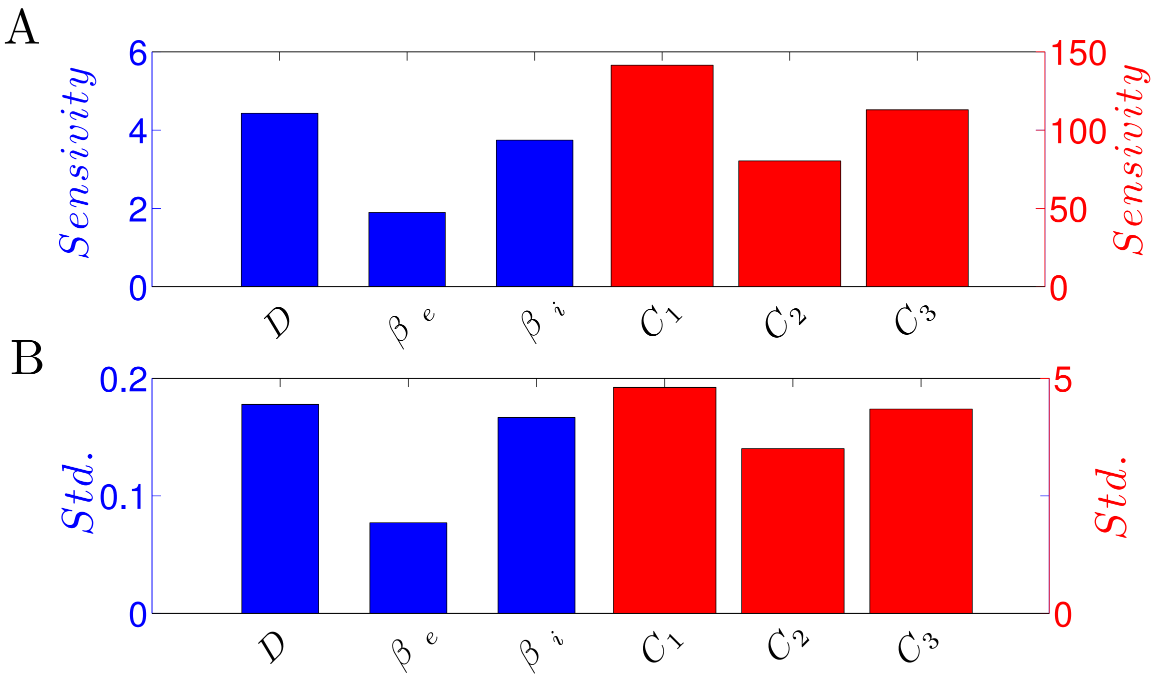

Figure 5.22. Sensitivity of the reduced thalamo-cortical model to its model parameter. (**A**) The sensitivity elements computed through the Hessian matrix. (**B**) Each sensitivity index is the standard deviation of the Gaussian distribution fitted to the normalized fitness function for the corresponding parameters.

In the following, in order to survey more measurements, the model is fitted to the EEG spectral power of 8 patients recorded during pre- and post-incision anesthesia states induced by Desflurane and Propofol, as shown in Figs. 5.23 and 5.24 respectively. In these figures we also observe that in the delta $(0 - 4Hz)$ and alpha $(8 - 13Hz)$ frequency bands, the model fits the measured data very well. These results indicate that the considered thalamo-cortical model in this study is able to reproduce the specific features observed in EEG spectral power data adequately. The values of the estimated parameters are listed in Table 5.2. In addition, the values of pre-factors c_1, c_2, c_3, and c_4 accompanied with the values of the obtained fitness function for these estimations are listed in Table 5.3.

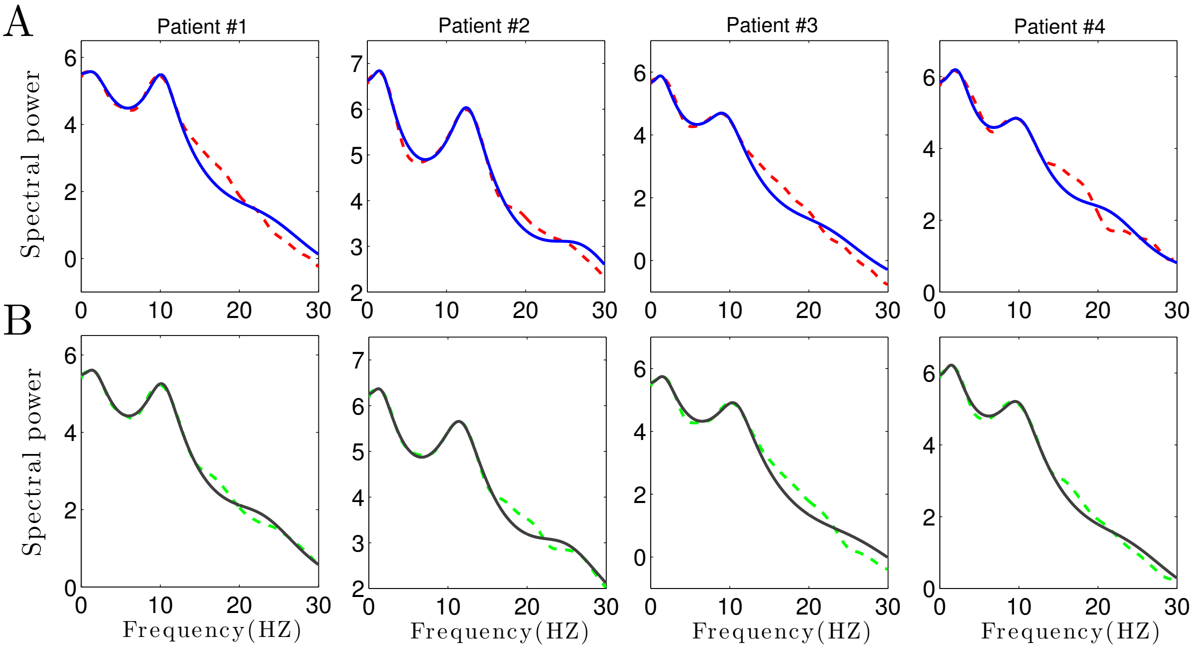

Figure 5.23. Fitting a reduced thalamo-cortical model to the EEG spectral power in pre- and post-incision anesthesia condition induced by Desflurane. The recorded EEG data for four patients are shown by the dashed red lines, whereas the corresponding fitted model are illustrated in solid lines. (**A**) The recorded EEG spectral power in pre-incision condition and the fitted model are shown in the dashed red and solid blue lines, respectively. (**B**) Shown are the EEG power spectra recorded in post-incision condition and the fitted model encoded in dashed green and solid black lines, respectively.

5.7 Discussion

In a great variety of scientific fields, stochastic differential equations arise naturally in the modeling of systems subjected to random forcing or other noisy input. Numerical integration of differential equations is a major time consuming problem in the parameter estimation of nonlinear dynamics in biological systems. It has been shown that decoupling strategy (slope approximation) which consider the derivative values of system state variables avoids numerical integration altogether by fitting models to the slope of time-series data [450, 451]. However, this technique is not applicable in most of optimization problems. For instance, if an equation is affected by a state variable for which there is no data available for it, then the decoupling technique can not be applied to that equation. Moreover, this strategy can not provide a model readily applicable to the computational simulation when the given time-series data contain measurement errors [452].

In another work, a modified collocation approximation technique has been proposed to convert differential equations into a set of algebraic equations [339]. This method has the obvious advantage of avoiding numerical integration of differential equations. They have shown that their method yields accurate parameter estimation for S-system models of genetic networks which also save a lot of computational time. However, such an approximation can not be generally employed in the complex nonlinear inverse problems. To the best of our knowledge, in the previous studies investigating parameter estimation in the context of biological systems while the experimental data are noisy, the additive noise term in the system equations have been neglected. In the

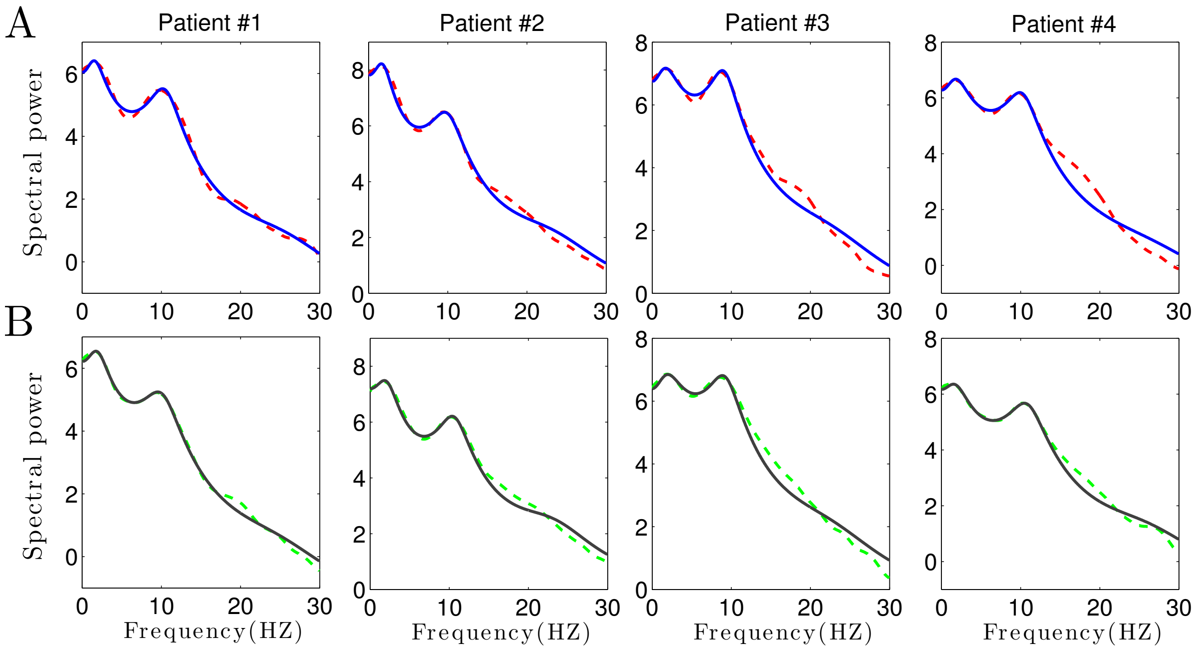

Figure 5.24. Fitting a reduced thalamo-cortical model to the EEG power spectra in pre- and post-incision conditions during the propofol anesthesia. The recorded EEG spectral power and the corresponding fitted model for four patients are shown in the dashed and solid lines, respectively. Panels (**A**) and (**B**) display pre- and post-incision states, respectively.

estimation technique presented in this work, by the aid of Green's function method, we can easily compute the power spectrum of a system whose dynamics are governed by a set of coupled stochastic ordinary or delay differential equations. By fitting the computed spectral power to the corresponding measurements, we can estimate the model parameters without solving the model equations which dramatically reduces the computational time burden. Although evolutionary algorithms such as PSO and DE need a high number of function evaluations, they are able to provide accurate parameter estimates while using spectral power fitting technique, their high computational costs can be compensated for. Furthermore, POS algorithm has this advantage that during the optimization process we can use the performed functional evaluations to construct the confidence regions of the estimated parameters in a reliable manner (see Figs. 5.6 and 5.16).

In recent years, optimization algorithms has received a great deal of attention in particular to solve the estimation problems. An important conclusion that can be drawn from iur results is that not only the search algorithm, but also the formulation of fitness function plays a decisive role in reproducing the key features of the measured data. We showed that using the standard least squares function the model fails to be fitted with the spectral power peak observed in delta frequency band. However, by adding more weights to the fitness function in certain frequency bands than the others, we are able to fit the model in those interested ranges (c.f. Fig 5.20).

In this work, for unimodal and multimodal optimization (Case Study I and Case Study II, respectively), we compared the performance of LM as a local search algorithm to that of well-known EAs including GA (not shown) PSO, DE, MH, and SA (see Figs. 5.12, and 5.19). Our results showed that LM algorithm as a local search method converge rapidly, but to a local minimum. In contrast, although global search algorithms such as PSO and DE algorithms

Table 5.2. Estimated values of parameters of the thalamo-cortical model given by Eq. (5.40) obtained by fitting to the EEG spectral power during pre- and post-incision anesthesia states induced by Desflurane and Propofol.

			Parameters						
		patient #	D	τ	β_e	β_i	$C1$	C_2	C_3
Anesthesia induced by Desflurane	Pre-incision	1	37.54	0.031	31.83	16.58	1.70	2.98	0.10
		2	25.74	0.028	72.04	19.40	0.90	0.45	0.38
		3	23.91	0.033	36.85	12.33	1.03	1.33	0.11
		4	19.88	0.036	54.85	29.54	0.61	0.1	0.57
	Post-incision	1	22.95	0.033	47.38	15.59	0.96	1.33	0.12
		2	21.93	0.031	73.09	13.62	0.64	0.50	0.11
		3	35.62	0.028	30.74	14.66	1.85	2.98	0.14
		4	34.25	0.030	34.99	13.16	1.24	1.89	0.10
Anesthesia induced by Propofol	Pre-incision	1	50.91	0.028	27.62	12.55	2.29	3.68	0.11
		2	107.18	0.031	23.94	22.76	2.68	1.92	2.76
		3	146.65	0.031	19.27	10.95	2.89	6.82	0.11
		4	164.16	0.026	15.63	13.36	5.04	9.24	1.90
	Post-incision	1	79.08	0.028	20.04	19.37	3.07	3.71	1.88
		2	61.56	0.032	33.56	32.43	1.88	1.09	1.48
		3	110.95	0.031	22.49	12.02	1.99	5.43	0.14
		4	50.27	0.028	31.65	15.24	1.77	2.97	0.12

need a high number of fitness function evaluations, they are able to find the global minimum independent of the initial values of the parameters. More precisely, for unimodal optimization problems, LM method can converge rapidly to the global solution. However, in the case of multimodal optimization problems it fails to converge at the global minimum unless it starts with an initial guess very close to the global solution. Our results (c.f. Fig. 5.19) indicate that in the case of multimodal objective function, the meta-heuristic methods such as PSO and DE significantly outperform the other algorithms in finding the global solution.

For each parameter estimation problem, we also employed the practical identifiability analysis to check the reliability of the estimates. The identifiability analysis in this study comprised of building the Fisher information matrix (FIM) to compute the sensitivity and the correlation matrices, in addition to plotting the confidence regions for estimated parameters, as described in section 5.4. In the current work, we illustrated that the identifiability analysis can be easily exploited by plotting the confidence regions. For instance, the confidence regions obtained through Hessian and FIM approaches were compared in Figs. 5.6. and 5.16. By virtue of the the conceptual difference of these approaches in the derivative terms, the exact coincidence of the ellipsoids obtained by Hessian and FIM methods indicates that the estimated parameters are uniquely identifiable and we were able to obtain reliable estimates [436]. Furthermore, by measuring the sensitivity values, we can investigate how the system output will change in the

Table 5.3. The pre-factors c_1, c_2, c_3, and c_4 in the biased chi-squared function defined by Eq. (5.6), accompanied with the values of the obtained fitness function (χ^2) for the estimates shown in Figs. 5.23 and 5.24.

			Pre-factors				
		patient #	c_1	c_2	c_3	c_4	χ^2
Anesthesia induced by Desflurane	Pre-incision	1	200	1	30	1	6.00
		2	100	1	50	1	17.31
		3	20	1	30	1	6.61
		4	20	1	50	1	13.69
	Post-incision	1	50	1	30	1	3.68
		2	100	1	50	1	2.76
		3	20	1	30	1	4.01
		4	30	1	20	1	9.50
Anesthesia induced by Propofol	Pre-incision	1	10	1	10	1	3.68
		2	20	1	10	1	2.76
		3	20	1	10	1	4.01
		4	100	1	100	1	9.50
	Post-incision	1	10	1	10	1	1.18
		2	20	1	10	1	3.56
		3	30	1	20	1	4.93
		4	100	1	1	100	7.65

response to small modification in the model parameters [64, 55]. This allows us to find out which model parameters play a decisive role in the model behaviors. A high sensitivity index for a parameter shows that the small changes on that parameter cause a strong response in the model output. This indicates that the parameters with higher sensitivity values are more identifiable than those parameters with low sensitivity indices, c.f. Figs. 5.10 and 5.17. The correlation plots also provide us information about the parameter identifiability. The lack of correlation among the estimated parameters reveals that the parameters are identifiable, as shown in Fig. 5.9 for the first case study. On the contrary, the highly correlated parameters are not identifiable since there exists many combinations of them that lead to an identical fitness value, c.f. Fig. 5.15 for the second case study. The high correlation between parameters can also cause a discrepancy between the elliptical and likelihood-based confidence regions, as illustrated in Fig. 5.14. To surmount this problem, the pairs of correlated parameters must be removed by introduction of new variables.

Up to now, a few studies have investigated the parameter estimation problems in the context of neural population modeling, which is a well-tried method to reproduce the measured EEG data during different behavioral states. To our best knowledge, this is the first study that using some analytical constrains for the system stability, a thalamo-cortical model is fitted to EEG spectral power peaks observed in both delta and alpha frequency ranges. A pioneer study by Bojak & Liley [24] fitted a neural population model comprising excitatory and inhibitory cortical neurons to a set of pseudo-experimental data. In another study, Rowe *et al.* [32] have estimated the values of key neurophysiological parameters by fitting the model's spectrum to EEG spectra of 100 subjects in awake eyes-closed and eyes-open states. Although Rowe *et al.* have achieved close predictions to the measured data, their data do not exhibit a spectral power peak in delta frequency range. Moreover, while they have used LM method which require initial guess for the parameters, the parameters that do not impact on the variance of data have been fixed at constant values. For instance, they have held the ratio of synaptic rise rate to the corresponding decay rate at a fixed value. Their work has also concentrated on excitatory quantities by slaving the potential of cortical inhibitory population to that of the excitatory population. They have assumed that cortico-cortical connectivities are proportional to the numbers of synapses involved ($K_{ee} = K_{ie}$, $K_{ei} = K_{ii}$) and cortical populations have a same firing rate functions ($S(V_e) = S(V_i)$), which results in an identical mean potential for excitatory and inhibitory cortical populations ($V_e = V_i$). In a similar approach, VanAlbada *et al.* [206] have fitted the Robinson model [29, 30] to eyes-closed EEG spectra of a large number of subjects to probe the age-associated changes in the physiologically model's parameters. Their findings suggest that the inverse modeling of EEG spectral power is a reliable and non-invasive method for investigating large-scale dynamics, which allows us to extract physiological information from EEG spectra. In line with this work, the data-driven approach presented in the current study provides us a proper guidance for fitting the thalamo-cortical model to a large set of experimental recordings. This enable us to investigate the parameter changes during the transition from awake to anesthesia state, especially those parameters that can not be measured directly. Inferring the parameter changes associated to the changes in brain activities from model fitting to a large data set remains to be investigated in future work.

A key finding of our data-based analysis in fitting a thalamo-cortical model to the EEG spectra is that the model is heavily sensitive to the delay transmission in the system (c.f. Fig. 5.21), This is in agreement with previous studies suggesting that the location of spectral power peaks especially in alpha frequency range strngly depends to the delay values in the thalamo-cortical circuits [29, 30, 32, 35]. Considering this finding that time delay plays a critical role in determining the spectral power peaks can provide a basis for the reproduction of some certain features in experimental data seen at high concentration of anesthetics. For instance, if we aim to reproduce the beta power surging observed in EEG power spectrum close to loss of consciousness, we might put forward this hypothesis that the peaks shift in EEG spectra can be reproduced by considering the effect of anesthetics on the axonal transmission delay. However, this effect needs more experimental evidences.

In the last years, Kalman filtering is receiving increased attention for solving the parameter estimation problems [453, 454, 455]. Recently, Lillacci & Khammash [56] have proposed a new hybrid extended Kalman filtering algorithm to estimate parameters in stochastic models of biological systems from noisy and sparse measurements. Their approach can also be used to select a model among different candidate models of the same biological process. However, these methods based on Kalman filtering need an initial guess of the parameters to start and the filter may diverge if it is not initialized with good estimates. The choice of the initial covariance matrices plays a crucial role in ensuring convergence of the filter. Furthermore, the statistics of the process noise as well as the measurement noise are assumed to be known and the filter may give biased estimates or produce unreliable estimates [456]. Comparing the performance of evolutionary algorithms with Kalman filtering is beyond the scope of the present study and it would be the aim of future work.

In a recent study, Rodriguez-Fernandez *et al.* [55] have proposed a mixed-integer nonlinear optimization approach that discriminates a model among a subset of nested models and simultaneously estimate the model parameters in a single step. Although their method shows promising results, the proposed strategy requires the gradient information of the model which it is impossible to utilize in those cases that we face to non-differentiable functions. Moreover, since their proposed method is based on iteratively refinement of the a prior knowledge of the system, in the case of large-scale models the computational effort needed to find satisfactory results might become prohibitive. Most of previous modeling studies have described the EEG spectra by considering the thalamo-cortical loops [186, 29, 30, 35, 36, 37] or even by purely cortical interactions [39, 40, 28]. The reduced model considered in the this work was sufficient to generate the specific features observed in the EEG rhythms, while its low dimensionality allows us to obtain some inequality conditions for the stability of the system (see Figs. 5.23, and 5.24). It is important to note that the analytical constrains shrink the parameter space which facilitates the global exploration ability (searching new areas). In addition, using a model with too many parameters increases the fitting errors, which leads to an inability to obtain accurate estimates. Our preliminary simulations (not shown) demonstrate that using a more complex model with additional parameters, it is very challenging to capture key features of the EEG rhythms. Comparing different topological configurations for the thalamo-cortical model fitted to the EEG spectral power was not aimed in the current study. The future work aims to compare different candidate models to reveal the optimal topology that is able to reproduce the observed characteristic features in experimental data in the best possible way.

5.8 Conclusion

The results obtained in the present work reveal that given a set of stochastic ordinary or delay differential equations and a set of experimental data, by the aid of Green's function method and evolutionary algorithms such as PSO and DE, we are able to fit the model power spectrum to the related data with a high accuracy and very low computational costs. We demonstrated that in multimodal optimization problems with a large number of local minima, the local search methods such as LM algorithm fails to arrive at the global solution, and therefore the use of a global optimization approach such as PSO or DE is required in order to accurately estimate the model parameters. Our analyses indicate that we can employ a data-driven approach to provide new valuable insights into the mechanisms underlying the behavior of complex systems. This approach will provide an appropriate guidance in future brain experiments to better understand different behavioral activities.

General Conclusions

In this thesis we used a modeling approach to understand the mechanisms underlying propofol sedation. To this end, we employed mean field approximation to reach more precise elucidation of physiological mechanisms. This study investigated the construction and performance of mean field thalamo-cortical models for the effects of anesthetic propofol on EEG signals. The models used in this study include excitatory and inhibitory cortical populations that are synaptically connected to thalamic reticular and relay neuron populations by delayed thalamo-cortical axonal fibres. In addition, they incorporate the propofol actions at synaptic and extra-synaptic inhibitory GABAergic receptors in both cortical inhibitory neurons and thalamic relay cells. Although mean field models cannot describe the certain anesthetic effects at the single neuron properties such as action potentials or ion currents, they provide us a well-suited link between the molecular actions of anesthetics at microscopic level and the changes in EEG and behavior that can be observed at macroscopic scales. The general advantage of mean field models over network models is that such models require only a small number of parameters, and thereby they are more tractable than detailed biophysical modeling of synapses and spiking neurons, both numerically and analytically. Our simulation results were in qualitative and quantitative agreement with the empirical observations. The results showed that a population-level model of thalamo-cortical system is able to successfully reproduce the certain spectral changes observed experimentally within the $\delta-$ and $\alpha-$frequency bands. In consistent with previous theoretical studies using neural field models, this study indicate that mean field description is a plausible candidate for investigating the mechanisms responsible for the various features observed in EEG data.

We also revealed the impact of propofol concentration on the resting states of the system. The linear stability analysis of the model equations showed that the propofol-induced changes in the system resting states play a deceive role in generation of key EEG signatures, in particular within the $\alpha-$frequency range. Our findings indicated that propofol concentration acts as a control parameter of the system in such a way that the propofol-induced changes in the system resting states lead to changes in the corresponding nonlinear gain functions that in turn result in the EEG power modulations. Typically the sigmoidal shape of the transfer function leads to multiple resting states. In this study, the models exhibited two stable resting states which are separated by an unstable state. As the concentration of propofol increases, dependent on the potential values of the resting states, it causes an increase or decrease in the gain functions within the thalamo-cortical loops what then results in an increase or decrease in the spectral power in the $\alpha-$frequency band; the increase in the frontal $\alpha-$power can be caused by an increase in the gain function of thalamo-cortical network, whereas the decrease in the $\alpha-$power over occipital area results from a decrease in the thalamo-cortical gain functions. Therefore, considerable care is required when we interpret the role of cortical and thalamic inhibitions in generation of the observed certain changes in EEG signals during propofol-induced sedation. For instance, in chapter 3 we concluded that the cortical inhibition plays a critical role in reproducing the characteristic features of frontal EEG rhythms observed experimentally. However, in chapter 4 we stressed the importance of thalamic inhibition for neural effects under anesthesia sedation, since the results illustrated that the specific observed changes in EEG rhythms can be reproduced with and without the propofol effect in cortical cells. Although these results may seem inconsistent initially, a careful look at the values of system resting states reveals a common mechanism. To reveal this mechanism, it is critical to note that the model equations are linearized about which resting state. In chapter 3, we linearized the system equations about the lower resting state. In this situation, the cortical inhibition is necessary to be taken into account in order to obtain an increase in the gain functions and consequently an increase in the power of $\alpha-$activity. In contrast, the system equations of the model used in chapter 4 were linearized about the upper resting state to generate the $\alpha-$power enhancement. In this situation, it is possible to reproduce the $\alpha-$power surge with and without the propofol effect in cortical cells. Note that, when the system is lying on the lower resting state, stronger inhibition in the thalamus compared to the cortex or considering only the thalamic inhibition results in a decrease in the gain functions and thereby a decrease in the $\alpha-$band power activity. Therefore, neglecting inhibitory action in the cortex but considering thalamic GABAergic action suffices to reproduce an increase or decrease in the $\alpha-$power when the system equations are linearized about the upper or lower resting state, respectively. However, if we aim to reproduce the enhanced $\alpha-$power activity by system linearization about the lower resting state, it is necessary to take into account the cortical inhibition. Taken together, our results suggest a common mechanism for the $\alpha-$power modulations during propofol-induced sedation: dependent on the mean potential values of the system resting states, an increase or decrease in the gain functions within the thalamo-cortical circuits results in an increase or decrease in the spectral power in the $\alpha-$band activity.

In this study, our major aim was to understand the mechanisms that produce the certain power modulations in $\delta-$ and $\alpha-$frequency ranges observed during propofol-induced sedation. To this end, we used topology manipulations to identify the contribution of model populations and the system sub-circuits to generation of $\delta-$ and $\alpha-$power activities. A key finding of this work is that the origin of the $\delta-$rhythm is fundamentally different from the $\alpha-$rhythm. Our detailed analysis revealed that strong $\alpha-$power originates from the cortico-thalamic relay interaction, which is associated with a constant time delay around the inverse of peak frequency within the $\alpha-$frequency range. This finding supports this hypothesis that the $\alpha-$activity results from an interaction between two brain structures rather than being generated in single area. As mentioned above, increasing nonlinear gain functions within this loop induces a power surge in the $\alpha-$range, whereas decreasing thalamo-cortical gain functions diminishes the $\alpha-$power. This is in line with the cortical activation hypothesis, which states that an increase or decrease in the firing rates of cortical pyramidal neurons leads to an increase or decrease in $\alpha-$power activity, respectively. In contrast, the evolution of the $\delta-$power is rather independent of the system resting states, and increases for increasing propofol concentrations for both increasing and decreasing nonlinear gain functions. Our results indicated that the strong $\delta-$power occurs primarily when there is a strong connections from cortex to the reticular nucleus, reticular to relay nucleus and relay to cortex. We showed that the emergence of $\delta-$power during anesthesia results from the increased synaptic or extra-synaptic GABAergic inhibition, either in the cortex or in the thalamus. This finding suggests that the level of inhibition plays an important role in generation of $\delta-$waves while its origin, i.e. synaptic or extra-synaptic, plays a secondary role. In consistent with in vitro studies, this result implies that both the thalamus and the cortex are capable of inherently generating $\delta-$rhythm. However, it remains challenging to determine whether $\delta-$waves have several sources or arise from single brain region.

The aim of second elaboration of this thesis was to identify the parameters of a thalamo-cortical model by fitting the model power spectrum to the EEG recordings. To this end, we addressed the task of parameter estimation in the models that are described by a set of stochastic ordinary or delay differential equations. In three case studies, the model spectral power was fitted to the measured data by using different optimization algorithms namely LM, PSO, DE, MCMC and SA. We carried out two case studies dealing with noisy pseudo-experimental data to compare the performance of employed optimization methods. Our results demonstrated that in the case of multimodal optimization problems, which are more challenging to solve compared to the unimodal cases, the bio-inspired meta-heuristic methods such as PSO and DE significantly outperform the other algorithms whereas the gradient-based LM fails to converge at the global minimum. Following this part, the results of third case study illustrated that the reduced thalamo-cortical model neglecting cortical inhibition fits very well to the power spectra of EEG recordings, particularly to the spectral power peaks observed in $\delta-$ and $\alpha-$frequency ranges. The low dimensionality of the model allowed us to derive some inequality conditions for the stability of the system, which reduce the parameter searching space and thereby greatly facilitate the nonlinear estimation problem. In addition, for each considered case study, we investigated the practical identifiability of the model parameters by plotting the confidence regions of the estimates. The correlation and sensitivity matrices were also analyzed to assess the accuracy of the estimated parameter. Our results show that the method used in this study is able to accurately estimate the independent model parameters while it allows us to avoid the computational costs of the numerical integrations. Moreover, the results imply that the parameter estimation as a crucial step in model building of biological systems allows us to gain further insights into the mechanisms of the system under study.

This thesis focused on the sedation level of anesthesia and the mechanisms that produce additional spectral EEG features such as $\beta-$power surge and burst suppression patterns which emerge at high concentration of anesthetics remain to be investigated in the future work. Furthermore, a future work will compare the performance of evolutionary algorithms used in this work with other estimation methods such as Kalman filter and its variations. We will also aim to investigate the structural identifiability (model selection practice) in order to identify the optimal mean field model among a set of different model candidates. The approach used in this thesis could be applied in the future works to achieve these goals.

References

[1] E.N. Brown, P. Purdon, and C.J. Dort. General anesthesia and altered states of arousal: A systems neuroscience analysis. *Annu Rev Neurosci.*, 34:601–628, 2011.

[2] B.A. Orser. Lifting the fog around anesthesia. *Scientific American*, 7:54–61, 2007.

[3] P-L. Chau. New insights into the molecular mechanisms of general anaesthetics. *Br. J. Pharmacol.*, 161:288–307, 2010.

[4] D. San-Juan, K.H. Chiappa, and A.J. Cole. Propofol and the electroencephalogram. *Clin. Neurophysiol.*, 121(7):998–1006, 2010.

[5] H.H. Meyer. Zur theorie der alkoholnarkose. iii. der einfluss wechselender temperatur auf wikungs-starke and teilungs koefficient der nalkolicka. *Arch. Exp. Pathol. Pharmakol.*, 154:338–46, 1901.

[6] C.E. Overton. Studien uber narkose, zugleich ein beitrag zur allgemeinen pharmakologie. *Pharmakologie. Fischer*, 1901.

[7] N.P. Franks and W.R. Lieb. Do general anaesthetics act by competitive binding to specific receptors. *Nature*, 310:599–601, 1984.

[8] N.P. Franks and W.R. Lieb. Seeing the light: protein theories of general anesthesia. *Anesthesiology*, 101:235–7, 2004.

[9] N.P. Franks. General anesthesia: from molecular targets to neuronal pathways of sleep and arousal. *Nat.Rev.Neurosc.*, 9:370–386, 2008.

[10] U. Rudolph and B. Antkowiak. Molecular and neuronal substrates for general anaesthetics. *Nat. Rev. Neurosci*, 5:709–720, 2004.

[11] A.K. Luglia, C.S. Yostb, and C.H. Kindlerc. Anaesthetic mechanisms: update on the challenge of unravelling the mystery of anaesthesia. *Eur. J. Anaesthesiol.*, 26(10):807–820, 2009.

[12] L. Uhrig, S. Dehaene, and B. Jarraya. Cerebral mechanisms of general anesthesia. *Ann Fr Anesth Reanim.*, 33(2):72–82, 2014.

[13] M.T. Alkire, A.G. Hudetz, and G.Tononi. Consciousness and anesthesia. *Science*, 322:876–880, 2008.

[14] E Siegel and M. S. Steinmann. Structure, function, and modulation of GABA$_A$ receptors. *The journal of biological chemistry*, 277(48):40224–40231,, 2012.

[15] P.S. Garcia, S. E. Kolesky, and A. Jenkins. General anesthetic actions on $GABA_A$ receptors. *Current Neuropharmacolog*, 8:2–9, 2010.

[16] C. Zhou, J. Liu, and X.D. Chen. General anesthesia mediated by effects on ion channels. *World Journal of Critical Care Medicine*, 1:80–93, 2012.

[17] E.N. Brown, R.L. Lydic, and N.D. Schiff. General anesthesia, sleep, and coma. *N Engl J Med*, 363:2638–2650, 2010.

[18] A. Cimenser, P. L. Purdon, E. T. Pierce, J. L. Walsh, A. F. Salazar-Gomez, P. G. Harrell, C. Tavares-Stoeckel, K. Habeeb, and E. N. Brown. Tracking brain states under general anesthesia by using global coherence analysis. *Proc. Natl. Acad. Sci. USA*, 108(21):8832–8837, 2011.

[19] M. Murphy, M.-A. Bruno, B. A. Riedner, P. Boveroux, Q. Noirhomme, E. C. Landsness, J.-F. Brichant, C. Phillips, M. Massimini, S. Laureys, G. Tononi, and M. Boly. Propofol anesthesia and sleep: A high-density EEG study. *Sleep*, 34(3):283–291, 2011.

[20] G. Deco, V.K. Jirsa, P.A. Robinson, M. Breakspear, and K. Friston. The dynamic brain: from spiking neurons to neural masses and cortical fields. *PloS Comp. Biol.*, 4(8), 2008.

[21] P.L. Nunez. *Electrical Fields of the Brain.* Oxford University Press, Oxford, 1981.

[22] P.L. Nunez and R. Srinivasan. *Electric Fields of the Brain: The Neurophysics of EEG.* Oxford University Press, New York - Oxford, 2006.

[23] P.A. Robinson, C.J. Rennie, and D.L. Rowe. Dynamics of large-scale brain activity in normal arousal states and eplieptic seizures. *Phys. Rev. E*, 65(4):041924, 2002.

[24] I. Bojak and D.T.J. Liley. Modeling the effects of anesthesia on the electroencephalogram. *Phys. Rev. E*, 71:041902, 2005.

[25] B.L. Foster, I. Bojak, and D.T. J. Liley. Population based models of cortical drug response: insights from anaesthesia. *Cogn. Neurodyn.*, 2:283–296, 2008.

[26] S. Coombes. Large-scale neural dynamics: Simple and complex. *NeuroImage*, 52:731–739, 2010.

[27] P. Bressloff. Spatiotemporal dynamics of continuum neural fields. *J. Phys. A*, 45:033001, 2012.

[28] A. Hutt and A. Longtin. Effects of the anesthetic agent propofol on neural populations. *Cogn. Neurodyn.*, 4(1):37–59, 2009.

[29] P.A. Robinson, C.J. Rennie, J.J. Wright, H. Bahramali, E. Gordon, and D. Rowe. Prediction of electroencephalographic spectra from neurophysiology. *Phys. Rev. E*, 63:201903, 2001a.

[30] P.A. Robinson, P.N. Loxley, and S.C.O'Connor C.J. Rennie. Modal analysis of corticothalamic dynamics, electroencephalographic spectra, and evoked potentials. *Phys. Rev. E*, 63:041909, 2001b.

[31] D.T.J. Liley and I. Bojak. Understanding the transition to seizure by modeling the epileptiform activity of general anaesthetic agents. *J. Clin. Neurophysiol.*, 22:300–313, 2005.

[32] D.L Rowe, P.A. Robinson, and C.J. Rennie. Estimation of neurophysiological parameters from the waking EEG using a biophysical model of brain dynamics. *J. Theor. Biol*, 231(3):413–433, 2004.

[33] P.A. Robinson, C.J.Rennie, D.L.Rowe, and S.C.O'Connor. Estimation of multiscale neurophysiologic parameters by electroencephalographic means. *Human Brain Mapping*, 23:53–72, 2004.

[34] P.A. Robinson. Neurophysical theory of coherence and correlations of electroencephalographic signals. *J. Theor. Biol.*, 222:163–175, 2003.

[35] R. Hindriks and M. J. A. M. van Putten. Meanfield modeling of propofol-induced changes in spontaneous EEG rhythms. *Neuroimage*, 60:2323–2344, 2012.

[36] M. Hashemi, A. Hutt, and J. Sleigh. Anesthetic action on extra-synaptic receptors: effects in neural population models of EEG activity. *J. Front. Syst. Neurosci.*, 8(232), 2014.

[37] M. Hashemi, A. Hutt, and J. Sleigh. How the cortico-thalamic feedback affects the EEG power spectrum over frontal and occipital regions during propofol-induced sedation. *J. Cpmput. Neurosc.*, 39(2):155–179, 2015.

[38] M.L. Steyn-Ross, D.A. Steyn-Ross, J. W. Sleigh, and D. T. J. Liley. Theoretical electroencephalogram stationary spectrum for a white-noise-driven cortex: Evidence for a general anesthetic-induced phase transition. *Phys. Rev. E*, 60(6):7299–7311, 1999.

[39] M.L. Steyn-Ross, D.A. Steyn-Ross, J.W. Sleigh, and L.C. Wilcocks. Toward a theory of the general-anesthetic-induced phase transition of the cerebral cortex: I. a thermodynamic analogy. *Phys. Rev. E*, 64:011917J, 2001.

[40] M.L. Steyn-Ross, D.A. Steyn-Ross, J.W. Sleigh, and L.C. Wilcocks. Toward a theory of the general-anesthetic-induced phase transition of the cerebral cortex: Ii. numerical simulations, spectra entropy, and correlation times. *Phys. Rev. E*, 64:011918, 2001.

[41] B. Molaee-Ardekani, L. Senhadji, M.B. Shamsollahi, B. Vosoughi-Vahdat, and E.Wodey. Brain activity modeling in general anesthesia: Enhancing local mean-field models using a slow adaptive firing rate. *Phys. Rev. E*, 76:041911, 2007.

[42] S. Ying and P. Goldstein. Propofol effects on the thalamus: Modulation of GABAergic synaptic inhibition and suppression of neuronal excitability. *Abstract Viewer/Itinerary Planner Washington, DC: Society for Neuroscience*, 89(411), 2001.

[43] M. Zhang, G.W. Wei, and C.-H. Wei. Transition from intermittency to periodicity in lag synchronization in coupled roessler oscillators. *Phys. Rev. E*, 65:036202, 2002.

[44] M.T. Alkire, R. J. Haier, and J. H. Fallon. Toward a unified theory of narcosis: brain imaging evidence for a thalamocortical switch as the neurophysiologic basis of anesthetic-induced unconsciousness. *Conscious Cogn.*, 9:370–386, 2000.

[45] M.T. Alkire and J. Miller. General anesthesia and the neural correlates of consciousness. *Prog Brain Res.*, 150:229–44, 2005.

[46] M.T. Scharf and M.B. Kelz. Sleep and anesthesia interactions: A pharmacological appraisal. *Curr Anesthesiol Rep*, 3:1–9, 2013.

[47] A. Kitamura, W. Marszalec, J.Z. Yeh, and T. Narahashi. Effects of halothane and propofol on excitatory and inhibitory synaptic transmission in rat cortical neurons. *J. Pharmacol.*, 304(1):162–171, 2002.

[48] S.W. Ying and P.A. Goldstein. Propofol-block of SK channels in reticular thalamic neurons enhances GABAergic inhibition in relay neurons. *J. Neurophysiol.*, 93:1935–1948, 2005.

[49] Julio Banga and Eva Balsa-Canto. Parameter estimation and optimal experimental design. *Essays Biochem*, 45:195–210, 2008.

[50] van Riel NA. Dynamicmodelling and analysis of biochemical networks: mechanism-basedmodels and model-based experiments. *Brief Bioinform*, 7(4):364, 2006.

[51] J. Stelling. Mathematical models in microbial systems biology. *Curr. Opin. Microbiol.*, 7(5):513–518, 2004.

[52] D.B. Kell. Metabolomic and systems bilogy: making sense of the soup. *Curr. Opin. Microbiol.*, 7(3):296–307, 2004.

[53] H. Kitano. Computational systems biology. *Nature*, 420(6912):206–210, 2002.

[54] Maria Rodriguez-Fernandez, Jose A. Egea, and Julio R. Banga. Novel metaheuristic for parameter estimation in nonlinear dynamic biological systems. *BMC bioinformatics*, 7:483, 2006.

[55] Maria Rodriguez-Fernandez, Markus Rehberg, Andreas Kremling, and Julio R. Banga. Simultaneous model discrimination and parameter estimation in dynamic models of cellular systems. *BMC systems biology*, 7(1):76, 2013.

[56] Gabriele Lillacci and Mustafa Khammash. Parameter estimation and model selection in computational biology. *PLoS computational biology*, 6(3):e1000696, 2010.

[57] Katerina Tashkova, Peter Korosec, Jurij Silc, Ljupco Todorovski, and Saso Dzeroski. Parameter estimation with bio-inspired meta-heuristic optimization: modeling the dynamics of endocytosis. *BMC systems biology*, 5(1):159, 2011.

[58] Maksat Ashyraliyev, Johannes Jaeger, and Joke G Blom. Parameter estimation and determinability analysis applied to Drosophila gap gene circuits. *BMC Systems Biology*, 2(1):83, 2008.

[59] Maksat Ashyraliyev, Yves Fomekong-Nanfack, Jaap A. Kaandorp, and Joke G. Blom. Systems biology: parameter estimation for biochemical models: Parameter estimation in systems biology. *FEBS Journal*, 276(4):886–902, 2009.

[60] Choujun Zhan and Lam F. Yeung. Parameter estimation in systems biology models using spline approximation. *BMC systems biology*, 5(1):14, 2011.

[61] Carmen G. Moles, Pedro Mendes, and Julio R. Banga. Parameter estimation in biochemical pathways: a comparison of global optimization methods. *Genome research*, 13(11):2467–2474, 2003.

[62] P. Mendes. Modeling large biological systems from functional genomic data: Parameter estimation. *In: Foundations of systems biology MIT Press, Cambridge, MA*, pages 163–186, 2001.

[63] P. Mendes and D. Kell. Non-linear optimization of biochemical pathways: applications to metabolic engineering and parameter estimation. *Bioinformatics (Oxford, England)*, 14(10):869–883, 1998.

[64] Maria Rodriguez-Fernandez, Pedro Mendes, and Julio R. Banga. A hybrid approach for efficient and robust parameter estimation in biochemical pathways. *Biosystems*, 83:248–265, 2006.

[65] J.L. Tremoleda, A. Kerton, and W. Gsell. Anaesthesia and physiological monitoring during in vivo imaging of laboratory rodents: considerations on experimental outcomes and animal welfare. *EJNMMI Research*, 2(44), 2012.

[66] A.S. Evers, M. Maze, and E.D. Kharasch (Editors). *Anesthetic Pharmacology: Basic Principles and Clinical Practice, 2nd Edition.* Cambridge University Press, 2001.

[67] DH. Robinson and AH. Toledo. Historical development of modern anesthesia. *J Invest Surg.*, 25(3):141–9, 20012.

[68] H. Mohler, editor. *Pharmacology of GABA and Glycine Neurotransmission.* Springer Science & Business Media, 4 edition, 2001.

[69] R. Lujan, R. Shigemoto, and G. Lopez-Bendito. Glutamate and gaba receptor signalling in the developing brain. *Neuroscience*, 130:567–580, 2005.

[70] R. L. Macdonald and R.W. Olsen. $GABA_A$ receptor channels. *Annual Review of Neuroscience*, 17:569–602, 1995.

[71] Y. Ben-Ari, J. Gaiarsa, R. Tyzio, and R. Khazipov. Gaba: A pioneer transmitter that excites immature neurons and generates primitive oscillations. *Physiological Reviews*, 87(4):1215–1284, 2007.

[72] O. Henschel, K.E. Gipson, and A. Bordey. $GABA_A$ receptors, anesthetics and anticonvulsants in brain development. *CNS Neurol Disord Drug Targets*, 7(2):211–224, 2008.

[73] D.L. Tanelian, P. Kosek, I. Mody, and M.B. MAclver. The role of the gabaa receptor/chloride channel complex in anesthesia. *Anesthesiology*, 78(4):757–76, 1993.

[74] B.A. Orser. Extrasynaptic GABA$_A$ receptors are critical targets for sedative-hypnotic drugs. *J. Clin. Sleep Med.*, 2:S12–8, 2006.

[75] D. Bai, P.S. Pennefather, J.F. MacDonald, and B.A.Orser. The general anesthetic propofol slows deactivation and desensitization of GABA$_A$ receptors. *J.Neurosc.*, 19(24):10635–10646, 1999.

[76] P. M. Baker, T.C. Gent, Q. Yang, S. Parker, A.L. Vyssotski, W. Wisden, S.G. Brickl, and N.P. Franks. Altered activity in the central medial thalamus precedes changes in the neocortex during transitions into both sleep and propofol anesthesia. *J. Neurosci.*, 34(40):13326–13335, 2014.

[77] E.R. John and L.S. Prichep. The anesthetic cascade : A theory of how anesthesia suppresses consciousness. *Anesthesiol.*, 102:447–471, 2005.

[78] L.J. Velly, M.F. Rey, N.J. Bruder, F.A. Gouvitsos, T. Witjas, J.M. Regis, J.C. Peragut, and F.M. Gouin. Differential dynamic of action on cortical and subcortical structures of anesthetic agents during induction of anesthesia. *Anesthesiology.*, 107(2):202–12, 2007.

[79] S.W. Ying and P.A. Goldstein. Propofol suppresses synaptic responsiveness of somatosensory relay neurons to excitatory input by potentiating $GABA_A$ receptor chloride channels. *Mol. Pain*, 1:2, 2005.

[80] B. Antkowiak. In vitro networks: cortical mechanisms of anaesthetic action. *Brit. J. Anaesth.*, 89(1):102–111, 2002.

[81] S. Ching, A. Cimenser, P. L. Purdon, E. N. Brown, and N. J. Kopell. Thalamocortical model for a propofol-induced-rhythm associated with loss of consciousness. *Proc. Natl. Acad. Sci. USA*, 107(52):22665–22670, 2010.

[82] P. L. Purdon, E. T. Pierce, E. A. Mukamel, M. J. Prerau, J. L. Walsh, K. F. Wong, A. F. Salazar-Gomez, P. G. Harrell, A. L. Sampson, A. Cimenser, S. Ching, N. J. Kopell, C. Tavares-Stoeckel, K. Habeeb, R. Merhar, and E. N. Brown. Electroencephalogram signatures of loss and recovery of consciousness from propofol. *Proc. Natl. Acad. Sci. USA*, 110:E1142–1150, 2012.

[83] M. Boly, R. Moran, M. Murphy, P. Boveroux, M. A. Bruno, Q. Noirhomme, D. Ledoux, V. Bonhomme, J. F. Brichant, G. Tononi, S. Laureys, and K. I. Friston. Connectivity changes underlying spectral EEG changes during propofol-induced loss of consciousness. *J. Neurosci.*, 32(20):7082–7090, 2012.

[84] V. A. Feshchenko, R. A. Veselis, and R. A. Reinsel. Propofol-induced alpha rhythm. *Neuropsychobiology*, 50(3):257–266, 2004.

[85] C. Hazeaux, D. Tisserant, H. Vespignani, L. Hummer-Sigiel, V. Kwan-Ning, and M.C. Laxenaire. Electroencephalographic changes produced by propofol. *Ann. Fr. Anesth. Reanim.*, 6:261–266, 1987.

[86] K. K. Sellers, D. V. Bennett, A. Hutt, and F. Frohlich. Anesthesia differentially modulates spontaneous network dynamics by cortical area and layer. *J. Neurophysiol.*, in press, 2013.

[87] L. D. Gugino, R. J. Chabot, L. S. Prichep, E. R. John, V. Formanek, and L. S. Aglio. Quantitative EEG changes associated with loss and return of conscious- ness in healthy adult volunteers anaesthetized with propofol or sevoflurane. *Br. J. Anaesth.*, 87:421–428, 2001.

[88] K. Kuizenga, C.J. Kalkman, and P.J.Hennis. Quantitative electroencephalographic analysis of the biphasic concentration-effect relationship of propofol in surgical patients during extradural analgesia. *Brit. J. Anaesth.*, 80:725–732, 1998.

[89] K. Kuizenga, J.M.K.H. Wierda, and C.J. Kalkman. Biphasic EEG changes in relation to loss of consciousness during induction with thiopental, propofol, etomidate, midazolam or sevoflurane. *Brit. J. Anaesth.*, 86(3):354–360, 2001.

[90] N.P. Franks and W.R. Lieb. Molecular and cellular mechanisms of general anesthesia. *Nature*, 367:607–614, 1994.

[91] J.D. Drover, N.D. Schiff, and J.D. Victor. Dynamics of coupled thalamocortical modules. *J. Comput. Neurosci.*, 28:605–616, 2010.

[92] V.K. Jirsa and H. Haken. Field theory of electromagnetic brain activity. *Phys. Rev. Lett.*, 77(5):960–963, 1996.

[93] D.T.J. Liley, P.J. Cadusch, and M.P. Dafilis. A spatially continuous mean field theory of electrocortical activity. *Network: Comput. Neural Syst.*, 13:67–113, 2002.

[94] D.R. Freestone, P. Aram, M. Dewar, K. Scerri, D.B. Grayden, and V. Kadirkamanathan. A data-driven framework for neural field modeling. *NeuroImage*, 56(3):1043–1058, 2011.

[95] D.A. Pinotsis, R.J. Moran, and K.J. Friston. Dynamic causal modeling with neural fields. *NeuroImage*, 59(2):1261–1274, 2012.

[96] D.T.J. Liley and J.J. Wright. Intracortical connectivity of pyramidal and stellate cells: estimates of synaptic densities and coupling symmetry. *Network:Comput.Neur.Syst.*, 5:175–189, 1994.

[97] J.J. Wright and D.T.J. Liley. Dynamics of the brain at global and microscopic scales: Neural networks and the EEG. *Behav. Brains Sc.*, 19:285–320, 1996.

[98] H.R. Wilson and J.D. Cowan. Excitatory and inhibitory interactions in localized populations of model neurons. *Biophys. J.*, 12:1–24, 1972.

[99] S. Amari. Dynamics of pattern formation in lateral-inhibition type neural fields. *Biol. Cybernetics*, 27:77–87, 1977.

[100] M.T. Alkire, R. J. Haier, S. J. Barker, N. K. Shah, J. C. Wu, and Y. J. Kao. Cerebral metabolism during propofol anesthesia in humans studied with positron emission tomography. *Anesthesiology*, 82:393–403, 1995.

[101] M.T. Alkire, R. J. Haier, N.K. Shah, and C.T. Anderson. Positron emission tomography study of regional cerebral metabolism in humans during isoflurane anesthesia. *Anesthesiology*, 86:549–557, 1997.

[102] M.T. Alkire. Quantitative eeg. correlations with brain glucose metabolic rate during anesthesia in volunteers. *Anesthesiology*, 89:323–33, 1998.

[103] J. Schrouff, V. Perlbarg, M. Boly, G. Marrelec, P. Boveroux, A. Vanhaudenhuyse, M.A. Bruno, S. Laureys, C. Phillips, M. Pelegrini-Issac, P. Maquet, and H. Benali. Brain functional integration decreases during propofol-induced loss of consciousness. *NeuroImage*, 57(1):198–205, 2011.

[104] M. Massimini, F. Ferrarelli, and G. Tononi. Cortical mechanisms of loss of consciousness: insight from TMS/EEG studies. *Archives Italiennes de Biologie,*, 150:44–55, 2012.

[105] A. Angel. The g. l. brown lecture. adventures in anaesthesia. *Experimental Physiology*, 76:1–38, 1991.

[106] A. Angel. Central neuronal pathways and the process of anaesthesia. *British Journal of Anaesthesia*, 71:148–163, 1993.

[107] George A Mashour and Michael T Alkire. Consciousness, anesthesia, and the thalamocortical system. *Anesthesiology*, 118(1):13–15, 2013.

[108] S. Ching, , and E. N. Brown. Tmodeling the dynamical effects of anesthesia on brain circuits. *Curr. Opin. Neurobiol.*, 25:116–122, 2014.

[109] G. Tononi. An information integration theory of consciousness. *BMC Neurosci.*, 5:42, 2004.

[110] GA. Mashour. Consciousness unbound: toward a paradigm of general anesthesia. *Anesthesiology*, 100(2):428–33, 2004.

[111] A. Hutt. The anaesthetic propofol shifts the frequency of maximum spectral power in EEG during general anaesthesia: analytical insights from a linear model. *Front. Comp. Neurosci.*, 7:2, 2013.

[112] S. Vijayan, S. Ching, A. Cimenser, P. L. Purdon, E. N. Brown, and N. J. Kopell. Thalamocortical mechanisms for the anteriorization of alpha rhythms during propofol-induced unconsciousness. *J. of Neurosc.*, 33(27):11070–11075, 2013.

[113] M. M. McCarthy, E. N. Brown, and N. Kopell. Potential network mechanisms mediating electroencephalographic beta rhythm changes during propofol-induced paradoxical excitation. *J. Neurosci.*, 28(50):13488–13504, 2008.

[114] S. Ching, P. L. Purdon, S. Vijayand, N. J. Kopell, and E. N. Brown. A neurophysiological metabolic model for burst suppression. *Proc. Natl. Acad. Sci. USA*, 109(8):3095–3100, 2012.

[115] A. Destexhe, D. Contreras, and M. Steriade. Cortically-induced coherence of a thalamic-generated oscillation. *J. Neuroscience.*, 92:427–443, 1998.

[116] A. Hutt, J. Sleigh, A. Steyn-Ross, and M. L. Steyn-Ross. General anaesthesia. *Scholarpedia*, 8(8):30485, 2013.

[117] David Halliday, 1923 Resnick, Robert, and 1945 Walker, Jearl. *Principles of physics.* Hoboken, N.J. : John Wiley & Sons, 9th ed., international student version edition, 2011.

[118] R. Resnick, D. Halliday, and K. Krane. *Physics Volume One.* New York: John Wiley & Sons, Inc, 1992.

[119] V. Barger. *Classical Mechanics: A Modern Perspective.* New York: McGraw-Hill, 1973.

[120] A. Papoulis. *Motion of a Harmonically Bound Particle. 15-2 in Probability, Random Variables, and Stochastic Process.* New York: McGraw-Hill, 2nd ed edition, 1984.

[121] B. Øksendal. *Stochastic Differential Equations. An Introduction with Applications.* Springer-Verlag, Berlin Heidelberg, 2007.

[122] H. Risken. *The Fokkerr-Planck Equation.* Springer, Berlin, 1984.

[123] H. Risken. *The Fokker-Planck Equation: Methods of Solutions and Applications.* Springer-Verlag, New York, 1996.

[124] M.C. Wang and G.E. Uhlenbeck. On the theory of the brownian motion. *Phys. Rev. Mod*, 17(2):323, 1945.

[125] J. Masoliver and J.M. Porrá. Harmonic oscillators driven by colored noise: Crossovers, resonances, and spectra. *Phys. Rev. E*, 48(6):4309–4319, 1993.

[126] W. Michiels and $S-l$. Niculescu. *Stability and Stabilization of Time-Delay Systems (Advances in Design & Control) (Advances in Design and Control).* Society for Industrial & Applied Mathematics, U.S., 2007.

[127] M. Muthusamy and D.V. Senthilkumar. *Dynamics of Nonlinear Time-Delay Systems.* Springer Series in Synerfetics, 2010.

[128] T. D. Frank and P. J. Beek. Stationary solutions of linear stochastic delay differential equations: Applications to biological systems. *Phys. Rev. E*, 64:021917, 2001.

[129] N. Buric and D. Todorovic. Dynamics of fitzhugh-nagumo excitable systems with delayed coupling. *Phys. Rev. E.*, 67(6):066222, 2003.

[130] A. Roxin, N. Brunel, and D. Hansel. The role of delays in shaping the spatio-temporal dynamics of neuronal activity in large networks. *Phys.Rev.Lett.*, 94:238103, 2005.

[131] Y. Yuan. Dynamics in a delayed-neural network. *Chaos, Solitons and Fractal*, 33(2):443–454, 2007.

[132] Y. Song, V.A. Makarov, and M.G. Velarde. Stability switches, oscillatory multistability, and spatio-temporal patterns of nonlinear oscillations in recurrently delay coupled neural networks. *Biological Cybernetics*, 101(2):147–167, 2009.

[133] Q. Wang, Q. LuGR. Chen, Z. feng, and L. Duan. Bifurcation and synchronization of synaptically coupled FHN models with time delay. *Chaos, Solitons and Fractal*, 39(2):918–925, 2009.

[134] J. Belair and S. A. Campbell. Stability and bifurcations of equilibria in a multiple-delayed differential equation. *SIAM J. Appl. Math.*, 54(19):1402–1424, 1994.

[135] M. Hashemi, A. Valizadeh, and Y. Azizi. Effect of duration of synaptic activity on spike rate of a hodgkin-huxley neuron. *Phys. Rev. E*, 85:021917, 2012.

[136] A. Hutt, J. Lefebvre, and A. Longtin. Delay stabilizes stochastic systems near an non-oscillatory instability. *Europhysics Letters*, 98:20004, 2012.

[137] M. Bonnin, F. Corinto, and M. Gilli. Bifurcation. stability and synchronization in delayed oscillatory networks. *International Journal of Bifurcation and Chaos*, 17(1):1402–1424, 2007.

[138] D. Fan and L. Hong. Hopf bifurcation analysis in a synaptically coupled FHN neuron model with delays. *Communications in Nonlinear Science and Numerical Simulation*, 15(7):1873–1886, 2010.

[139] L. Duan D. Fan and Q. Lu. Hopf bifurcation and bursting synchronization in an excitable systems with chemical delayed coupling. *Cogn Neurodyn*, 7(4):341–349, 2013.

[140] H. Haken. Effect of delay on phase locking in a pulse coupled neural network. *Europ. Phys. J. B*, 18:545–550, 2000.

[141] H. Haken. Delay, noise and phase locking in puls coupled neural networks. *Biosystems*, 63:15–20, 2001.

[142] M. Dhamala, V.K. Jirsa, and M.Z. Ding. Enhancement of neural synchrony by time delay. *Phys. Rev. L.*, 92(7):74104, 2003.

[143] T-W. Ko and G.B. Ermentrout. Effects of axonal time delay on synchronization and wave formation in sparsely coupled neuronal oscillators. *Phys.Rev.E*, 76:056206, 2007.

[144] W. Michiels and H. Nijmeijer. Synchronization of delay-coupled nonlinear oscillators: an approach based on the stability analysis of synchronized equilibria. *Chaos*, 19(3):033110, 2009.

[145] N. Buric, D. Todorovic, and N. Vasovic. Synchronization of bursting neurons with delayed chemical synapses. *Phys. Rev. E.*, 78(3):036211, 2003.

[146] A. Bellen and M. Zennaro. *Numerical Methods for Delay Differential Equations.* Oxfird Science Publications, 2003.

[147] L.S. Pontriagin. On the zeros of some elementary transcendental functions. *zv. Acad. Nauk SSSR*, 6(3):115–134, 1942.

[148] O. J. Smith. Closer control of loops with dead time. *Chem. Eng. Prog.*, 53, 1957.

[149] L. E. El'sgol'ts and S. B. Norkin. *An Introduction to the Theory and Application of Differential Equations with Deviating Arguments.* Academic Press, New York, 1973.

[150] H. Gorecki, S. Fuksa, P. Grabowski, and A. Korytowski. *Analysis and Synthesis of Time Delay Systems.* John Wiley & Sons, PWN-Polish Scientific Publishers-Warszawa, 1989.

[151] H. Matsunaga. Exact stability criteria for delay differential and difference equationss. *Applied Mathematics Letters*, 20:183–188, 2007.

[152] W. Michiels and S. Niculescu. *Stability, Control, and Computation for Time-Delay Systems: An Eigenvalue-Based Approach, Second Edition.* SIAM, 2014.

[153] F. M. Asl and A. G. Ulsoy. Analysis of a system of linear delay differential equation. *J. Dyn. Syst. Meas. Control.*, 125:215–223, 2003.

[154] E. Jarlebring and T. Damm. The lambert w function and the spectrum of some multidimensional time-delay systems. *Automatica*, 43(12):2124–2128, 2003.

[155] K. Engelborghs, T. Luzyanina, and D. Roose. Numerical bifurcation analysis of delay differential equations. *J. Comput. Appl. Math.*, 125(12):265–275, 2000.

[156] K. Engelborghs and D. Roose. On stability of lms methods and characteristic roots of delay differential equations. *SIAM J. Numer. Anal.*, 40(2):629–550, 2002.

[157] K. Engelborghs, T. Luzyanina, and D. Roose. Numerical bifurcation analysis of delay differential equations using dde-biftool. *ACM Trans. Math. Software*, 28(1):1–24, 2002.

[158] D. Breda, S. Maset, and R. Vermiglio. Pseudo spectral difference methods for characteristic roots of delay differential equation. *SIMA J. Numer. Anal.*, 24(1):1–19, 2004.

[159] D. Breda, R. Vermiglio, and S. Maset. Trace-dde, tool for robust analysis characteristic equation of delay differential equations. *URL<http://www.dimi.uniud.it/dimitri.breda/traceDDE.html>*, 2006.

[160] E. J. Routh. *A Treatise on the Stability of a Given State of Motion: Particularly Steady Motion.* Macmillan, 1877.

[161] A. Hurwitz. Ueber die bedingungen, unter welchen eine gleichung nur wurzeln mit negativen reellen theilen besitzt. *Math. Ann.*, 46(2):273–284, 1985.

[162] Q. I. Rahman and G. Schmeisser. *Analytic theory of polynomials. London Mathematical Society Monographs.* New Series 26. Oxford: Oxford University Press, 2002.

[163] R. Bellman and K. L. Cooke. *Differential-Difference Equations.* Academic Press, New York, 1963.

[164] C.E. Falbo. *Analytic and Numerical Solutions to the Delay Differential Equations.* Joint Meeting of the Northern and Southern California Sections of the MAA, San Luis Obispo, CA, 1995.

[165] J.H. Lambert. Observationes varies in mathesin puram. *Acta Helvetica, Physico-mathematico-anatomico-botanico-medica*, 3:128–168, 1758.

[166] S. Yi, A. G. Ulsoy, and P.W. Nelson. Solution of systems of linear delay differential equations via laplace transformation. *Proceedings of the 45th IEEE Conference on Decision & Control, San Diego, CA, USA*, pages 2433–2438, 2006.

[167] S. Yi and A. G. Ulsoy. Solution of a system of linear delay differential equations using the matrix lambert function. *Proceedings of the 2006 American Control Conference, Minnesota, USA*, pages 2433–2438, 2006.

[168] A. Bellen and S. Maset. Numerical solution of constant coefficient linear delay differential equations as abstract cauchy problems. *Numer. Math*, 84:351–374, 2000.

[169] D. Breda, S. Maset, and R. Vermiglio. Pseudospectral approximation of eigenvalues of derivative operators with non-local boundary conditions. *Appl. Numer. Math.*, 27(1):318–331, 2006.

[170] Lloyd N. Trefethen. *Spectral Methods in MATLAB.* Oxford Univ., Oxford, UK, 2000.

[171] J. Forde and P. Nelson. Applications of sturm sequences to bifurcation analysis of delay differential equation models. *J. Math. Anal. Appl.*, 300:273–284, 2004.

[172] N. Hayes. Roots of the transcendental equation associated to a certain difference-differential equation. *J. London Math. Soc*, 25:226–232, 1950.

[173] C.J. Rennie, P.A. Robinson, and J.J. Wright. Unified neurophysical model of EEG spectra and evoked potentials. *Biol. Cybern.*, 86:457–471, 2002.

[174] P.A. Robinson, C.J. Rennie, J.J. Wright, and P.D. Bourke. Steady states and global dynamics of electrical activity in the cerebral cortex. *Phys. Rev. E*, 58:3557–3571, 1998.

[175] P.L. Nunez. The brain wave equation: A model for the EEG. *Math.Biosc.*, 21:279–291, 1974.

[176] M. Breakspear, J. Roberts, J.R. Terry, S. Rodrigues, N. Mahant, and P.A. Robinson. A unifying explanation of primary generalized seizures through nonlinear brain modeling and bifurcation analysis. *Cereb. Cortex*, 16:1296–1313, 2006.

[177] D.A. Pizzagalli. *Electroencephalography and High-Density Electrophysiological Source Localization.* Handbook of Psychophysiology, 2007.

[178] J. Fell, G. Widman, B. Rehberg, C.E. Elger, and G. Fernandez. Human mediotemporal EEG characteristics during propofol anesthesia. *Biol.Cybern.*, 92:92–100, 2005.

[179] L.D. Lewis, V.S. Weiner, E.A. Mukamel, J.A. Donoghue, E.N. Eskandar, J.R. Madsen, W.S. Anderson, L.R. Hochberg, S.S. Cash, E.N. Brown, and P.L. Purdon. Rapid fragmentation of neuronal networks at the onset of propofol-induced unconsciousness. *Proc Natl Acad Sci USA*, 109(21):E3377–3386, 2012.

[180] F. H. Lopes da Silva, A. Hoeks, A. Smits, and L. H. Zetterberg. Model of brain rhythmic activity. *Kybernetik*, 15:24–37, 1974.

[181] P.L. Nunez. Toward a quantitative description of large-scale neocortical dynamic function and EEG. *Behav. Brain Sci.*, 23:371–437, 2000.

[182] O. David and K. J. Friston. A neural mass model for meg/eeg: coupling and neuronal dynamics. *NeuroImage*, 20:1743–1755, 2003.

[183] W.J. Freeman. A field-theoretic approach to understanding scale-free neocortical dynamics. *Biol. Cybern.*, 92:350–359, 2005.

[184] V.K. Jirsa. Neural field dynamics with local and global connectivity and time delay. *Philos. Trans. R. Soc. A.*, 367:1131–1143, 2009.

[185] M.R. Qubbaj and V.K. Jirsa. Neural field dynamics under variation of local and global connectivity and finite transmission speed. *Physica D.*, 238:2331–2346, 2009.

[186] P.A. Robinson, C.J. Rennie, and J.J. Wright. Propagation and stability of waves of electrical activity in the cerebral cortex. *Phys. Rev. E*, 56:826–840, 1997.

[187] C.J. Rennie, P.A. Robinson, and J.J. Wright. Effects of local feedback on dispersion of electrical waves in the cerebral cortex. *Phys. Rev. E*, 59:3320–3329, 1999.

[188] P.A. Robinson, J.J. Wright, and C.J. Rennie. Synchronous oscillations in the cerebral cortex. *Phys. Rev. E*, 57:4578–4588, 1998.

[189] Dimitris Pinotsis, Peter Robinson, Peter beim Graben, and Karl Friston. Neural masses and fields: Modelling the dynamics of brain activity. *Frontiers in Computational Neuroscience*, 8(149), 2014.

[190] D.A. Pinotsis and K.J. Friston. *Neural field modelling of the electroencephalogram: physiological insights and practical applications. In: Coombes, S., beim Graben, P., Potthast, R., Wright, J. (eds.) Neural Fields: Theory and Applications.* Springer, Berlin/Heidelberg, 2014.

[191] E.D. Lumer, G.M. Edelman, and G. Tononi. Neural dynamics in a model of the thalamocortical system. i. layers, loops and the emergence of fast synchronous rhythms. *Cereb. Cortex*, 7(207), 19997.

[192] P.A. Valdes, J.C. Jimenez, J. Riera, R. Biscay, and T. Ozaki. Nonlinear eeg analysis based on a neural mass model. *Biol. Cybern.*, 81:415–424, 1999.

[193] R.J. Moran, S.J. Kiebel, K.E. Stephan, R.B. Reilly, J.Daunizeau, and K.J. Friston. A neural mass model of spectral responses in electrophysiology. *NeuroImage*, 37:706–720, 2007.

[194] J.J. Riera, J.C. Jimenez, X. Wan, R. Kawashima, and T. Ozaki. Nonlinear local electrovascular coupling. II: From data to neuronal masses. *Hum. brain mapp*, 28:335–354, 2007.

[195] R.C. Sotero, J. Nelson, and N. J. Tujillo-Barreto. Biophysical model for integrating neuronal activity, EEG, fMRI and metabolism. *NeuroImage*, 39:290–309, 2008.

[196] S.J. Kiebel, M.I. Garrido, R. Moran, C.C. Chen, and K.J. Friston. Dynamic causal modeling for eeg and meg. *Hum. Brain Mapp*, 30:1866–1876, 2009.

[197] F. Freyer, J.A. Roberts, R. Becker, P.A. Robinson, P. Ritter, and M. Breakspear. Dynamic mechanisms of multistability in the human alpha rhythm. *J. Neurosci.*, 31:6353–6361, 2011.

[198] B.H. Jansen and V.G. Rit. Electroencephalogram and visual evoked potential generation in a mathematical model of coupled cortical columns. *Biol. Cybern*, 73:357–366, 1995.

[199] D.T.J. Liley, D.M. Alexander, J.J. Wright, and M.D. Aldous. Alpha rhythm emerges from large-scale networks of realistically coupled multicompartmental model cortical neurons. *Network: Comput. Neural Syst.*, 10:79–92, 1999.

[200] P.A. Robinson, C.J.Rennie, D.L.Rowe, S.C.O'Connor, and E. Gordon. Multiscale brain modelling. *Phil. Trans. R. Soc. B*, 360:1043–1050, 2005.

[201] R.C. Sotero, N. J. Tujillo-Barreto, and Y. turria Medina. Realistically coupled neural mass models can generate EEG rhythms. *Neural Comput.*, 19:479–512, 2007.

[202] W. Klimesch. Alpha-band oscillations, attention, and controlled access to stored information. *Trends Cogn Sci*, 16(12):606–617, 2012.

[203] O.M. Bazanovaa and D. Vernon. Interpreting eeg alpha activity. *Neuroscience and Biobehavioral Reviews*, 44:94–110, 2014.

[204] A.K.I. Chiang, C.J. Rennie, P.A. Robinson, J.A. Roberts, M.K. Rigozzi, R.W. Whitehouse, R.J. Hamilton, and E. Gordon. Automated characterization of multiple alpha peaks in multi-site electroencephalograms. *J. Neurosci. Methods*, 168:396–411, 2008.

[205] A.K.I. Chiang, C.J. Rennie, P.A. Robinson, S.J. van Albada, and C.C. Kerr. Age trends and sex differences of alpha rhythms including split alpha peaks. *Clin. Neurophysiol.*, 122:1505–1517, 2011.

[206] S.J. Van Albada, C.C. Kerr, A.K.I. Chiang, C.J. Rennie, and P.A. Robinson. Neurophysiological changes with age probed by inverse modeling of eeg spectra. *Clinical Neurophysiology*, 121:21–38, 2010.

[207] S.J. Van Albada and P.A. Robinson. Relationships between electroencephalographic spectral peaks across frequency bands. *Frontiers in Human Neuroscience*, 7(58), 2013.

[208] D. Steyn-Ross, M.L. Steyn-Ross, J.W. Sleigh, M. Wilson, I. Gillies, and J. Wright. The sleep cycle modelled as a cortical phase transition. *J. Biol. Phys.*, 31(3-4):547–569, 2005.

[209] A. Hutt, editor. *Sleep and Anesthesia: Neural Correlates in Theory and Experiment.* Number 15 in Springer Series in Computational Neuroscience. Springer, New York, 2011.

[210] M.L. Steyn-Ross, D.A. Steyn-Ross, and J.W. Sleigh. Modelling general anaesthesia as a first-order phase transition in the cortex. *Prog. Biophys. Molecul. Biol.*, 85(2-3):369–385, 2004.

[211] I. Bojak, H.Day, and D.T.J. Liley. Ketamine, propofol, and the EEG: aneural field analysisofhcn1-mediatedinteractions. *Front.Comput.Neurosci.*, 7(22), 2013.

[212] F. Wendling, F. Bartolomei, J.J. Bellanger, and P. Chauvel. Epileptic fast activity can be explained by a model of impaired gabaergic dendritic inhibition. *European Journal of Neuroscience*, 15(9):1499–1508, 2002.

[213] P. Suffczynski, S. Kalitzin, and F. H. Lopes da Silva. Dynamics of non-convulsive epileptic phenomena modelled by a bistable neuronal network. *Neuroscience*, 126:467–484, 2004.

[214] P. Suffczynski, S. Kalitzin, F. H. Lopes da Silva, J. Parra, D.Velis, and F. Wendling. Active paradigms of seizure anticipation: computer model evidence for necessity of stimulation. *Phys..Rev. E.*, 78:051917, 2008.

[215] M.T. Wilson, J.W. Sleigh, A. Steyn-Ross, and M.L. Steyn-Ross. General anesthetic-induced seizures can be explained by a mean-field model of cortical dynamics. *Anesthsiol.*, 104(3):588–593, 2006.

[216] B. Molaee-Ardekani, P. Benquet, F. Bartolomei, , and F. Wendling. Computational modeling of high-frequency oscillations at the onset of neocortical partial seizures: From 'altered structure' to 'dysfunction'. *NeuroImage*, 52:1109–1122, 2010.

[217] M.L. Steyn-Ross, D.A. Steyn-Ross, and J.W.Sleigh. Gap junctions modulate seizures in a mean-field model of general anesthesia for the cortex. *Cog. Neurodyn.*, 6(3):215–225, 2012.

[218] R.C. Sotero and R. Martinez-Cancino. Dynamical mean field model of a neural-glial mass. *Neural Comput.*, 22:969–997, 2009.

[219] A.J. Pons, J.L> Cantero, M. Atienza, and J. Garcia-Ojalvo. Relating structural and functional anomalous connectivity in the ageing brain via neural mass modelling. *NeuroImage*, 52:848–861, 2010.

[220] J. Modolo, B. Bhattacharya, R. Edwards, J. Campagnaud, A. Legros, and A. Beuter. Using a virtual cortical module implementing a neural field model to modulate brain rhythms in parkinson's disease. *Fron. in Neurosc.*, 4(45), 2010.

[221] B.S. Bhattacharya, Y. Cakir, N. Serap-Sengor, L. Maguire, and D. Coyle. Model-based bifurcation and power spectral analyses of thalamocortical alpha rhythm slowingin alzheimer's disease. *Neurocomputing*, 115:11–22, 2013.

[222] P.A. Robinson, A.J. Mandell, and R. Coppola. Multiscale brain modelling. *Front Comput Neurosci.*, 6(101), 2012.

[223] C.C. Kerr, S.J. Van Albada, S.A. Neymotin, G.L. Chadderdon, P.A. Robinson, and W.W. Lytton. Cortical information flow in parkinson's disease: a composite network/field model. *Front Comput Neurosci.*, 7(39), 2013.

[224] F. Mina, P. Benquet, A. Pasnicu, A. Biraben, and F. Wendling. Modulation of epileptic activity by deep brain stimulation: a model-based study of frequency-dependent effects. *Front Comput Neurosci*, 7(94), 2013.

[225] R. Srinivasan, S. Thorpe, and P.L. Nunez. Top-down influences on local networks: basic theory with experimental implications. *Front Comput Neurosci.*, 7(29), 2013.

[226] N.D. Schiff and F. Plum. The role of arousal and gating systems in the neurology of impaired consciousness. *Journal of Clinical Neurophysiology*, 17:438–452, 2000.

[227] R. Hindriks and M. J. A. M. van Putten. Thalamo-cortical mechanisms underlying changes in amplitude and frequency of human alpha oscillations. *Neuroimage*, 70:150–163, 2013.

[228] M. Steriade, D.A. McCormick, and T.J. Sejnowski. Thalamocortical oscillations in the sleeping and aroused brain. *Science*, 262:679–685, 1993.

[229] J.D. Victor, J.D. Drover, M.M. Conte, and N.D. Schiff. Mean-field modeling of thalamocortical dynamics and a model-driven approach to EEG analysis. *Proceed. Natl. Acad. Science USA*, 118:15631–15638, 2011.

[230] M. Steriade, D. Contreras, R. Curro Dossi, and A. Nunez. The slow ($<$ 1 hz) oscillation in reticular thalamic and thalamocortical neurons: scenario of sleep rhythm generation in interacting thalamic and neocortical networks. *J. Neurosci.*, 13(8):3284–3299, 1993.

[231] R.R. Llinás and M. Steriade. Bursting of thalamic neurons and states of vigilance. *J. Physiol.*, 95(6):3297–3308, 2006.

[232] S. Astori, R. Wimmer, and A. Luthi. Manipulating sleep spindles expanding views on sleep, memory, and disease. *Trends in Neurosciences*, 36(12):738–748, 2013.

[233] C.E. Stafstrom. Epilepsy: a review of selected clinical syndromes and advances in basic science. *Journal of Cerebral Blood Flow & Metabolism*, 26:983–1004, 2006.

[234] M. Steriade and I. Timofeev. Neuronal plasticity in thalamocortical networks during sleep and waking oscillations. *Neuron*, 37(8):563–576, 2003.

[235] Y. Chen, W.D. Parker, and K. Wang. The role of t-type calcium channel genes in absence seizures. *Front. Neurol.*, 5, 2014.

[236] X. Ma, Y. Zhang, Z. Yang, X. Liu, H. Sun, and et al. J. Qin. Childhood absence epilepsy: Elctroclinical features and diagnostic criteria. *Brain Dev.*, 33:114–119, 2011.

[237] R.R. Llinás, U. Ribary D. Contreras, and C. Pedroarena. Tthe neuronal basis for consciousness. *Philosophical Transactions of the Royal Society of London Series B: Biological Sciences*, 353:1841–1849, 1999.

[238] X. Liu, K.K. Lauer, B.D. Ward, S-J Li, and A.G. Hudetz. Differential effects of deep sedation with propofol on the specific and nonspecific thalamocortical systems: A functional magnetic resonance imaging study. *Anesthesilogy*, 118:59–69, 2013.

[239] U. León-Domínguez, A. Vela-Bueno, M. Froufé-Torres, and J. León-Carrión. A chronometric functional sub-network in the thalamo-cortical system regulates the flow of neural information necessary for conscious cognitive processes. *Neuropsychologia*, 51:13336–1349, 2013.

[240] S.M. Sherman and R. W. Guillery. The role of the thalamus in the flow of information to the cortex. *Philos. Trans. R. Soc. Lond. B. Biol. Sci.*, 357:1695–1708, 2002.

[241] M.A. Castro-Alamancos. Dynamics of sensory thalamocortical synaptic networks during information processing states. *Prog. Neurobiol.*, 74:231–247, 2004.

[242] Y.W. Lam and S.M. Sherman. Functional organization of the somatosensory cortical layer 6 feedback to the thalamus. *Cereb. Cortex 20*, 20:13–24, 2010.

[243] F. Crick. Function of the thalamic reticular complex: the searchlight hypothesiss. *Proc. Natl. Acad. Sci. U.S.A.*, 81:4586, 1984.

[244] A.B. Newberg and J. Iversen. The neural basis of the complex mental task of meditation: neurotransmitter and neurochemical considerations. *Medical Hypotheses*, 61(2):282–291, 2003.

[245] S. Kastner, Y.B. Saalmann, and K.A. Schneider. *Thalamic Control of Visual Attention.* Oxford University Press, 2012.

[246] J.H. Austin. Zen and the brain: mutually illuminating topics. *Front. Psychol.*, 4(784), 2013.

[247] M. Steriade, F. Amzica, and D. Contreras. Synchronization of fast (30-40hz) spontaneous cortical rhythms during brain activation. *J. Neurosci.*, 16:392–417, 1996.

[248] R.R. Llinás, U. Ribary, D. Jeanmonod, E. Kronberg, and P.P. Mitra. Thalamocortical dysrhythmia: a neurological and neuropsychiatric syndrome characterized by magnetoencephalography. *Proc Natl Acad Sci USA*, 96:1841–15227, 1999.

[249] Y. Banitt, K.A. Martin, and I. Segev. A biologically realistic model of contrast invariant orientation tuning by thalamocortical synaptic depression. *J. Neurosci.*, 27:10230–10239, 2007.

[250] H.P. Wang, D. Spencer, J.M. Fellous, and T.J. Sejnowski. Synchrony of thalamocortical inputs maximizes cortical reliability. *Science*, 328:106–109, 2010.

[251] R.M. Bruno. Synchrony in sensation. *Curr Opin Neurobiol*, 21:701–708, 2011.

[252] I. Timofeev, M. Bazhenov, J. Seigneur, and T. Sejnowski. Neuronal synchronization and thalamocortical rhythms in sleep, wake and epilepsy. *Jasper's Basic Mechanisms of the Epilepsies, 4th edition*, 2012.

[253] P. Fuentealba and M. Steriade. The reticular nucleus revisited: intrinsic and network properties of a thalamic pacemaker. *Prog. Neurobiol.*, 75:125–141, 2005.

[254] D. Pinault and T.J. O'Brien. Cellular and network mechanisms of genetically-determined absence seizures. *Thalamus Relat. Syst.*, 3:181–203, 2005.

[255] M. Steriade and D. Contreras. Relations between cortical and thalamic cellular events during transition from sleep patterns to paroxysmal activity. *J. Neurosci.*, 15:623–642, 1995.

[256] J.R. Huguenard and D. A. McCormick. Thalamic synchrony and dynamic regulation of global forebrain oscillations huguenard. *J. Physiol*, 26:994

[257] O. Steinlein. Genetic mechanisms that underlie epilepsy. *Nature Reviews Neuroscience*, 5:400–408, 2004.

[258] J.A. Roberts and P.A. Robinson. Modeling absence seizure dynamics: Implications for basic mechanisms and measurement of thalamocortical and corticothalamic latencies. *Journal of Theoretical Biology*, 253:189–201, 2008.

[259] A. Hutt, M. Hashemi, and P. beim Garben. *How to render neural field more realistic.* In: B. Bhattacharya and F. N. Chowdhury (Eds.), Validating Neuro Computational Models of Neurological and Psychiatric Disorders, Springer Series in Computational Neuroscience, 2015.

[260] A. Hutt and L. Buhry. Study of GABAergic extra-synaptic tonic inhibition in single neurons and neural populations by traversing neural scales: application to propofol-induced anaesthesia. *J. Comput. Neurosci.*, in press, 2014.

[261] A. Hutt. The population firing rate in the presence of GABAergic tonic inhibition in single neurons and application to general anaesthesia. *Cogn. Neurodyn.*, 6:227–237, 2012.

[262] W.J. Freeman. Nonlinear gain mediating cortical stimulus-response relations. *Biol. Cybern.*, 33:237–247, 1979.

[263] A. Hutt, M. Bestehorn, and T. Wennekers. Pattern formation in intracortical neuronal fields. *Network: Comput. Neural Syst.*, 14:351–368, 2003.

[264] J.A. Vizuete, S. Pillay, K.M. Ropella, and A.G. Hudetz. Graded defragmentation of cortical neuronal firing during recovery of consciousness in rats. *Neuroscience*, 275:340–351, 2014.

[265] M.L. Steyn-Ross, D.A. Steyn-Ross, and J.W. Sleigh. Interacting turing-hopf instabilities drive symmetry-breaking transitions in a mean-field model of the cortex: A mechanism for the slow oscillation. *Phys. Rev. X*, 3:021005, 2013.

[266] D.T.J. Liley and M. Walsh. The mesoscopic modeling of burst suppression during anesthesia. *Front. Comput. Neurosci.*, 7:46, 2013.

[267] S. G. Brickley and S. Mody. Extrasynaptic GABA$_A$ receptors: Their function in the cns and implications for disease. *Neuron*, 73:23–34, 2012.

[268] G. E. Hardingham and H. Bading. Synaptic versus extrasynaptic nmda receptor signalling: implications for neurodegenerative disorders. *Nature Rev. Neurosci.*, 11:682–696, 2012.

[269] D. Belelli, N. L. Harrison, J. Maguire, R. L. Macdonald, M. C. Walker, and D. W. Cope. Extra-synaptic GABA$_A$ receptors: form, pharmacology, and function. *J. Neurosc.*, 29(41):12757–12763, 2009.

[270] J. Y. T. Yeung, K. J. Canning, G. Zhu, P. Pennefather, J. F. Macdonald, and B. A. Orser. Tonically activated GABA$_A$ receptors in hippocampal neurons are high-affinity, low-conductance sensors for extracellular gaba. *Molec. Pharmacol.*, 63(1):2–8, 2003.

[271] S. G. Brickley, S. G. Cull-Candy, and M. Farrant. Development of a tonic form of synaptic inhibition in rat cerebellar granule cells resulting from persistent activation of GABA$_A$ receptors. *J. Physiol.*, 497(3):753–759, 1996.

[272] A. Semyanov, M. C. Walker, and D. M. Kullmann. GABA uptake regulates cortical excitability via cell-type specific tonic inhibition. *Nat. Neurosci.*, 6:484–490, 2003.

[273] A. Semyanov, M. C. Walker, D. M. Kullmann, and R. A. Silver. Tonically active GABAA receptors: modulating gain and maintaining the tone. *Trends Neurosc.*, 27(5):262–269, 2004.

[274] M. Kaneda, M. Farrant, and S. G. Cull-Candy. Whole-cell and single-channel currents activated by GABA and glycine in granule cells of the rat cerebellum. *J. Physiol.*, 485(2):419–435, 1995.

[275] P. Cavalier, M. Hamann, D. Rossi, P. Mobbs, and D. Attwell. Tonic excitation and inhibition of neurons: ambient transmitter sources and computational consequences. *Prog. Biophys. Mol. Biol.*, 87:3–16, 2005.

[276] M. Hamann, D. Rossi, and D. Attwell. Tonic and spillover inhibition of grnule cells control information flow through cerebellar cortex. *Neuron*, 33:625–633, 2002.

[277] M. Farrant and Z. Nusser. Variations on an inhibitory theme: phasic and tonic activation of GABA$_A$ receptors. *Nature Rev. Neurosci.*, 6:215–229, 2005.

[278] D. P. Bright, M. Renzi, J. Bartram, T. P. McGee, G. MacKenzie, A. M. Hosie, M. Farrant, and S. G. Brickley. Profound desensitization by ambient GABA limits activation of delta-containing GABA$_A$ receptors during spillover. *J. Neurosci.*, 31(2):753–763, 2011.

[279] Z. Nusser, S. Cull-Candy, and M. Farrant. Differences in synaptic GABA$_A$ receptor number underlie variation in GABA mini amplitude. *Neuron*, 19:697–709, 1997.

[280] D. P. Bright, M.I. Aller, and S.G. Brickley. Synaptic relase generates a tonic GABA$_A$ receptor-mediated conductance that modulates burst precision in thalamic relay neurons. *J. Neurosci.*, 27(10):2560–2569, 2007.

[281] M. V. Kopanitsa. Extrasynaptic receptors of neurotransmitters: Distribution, mechanisms of activation, and physiological role. *Neurophysiology*, 29(6):448–458, 1997.

[282] Z. Nusser, W. Sieghart, and P. Somogyi. Segregation of different GABA$_A$ receptors to synaptic and extrasynaptic membranes of cerebellar granule cells. *J. Neurosc.*, 18:1693–1703, 1998.

[283] W. Wei, N. Zhang, Z. Peng, C. R. Houser, and I. Mody. Perisynaptic localization of delta subunit-containing GABAA receptors and their activation by GABA spillover in the mouse dentate gyrus. *J. Neurosci.*, 23:10650–10661, 2003.

[284] Z. Ye, T.P. McGee, C.M. Houston, and S.G. Brickley. The contribution of δ subunit-containing GABA$_A$ receptors to phasic and tonic conductance changes in cerebellum, thalamus and neocortex. *Front. Neural Circ.*, 7:1–8, 2013.

[285] C.M. Houston, T.P. McGee, G. MacKenzie, K. Troyano-Cuturi, P. Mateos Rodriguez, E. Kutsarova, E. Diamanti, A.M. Hosie, N.P. Franks, and S.G. Brickley. Are extrasynaptic GABA$_A$ receptors important targets for sedative/hypnotic drugs ? *J. Neurosci.*, 32(11):3887–3897, 2012.

[286] D. Bai, G. Zhu, P.S. Pennefather, M. F. Jackson, J. F. MacDonald, and B.A. Orser. Distinct functional and pharmacological properties of tonic and quantal inhibitory postsynaptic currents mediated by $\gamma-$aminobutyric acid a receptors in hippocampal neurons. *Molec. Pharmacol.*, 59:814–824, 2001.

[287] S. J. McDougall, T. W. Bailey, D. Mendelowitz, and M. C. Andresen. Propofol enhances both tonic and phasic inhibitory currents in second-order neurons of the solitary tract nucleus (nts). *Neuropharmacol.*, 54:552–563, 2008.

[288] K Kretschmannova, R. M. Hines, R. Revilla-Sanchez, M. Terunuma, V. Tretter, R. Jurd, M. B. Kelz, S. J. Moss, and P. A. Davies. Enhanced tonic inhibition influences the hypnotic and amnestic actions of the intravenous anesthetics etomidate and propofol. *J. Neurosci.*, 33(17):7264–7273, 2013.

[289] T. Papouin, L. Ladépêche, J. Ruel, S. Sacchi, M. Labasque, M. Hanini, L. Groc, L. Pollegioni, J.-P. Mothet, and S.H.R. Oliet. Synaptic and extrasynaptic nmda receptors are gated by different endogeneous coagonists. *Cell*, 150:633–646, 2012.

[290] J.P. Mothet, A.T. Parent, H. Wolosker, R.O. Brady Jr., D.J. Linden, C.D. Ferris, M.A. Rogawski, and S.H. Snyder. d-serine is an endogenous ligand for the glycine site of the n-methyl-d-aspartate receptor. *Proc. Natl. Acad. Sci. USA*, 97:4926–4931, 2000.

[291] P. Sah, S. Hestrin, and R.A. Nicoli. Tonic activation of nmda receptors by ambient glutamate enhances excitability on neurons. *Science*, 246:815–818, 1989.

[292] T.M. Fleming, V. Scott, K. Naskar, N. J, Cl.H. Brown, and J.E. Stern. State-dependent changes in astrocyte regulation of extrasynaptic nmda receptor signalling in neurosecretory neurons. *J. Physiol.*, 589(16):3929–3941, 2011.

[293] K. Le Meur, M. Galante, M.-C. Angulo, and E. Audinat. Tonic activation of NMDA receptors by ambient glutamate of non-synaptic origin in the rat hippocampus. *J. Physiol.*, 580:373–383, 2007.

[294] A. Panatier, D.T. Theodosis, J.-P. Mothet, B. Touquet, L. Pollegioni, D.A. Poulain, and S.H.R. Oliet. Glia-derived d-serine controls nmda receptor activity and synaptic memory. *Cell*, 125(4):775–784, 2006.

[295] H. Wolosker, S. Blackshaw, and S.H. Snyder. Serine racemase: a glial enzyme synthesizing d-serine to regulate glutamate-n-methyl-d-aspartate neurotransmission. *Proc. Natl. Acad. Sci. USA*, 96:13409–13414, 1999.

[296] D.C. Martin, M. Plagenhoef, J. Abraham, R.L. Dennison, and R.S. Aronstam. Volatile anesthetics and glutamate activation of n-methyl-d-aspartate receptors. *Biochem Pharmacol.*, 49(6):809–817, 1995.

[297] S. Daniels and R.J. Roberts. Post-synaptic inhibitory mechanisms of anaesthesia: glycine receptors. *Toxicol. Lett.*, 100-101:71–76, 1998.

[298] J.W. Pender. Dissociative anesthesia. *Calif. Med.*, 113(5):73, 1970.

[299] R. Dickinson, B.K. Peterson, P. Banks, C. Simillis, J.C. Martin, C.A. Valenzuela, M. Maze, and N.P. Franks. Competitive inhibition at the glycine site of the n-methyl-d-aspartate receptor by the anesthetics xenon and isoflurane: evidence from molecular modeling and electrophysiology. *Anesthesiology*, 107(5):756–767, 2007.

[300] S. Kratzer, C. Mattusch, E. Kochs, M. Eder, R. Haseneder, and G. Rammes. Xenon attenuates hippocampal long-term potentiation by diminishing synaptic and extrasynaptic n-methyl-d- aspartate receptor currents. *Anesth.*, 116(3):673–682, 2012.

[301] S. Coombes. Neural Fields. *Scholarpedia*, 1(6):1373, 2006.

[302] J.A. Talavera, S.K. Esser, F. Amzica, S. Hill, and J.F. Antognini. Modelingthe GABAergic action of etomidate on the thalamocortical system. *Anesth Analg.*, 108:160–167, 2009.

[303] B.W. Johnson, J.W. Sleigh, I.J. Kirk, and M.L. Williams. High-density EEG mapping during general anaesthesia with xenon and propofol: a pilot study. *Anaesth Intensive Care.*, 31(2):155–163, 2003.

[304] M. Hashemi and A. Hutt. *A thalamocortical model to explain EEG during anaesthesia.* In: International Symposium Selforganization in Complex Systems: The Past, Present, and Future of Synergetics, Delmenhorst, 2013.

[305] A. Destexhe, D. Contreras, and M. Steriade. Mechanisms underlying the synchronizing action of corticothalamic feedback through inhibition of thalamic relay cells. *J. Neurophysiol.*, 79:999–1016, 1999.

[306] D. Contreras, A. Destexhe, T.J. Sejnowski, and M. Steriade. Control of spatiotemporal coherence of a thalamic oscillation by corticothalamic feedback. *Science*, 274:771–774, 1996.

[307] C.V. Mulholland, A.A. Somogyi, D.T. Barratt, J.K. Coller, M.R. Hutchinson, G.M. Jacobson, R.T. Cursons, and J.W. Sleigh. Association of innate immune single-nucleotide polymorphisms with the electroencephalogram during desflurane general anaesthesia. *J. Mol. Neurosci.*, 52(4):497–506, 2014.

[308] A.H. Taub, Y. Katz, and I. Lampl. Cortical balance of excitation and inhibition is regulated by the rate of synaptic activity. *J. Neurosci.*, 33:14359–14368, 2013.

[309] M. Okun and I. Lampl. Instantaneous correlation of excitation and inhibition during ongoing and sensory-evoked activities. *Nat. Neurosci.*, 11:535–537, 2008.

[310] M. Kelz, Y. Sun, J. Chen, Q. Cheng Meng, J.T. Moore, S.C. Veasey, S. Dixon, M. Thornton, H. Funato, and M. Yanagisawa. An essential role for orexins in emergence from general anesthesia. *Proc. Natl. Acad. Sci. U S A*, 105(4):1309–1314, 2008.

[311] H.T. Nguyen, K.Y. Li, R.L. da Graca, E. Delphin, M. Xiong, and J.H. Ye. Behavior and cellular evidence for propofol-induced hypnosis involving brain glycine receptors. *Anesthesiology*, 110(2):326–332, 2009.

[312] J.W. Lynch. Molecular structure and function of the glycine receptor chloride channel. *Physiol. Rev.*, 84(4):1051–1095, 2004.

[313] C. Grasshoff, B. Drexler, U. Rudolph, and B. Antkowiak. Anaesthetic drugs: linking molecular actions to clinical effects. *Curr. Pharm. Des.*, 12(28):3665–3679, 2006.

[314] R.H. Granger and R.A. Hearn. Models of thalamocortical system. *Scholarpedia*, 2(11):1796, 2007.

[315] H.W. Magoun. An ascending reticular activating system in the brain stem. *AMA Arch. Neurol. Psych.*, 67(2):145–154, 1952.

[316] G. Vanini and H.A. Baghdoyan. Extrasynaptic GABA$_A$ receptors in rat pontine reticular formation increase wakefulness. *Sleep*, 36(3):337–343, 2013.

[317] P. Fiset, T. Paus, T. Daloze, G. Plourde, P. Meuret, V. Bonhomme, N. Hajj-Ali, S.B. Backman, and A.C. Evans. Brain mechanisms of propofol-induced loss of consciousness in humans: a positron emission tomographic study. *J. Neurosci.*, 19(13):5506–5513, 1999.

[318] F.Z. Laalou, A.P. de Vasconcelos, P. Oberling, H. Jeltsch, J.C. Cassel, and L. Pain. Involvement of the basal cholinergic forebrain in the mediation of general (propofol) anesthesia. *Anesthesiology*, 108(5):888–896, 2008.

[319] M. Byoung-Kyong. A thalamic reticular networking model of consciousness. *Theor Biol Med Model*, 7, 2010.

[320] O. David, S. J. Kiebel, L. M. Harrison, J. Mattout, J. M. Kilner, and K. J. Friston. Dynamic causal modeling of evoked responses in eeg and meg. *NeuroImage*, 30:1255–1272, 2006.

[321] M. D. Reed, T. S. Yamashita, C. M. Marx, C. M. Myers, and J.L. Blumer. A pharmacokinetically based propofol dosing strategy for sedation of the critically ill, mechanically ventilated pediatric patient. *Crit. Care Med.*, 24(9):1473–1481, 1996.

[322] E. A. Mukamel, E. Pirondini, B. Babadi, K. F. k. Wong, E.T. Pierce, P.G. Harrell, J.L. Walsh, A.F. Salazar-Gomez, S.S. Cash, E.N. Eskandar, V.S. Weiner, E.N. Brown, and P.L. Purdon. A transition in brain state during propofol-induced unconsciousness. *Journal of Neuroscience.*, 34(3):839–845, 2014.

[323] M. Massimini, F. Ferrarelli, R. Huber, S. K. Esser, H. Singh, and G. Tononi. Breakdown of cortical effective connectivity during sleep. *Science*, 309:2228–2232, 2005.

[324] P. S. Garcia, S. E. Kolesky, and A. Jenkins. General anesthetic actions on GABA$_A$ receptors. *Curr. Neuropharmacol.*, 8(1):2–9, 2010.

[325] A. Spiegler, S.J. Kiebel, F.M. Atay, and T.R. Knosche. Bifurcation analysis of neural mass models: Impact of extrinsic inputs and dendritic time constants. *NeuroImage*, 52(3):1041–1058, 2010.

[326] A. Spiegler, T.R. Knosche, K. Schwab, J. Haueisen, and F.M. Atay. Modeling brain resonance phenomena using a neural mass model. *PLoS Comput. Biol.*, 7(12):e1002298, 2011.

[327] U. Lee, G. Oh, S. Kim, G. Noh, B. Choi, and G. A. Mashour. Brain networks maintain a scale-free organization across consciousness, anesthesia, and recovery: Evidence for adaptive reconfiguration. *Anesthesiology*, 113(5):1081–1091, 2010.

[328] J. M. Siegel. Sleep viewed as a state of adaptive inactivity. *Nature Rev. Neurosci.*, 10:747–753, 2009.

[329] T. Wieloch and K. Nikolich. Mechanisms of neural plasticity following brain injury. *Current Opinion in Neurobiology*, 16(3):258–264, 2006.

[330] T.T. Dang-Vu, M. Schabus, M. Desseilles, G. Albouy, M. Boly, A. Darsaud, S. Gais, G. Rauchs, V. Sterpenich, G. Vandewalle, J. Carrier, G. Moonen, E. Balteau, C. Degueldre, A. Luxen, C. Phillips, and P. Maquet. Spontaneous neural activity during human slow wave sleep. *Proc. Natl. Acad. Sci. USA*, 105(39):15160–15165, 2008.

[331] P. Maquet, C. Degueldre, G. Delfiore, J. Aerts, J. Peters, A. Luxen, and G. Franck. Functional neuroanatomy of human slow wave sleep. *J. Neurosci.*, 17(8):2807–2812, 1997.

[332] K.J. Friston, L. Harrison, and W. Penny. Dynamic causal modelling. *NeuroImage.*, 19:273–1302, 2003.

[333] I-C. Chou and E.O. Voit. Recent developments in parameter estimation and structure identification of biochemical and genomic systems. *Math Biosci*, 219(2):57–83, 2014.

[334] A. F. Villaverde and J.R. Banga. Reverse engineering and identification in systems biology: strategies, perspectives and challenges. *Journal of The Royal Society Interface*, 11(91), 2013.

[335] J. Sun, J.M. Garibaldi, and C. Hodgman. Parameter estimation using metaheuristics in systems biology: A comprehensive review. *IEEE/ACM Transactions Computational Biology and Bioinformatics*, 9(1):185–202, 2012.

[336] Jun Sun, Vasile Palade, Yujie Cai, Wei Fang, and Xiaojun Wu. Biochemical systems identification by a random drift particle swarm optimization approach. *BMC bioinformatics*, 15(Suppl 6):S1, 2014.

[337] E Balsa-Canto, J R Banga, J A Egea, A Fernandez-Villaverde, and G M de Hijas-Liste. Global optimization in systems biology: Stochastic methods and their applications. *Advances in Systems Biology (Advances in Experimental Medicine and Biology)*, 736:409–424, 2012.

[338] Carl-Magnus Svensson, Stephen Coombes, and Jonathan Westley Peirce. Using Evolutionary Algorithms for Fitting High-Dimensional Models to Neuronal Data. *Neuroinformatics*, 10(2):199–218, 2012.

[339] K.-Y. Tsai and F.-S. Wang. Evolutionary optimization with data collocation for reverse engineering of biological networks. *Bioinformatics*, 21(7):1180–1188, 2005.

[340] D.M. Bates and D.G. Watts. *Nonlinear Regression Analysis and its Applications.* Wiley, 1988.

[341] J. Aldrich. R. a. fisher and the making of maximum likelihood 1912-1922. *Stat. Sci.*, 12(3):162–176, 1997.

[342] S.M. Kay. *Fundamentals of Statistical Signal Processing: Estimation Theory.* Prentice-Hall, Upper Saddle River, New Jersey, 1993.

[343] L. Ljung. *System Identification: Theory for the User.* Prentice Hall, Englewood Cliffs, NJ., 1999.

[344] In Jae Myung. Tutorial on maximum likelihood estimation. *Journal of Mathematical Psychology*, 47(1):90–100, 2003.

[345] F.J. Samaniego. *Comparison of the Bayesian and Frequentist Approaches to Estimation.* Springer, New York, 2010.

[346] D.M. Bates and D.G. Watts. Relative curvature measures of nonlinearity. *J R Stat Soc Ser B (Methodological)*, 42(1):1–25, 1980.

[347] E. Walter and L. Pronzato. *Identification of Parametric Models from Experimental Data.* Springer, 1997.

[348] L. Hamm, B.W. Brorsen, and M.T. Hagan. Comparison of stochastic global optimization methods to estimate neural network weights. *Neural Process Lett.*, 26:145–158, 2007.

[349] H. Horst and H. Tuy. *Global optimization: Deterministic approaches.* Springer-Verlag, Berlin, 1990.

[350] I.E. Grossmann. *Global optimization in engineering design.* Kluer Academic Publishers, Dordrecht, The Netherlands, 1996.

[351] C. Guus, E. Boender, and H.E. Romeijn. *Stochastic method. In Handbook of global optimization.* Kluer Academic Publishers, Dordrecht, The Netherlands, 1995.

[352] M.M. Ali, C. Storey, and A. Torn. Application of stochastic global optimization algorithms to practical problems. *J. Optim. Theory Appl.*, 95:545–563, 19997.

[353] A. Torn, M. Ali, and S. Viitanen. Stochastic global optimization: Problem classes and solution techniques. *L. Global Opt.*, 14:437–447, 1999.

[354] C.A. Floudas and C. E. Gounaris. A review of recent advances in global optimization. *J Glob Optim*, (45):3–38, 2009.

[355] L. Ming-Hua, T. Jung-Fa, and Y. Chian-Son. A review of deterministic optimization methods in engineering and management. *Mathematical Problems in Engineering*, page 15 pages, 2012.

[356] Panos M. Pardalos, H. Edwin Romeijn, and Hoang Tuy. Recent developments and trends in global optimization. *Journal of Computational and Applied Mathematics*, 124(1):209–228, 2000.

[357] I. Papamichail and C.S. Adjiman. Global optimization of dynamic systems. *Computers & Chemical Engineering*, 28(3):403–415, March 2004.

[358] D. Lera and Ya. Dergeyev. Lipschitz and holder global optimization using space-filling curves. *Appl Numer Math*, 60:115–129, 2010.

[359] A. Georgieva and I. Jordanov. Global optimization based on novel heuristics, low-discrepancy sequences and genetic algorithms. *Eur J Oper Res*, 196:413–422, 2009.

[360] Erik Cuevas, Alonso Echavarria, and Marte A. Ramirez-Ortegon. An optimization algorithm inspired by the States of Matter that improves the balance between exploration and exploitation. *Applied Intelligence*, 40(2):256–272, 2014.

[361] D. Corne, M. Dorigo, and F. Glover. *New ideas in optimization.* McGraw-Hill, New York, 1999.

[362] D. B. Fogel. *Evolutionary computation: Toward a new philosophy of machine intelligence.* IEEE Press, New Yourk, 2000.

[363] S.H. Brooks. A discussion of random methods foe seeking maxima. *Op. Res.*, 6:244–251, 1958.

[364] J. Matyas. Random optimization. *Automat. Remote Control*, 26:246–253, 1965.

[365] L.A. Rastrigin and Y. Rubinstein. The comparison of random search and stochastic approximation while solving the problem of optimization. *Automat. Remote Control*, 2:23–29, 1969.

[366] A.A. Torn. *Global optimization as a combination of global and local search.* Gothenburg, Sweden, 1973.

[367] A.H.G. Rinnooy-Kan and G.T. Timmer. Stochastic global optimization. *Computer Meth. Appl. Mech. Eng.*, 186:125–140, 1987.

[368] A. Gilman and J. Ross. Genetic-algorithm selection of a regulatory structure that directs flux in a simple metabolic model. *Biophys. J.*, 69:1321–1333, 1995.

[369] L. J. Park, C. H. Park, C. Park, and T. Lee. Application of genetic algorithms to parameter estimation of bioprocesses. *Biol. Eng. Comput.*, 35:57–49, 1997.

[370] J. Pinchuk, W. A. Brown, S.M. Hughes, and D.G. Cooper. Modeling of biological process using self-cycling fermentation and genetic algorithm. *Biotechnol. Bioeng.*, 67:19–24, 2000.

[371] O. R. Gonzalez, C. Kuper, K. Jung, P. C. Naval, and E. Mendoza. Parameter estimation using Simulated Annealing for S-system models of biochemical networks. *Bioinformatics*, 23(4):480–486, 2007.

[372] J. Vesterstram and R. Thomsen. A comparative study of differential evolution, particle swarm optimization, and evolutionary algorithms on numerical benchmark problems. *IEEE Congress on Evolutionary Computation - CEC*, pages 1980–1987, 2004.

[373] P. J. Angeline. Evolutionary optimization versus particle swarm optimization: Philosophy and performance differences. *Evolutionary Programming VII*, 1447:601–610, 2005.

[374] M. A. Panduro, C. A. Brizuela, L. I. Balderas, and D. A. Acosta. A comparison of genetic algorithms, particle swarm optimization and the differential evolution method for the design of scannable circular antenna arrays. *Progress In Electromagnetics Research B*, 13:171–186, 2009.

[375] W.H. Press, S.A. Teukosky, W.T. Vetterling, and B.P. Flannery. *Numerical Recipes in C.* Cambridge University Press, second edition, 1992.

[376] J. Dennis and R. Schnabel. *Numerical Methods for Unconstrained Optimization and Nonlinear Equations.* Classics in Applied Mathematics. SIAM Publications, Philadelphia, 1996.

[377] K. Levenberg. A method for the solution of certain nonlinear problems in least squares. *Quart. Appl. Math.*, 2:164–168, 1944.

[378] K. Madsen, N.B. Nielsen, and O. Tingleff. *Methods for nonlinear least squares problems.* Technical Report. Informatics and Mathematical Modeling, Technical University of Denmark,, 2004.

[379] M. I. A. Lourakis and A. A. Argyros. Is levenberg-marquardt the most efficient optimization algorithm for implementing bundle adjustment? *Proceedings of the Tenth IEEE International Conference on Computer Vision, Washington, DC, USA*, 2:1526– 1531, 2005.

[380] D. W. Marquardt. An algorithm for least squares estimation of nonlinear parameters. *SIAM J. Appl. Math.*, 11:431–441, 1963.

[381] Henri Gavin. The levenberg-marquardt method for nonlinear least squares curve-fitting problems. *Department of Civil and Environmental Engineering, Duke University*, pages 1–15, 2011.

[382] W.T. Reeves. Particle systems. a technique for modeling a class of fuzzy objects. *CM Transactions on Graphics*, 2:91–108, 1983.

[383] C.W. Reynolds. Flocks, herds and schools: a distributed behavioural model. *Computer Graphics*, 21:25–34, 1987.

[384] F. Heppner and U. Grenander. *a stochastic nonlinear model for coordinated bird flocks.* In S. Krasner, Ed., The Ubiquity of Chaos, AAAS Publications, Washington DC, 1990.

[385] J. Kennedy and R.C. Eberhart. Particle swarm optimization. *In Proceedings of IEEE International Conference on Neural Networks*, pages 1942–1948, 1995.

[386] Y. Shi and R. C. Eberhart. A modified particle swarm optimizer. *Proceedings of the IEEE Congress on Evolutionary Computation, Piscataway, USA*, pages 69–73, 1998.

[387] Y. Shi and R.C. Eberhart. Fuzzy adaptive particle swarm optimization. *Proceedings of the Congress on Evolutionary Computation, IEEE Press, Seoul, Korea*, pages 101–106, 2001.

[388] R. C. Eberhart and Y. Shi. Particle swarm optimization: Developments, applications and resources. *Proceedings of the IEEE Congress on Evolutionary Computation, IEEE Press, Seoul, Korea*, 2001.

[389] M. Clerc and J. Kennedy. The particle swarm-explosion, stability, and convergence in a multidimensional complex space. *IEEE Transactions on Evolutionary Computation*, 6(1):58–73, 2002.

[390] J. Kennedy and R. Mendes. Population structure and particle swarm performance. *In Proceedings of the Congress on Evolutionary Computation*, pages 1671–1676, 19920025.

[391] R. Mendes, J. Kennedy, and J. Neves. The fully informed particle swarm: simpler, maybe better. *IEEE Transactions on Evolutionary Computation*, 8(3):204–210, 2004.

[392] F. van den Berghand and A.P. Engelbrecht. cooperativeapproach to participle swam optimization,. *IEEE Transactions on Evolutionary Computation*, 8(3):225–239, 2004.

[393] D. Bratton and J. Kennedy. Nonlinear inertia weight variation for dynamic adaptation in particle swarm optimization. *In Proceedings of the 2007 IEEE Swarm Intelligence Symposium*, 33(3):859–871, 2006.

[394] Hui Liu, Zixing Cai, and Yong Wang. Hybridizing particle swarm optimization with differential evolution for constrained numerical and engineering optimization. *Applied Soft Computing*, 10(2):629–640, 2010.

[395] Y. Wang, B. Li, T. Weise, J. Wang, B. Yuan, and Q. Tian. Self-adaptive learning based particle swarm optimization,. *Information Sciences*, 181(20):4515–4538, 2011.

[396] G. Wu, W. Pedrycz, M. Ma, D. Qiu, H. Li, and J. Liu. A particle swarm optimization variant with an inner variable learning strategy. *ScientificWorldJournal*, 2014, 2014.

[397] R. Poli, J. Kennedy, and T. Blackwell. Particle swarm optimization. *Swarm Intelligence*, 1:33–57, 2007.

[398] A. Banks, J. Vincent, and C. Anyakoha. Defining a standard for particle swarm optimization. *Natural Computing*, 6(4):120–127, 2007.

[399] M.E. H. Pedersen. *Tuning & Simplifying Heuristical Optimization (PhD thesis)*. School of Engineering Sciences, University of Southampton, England, 2010.

[400] R. C. Eberhart, P. Simpson, and R. Dobbins. Computational intelligence pc tools. *AP Professional, San Diego, CA, Chapter 6*, pages 212–226, 1996.

[401] F. van den Berghand and A.P. Engelbrecht. A study of particle swarm optimization particle trajectories. *Information Sciences*, 176(8):937–971, 2006.

[402] R.C. Eberhart and Y. Shi. Comparing inertia weights and constriction factors in particle swarm optimization. pages 84–88, 2000.

[403] R.E. Perez and K. Behdinanb. Particle swarm approach for structural design optimization. *IComputers & Structures*, 85(19-20):1579–1588, 2007.

[404] Dong ping Tian. A Review of Convergence Analysis of Particle Swarm Optimization. *International Journal of Grid and Distributed Computing*, 6(6):117–128, 2013.

[405] A. Banks, J. Vincent, and C. Anyakoha. A review of particle swarm optimization-part i: background and development. *Natural Computing*, 6(4):467–484, 2007.

[406] A. Banks, J. Vincent, and C. Anyakoha. A review of particle swarm optimization-part i: hybridisation, combinatorial, multicriteria and constrained optimization, and indicative applications. *Natural Computing*, 7(1):109–124, 2008.

[407] R. Storn and K. Price. Differential evolution-a simple and efficient heuristic for global optimization over continuous spaces. *J. Global. Optim.*, 11:341–359, 1997.

[408] D. Zaharie. Control of population diversity and adaptation in differential evolution algorithms. *in Proc. Mendel 9th Int. Conf. Soft Comput., R. Matousek and P. Osmera, Eds., Brno, Czech Republic*, pages 41–46, 2003.

[409] J. Liu and J. Lampinen. A fuzzy adaptive differential evolution algorithm. *Soft Comput.*, 9(6):448–462, 2005.

[410] A. Qin, V.L. Huang, and P.N. Suganthan. Differential evolution algorithm with strategy adaptation for global numerical optimization. *IEEE TRANSACTIONS ON EVOLUTIONARY COMPUTATION*, 13(2):398–417, 2009.

[411] C.P. Robert and G. Casella. *Monte Carlo Statistical Methods*. Springer Verlag, second edition, 2004.

[412] W.R. Gilks, S. Richardson, and D.J. Spiegelhalter. *Markov Chain Monte Carlo in Practice.* Chapman & Hall/CRC, New York, USA, 1996.

[413] N. Metropolis, A.W. Rosenbluth, M.N. Rosenbluth, and E. Teller. Equation of state calculations by fast computing machines. *J. Chem. Phys.*, 21:1087–1092, 1953.

[414] W.K. Hastings. Monte carlo sampling methods using markov chains and their applications. *Biometrika*, 57(1):97–109, 1970.

[415] A. Gelman, J.B. Carlin, H.S. Stern, and D.B. Rubin. *Bayesian Data Analysis*. 2nd Ed.Chapman & Hall, 2004.

[416] S. Kirkpatrick, C.D. Gellatt, and M.P. Vecchi. Optimization by simulated annealing. *Science*, 220:671–680, 1983.

[417] K.A.P. McLean and K.B. McAuley. Mathematical modelling of chemical processes- obtaining the best model predictions and parameter estimates using identifiability and estimability procedures. *Can. J. Chem. Eng.*, 90:120, 2012.

[418] S. Vajda, H. Rabitz, E. Walter, and Y. Lecourtier. Qualitative and quantitative identifiability analysis of nonlinear chemical kinetic-models. *Chem. Eng. Commun.l*, 83(1):191–219, 1989.

[419] O-T. Chis, J. Banga, and E. Balsa-Canto. Structural identifiability of systems biology models: a critical comparison of methods. *PLos ONE*, 6:e27755, 2011.

[420] J.A. Jacquez and P. Greif. Numerical parameter identifiability and estimability: integrating identifiability, estimability, and optimal sampling design. *Math. Biosci.*, 77:201–227, 1985.

[421] A. Raue, C. Kreutz, T. Maiwald, U. Klingmuller, and J. Timmer. Addressing parameter identifiability by model-based experimentation. *IET Syst. Biol*, 5(2):120, 2011.

[422] A. Raue, C. Kreutz, T. Maiwald, J. Bachmann, M. Schilling, and U. Klingmuller J. Timmer. Structural and practical identifiability analysis of partially observable dynamical models by exploiting the profile likelihood. *Bioinformatics*, 25:1923–1929, 2009.

[423] T. Quaiser and M. Monnigmann. Systematic identifiability testing for nambiguous mechanistic modeling - application to JAK-STAT, MAP kinase, and NF-kB signaling pathway models. *BMC Syst. Biol.*, 3:50, 2009.

[424] M.S. Grewal and K. Glover. Identifiability of linear and nonlinear dynamical systems. *IEEE Trans. Auto. Control*, 21(6):833–836, 1976.

[425] H. Pohjanpalo. System identifiability based on power series expansion of solution. *Math. Biosci.*, 41(1-2):21–33, 1978.

[426] S. Vajda, K. R. Godfrey, and H. Rabitz. Similarity transformation approach to identifiability analysis of nonlinear compartmental-models. *Math. Biosci.*, 93(2):217–248, 1989.

[427] M.J. Chappell and K. R. Godfrey. Structural identifiability of the parameters of a nonlinear batch reactor model. *Math. Biosci.*, 108(2):21–33, 1992.

[428] L. Ljung and T. Glad. On global identifiability for arbitrary model parametrisations. *Automatica*, 30(2):265–276, 1994.

[429] D. Dochain, P.A. Vanrolleghem, and M. Van Daele. Structural identifiability of biokinetic models of activated sludge respiration. *Water Res.*, 29(11):2571–2578, 1995.

[430] B. Petersen, K. Gernaey, M. Devisscher, D. Dochain, and P. A. Vanrolleghem. Practical identifiability of model parameters by combined respirometric-titrimetric measurements. *Water Sci. Technol.*, 43(7):347–355, 2001.

[431] K.E. Hines, T.R. Middendorf, and R.W. Aldrich. Determination of parameter identifiability in nonlinear biophysical models: A bayesian approach. *J. Gen. Physiol..*, 143(3):401–16, 2014.

[432] J.E. Jimenez-Hornero, I. M. Santos-Duenas, and I. Garcia-Garcia. Structural identifiability of a model for the acetic acid fermentation process. *Math. Biosci*, 216(2):154–162, 2008.

[433] J.E. Jimenez-Hornero, I. M. Santos-Duenas, and I. Garcia-Garcia. Optimisation of biotechnological processes. the acetic acid fermentation. part ii: Practical identifiability analysis and parameter estimation. *Biochem. Eng. J.*, 45(1):7–21, 2009.

[434] N.R. Draper and H. Smith. *Applied Regression Analysis.* New York: John Wiley & Sons, 1998.

[435] J.O. Rawlings, S.G. Pantula, and Dickey DA. *Applied Regression Analysis: A Research Tool.* New York, NY: Springer-Verlag, 1998.

[436] S. Marsili-Libelli, S. Guerrizio, and N. Checchi. Confidence regions of estimated parameters for ecological systems. *Ecological Modelling*, 165:127–146, 2003.

[437] G.A.F. Seber and C.J. Wild. *Non Linear Regression.* Wiley, New York, 1997.

[438] G.C. Goodwin and R.L. Payne. *Dynamic System Identification, Experimental Design and Data Analysis.* Academic Press, New York, 1997.

[439] A. Munak. *Optimisation of sampling.* Biotechnology, A Multi-Volume Comprehensive Treatise, Vol. 4. Measuring, Modelling and Control. VCH, Weinheim, 1999.

[440] D. Dochain and P.A. Vanrolleghem. *Dynamical Modelling and Estimation in Wastewater Treatment Processes*, volume 165. IWA Publishing, London, 2001.

[441] J.R. Donaldson and R.B. Schnabel. Computational experience with confidence regions and confidence intervals for nonlinear least squares, in proceedings of 17th symposium on the interface of computer sciences and statistics. *Lexington, Kentucky,*, pages 83–93, 1985.

[442] K. Schmeink, R. Adam, and P. A. Hoeher. Joint communication and positioning based on soft channel parameter estimation. *EURASIP Journal on Wireless Communications and Networking*, 185, 2011.

[443] Marcio Schwaab, Evaristo Chalbaud Biscaia, Jr., Jose Luiz Monteiro, and Jose Carlos Pinto. Nonlinear parameter estimation through particle swarm optimization. *Chemical Engineering Science*, 63(6):1542–1552, 2008.